UNIVERSITY of CALIFORNIA
SANTA CRUZ

A STUDY OF TEV EMISSION FROM THE CRAB NEBULA AND SELECTED AGN USING THE MILAGRO GAMMA-RAY OBSERVATORY

A dissertation submitted in partial satisfaction of the
requirements for the degree of

DOCTOR OF PHILOSOPHY

in

PHYSICS

by

Wystan Benbow

December 2002

The dissertation of Wystan Benbow is approved:

Professor David E. Dorfan, Chair

Professor David Williams

Professor George Blumenthal

Frank Talamantes
Vice Provost and Dean of Graduate Studies

Table of Contents

List of Figures

List of Tables

Abstract

A Study of TeV Emission from the Crab Nebula and Selected AGN Using the Milagro Gamma-Ray Observatory

by

Wystan Benbow

The Milagro gamma-ray observatory, located near Los Alamos, New Mexico, employs a water-Cherenkov technique to continuously monitor the northern sky for astrophysical gamma-ray emission near 1 TeV. Milagro's high duty-cycle ($\sim$95%) and wide aperture ($\sim$2 sr) allow for the detection of flaring behavior associated with TeV active galactic nuclei, even during daytime transits. A search is performed with the Milagro 2000-2002 data set for TeV emission from the Crab Nebula and 27 selected AGN. The detection of both the Crab Nebula and Markarian 421, during its bright flare in early 2001, is reported. The fluxes from these two detections, as well as upper limits on the flux for the 26 undetected AGN, are presented.

To my mother, Camilla

Acknowledgments

There are many people and places that have played an important role in my career as a graduate student. I am thankful to all of them, however several deserve special mention, as their assistance was crucial to the completion of my career as a graduate student.

First and foremost, I would like to thank my adviser David Williams. David has spent countless hours mentoring and assisting me during my time at UCSC. It feels like his door is always open to help me. David's knowledge, advice, patience, and kind nature have been essential to my development as a scientist. Without it, none of my accomplishments would have been possible. The time David spent helping me, whether it was to attain funding, evaluate my ideas, revise my thesis, or to provide answers to my seemingly endless list of questions, is greatly appreciated and will not be forgotten.

I would also like to thank Don Coyne. Don played a large part in recruiting me to UCSC and getting me involved in Milagro. At the time I applied to UCSC, I didn't even know where Santa Cruz was and had never heard of Milagro. However, one phone call from Don was all it took for me to make UCSC my choice for graduate school and Milagro the choice for my research. I never reconsidered or regretted these choices and am extremely grateful that I made them. Don also deserves thanks because he served as my adviser during my first years at UCSC and was on my orals committee. The patience and kindness he has always shown me, especially during those early years which were very difficult for me on many levels, is sincerely appreciated.

Dave Dorfan also deserves special thanks. Although his physics knowledge is tremendous, Dave always felt like more of a friend than a faculty member. He was always willing to listen when personal things were going badly, as well as to discuss Milagro and teaching. Dave is also one of the few people in Santa Cruz that I am able to carry a good conversation with about sports, especially football. It was always a pleasure when he would stop by my office to chat. Dave was also on both my orals and reading committees and deserves thanks for spending the time listening to my lengthy presentations. I am glad to have gotten to know Dave, which is an achievement in and of itself, and will miss him as I venture onward in life.

I would also like to thank George Blumenthal for being on both my orals and reading committees. My presentations and thesis were not short, and the time that he spent reading and listening is appreciated. The many members of the Milagro collaboration, past and present, also deserve thanks as they are a great group of people to work with and have provided much constructive criticism of my research. They are always great fun to hang out with at conferences, collaboration meetings,

and during summers and shifts in Los Alamos. I am particularly thankful to Joe McCullough, Morgan Wascko, and Stefan Westerhoff. Not only are they great friends, but they provided me housing in Los Alamos, as well as useful advice and knowledge about a great many topics. Linda Kelly also deserves thanks for keeping my desktop running here at UCSC. Needless to say, without it I could not have done anything. I would also like to thank Brandon Allgood for setting up my laptop which I used to write this thesis.

I would like to thank Sue Tappero and the MESA program at Cabrillo Community College for providing me employment during my second year at UCSC. Not only was the extra money useful, but the work was fun, especially leading scientific tours of the Santa Cruz Mystery Spot, and provided me valuable knowledge about teaching and a great deal of respect for community colleges in general.

The staff at the Red Room Cocktail Lounge, past and present, deserve a great deal of thanks as well. Their kindness, friendship, and tasty concoctions provided me much relief from the rigors of graduate school. The Red Room not only served as a place of employment, but in many respects was my extended living room here in Santa Cruz. The many friends I have made and the good times that I have had there will always be cherished. Specifically I would like to thank Judy Crowe, Jenny "Bunny" and Dan "The Man", "Sickman" Kim, Brent Erickson, Sara Rubio, "Dolly", Mike "The Cooler", Rigo, "Link", Jessica, Naka, Patti, Stephanie, Levanah, Jill, Jamie's 1 and 2, "Big J", Janet, Dan Bollwinkel, and last but not least Oscar.

I would like to thank Logan, Paula, Greg, Kindra, Jai, Kevin, Jason, Jordan and Sage for their friendship here in Santa Cruz. Sarah Vandrey and Theresa Beltramo deserve thanks for helping me understand a little bit about life's great mystery. I would also like to thank people at the Catalyst, Taqueria Santa Cruz, Taqueria Vallarta, Falafel of Santa Cruz, Pizza My Heart, and the Asian Rose.

I also need to thank all of the various educators that have been a part of my life. Without the knowledge that they have given me, I would have never been able to get as far as I have. These people include the teachers at Roland Park Elementary, Ames Middle School, Ames High School, especially Mike Wittmer, the faculty at the University of Iowa, the faculty at UCSC, Julian Stanley, and the staff at CY-TAG.

My family also deserves a great deal of thanks, as their love and support has always given me the strength to try to accomplish more. My dogs, Homer and Emma, also are deserving of thanks since "man's best friend" is not an overstatement.

Finally, I would like to thank my mother, Camilla, for just about everything moms do (way too long to list). Not only is she a great mother, but an inspiration as well. No matter what life seems to throw at her, she always perseveres and

ultimately succeeds.

Chapter 1

Introduction to Gamma-Ray Astronomy

Very high energy (VHE) gamma-ray astronomy, defined as observations at energies above 300 GeV up to 100 TeV, has recently become a viable branch of main stream astronomy. This field resulted from the extension of observations in gamma-ray astronomy, performed by satellites, upwards in energy, and the study of cosmic-rays, where the detection of cosmic photons above $\sim$1 TeV with ground based instruments was pursued. As VHE observations are at the high end of the observable electromagnetic spectrum there has been much difficulty in identifying sources of VHE gamma-rays. However, the development of the atmospheric Cherenkov imaging technique allowed for the detection of the first source of TeV photons, the Crab Nebula, about 13 years ago (Weekes et al., 1989). Since then, the discovery of multiple sources at these energies has allowed for the field to become a legitimate astronomical discipline. Detected VHE sources are galactic and extragalactic, and characterized by fluxes which are in some cases steady and in others variable. This chapter describes the various methods that are useful for detecting gamma-rays of energy 300 GeV and above, as well as the different classes of known and possible VHE sources. Recently published reviews contain more in-depth discussion of the techniques, science, and recent results of VHE gamma-ray astronomy (Hoffman et al., 1999; Catanese and Weekes, 1999; Ong, 1998).

1.1 Satellite Observations

The basic elements of a space-borne gamma-ray detector include a tracking detector which reconstructs the incident direction of the photon, a total-absorption

calorimeter which measures the energy of the photon, and an anticoincidence counter which ensures that only electrically neutral particles trigger the detector. The tracking detector follows the tracks of the electron-positron pair produced by the interaction of the primary photon with thin converters (*e.g.* tungsten plates or tantalum foils). The calorimeter, typically made from sodium iodide or cesium iodide, determines the energy of the photon by measuring the integrated path length of particles in the electromagnetic cascade produced by the incident photon. The detectors flown on satellites can unambiguously identify gamma-rays with an angular resolution of about 1°, an energy resolution of about 15%, and have a field of view of 20°-40° half-angle. Unfortunately, the detectors which can be flown on a satellite are small ($\sim$1500 cm^2) resulting in the energy range to which they are sensitive being below the VHE regime. This is because a typical source's flux decreases dramatically as energy increases, requiring a very large detection area for VHE observations. Nonetheless, the sources identified by these satellites are useful indicators of what objects may be bright in the VHE sky.

All the gamma-ray telescopes flown to date on satellites are of the form previously described. These include SAS 2 in 1973, COS B in 1975, and EGRET aboard the Compton Gamma Ray Observatory (CGRO) in 1991. The last is the most sensitive and successful of the three. CGRO contained 4 instruments, including the Burst and Transient Source Experiment (BATSE) and Energetic Gamma Ray Experiment Telescope (EGRET) instruments. The results of these two instruments have impacted gamma-ray astronomy significantly. BATSE, which served as the all-sky monitor for CGRO, was sensitive to photons with energies between 20 keV and 100 MeV. The main purpose of BATSE was the detection of gamma-ray bursts (GRBs) of which more than 2000 were discovered. EGRET covered the energy range between 20 MeV and 30 GeV. As this is the highest energy range to which a satellite has been sensitive, the results are briefly discussed since they provide indications of what may be bright at TeV energies.

The third EGRET catalog (Hartman et al., 1999), based on $\sim$4 years of observation, contains a listing of more than 250 sources with gamma-rays higher than 100 MeV. Figure 1.1 shows a galactic map of the gamma-ray point sources above 100 MeV detected by EGRET, as published in their third catalog. More than half of the sources detected by EGRET are unidentified with any known object. Many of these unidentified sources are located near the Galactic plane, suggesting a Galactic origin. The bulk of the unidentified sources detected away from the plane are believed to be extragalactic. Seven of the identified sources are pulsars. The majority of the extragalactic sources which have been identified are active galactic nuclei (AGN), almost all of which are blazars. The spectra of the identified sources are very flat with luminosities that peak in the high-energy region of the spectrum, providing indication that they may be sources of VHE photons. A

detailed map of diffuse gamma-ray emission, excluding the detected point sources, along the plane of the Milky Way was also generated by EGRET. Finally, high-energy gamma rays, in some cases with photons above 1 GeV, were found for 6 gamma-ray bursts which EGRET detected in coincidence with BATSE. These bursts are characterized by hard energy spectra (differential spectral index $\sim$2) which show no sign of a high-energy cutoff. The varied properties of the sources detected by EGRET indicate that there are many phenomena in the universe which may produce VHE gamma rays.

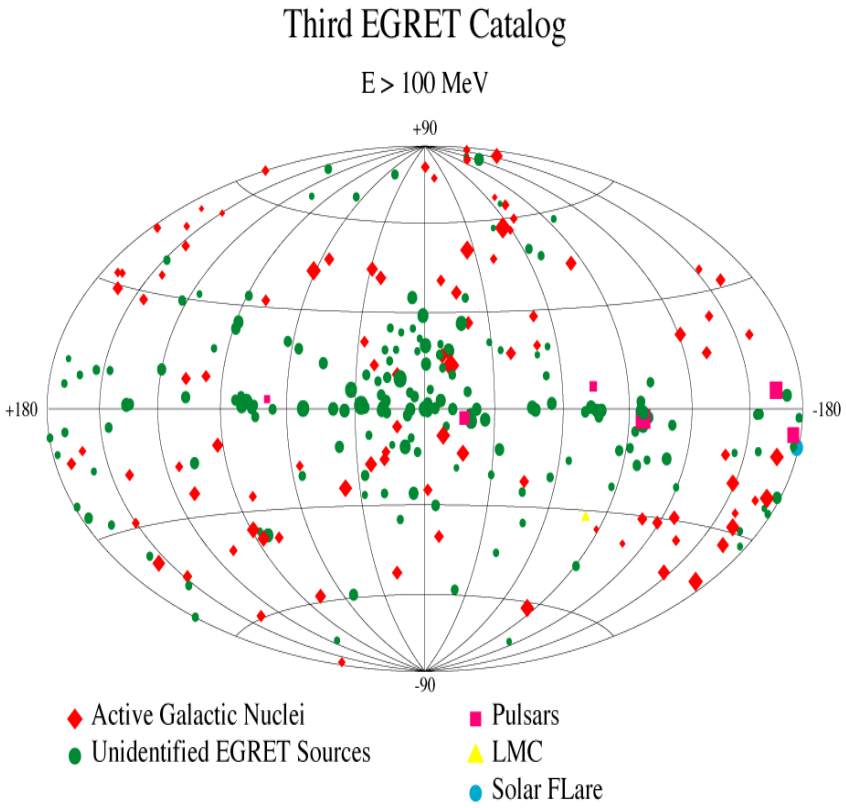

Figure 1.1: A Galactic map of the gamma-ray point sources in the third EGRET catalog (http://cossc.gsfc.nasa.gov/images/egret/3rd_EGRET_Cat.gif). The size of each symbol is proportional to the source intensity.

A next-generation telescope, the Gamma-Ray Large Area Space Telescope (GLAST) is scheduled for launch in 2006. GLAST has the same properties as the previous satellites with the exception that solid state tracking detectors are utilized resulting in an factor of 10-30 improvement in sensitivity. This instrument should provide an even better understanding of the VHE sky.

1.2 Ground-Based Techniques

The flux of VHE gamma rays is low and decreases dramatically with energy. Thus, a large detector is required for observations of VHE sources. This results in a satellite not being large enough to do TeV gamma-ray astronomy. Therefore, observations must be done from ground level. However, the atmosphere is opaque to VHE photons. Therefore the secondary effects of the atmospheric absorption of these photons must be detected. This is done by either detecting the shower of secondary particles from the electromagnetic cascade, known as an extensive air shower (EAS), which results from the interaction of the VHE photons in the upper atmosphere or by detecting a flash of Cherenkov light produced by these EAS as they propagate through the atmosphere. Astronomical observations are made possible because the EAS cascade retains the original direction of the incident photon to a high degree. Further, the spread of secondary particles, as well as Cherenkov photons, is very large allowing for a ground based detector to have a collection area that is large enough to make it sensitive to the flux of gamma-rays from sources at VHE energies. Unfortunately, gamma-ray observations are severely limited by the charged cosmic-ray particle flux which produces superficially similar EAS, and, for a photon of a given energy, are $\sim$10,000 times more numerous. Since it is not possible to veto the charged cosmic ray background with an anticoincidence counter, as is done in a satellite detector, subtle differences in the cascades initiated by photons and hadronic particles must be detected for gamma-ray astronomy to be successful.

1.2.1 Extensive Air Showers

The development of an EAS begins with the interaction of the primary particle in the upper atmosphere. The physics of the initial interaction of VHE photons is believed to be well known as the total cross section for photon-proton interactions has been measured for center-of-mass energies up to 200 GeV (Aid et al., 1995). This is equivalent to a 20 TeV photon colliding with a proton at rest.[1] The predominant interaction for a gamma-ray primary is electromagnetic, electron-positron pair production, because the cross sections for the production of hadrons and muon pairs are several orders of magnitude lower than that for pair production. In the development of an electromagnetic EAS, this initial electron-positron pair produces more photons through brehmsstrahlung, which in turn produce more electron-positron pairs. As a result, a cascade of particles develops

[1] An extrapolation is necessary to describe the initial interactions for photons of higher energies.

which grows nearly exponentially, dividing the primary energy among the resulting particles as it propagates through the atmosphere. This cascade grows until the mean energy of the electrons and positrons approach the critical energy in air ($\sim$80 MeV). After this, energy loss through ionization becomes dominant. This process, which does not produce more particles, removes energy from the EAS, and the number of particles in the cascade decreases. The point at which this occurs is known as shower maximum and occurs at a height between 10 and 7 km above sea level for gamma-rays of energies between 100 GeV and 10 TeV. Although the number of particles decreases, a large number reach ground level, especially at high altitudes. Since the particles in the EAS are ultrarelativistic and the dominant physical processes are sharply peaked forward, the EAS arrives at ground level in a thin front only a few meters thick. While the front is only a few meters thick, the lateral extent of the showers, primarily the result of multiple Coulomb scattering of the electrons and positrons in the EAS, is of order one hundred meters.

As previously discussed the more plentiful high energy charged cosmic-rays, protons and nuclei, also produce EAS through their interaction in the upper atmosphere. These initial interactions generate a hadronic cascade, which quickly divides the energy among a large number of particles. Some of the charged pions and hadrons formed initially decay before interacting, producing muons and neutrinos. These muons have a low probability of interacting and therefore have a high probability of reaching the ground. High energy neutral pions produced in the hadronic interactions decay quickly into photons. These photons in turn produce electromagnetic cascades. As a result, the particles reaching ground level in a hadronically initiated cascade are mostly electrons, positrons, photons, neutrinos, and muons. Thus, an EAS produced by hadronic particles is not very dissimilar to one produced by a VHE photon. A notable exception to this is the presence of roughly 20 times more muons in a hadronically initiated EAS. While the lateral distribution of the muons is considerably larger than that of the electromagnetic particles, enough are present within the electromagnetic front to enable their identification and allow for rejection of the hadronically initiated EAS. Another difference between the two types of showers is that those generated by hadrons are not as smooth and have a larger lateral extent in the overall distribution of particles. This is the result of the larger transverse momentum in the early hadronic interactions, which produce hadronic particles, that subsequently produce small sub-showers with high densities of particles.

Since the shower particles in both types of EAS are traveling faster than the speed of light in air, Cherenkov photons are also produced during propagation of the shower front. The energy threshold and angle at which this light is emitted is governed by the refractive index of air which is proportional to the atmospheric

density. As a result, the median altitude for Cherenkov emission from a 1 TeV gamma-ray shower is 8 km, and is slightly lower for a proton shower on average. The maximum angle of Cherenkov emission in air is small (1° at 8 km above sea level, and increases to 1.3° at sea level) and independent of the mass of the emitting particle. Due to the small emission angle, the Cherenkov light from an EAS illuminates a "light-pool" on the ground similar in size to the front of the EAS (radius $\sim$ 130 m, 2-3 ns thick for a gamma-ray primary). Half of the emission occurs within 21 m of the shower axis for gamma-initiated EAS and 70 m for a proton-initiated EAS (Hillas, 1996). The difference in size is due to the larger lateral extent of hadronically initiated EAS. The average density of Cherenkov photons in the light-pool ($\sim$200 photons/m^2 for a 1 TeV shower) is flat and is related to the energy of the primary particle. This latter effect is the result of of the total distance traveled by all particles above the Cherenkov threshold being associated with the energy of the primary particle.

1.2.2 Atmospheric Cherenkov Detectors

Ground-based VHE astronomy can be performed by detecting the Cherenkov radiation produced in an EAS reaching ground level. By detecting the pool of Cherenkov light, these instruments can accurately infer the properties (direction, energy) of the primary particle that initiated the EAS. There are two types of detectors which perform VHE observations using this method. These are imaging atmospheric Cherenkov telescopes (IACTs) and solar tower experiments. IACTs are typically sensitive to EAS in the energy range 300 GeV to 30 TeV, and the solar tower experiments are sensitive to EAS in the energy range 50 GeV to 500 GeV.

Imaging Atmospheric Cherenkov Telescopes

Imaging atmospheric Cherenkov telescopes use one or more mirrors to focus the Cherenkov photons onto a tightly packed array of fast photomultiplier tubes (PMTs) in the focal plane. The PMTs are read out through standard fast amplifiers, discriminators, and analog to digital converters. IACTs have large collection areas (>50,000 m^2) since a single detector anywhere within the Cherenkov light-pool can detect the EAS which produced that light. These instruments also have a good angular resolution ($\sim$0.1°) and reasonably good energy resolution ($\sim$20%-40%). However, they are limited by their small field of view (<5°) and low duty cycle (<10%). This latter effect is the result of the requirement that observations be made on moonless, cloudless nights because the Cherenkov signals are faint and produced at altitudes of several kilometers. The success of these instruments

is based in large part on their ability identify the nature, hadronic or electromagnetic, of the primary particle of the detected EAS with 99.7% efficiency. IACTs perform this identification using the imaging technique, in which shape of the angular distribution of the Cherenkov photons on the sky is measured. Since cosmic-ray induced EAS have broader and more chaotic Cherenkov light pools than gamma-ray induced EAS, the images when focused on the PMTs have similar attributes. Thus, a parameterization of the shape allows for background rejection to be performed with high efficiency.

The field of VHE gamma-ray astronomy has advanced dramatically due to IACTs. The most successful is the Whipple 10 m telescope (Cawley et al., 1990), shown in Figure 1.2, which developed the imaging technique and discovered the first source of TeV photons (the Crab Nebula; (Weekes et al., 1989)). Other successful versions include the Cherenkov Array at Themis (CAT), which is a French IACT with 3 m aperture located in the Pyrennes (Barrau et al., 1998), and CANGAROO (Hara et al., 1993), a Japanese-Australian IACT located in Australia with 3.8 m aperture. Arrays of IACTs which can view independent showers, as well as the same shower simultaneously, have also been constructed and utilized successfully. The High Energy Gamma Ray Astronomy (HEGRA) experiment which uses five 3 m aperture IACTs (Daum et al., 1997) is the most significant example of this to date.

Future IACT detectors include a German-Spanish project known as MAGIC (Barrio et al., 1998) which uses a 17 m aperture telescope to reduce the energy threshold to as low as 20-30 GeV. Reduction of the energy threshold will help bridge the gap between satellite observations and those of ground-based detectors. New IACT arrays with much larger telescopes have also been proposed and are under construction. These include HESS, a German-French-Italian experiment in Namibia which will use 4 (initially) and perhaps 16 12 m IACTs (Hofmann, 2001), and VERITAS, an American experiment in Arizona which will use 7 10 m IACTs (Quinn et al., 2001).

Solar Tower Experiments

In the solar tower experiments, pre-existing arrays of heliostat mirrors used in solar power plants are utilized to focus the atmospheric Cherenkov radiation onto a secondary mirror which then focuses the light onto an array of PMTs. These experiments have the advantage over IACTs in that their collection area is much larger resulting in a lower energy threshold. These experiments include STACEE (Chantell et al., 1998), CELESTE (Quebert et al., 1995) and Solar-2 (Tümer et al., 1999). Figure 1.3 shows a picture of the National Solar Tower Test Facility in Albuquerque, NM, which is used by STACEE. STACEE has an angular

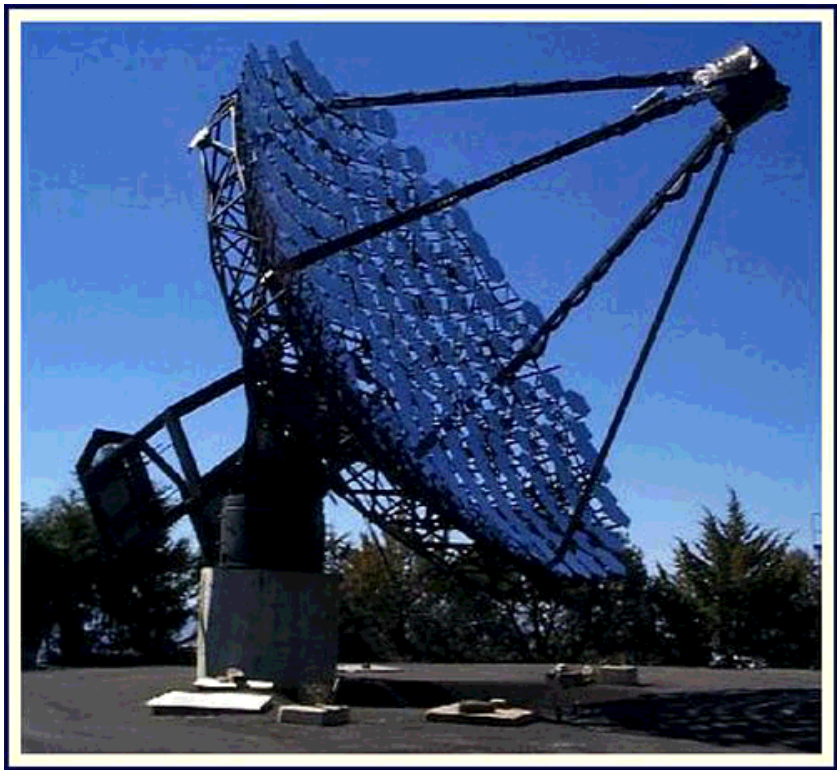

Figure 1.2: Photograph of the Whipple 10 m telescope (http://egret.sao.arizona.edu).

resolution of $\sim 0.1^{\circ}$ and an energy threshold below 100 GeV (Oser et al., 2001). These experiments are also limited by their small field of view and low duty cycle, and are limited in their ability to perform background rejection. Nevertheless, several sources of TeV photons have been detected using these instruments (Oser et al., 2001; Hinton et al., 2001).

1.2.3 Traditional Extensive Air Shower Arrays

The shower particles reaching ground level in an EAS can be detected and the information utilized to infer the properties of the primary particle. The instruments which use this methodology to perform gamma-ray astronomy are known as extensive air shower arrays (EAS arrays). Typical EAS arrays consist of 50 to 1000 charged particle detectors (usually ~ 1 m^2 scintillation counters) spread over an area of 10^4 to 2×10^5 m^2 with 10 to 20 m spacing. To improve the performance of the array, the scintillation counters are covered with ~ 1 radiation

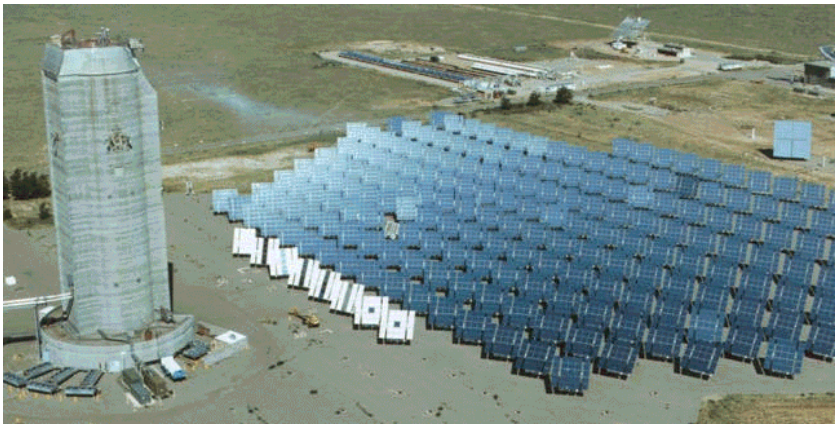

Figure 1.3: Photograph of the National Solar Thermal Test Facility used by STACEE (http://www.astro.ucla.edu/∼stacee).

length of lead to convert the more plentiful shower photons into charged particles. Since the cost of a uniformly sensitive detector is prohibitive, only <1% of the total enclosed area is actually sensitive. This is reasonable for energies around 100 TeV because a sufficient number of particles reach ground level that only a small fraction of total number needs to be sampled to infer the properties of the EAS. In an EAS array, the direction of the primary particle is reconstructed using the relative times at which the individual showers in the array are struck by the shower front. The angular resolution, which is limited by shower fluctuations, resulting from this method of reconstruction is $\sim 0.5^{\circ}$. Background rejection is performed by rejecting muons, using muon detectors placed around the scintillation counters. However, the ability to discriminate gamma-ray initiated EAS from those initiated by hadrons is limited. Due to the sparse sampling of the total number of particles, EAS have a high energy threshold (∼50 TeV) and moderate energy resolution (∼100%). Although the angular and energy resolution of these instruments is worse than the IACTs, their field of view is large (∼2 sr) and they have a large duty cycle (∼100%) which provides the ability for these instruments to continuously monitor all sources in the overhead sky. Although this capability gives EAS arrays the ability to serve as an all-sky monitor, no new sources of TeV photons have been discovered using these detectors. This is primarily due to the high energy threshold of these instruments. Examples of EAS arrays include CYGNUS (Alexandreas et al., 1992), CASA (Borione et al., 1994), and Tibet (Amenomori et al., 1997).

A next generation EAS array known as Milagro achieves a low energy threshold by increasing the sampling of the shower particles through the use of a water-

Cherenkov technique. This technique also allows for the identification of hadronic EAS through the identification of muons and hadrons and by imaging the incident particle shower. Milagro and the water-Cherenkov technique are described in detail in Chapter 3.

1.3 Motivation for VHE Gamma-Ray Astronomy

VHE gamma-ray astronomy can provide insights into a number of scientific areas. One such area is the nature of cosmic-particle acceleration mechanisms. The photon spectra observed at VHE energies are non-thermal and must be explained using complex models. Thus, observations of TeV sources can provide constraints on the models, ultimately increasing the understanding of the underlying phenomena. Another area is the origin of cosmic rays. Since the trajectories of cosmic rays are bent in the Galactic magnetic field, their origin is unknown. However, gamma rays, which do not bend in the Galactic magnetic field, are expected to be produced in the same areas as the source of cosmic rays. Thus, observations of VHE gamma-rays can possibly provide a "marker" for acceleration of charged particles and trace the origin of cosmic rays. The study of exotic objects is another motivation for VHE gamma-ray astronomy. All of the sources detected at TeV energies contain compact objects such as black holes and neutron stars. In addition, there are many speculative objects, such as cosmic strings and primordial black holes, that may produce TeV photons. VHE gamma-ray astronomy can provide further insight into the known as well as speculative phenomena. Finally, the study of photon propagation through the intergalactic medium is addressed by VHE gamma-ray astronomy. Observations of TeV sources can provide a direct measurement of the density of the infrared component of the extragalactic diffuse photon background which is currently unknown. This is detailed in Section 2.5, and has cosmological implications regarding the epoch of star and galaxy formation as well as various dark matter hypotheses.

1.4 Known TeV Sources

There are currently only a limited number ($\sim$10) of known sources of VHE gamma-rays. These include both Galactic (pulsars and supernova remnants) and extragalactic objects (AGN). As a result of the limited number detections, much of the current focus of VHE gamma-ray astronomy is the discovery of new sources. Searches are performed in the directions of classes of objects known to be emitters

of TeV photons, as well as for classes of objects where VHE gamma-ray production is only speculated. With the discovery of more sources, a greater understanding of the scientific areas previously motivated can be achieved.

1.4.1 Pulsars

A pulsar is a rapidly rotating neutron star, the densest known form of stable matter, created during a supernova explosion. Pulsars are characterized by a period ranging from a few milliseconds to a few seconds, strong magnetic fields (10^{12} Gauss), and relativistic jets of plasma and radiation emanating from their magnetic poles. The term pulsar stems from the pulsed emission that is observed from the jets as they rotate on an axis, different than the magnetic axis, through the Earth's line of sight (similar to a lighthouse). Gamma-ray pulsars are characterized by power spectra that are extremely flat with a peak often found in the GeV energy range (Thompson, 1997). This is in agreement with pulsar models that often involve electrons with energies up to 10^{15} eV. Therefore, it would not be surprising if pulsars were sources TeV gamma-rays.

To date, 3 pulsars, the Crab Nebula, PSR1706-44, and Vela, all belonging to a subclass known as plerions, have been detected at TeV energies. A plerion is a pulsar surrounded by a supernova remnant filled with ionized gas. Models of plerions indicate that TeV photons are produced when relativistic electrons powered by a central pulsar interact with the surrounding nebula. In these models, electrons are stripped from the surface of the neutron star by strong electric fields generated by the spinning magnetic fields. These electrons, as well as other electrons and positrons created by pair production in the high magnetic fields, anchor themselves to the magnetic fields lines in the magnetosphere in a manner ($\vec{E} \cdot \vec{B} = 0$) required by the plasma which prohibits particle acceleration. However, regions devoid of plasma, known as "vacuum gaps," are believed to form near the magnetic poles as well as near the "light cylinder," defined as the radius at which the field lines are traveling at the speed of light. It is believed that the pulsed emission from radio wavelengths to x-rays originate in these regions. The aforementioned electrons and positrons escape from the magnetosphere into the "pulsar wind region" along open field lines. The pulsar wind region begins at the edge of the light cylinder and terminates with a shock that accelerates the electrons and positrons to high energies. Eventually, these high energy particles escape the shock front and enter the nebular region. A model known as the synchrotron self-Compton model (SSC) describes the process by which the TeV photons are believed to be produced in this nebular region[2] (deJager and Harding,

[2]Another possible contribution to the TeV flux is from gamma-rays produced by π° decay.

1992). In the SSC model, the high energy electrons and positrons spiral around the magnetic field lines in the nebula, and as a result emit synchrotron radiation. These synchrotron photons are then boosted to TeV energies via inverse Compton scattering off the same electrons. Due to this process the flux of VHE photons is a function of the magnetic field in the nebula.

The Crab Nebula

The first, and perhaps most important, source detected at TeV energies is the Crab Nebula. The Crab Nebula, located about 2000 pc away, is the remnant from a supernova explosion (likely type II) observed by Chinese and Japanese astronomers in 1054. At the heart of the Crab Nebula is a young optical pulsar (33.1 ms period), which is surrounded by a nebula (expanding mass of gas and dust) $\sim$4 pc in diameter. This pulsar powers the nebula, and as a result is slowing down due to the energy loss which is approximately the same amount as the total energy that is radiated from the nebula. The initial detection of the Crab at TeV energies, 9σ in 60 hours of observations, was made by a less sophisticated version of Whipple in 1989 (Weekes et al., 1989). After upgrades to the Whipple camera, allowing for improvements in the imaging technique discussed in Section 1.2.2, the Crab was later detected at the 20σ level (Vacanti et al., 1991). Further refinements of the Whipple camera and analysis techniques currently allow for the routine detection of Crab at the 5-6 σ level in a hour of observation (Catanese and Weekes, 1999). The detected photon rate ($\sim$2 per minute) is greater than that found by EGRET at its optimum energy (100 MeV). Since the initial detection, the Crab has been observed at TeV energies by at least 8 different groups using imaging atmospheric-Cherenkov Telescopes (Catanese and Weekes, 1999) and one EAS array (Amenomori et al., 1999).

The energy spectrum of the Crab Nebula is well determined between energies of 300 GeV and 50 TeV, and is characterized by a falling power law with differential index of about $\alpha = 2.6$. Unlike many known sources of TeV photons, the TeV flux from the Crab is strong, steady in time, and shows no evidence for a cutoff out to energies of 50 TeV. The lack of any pulsed emission observed at TeV energies from the Crab indicates that the emission is due to processes in the supernova remnant surrounding the pulsar. The TeV flux observed[3] from the Crab is much higher than expected from an extrapolation of the spectrum detected by satellites at lower energies. However, this is reconciled by the SSC models, which predict a spectrum that possesses 2 bumps, one at lower energies ($\sim$10 MeV) due to synchrotron emission of the electrons, and another at higher energies ($\sim$100 GeV)

[3]The observed TeV flux is quantified in Section 5.6.

due to the inverse Compton scattering of the synchrotron photons with the same electrons that produced them (deJager and Harding, 1992).

TeV observations of the Crab Nebula provide a probe of the acceleration mechanisms present and can be used to determine the properties of the object. Fits of data observed from the Crab to the SSC model are useful for determining properties such as the maximum electron energy in the pulsar magnetosphere ($\sim 2 \times 10^{15}$ eV), the strength of the nebular magnetic field ($\sim 1.4 \times 10^{-4}$ G), and the nature of the seed photons (Hoffman et al., 1999). While the constraints on the theoretical models provided by observations of the Crab are important, this is not where the Crab has benefited TeV astronomy the most. As previously discussed, observations from a number of observatories have shown that the TeV flux from the Crab is both strong and steady in time. As a result, the Crab has become the standard reference for TeV gamma-ray astronomy. Thus, observations of the Crab are used to demonstrate that an observatory functions, how well it functions, as well as to refine the techniques and data-analysis methods utilized. It is in this sense that the Crab Nebula is studied in this thesis. Results of observations of the Crab Nebula with Milagro are provided in Chapter 5. The purpose of these observations is to:

- Demonstrate that Milagro works.
- Elucidate the sensitivity of the detector.
- Show that the sensitivity of the detector is stable in time.
- Demonstrate that the analysis techniques are reasonable.
- Determine the TeV flux from the Crab using an independent technique.
- Isolate any systematic effects present within the detector, as well as the Monte Carlo Simulations.

Other Plerions

The Crab Nebula, whose detection at TeV energies was discussed earlier, is the only plerion to be detected in the Northern Hemisphere. Two other plerions, PSR 1706-44 (Kifune et al., 1995) and Vela (Yoshikoshi et al., 1997), located in the Southern Hemisphere, have been detected at TeV energies by the CANGAROO group. PSR1706-44 is identified with a pulsar (period = 102 ms), is associated with an x-ray synchrotron nebula, and possibly associated with a shell-type supernova remnant. EGRET detected 102 ms pulsations in PSR1706-44 allowing for the association with the radio pulsar. However, no evidence for pulsed emission is

observed from this object at TeV energies, as is also the case at optical and x-ray energies. Vela is a young ($\sim 10^4$ years), nearby ($\sim$500 pc) pulsar, that was first detected at radio wavelengths, but has also been observed in the optical, x-ray, and gamma-ray bands. It is the brightest discrete object in the energy range covered by EGRET, and is characterized by 100% pulsed emission at EGRET energies. Although this is the case, all of the emission from Vela at TeV energies is unpulsed. The observed TeV signal from Vela is offset from the pulsar position by 0.14°, which makes it likely that the source is a synchrotron nebula, as well as making pulsed emission unexpected.

1.4.2 Supernova Remnants

Supernova remnants are an expanding shell of material that remains after the explosive death of a star (a supernova). If some ($\sim$10%) of the tremendous amount of kinetic energy ($\sim 10^{53}$ ergs) released in a supernova is utilized in the acceleration of protons and nuclei, then SNRs have sufficient power to be the source of hadronic cosmic rays. In this scenario, which is widely accepted, SNRs are the source of hadronic cosmic rays up to energies of $\sim Z \times 10^{14}$ eV, where Z is the atomic number of the particle. Models show that the luminosity of gamma-rays created through the decay of neutral pions produced by interactions of cosmic-rays with ambient matter may be detectable by ground based gamma-ray detectors (Drury et al., 1994). Further, it is well established from observations of synchrotron emission in the shells of supernova remnants (SNRs) at radio and x-ray wavelengths that electrons are accelerated to high energies in SNRs (Catanese and Weekes, 1999). These high energy electrons could also produce VHE gamma-rays through inverse Compton scattering of photons. Therefore, SNRs may likely be sources of TeV photons. Discovery of such a source would provide direct evidence of the acceleration of particles to TeV energies in the shocks of SNRs. This in turn could provide indication that SNRs are the source of hadronic cosmic rays, since directional information is not lost in the propagation of photons through the interstellar magnetic fields, unlike cosmic rays.

To date, no SNRs have been detected at TeV energies in the Northern Hemisphere. However, CANGAROO, located in the Southern Hemisphere, has reported evidence for TeV gamma-ray emission from the shell-type SN 1006 (Tanimori et al., 1998a). Their observations show a statistically significant excess from the northeast rim of the SNR shell, consistent with the location of non-thermal x-rays detected by the Advanced Satellite for Cosmology and Astrophysics (ASCA) experiment (Koyama et al., 1995). However, this detection at TeV energies has not been verified by an independent instrument and is presently considered tentative. Confirmation of this detection, as well as discovery of other TeV bright

SNRs, would be a large step in the understanding of the origin of hadronic cosmic rays, although it should be noted that the TeV emission detected from SN 1006 does not require the presence of hadronic cosmic rays.

1.4.3 AGN

Several AGN, all belonging to a subclass known as blazars, have been detected at TeV energies. These objects, which are known to be highly variable at all wavelengths, are characterized by a flux of TeV photons which is low at their quiescent level, but increases dramatically during flaring episodes. During such flares, the gamma-ray emission greatly exceeds the the energy output of the AGN at all other wavelengths. As a result, any model for these objects must account for the TeV flux. The models, which have broad implications for several classes of objects, as well as relevant TeV observations of AGN are discussed in detail in Chapter 2. Results from observations of 27 selected[4] AGN using Milagro are presented in Chapter 6.

1.5 Possible TeV Sources

As discussed previously, there are only a limited number of known TeV sources. Therefore, the other classes of objects which may be emitters of VHE photons must also be examined. These include both steady and transient phenomena located both inside and outside of the Milky Way. Some possible sources of VHE photons are described below.

1.5.1 Gamma Ray Bursts

Since their discovery over 30 years ago, several thousand gamma-ray bursts (GRBs), short bursts (1 ms to 10's of seconds) of hard x-rays and low energy gamma rays coming from random locations in the sky, have been observed. While GRBs are usually associated with energies of 100 keV to 1 MeV, results from EGRET demonstrate that a component exists at high energies. Although it is known that the distance to these objects is cosmological, the physics of these objects is not understood. However, many models of GRBs predict emission up to TeV energies. Therefore, this phenomena has the potential to be observed at TeV energies. This argument is strengthened by observations with a smaller less sensitive version of Milagro (described in Chapter 3), known as Milagrito, which detected evidence for TeV emission from GRB 970417a (Atkins et al., 2000). It

[4]The selection criteria, as well as the AGN chosen, are discussed in Section 2.7.

has been shown that if emission from this GRB has been observed, it must contain photons with energies above 650 GeV (Atkins et al., 2002).

1.5.2 Galactic Plane

Cosmic rays, accelerated by presently unknown objects, are trapped in the Milky Way by Galactic magnetic fields. The interaction of these cosmic rays with interstellar material creates gamma rays by a variety of physical processes. Therefore it is expected that some fraction of cosmic rays will produce gamma rays in regions of enhanced density (clouds of atomic and molecular hydrogen). Therefore, these gamma rays should appear as a diffuse glow, concentrated in a narrow band, along the Galactic Equator. Diffuse gamma-ray emission along the Galactic plane has been observed up to energies of 30 GeV by EGRET. Therefore it is likely that the Galactic plane is a source of TeV photons.

1.5.3 X-Ray Binaries

An x-ray binary system consists of a main sequence star and a compact object (typically a neutron star or black hole) in close orbit around a common center of mass. Matter pulled from the companion star by the intense gravity of the compact object spirals onto the collapsed star forming an accretion disk. The high flux of x-rays which characterizes these objects is believed to be created from the inner region of this disk. Since many of these objects are observed to have relativistic jets of particles and plasma, found in known sources of TeV photons, they may be emitters of VHE gamma-rays. Reports of the detection of 2 of these objects, Cygnus X-3 and Hercules X-1, at TeV energies circulated during the 1980s (Hoffman et al., 1999). However, flaws in assessing the significance of these observations were found later drawing the detections into question. Further, the detections have not been verified by more sensitive detectors. Thus, no x-ray binaries have been conclusively detected at VHE energies to date. Regardless, x-ray binaries must be considered a possible source of TeV gamma-rays.

1.5.4 Unidentified Sources

As discussed in Section 1.1, many of the point sources found by the EGRET experiment, mostly along the galactic plane, have no counterparts observed at other wavelengths, and hence are unidentified. Further, some of the unidentified sources have been shown to possess properties that differ from the others, making it likely that there are many classes of objects in these unidentified sources (Gehrels et al., 2000). Possible classes include unresolved AGN, radio quiet pulsars, supernova

remnants, and even a new type of gamma-ray source (Ong, 1998). Since EGRET was sensitive to photons up to 30 GeV, it is likely that some of these unidentified objects may be emitters of TeV photons.

1.5.5 Primordial Black Holes

Density fluctuations in the early universe could have formed small black holes, known as primordial black holes (PBHs). Although called black holes, these objects are not actually black, since they emit a nearly thermal spectrum known as Hawking radiation. As a black hole releases energy its temperature, as well as luminosity, increases due to a negative specific heat associated with gravitationally bound systems. Eventually the black hole completely evaporates due to this runaway process. The final stage of this evaporation is a tremendous explosion with infinite luminosity.[5] Depending on the model of evaporation these objects may emit TeV photons during this explosion. Black holes initially formed with a mass of $\sim 10^{14}$ g during the Big Bang would be evaporating presently. Thus, VHE observations can provide evidence which will help verify or rule out the existence of these objects.

1.5.6 Exotic Phenomena

VHE gamma-rays may also be produce by other exotic phenomena. This includes neutralino annihilation and cosmological strings. A neutralino is a theoretical neutral supersymmetric particle that may undergo pair annihilation resulting in the creation of TeV photons under proper conditions. Cosmic strings are topological defects that may have formed during phase transitions in the early universe. Cusps in these strings would emit massive particles that would fragment and decay creating jets, which in turn could generate TeV photons. However, even if these phenomena exist, as well as create TeV photons, it is uncertain if the signal would be observable with current ground-based detectors.

[5] The flux is finite.

Chapter 2

Active Galactic Nuclei

Several active galactic nuclei (AGN) have been detected at TeV energies in the past 10 years. Milagro's ability to continuously monitor all sources in the overhead sky, even during daytime transits, makes it well suited for VHE studies of AGN, which are known to be highly variable. In this chapter, the general properties of AGN, particularly TeV bright AGN, as well as the acceleration mechanisms which may be responsible for the production of TeV photons are discussed. The AGN which have been detected, the extragalactic background light which may be responsible for the limited number of AGN detected, and the implications of VHE observations of active galaxies are described as well. The reasoning for selecting a limited number of AGN for study in this thesis, the selection criteria, and the actual AGN selected are also presented in this chapter.

2.1 General Properties

AGN are known to emit radiation over the entire electromagnetic spectrum, from radio waves to TeV gamma rays. These objects, which only comprise of a few percent of the total number of galaxies observed, are very luminous, extremely compact objects that exhibit large luminosity variations on time scales of hours to years. The combination of high luminosity and short time scale variability observed implies that the energy release mechanism in AGN is very efficient (more so than ordinary stellar processes). This efficiency suggests that massive black holes are at the core of the AGN, which power the AGN through the highly efficient process of mass accretion, as well as the extraction of their rotational energy.

2.1.1 Unified Model of AGN

The behavior of individual AGN varies dramatically, and as a result numerous classes and sub-classes of AGN exist. These classes are based on the observed optical and radio properties of the AGN and not the physics of the underlying object. Although many classes exist, a unified theory of AGN has emerged which consists of a supermassive black hole (10^7–10^{10} solar masses), surrounded by a region of optically thick plasma. In the innermost region of the AGN, a thin accretion disk of transparent plasma (possibly mixed with the optically thick plasma) that creates the medium and hard x-ray emission is found. The outer regions of the AGN consist of a thick torus of gas and dust, which glows brightly in the UV and soft x-ray wavelengths, lying in the equatorial plane of the black hole. Thermal radiation also emanates from both the accretion disk (infrared to x-ray) and the torus (infrared). The core of the AGN is also surrounded by clouds of line-emitting gas moving at high velocity. The entire volume, within and above the torus, is permeated by electrons. In some AGN, a highly relativistic flow of energetic particles along the poles of the rotating black hole, perpendicular to the accretion disk or torus, exists. This flow forms collimated radio emitting jets which provide the non-thermal emission (radio and gamma rays). AGN which possess these jets ($\sim$10%) are referred to as radio loud due to their comparatively strong radio emission (radio to optical luminosity ratio greater than ten). Radio quiet AGN are those without the jets and therefore have weaker radio emission (radio to optical luminosity ratio less than ten) as well as overall luminosity. Figure 2.1 illustrates the AGN paradigm.

Apart from the distinction between radio-loud and radio-quiet AGN, it is believed that the different AGN classifications are due to the consequences of viewing similar objects, described by the unified model, at different viewing angles with respect to the rotation axis. The differing view angles result in several effects on the observations. The first is due to the torus obscuring certain emission regions from view at large angles with respect to the jet axis. For example, in AGN viewed at large angles, the torus obscures only the clouds that are close to the black hole. Thus, only the distant, slow-moving clouds are unobscured, leading to the observation of narrow emission lines. For AGN viewed at smaller angles, the high velocity clouds are visible, resulting in the observation of broad emission lines. Another effect is the result of Doppler boosting of a relativistic jet viewed at a small angle. Superluminal motion, apparent motion that is greater than the speed of light, is observed in many AGN and is a consequence of viewing a relativistic flow at small angles. The relativistic beaming, which increases as the line of sight gets closer to the jet axis, is responsible for the large variations in luminosity observed as well as a decrease in the apparent size of the emission region.

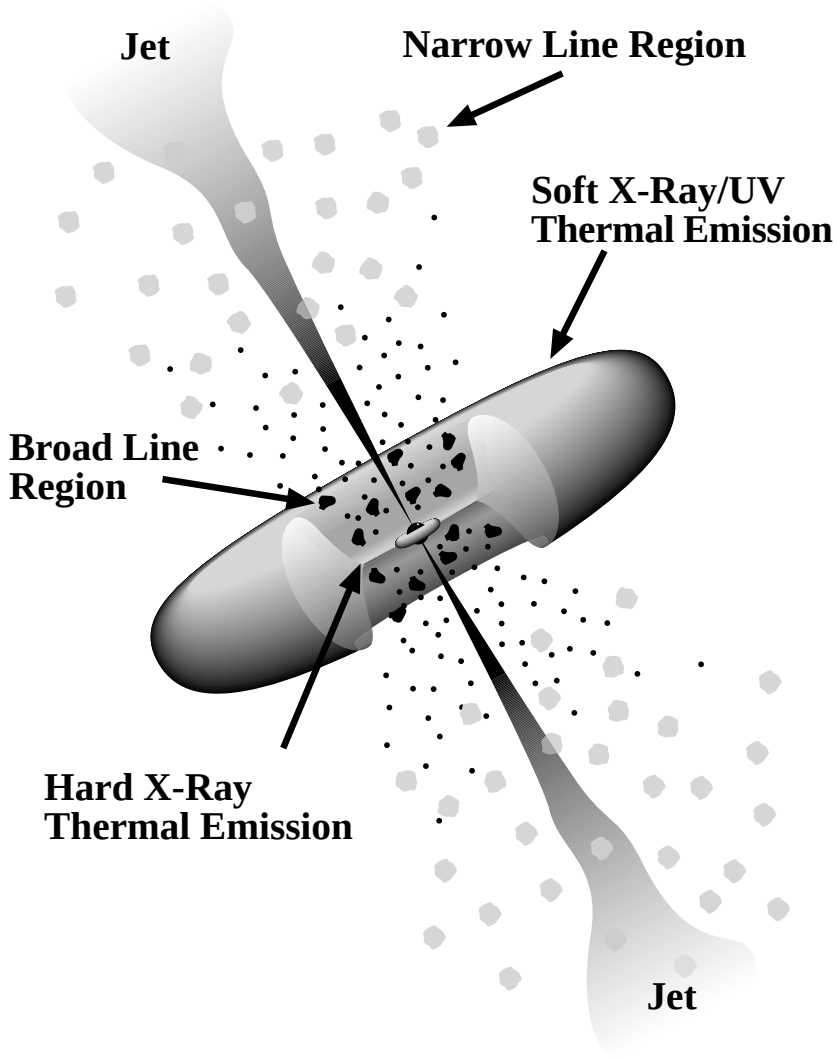

Figure 2.1: Illustration of the unified AGN model (Urry and Padovani, 1995). The original figure was annotated by Lowell Boone.

It is also responsible for the time scale of the variability being reduced due to the Doppler contraction of the time scale. The relativistic beaming also allows high energy photons, otherwise absorbed, to escape from regions with high radiation fields. As a result, the viewing axis must be within $\sim 10^{\circ}$ of the jet axis for TeV gamma rays to be observed (Hoffman et al., 1999). Finally, the viewing angle affects the amount of polarization in the light observed from the AGN. This is because at larger viewing angles, a greater amount of reflected light, which tends to be polarized, from the torus is seen.

2.2 VHE AGN

All of the known sources of TeV photons, as well as all of the extragalactic sources positively identified by EGRET (20 MeV–30 GeV photons), belong to a class of AGN known as blazars. Blazars are radio-loud AGN, with the radio emission originating primarily for the core region rather than the lobes, and include BL Lac objects (AGN with properties of the prototype BL Lac) as well as Flat Spectrum Radio Quasars (FSRQs). Other blazars include optically violent variables and superluminal sources. While there are many different subclasses of blazars, there is a growing consensus that all blazars are the same type of object, differing in only luminosity and perhaps viewing angle. The distinction between BL Lacs and FSRQ is currently provided by optical emission lines that are either faint and narrow ($<$0.5 nm) or completely absent in BL Lacs.

2.2.1 Blazar Properties

The emission from blazars is predominantly non-thermal and exhibits the most rapid and largest amplitude variations of all AGN. As discussed earlier, the rapid variability and large variations imply that the emission originates from a relativistic jet along the line of sight, resulting in strong amplification of the emission by relativistic beaming. This is supported by direct evidence obtained with VLBI observations which demonstrate that apparent superluminal motion is the rule in blazars (Vermeulen and Cohen, 1994). The faintness of the emission lines in BL Lacs previously discussed would be consistent with their intensity being small compared to the core-dominated emission (from relativistic boosting) and therefore unobservable. This may indicate why all of the blazars detected at TeV energies are BL Lac objects.

Spectral Energy Distributions

The spectral energy distribution (SED) of blazars, when plotted as νF_ν (or equivalently $E^2 dN/dE$), consists of 2 components in a double-peaked shape with each peak separated by 8–10 decades in energy. Figure 2.2 shows the average SED for three types of blazars (Sambruna et al., 1996). A low-energy component exhibits a distribution which gradually rises from radio wavelengths up to a broad peak. Depending on the specific type of blazar, this peak is located anywhere from the infrared to soft x-ray wavelengths. After the peak, the power output rapidly drops off in the low-energy component. The other component occurs at higher energies and is not smoothly extended from the first. This distinct component follows the same shape as the first. It gradually appears in the x-ray regime, increases to a broad peak located somewhere between 1 GeV and 1 TeV, after which it falls off rapidly. The location of this second peak also depends on the specific type of blazar. Regardless of the type of blazar the ratio of peak energies is similar.

Blazar Types

Figure 2.2 shows a systematic trend which exists in blazar properties that is related to the overall luminosity of the object. As the luminosity of the blazar increases, the location of the two peak energies in the spectral energy distribution, as well as the overall spectral shape changes. This was demonstrated for x-ray selected BL Lac objects (XBL), radio-selected BL Lac objects (RBL) and flat-spectrum radio quasars (FSRQ) in a manner that could not be explained by beaming (Urry, 1999). Specifically, high-luminosity BL Lac objects were found to have both their SED peaks at lower energies than those with lower overall luminosity. Although the location of the peaks differed with luminosity, the overall ratio of peak energies were found to be similar in all cases. Figure 2.2 also shows that the ratio of the luminosity of the high-energy component of the SED to the luminosity of the low-energy is larger for LBL than XBL. The luminosity of emission-lines in LBL is also larger than XBL (Urry, 1999).

As a result of these trends two classes of SEDs are found: One for low-frequency peaked blazars (LBL) and one for high-frequency peaked blazars (HBL). HBL are BL Lacs generally found in x-ray surveys (XBLs). Radio surveys typically found BL Lacs (RBLs) with the properties of LBL. Most FSRQs were found in radio surveys and thus are LBL. However, this generalization is becoming obsolete as high-frequency peaked FSRQ are being discovered in new multi-wavelength surveys. The major differences between LBL and HBL are:

- LBL have a higher bolometric luminosity than HBL (Perlman, 1999).

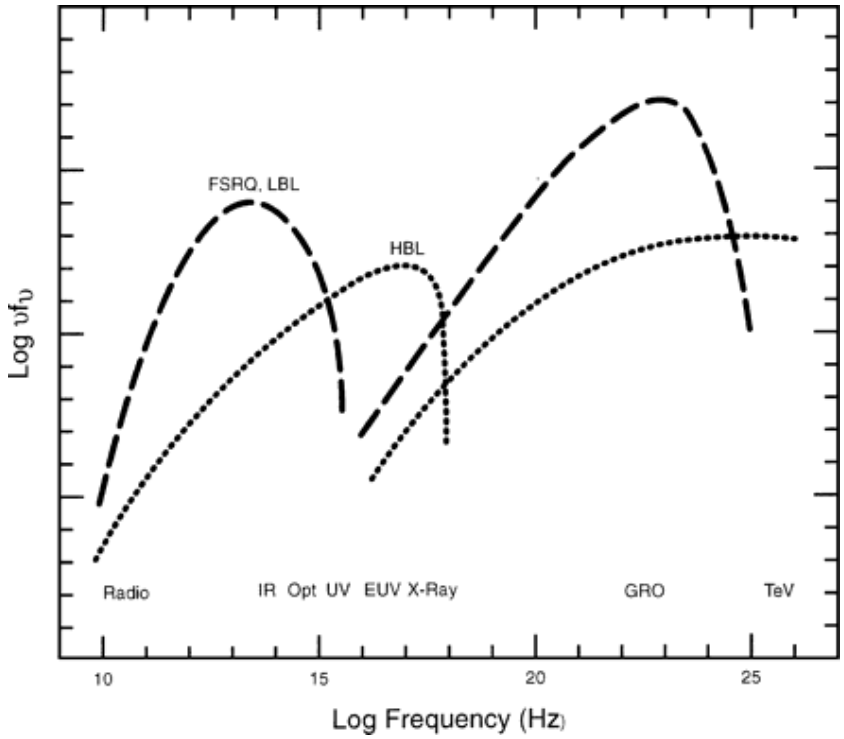

Figure 2.2: Average spectral shapes of blazars from radio through TeV gamma-rays (Sambruna et al., 1996). The low-energy component is probably due to synchrotron radiation and the high energy component to inverse Compton scattering of lower energy seed photons. The various acceleration mechanisms which produce these bumps are detailed in Section 2.3. The two different curves represent the average spectral shapes of high-frequency peaked BL Lacs (HBL) and low-frequency peaked BL Lacs (LBL) as defined by their ratios of x-ray to radio flux. FSRQs have continua like those of LBL.

- The low-frequency peak of LBL occurs in the IR/optical regime as opposed to the UV/soft x-ray regime for HBL (Sambruna et al., 1996).

- LBL are more powerful gamma-ray sources than HBL. However the peak of the high-frequency emission occurs at energies of $\sim$1 GeV for LBL and $\sim$1 TeV for HBL. Therefore, HBL are more likely to be sources of TeV photons, and in fact are the only blazars detected at TeV energies (Perlman, 1999).

- HBL are less luminous, as well as less core-dominated, at radio wavelengths than LBL (Perlman, 1999).

- Rapid (week scale), large amplitude (x2) variations in the far IR are only seen in LBL (Ulrich et al., 1997).

- Variations in the optical and UV regime are faster in LBL than in HBL (Ulrich et al., 1997).

- HBL have rapid (hour scale), large amplitude (x2) variations in the x-ray regime, whereas LBL experience variations on the time scale of $\sim$10 days (Ulrich et al., 1997).

- HBL occupy a different region of parameter space than LBL in scatter plots of the radio flux vs. x-ray flux, radio flux vs. optical flux, and x-ray–optical spectral index vs. radio–optical spectral index (Constamante and Ghisellini, 2002).

- HBL are less polarized than LBL, with a smaller duty cycle. Further, HBL have a preferred position angle of polarization, while LBL do not (Perlman, 1999).

- HBL are distributed differently in space, with either more objects or more luminous objects located at low redshifts; while LBL are consistent with either a uniform distribution with redshift or more objects at high redshifts (Perlman, 1999).

Although these two types of blazars are distinct, the relative fraction of LBL to HBL, which has important ramifications as to the types of jets nature prefers, is unknown. This is due to biases inherent in the surveys which identify these objects. X-ray surveys, which identify HBL because of their high-frequency synchrotron peaks, span a different range in flux and energy than radio surveys, which identify LBL because of their low-frequency peaks. Due to the differing ranges, extrapolations using only a limited amount of information from each type of survey are required to predict the total number density of each type of blazar. Depending

on which survey is used for the prediction, the results are conflicting (Urry, 1999). Although model dependent corrections could in principle eliminate the biases, the present samples of each type of blazar are small, limiting the conclusions that can be drawn. Therefore, a larger sample of blazars is needed to determine which blazars are more numerous. It is also not clear how LBL and HBL are related. Some theories explain the difference through combinations of the consequences of viewing angle and luminosity. Other theories propose that HBL and LBL represent opposite ends of a continuous distribution of peak frequencies, explaining the differences to be a result of some combination of this distribution and luminosity. Each of the theories has strengths and weaknesses, however the unification theories only represent works in progress as current data can not distinguish between the competing models. Therefore, deeper samples of blazars, especially FSRQs which as previously mentioned are showing hybrid behavior between the two classes, are required to distinguish the models.

Blazar Variability

As the emission from blazars is highly variable so are the SEDs. Typically the observed energy spectrum becomes harder as the intensity of emission increases. While variations are frequent, no periodicity has been found in the changed emission levels. More variability, both larger amplitude and greater rapidity, is observed at and above the peak in both components of the SEDs. Correlated variations with only brief wavelength dependent lags have also been observed in both components of the SED. The correlations occur between two corresponding points on both curves. Specific correlations observed are between the TeV gamma ray and x-ray emission, as well as between the GeV gamma ray emission and the IR–UV regime. These correlations suggest that a single population of particles (likely electrons) is responsible for both bumps.

2.3 Acceleration Mechanisms

As previously mentioned the SEDs of blazars consist of 2 components. The low energy component of the SED is believed to be from incoherent synchrotron radiation from relativistic electrons in the jet. This is strongly supported by the observation that blazar emission is highly polarized at radio and optical wavelengths. While a general agreement exists on the origin of the low energy component of the SED, the mechanism responsible for the high energy component is widely debated. Regardless, a consensus exists that the TeV photons are created in the jets of AGN. There a two basic models for the high-energy component of

blazar emission. These are the inverse Compton models (Levinson and Blandford, 1991) and the proton-initiated cascade models (Mannheim, 1993; Protheroe et al., 1992).

2.3.1 Inverse Compton Model

In this model, electrons are accelerated to high energies in the blazar jets. These electrons then upscatter photons, via inverse Compton scattering, to high energies. As a result the maximum energy of the photons produced as well as the VHE flux is a function of the maximum electron energy and correspondingly the strength of the dynamic magnetic field which accelerates the electrons. Several variations on the inverse Compton model exist, with each likely contributing to the high energy component. The major differences between each of them are the nature of the seed photons present and where the acceleration occurs in the jet. The most popular variation is the synchrotron self Compton (SSC) model (Maraschi et al., 1992) which must occur on some level in the jets. In the SSC model the source of seed photons is the high-energy electrons (via synchrotron radiation) themselves. These synchrotron photons, which are responsible for the low-energy component of the SED, are then upscattered to higher energies by these same electrons. In another variation, the external Compton (EC) model, the source of the seed photons is outside the jet, either directly from an accretion disk (Dermer et al., 1992) or disk emission reprocessed in the broad emission-line clouds (Sikora et al., 1994). Another variant is the inhomogeneous model, where emission at different energies is produced in different regions of the jet. Regardless of the model, energy lost from the electrons due to rapid cooling via inverse Compton scattering or synchrotron radiation limits the maximum gamma-ray energy to $\sim$10 TeV (Hoffman et al., 1999). Although limited in the maximum energy produced, these models reproduce rapid flaring activity well due to the small mass of an electron (compared to protons) which allows for rapid acceleration and cooling.

The trends in the SEDs of blazars are best explained by inverse Compton models. The paradigm is that the high-energy electrons, which produce both components of the SED, cool on ambient photons through inverse Compton scattering. As the luminosity of the blazar increases, the number of ambient photons increases (as indicated by the higher luminosity of the emission lines), resulting in more cooling, naturally leading to lower overall electron energies and hence lower SED peak energies. In contrast, as the luminosity decreases there is less cooling and therefore higher peak energies. Currently it is believed that the EC process dominates the gamma-ray production in high-luminosity blazars (RBL), while the SSC process dominates in low-luminosity blazars (XBL) (Urry, 1999). The larger ratio of the luminosity of the high-frequency component to the low-frequency

component in high-luminosity blazars (LBL) is due to the larger number of seed photons which can be upscattered (through EC contributions). The x-rays production from either high or low-luminosity blazars are likely dominated by SSC processes (Urry, 1999).

2.3.2 Proton-Initiated Cascade Model

In the proton-initiated cascade models, protons are shock accelerated to ultra-high energies (10^{10} GeV). These protons then interact with ambient photons producing neutral pions that decay and initiate an electromagnetic cascade. This cascade results in the production of high energy photons. Similar to the inverse Compton models, the seed photons can come from the synchrotron photons or from an external source. Gamma-rays above 10–20 TeV are easily produced in proton models due to the ultra-high energies involved. Proton models have difficulty in reproducing rapid flaring activity since the protons are massive (compared to electrons) and are not as easily accelerated or cooled.

2.4 TeV Blazars

The detection of seven AGN has been reported at TeV energies to date. Of these seven, only four have been confirmed by detections from multiple observatories. These four AGN are Mrk 421 (Punch et al., 1992), Mrk 501 (Quinn et al., 1996), 1ES1426+428 (Horan et al., 2002), and 1ES1959+650[1]. Two of the remaining AGN, 1ES2344+514 (Catanese et al., 1998), PKS2155-304 (Chadwick et al., 1999), have been detected by with high significance by one observatory observatory during only one epoch. The other AGN for which a detection has been reported is 3C66A (Neshpor et al., 1998). However, the significance found for this AGN is low and the detection has not been confirmed by detectors with much higher sensitivity meaning that the detection must be considered tentative at best. The six AGN whose detection is considered firm are all relatively nearby, $z < 0.13$, and are high-frequency peaked, x-ray selected BL Lacs. The differential spectra found for the five solid detections in the northern hemisphere are discussed in Section 6.5.2. Mrk 421 and Mrk 501 are the two most extensively studied AGN at TeV energies. The TeV flux found from these objects is characterized by a low quiescent level, which increases dramatically (sometimes more than 10-fold) during flaring episodes, where they can become the brightest objects in the TeV sky. Significant flaring behavior in Mrk 421 and Mrk 501 has been observed on

[1]This detection is very recent and currently unpublished. It is reported on the Whipple website (http://egret.sao.arizona.edu).

timescales as small as 15 minutes for Mrk 421 (∼half-day for Mrk 501), up to months in length at TeV energies (Buckley, 1999). Further, the annual average flux from these two objects is found to vary significantly, but is less than that of the Crab Nebula. Multi-wavelength campaigns have shown that variations in the TeV flux of these two objects are correlated with variations in the x-ray flux with little or no time lag (Buckley, 1999). The fluxes detected from the other three solidly detected AGN in the northern hemisphere are discussed in Section 6.5.4.

2.5 Extragalactic Background Light

The presence of an extragalactic diffuse photon background, including the infrared and optical photons from stars and dust, and the 2.7 K cosmic microwave background radiation (CMBR) sets limits on the distance from which gamma rays can reach Earth. This is due to the absorption of gamma rays, through photon-photon pair production, by interactions with the background photons. The level of absorption depends on the energy of the gamma ray, the energy of the background photons, and the intensity of the background photons.

As a result of this absorption by the extragalactic background light, distant sources of gamma rays are either completely obscured or have their energy spectrum distorted. For example, the CMBR, which is the most intense source of background photons in the universe effectively absorbs all the extragalactic (some from nearby galaxies may survive) photons above 100 TeV. However, the presence of the CMBR does not affect lower energy (∼1 TeV) photons. These photons are attenuated by background light at optical to infrared wavelengths. The density of the infrared diffuse background is not yet measured, but is known to increase rapidly with wavelength. This results in the optical depth above 100 GeV increasing rapidly with increasing gamma-ray energy. This is perhaps the reason for the lack of detections at TeV energies of distant AGN, including many of those detected by EGRET. Current limits on the extragalactic background light (EBL) set by the detection of Mrk 421 and Mrk 501 at TeV energies imply that optical depth for photons at TeV energies, due to pair production with EBL, does not reach 1 until beyond a redshift of z=0.1 (Biller et al., 1998). Theoretical estimates of the amount of EBL give similar results (Primack et al., 2000).

2.6 Implication of TeV Observations

At present only a few AGN are known to be emitters of TeV photons, therefore the major focus of TeV observations of AGN is to discover new TeV sources. The discovery of more TeV bright AGN has several implications. Conclusively

determining which types of blazars are emitters of TeV photons can help resolve the differences between HBL and LBL discussed earlier. TeV observations of AGN can also distinguish which of the various acceleration mechanisms responsible for the production of TeV photons in AGN are appropriate. A range of observations, such as the time scale of flaring activity, the maximum energy of photons observed, and correlations of TeV flaring with other wavelengths, currently constrain each of the models, but do not rule any out. Further observations are required to determine the correct model. Studies of TeV AGN also constrain the parameters of the models, including the size and location of the emission region, the beaming factor, the strength of the magnetic fields in the jets, the nature (leptons or hadrons) and maximum energy of the particles responsible for TeV emission, and the nature of the seed photons.

Aside from the greater understanding of AGN which is gained from TeV observations, insight into the density of the IR/optical background can be attained. By identifying multiple sources of TeV photons at different redshifts, the density of the IR/optical background photons can be inferred. Currently there are only upper limits on the density. The density measurement is performed by viewing the effect of the absorption of TeV photons on the observed spectrum of the AGN. A cutoff or steepening of the spectrum should be seen at high photon energies. Using the distance to the source, as well as the energy at which the spectrum cuts off or steepens, the optical depth, which is related to the density of IR background photons, of the universe to TeV photons can be determined. Although it should be noted that multiple sources are required to decouple the effect of intrinsic absorption of TeV photons at the source. Not only does a measurement of the optical depth of the universe at VHE energies have implications for TeV astronomy in terms of how far a telescope can see, but also for cosmology. The major contributors to the extragalactic background light at IR/optical wavelengths (which affects TeV photons) are star formation and dust absorption and re-emission. The strength of the IR/optical background, determined from the optical depth, could provide information on the history of star and galaxy formation (Dwek et al., 1998), as well as more exotic processes such as pregalactic star formation and some dark matter candidates (Catanese and Weekes, 1999). The current limits on the EBL provided by TeV observations are well above those predicted for normal galaxy formation (Primack et al., 1999), but have provided constraints on more exotic mechanisms for sources of the EBL (Biller et al., 1998). The detection of more TeV AGN, particularly at higher redshift, has the potential to set very restrictive limits on the EBL density.

2.7 Selected AGN

Since observations in VHE astronomy consist of looking for a relatively small excess of events in a given direction above the more numerous cosmic-ray background, the results must be expressed statistically. When assessing the statistical significance of any possible detection, the number of sources studied needs to be accounted for. It is expected that, in the absence of any sources of TeV photons, the significance observed at the positions of objects chosen for study would follow a Gaussian distribution of probabilities. Therefore the probability of observing an effect of some significance (probability) in some number of attempts (the number of sources studied) assuming a Gaussian distribution of probabilities must be calculated before a detection can be claimed. For example, if one AGN were observed with 4σ significance in a study of 1000 AGN it would only be a 1.9σ effect after accounting for the number of AGN studied. However, if one AGN were observed with 4σ significance in a study of 27 AGN, it would be a 3.1σ effect. Clearly the number of trials can affect whether or not the excess detected at the position of an AGN can be claimed as a detection. Since the significance found from any object by Milagro is generally expected to be small, only AGN meeting certain selection criteria were selected for study in this thesis to reduce the number of trials, even though Milagro observes all AGN in the overhead sky.

Twenty-seven AGN within the field of view of Milagro, declination between 0° and 70°, were selected for continuous observation in this thesis. This sample includes 5 AGN already detected at TeV energies: Mrk 421 (Punch et al., 1992), Mrk 501 (Quinn et al., 1996), 1ES2344+514 (Catanese et al., 1998), 1ES1426+428 (Horan et al., 2002), and 1ES1959+650[2] (http://egret.sao.arizona.edu). For the remaining candidates, only relatively nearby AGN ($z<0.1$) are selected in order to minimize the attenuation of any possible signal by the extragalactic background photons. Since all of the AGN detected to date at TeV energies are x-ray selected BL Lacs (XBL), preference is given to these types of blazars. This is not exclusive as some FSRQs whose SEDs are high-frequency peaked, similar to that of XBL, have been found recently. A list of XBLs and high-frequency peaked FSRQs, with $z<0.1$, is found in Perlman (1999). All of the AGN on this list, within the field of view of Milagro, were selected amounting to 14 other XBLs and 5 FSRQ. Since EGRET is sensitive to photons up to 30 GeV, any additional AGN detected by EGRET (Mukherjee et al., 1997), meeting the field of view and redshift requirements, were selected for study, adding two radio-selected BL Lacs (RBL) to the list of candidates. Finally, any additional AGN meeting the selection criteria for

[2]This blazar was detected after this study began and is not yet published, but was on the initial list of objects chosen from Perlman (1999).

which an upper limit at TeV energies is published (Buckley, 1999) was chosen, adding one more RBL (3C371) to the list of candidates. The coordinates, common name, redshift, and relevant detections are listed in Table 2.1.

Nominal Coordinates	Name	Class	z	TeV / EGRET Detected
1101+384	Mrk 421	XBL	0.031	TeV, EGRET
1426+428	1ES	XBL	0.129	TeV
1652+398	Mrk 501	XBL	0.034	TeV, EGRET
1959+650	1ES	XBL	0.048	TeV
2344+514	1ES	XBL	0.044	TeV
0033+595	1ES	XBL	0.086	No
0110+418	RGB	XBL	0.096	No
0152+017	RGB	XBL	0.080	No
0153+712	RGB	XBL	0.022	No
0214+517	RGB	XBL	0.049	No
0314+247	RGB	XBL	0.054	No
0656+426	RGB	XBL	0.059	No
1133+704	Mrk 180	XBL	0.046	No
1532+302	RGB	XBL	0.064	No
1610+671	RGB	XBL	0.067	No
1727+502	I Zw 187	XBL	0.055	No
1741+196	1ES	XBL	0.083	No
2321+419	1ES	XBL	0.059	No
2322+346	RGB	XBL	0.098	No
0010+106	III Zw 2	FSRQ	0.090	No
0138+398	B2	FSRQ	0.080	No
0321+33	B2	FSRQ	0.062	No
1413+436	RGB	FSRQ	0.090	No
2209+184	PG	FSRQ	0.070	No
1219+285	W Comae	RBL	0.102	EGRET
1807+698	3C371	RBL	0.051	No
2200+420	BL Lac	RBL	0.069	EGRET

Table 2.1: Table showing the nominal coordinates, common name, class, and red shift of 27 AGN selected for study with Milagro. Also shown is whether or not the candidate AGN have been detected at TeV energies or by EGRET (sensitive to photons from 20 MeV to 30 GeV).

Chapter 3

The Milagro Detector

The Milagro gamma-ray observatory is a unique extensive air shower (EAS) array which employs a water-Cherenkov technique to continuously monitor the northern sky for astrophysical gamma-ray emission near 1 TeV. Milagro's ability to continuously monitor all sources in the overhead sky, even during daytime transits, makes it well suited for studies of sources of TeV photons, which are known to be highly variable and exhibit flaring behavior. In this chapter, the advantages and methods of the water-Cherenkov technique are detailed. Milagro is also described in detail, including the general characteristics of the detector, how the detected light from an EAS is transformed into raw data, and the algorithms which are employed to reconstruct the detected EAS.[1] Analysis of the general performance of Milagro is also presented. This performance includes the shower core location resolution, angular resolution, efficiency of the background rejection technique, effective area, and energy resolution.

3.1 Water-Cherenkov Technique

As discussed in the introductory chapter, most TeV observatories, such as Whipple and HEGRA, detect the Cherenkov light produced by EAS in the atmosphere. These instruments generally have a low energy threshold, excellent angular resolution, and the ability to reject most of the more numerous EAS initiated by hadronic particles. This gives these detectors a high sensitivity to TeV point sources. While these observatories have detected several sources of TeV photons, they are limited to observations on moonless, cloudless nights, resulting in a low duty cycle. Further, these instruments must be pointed and have

[1]More details regarding Milagro are found in an article describing a smaller, less sensitive version of Milagro, known as Milagrito (Alexandreas et al., 2000).

a small field of view. Given that the flux from TeV sources is generally highly variable, these limitations make the identification of new sources of TeV photons difficult. As there are only a limited number of known sources of TeV photons, an instrument that possess a large aperture and high duty cycle is desirable for the identification of new TeV sources. The ability to continuously monitor large portions of the overhead sky is also important for quickly identifying flaring states in known sources of TeV photons, as well as for observing transient sources, such as GRBs, whose positions are unknown.

Another form of detector, EAS arrays, such as CYGNUS and CASA, have the desired large field of view and high duty cycle. As discussed in the introductory chapter, these detectors typically detect the charged particles in an EAS with a sparse array of scintillation counters. Unfortunately, because <1% of the total area of the array is covered by detectors, only a small fraction of the surviving shower particles are detected. This effect is compounded by the fact that photons greatly outnumber ($\sim$4:1) the charged particles at ground level and scintillation counters do not detect gamma rays with high efficiency. The sparse sampling of the EAS results in these instruments having a high energy threshold. This is undesirable because the flux from TeV gamma-ray sources is low and typically characterized by a falling differential power law spectrum with spectral index of order $\alpha = 2.6$. No new sources of TeV photons have been discovered by such EAS arrays due to this limitation. Clearly, a detector that possesses the sensitivity and low energy threshold of the atmospheric-Cherenkov instruments, while having the large aperture and high duty cycle of the EAS arrays is desirable.

Milagro is a unique EAS array which achieves these desired characteristics by utilizing a water-Cherenkov technique. This technique allows Milagro to directly detect almost all of the secondary particles from an EAS, including the more numerous hard photons. The relativistic charged particles from an EAS enter the light tight detector, where they interact with the detection medium of very clean water. Since the particles are traveling faster than the speed of light in water, they emit Cherenkov radiation. The hard photons also interact with the water, creating more relativistic charged leptons by either pair production or Compton scattering of electrons. These newly created particles also emit Cherenkov radiation. This radiation, blue and ultraviolet light, is emitted in a cone with a large opening angle of $\sim 41^{\circ}$. The large opening angle allows for the detection of almost all the particles in the EAS with a relatively sparse array of light sensing photomultiplier tubes (PMTs). This enables a large area, which is critical for the detection of TeV point sources, to be cheaply instrumented. Since nearly every particle is detected with the use of the water-Cherenkov technique, Milagro has a low energy threshold (<1 TeV) that is unprecedented for an EAS array. Further, the large active detection area provides the ability to identify the nature, hadronic

or electromagnetic, of the primary particle initiating the EAS. This ability, which allows for the rejection of the more numerous hadronically initiated EAS, greatly increases the sensitivity of Milagro and is primarily responsible for the success experienced by the air-Cherenkov telescopes. While the water-Cherenkov technique gives Milagro a low energy threshold, good angular resolution, and the ability to perform background rejection characteristic of air-Cherenkov telescopes, it also maintains the advantages of the EAS arrays such as wide aperture and high duty cycle. Because of these attributes, Milagro has unique capabilities for discovering new sources of TeV photons.

3.2 The Detector

3.2.1 Location

Milagro is located approximately 35 miles west of Los Alamos National Laboratory (LANL) at the site of a former geothermal energy project (Hot Dry Rock) in the Jemez Mountains of northern New Mexico. The latitude and longitude of Milagro are 35° 52' 45" and 106° 40' 37" West respectively. The latitude is similar to that of several other TeV observatories, allowing for the same sources to be observed and comparisons of the results made. Since the number of particles in an EAS decreases after a height known as shower maximum ($\sim$7–10 km above sea level) is reached, the detector is located at high altitude in order to sample as many particles as possible. The elevation of 2630 meters above sea level corresponds to an atmospheric overburden of $\sim$750 g cm^{-2}. Figure 3.1 shows an aerial view of Milagro and the surrounding environment.

3.2.2 General Description

The Milagro detector consists of a man-made $\sim 6 \times 10^6$ gallon ($\sim 21 \times 10^6$ liter) water reservoir, referred to as the pond. The reservoir is rectangular and has dimensions 60×80 m^2 at the surface. The sides of the pond are sloping, leading to an area of 30×50 m^2 on the bottom. The bottom of the reservoir is at a depth of $\sim$7.5 m, and is lined to keep contaminants out of the filtered water which fills the detector. The dimensions of the pond are illustrated in Figure 3.2 which shows the reservoir when it is empty. The water in Milagro is very clean and continuously recirculated through a filtration system. The attenuation length of the water at 350 nm wavelength is $\sim$13 m. Unfortunately, the relative contributions of scattering and absorption to the attenuation length are not known. This is a source of uncertainty in accurately simulating the response of Milagro to an EAS.

Figure 3.1: Aerial photograph of the Milagro detector and surrounding environment.

Figure 3.2: Aerial photograph of the Milagro detector with the pond empty.

An opaque cover is installed at the top of the pond in order to keep out external light. The transmission of essentially no light through the cover is required for

Milagro to be able to operate during the day. Although the cover normally rests on top of the water during data taking, it can be inflated to allow for repairs within the detector. The top of the cover is painted with a highly reflective roofing paint to keep the interior from becoming too hot for repairs to take place. Figure 3.3 shows a close-up aerial photograph of Milagro with the cover inflated.

Figure 3.3: Aerial photograph of the Milagro detector with the cover inflated.

The Milagro detector contains 723 photomultiplier tubes (PMTs) anchored by 1.6 mm-diameter Kevlar strings to a grid of sand filled PVC pipe, 7.5 cm in diameter. The PVC pipes each weigh $\sim$35 kg and are arranged on the bottom of the pond in a square grid with 2.8 meter spacing. The grid is also located on the sloping sides of the pond and is arranged in a manner that allows the grid to appear continuous and uniformly spaced when viewed from directly overhead. Since the bottom of the pond is not flat, the length of each individual Kevlar string is calculated for each PMT, and is such that all the PMTs lie in 2 separate horizontal planes when they float upward. As there are no currents in the pond, a survey of the grid allows for the precise location of the PMTs to be determined to an accuracy of $\pm$3 cm horizontally and $\pm$1 cm vertically. The orientation of the grid with respect to true north, as well as the direction of the zenith, are both known to an accuracy of $\pm 0.02^{\circ}$. Figure 3.4 shows the interior of the Milagro detector while it is being filled with water. The grid and PMTs are clearly visible.

Milagro is located in one of the most lightning prone areas in the United

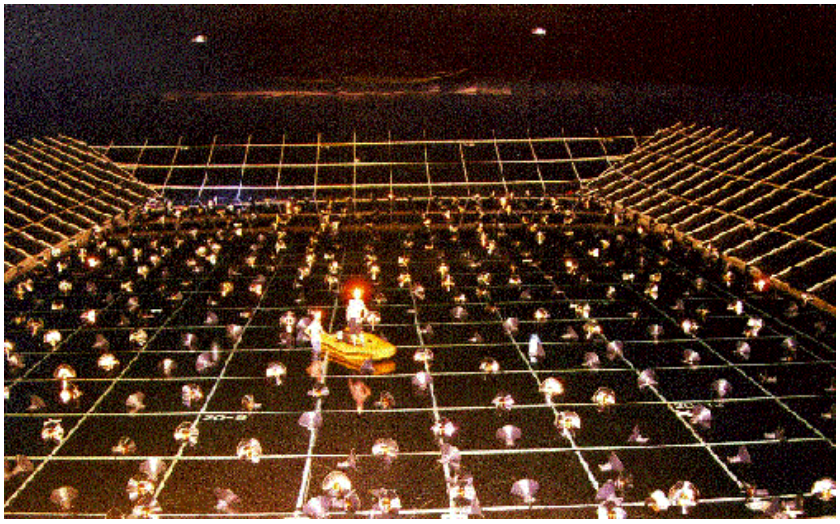

Figure 3.4: Photograph of the interior of Milagro with the cover inflated. This photo is taken during the filling of the detector with water.

States. Because of this, a 12,500 m^2 Faraday cage was built over the entire pond and surrounding buildings. While the Faraday cage does not divert lightning from the detector, it is designed to intercept lightning strokes and to shunt their current to ground, keeping the voltage gradients low within the environs of the experiment. This protection is required as one lightning strike to the pond would likely destroy all of the PMTs and most of the electronics in Milagro.

The site receives its electrical power from a local rural electric company. Due to intermittent power outages, uninterruptible power supply (UPS) crates are installed to power the electronics for Milagro. This enables the detector to remain operational during brief outages. The crates also condition the power to the electronics. While the data taking for Milagro is fully automated, network access via a T-1 line allows for remote monitoring and some control of the apparatus.

3.2.3 Photomultiplier Tubes

As mentioned previously, Milagro employs 2 layers of submerged PMTs (723 total) to detect Cherenkov light produced by secondary particles from an EAS in the covered reservoir of water. The first layer, consisting of 450 PMTs on a 2.8 x 2.8 m^2 grid under 1.5 m of purified water, utilizes the relative arrival time of the Cherenkov photons at the PMTs to reconstruct the direction of the incoming EAS with an accuracy of $\sim$0.75 degrees. The second layer of 273 PMTs located at

$\sim$6 m depth,[2] with a similar spacing, is used to identify penetrating particles such as muons, hadrons and very energetic electromagnetic particles. Due to the low cross section for photo-production of hadrons, one expects many more muons and hadrons at ground level in an EAS initiated by a hadronic cosmic ray, allowing this second layer to be useful for determining the species of the primary particle. This is crucial for the detection of TeV sources, as the EAS initiated by hadronic cosmic rays greatly outnumber ($\sim$10,000:1) those initiated by gamma rays. Figure 3.4 shows the interior of Milagro as it is being filled with water. The layout of the PMTs is apparent in the photograph.

The 20 cm-diameter Hammamatsu 10-stage R5912SEL PMT is utilized in Milagro. This PMT was selected because it has good time resolution, good charge resolution, good charge linearity up to $\sim$75 PEs, a large photocathode with high photon collection efficiency, a relative absence of significant prepulsing and afterpulsing, and it is relatively insensitive to the effects of the geomagnetic field. Each PMT is encapsulated to keep moisture away from the electronic components which include a passive base of resistance 20 MΩ. The PMTs operate at positive high voltage to ensure that the photocathode is at the same potential as the surrounding water. This high voltage is delivered by a single 75 Ω coaxial cable that also carries the PMT signal to the electronics. The cables for a given layer have the same length to eliminate systematic timing effects.

A reflective collar (baffle) is attached to the encapsulation of each PMT. A picture of the PMT, encapsulation and baffle is shown in Figure 3.5 As can be seen, the shape of the baffle is conical, with a small radius of 8.4 cm, a height of 16.4 cm, and a large radius of 26.8 cm. This corresponds to an opening half-angle of 48.4°. The baffle is attached below the photocathode of the PMT and ends at the top of the PMT glass. Each baffle is reflective on the inside to increase the collection area of the PMT, and dark on the outside to prevent the reflection of light from this surface. The main purpose of the baffles is to block out late arriving PMT pulses from light reflecting off the bottom of the pond, as well as light propagating horizontally across the pond. This late light is significant in quantity and degrades the angular resolution of the detector. Further, these baffles were not present in the prototype of Milagro, known as Milagrito, where a study of the Moon shadow showed a significant systematic pointing error attributable to this late light (Wascko, 2001). The use of the baffles eliminates this systematic effect as well as making the raw data $\sim$35% smaller in size by reducing the number of hit PMTs. This latter effect is important, as it allows for the detector to run

[2]This "layer" actually consists of two layers: an array of 19x11 PMTs (209 total) at $\sim$6 m depth, surrounded by a ring of 64 PMTs at $\sim$5 m depth. All told the "layer" is a 13x21 grid of PMTs.

at a ∼35% higher trigger rate, which increases the overall sensitivity of Milagro to sources of TeV gamma-rays.

Figure 3.5: Photograph of one of the encapsulated PMTs with baffle present as used in Milagro. A scuba diver is visible in this photograph as it was taken during downtime for PMT repairs.

3.2.4 Electronics

The signal from each PMT channel passes through custom-made electronics boards which provide timing and pulse height information. The pulse height for each PMT is determined using the time-over-threshold (TOT) technique. A dual-threshold system is utilized to eliminate PMT prepulsing, as well as to provide a large dynamic range on the pulse height measurement. In the electronics, the PMT signal is split between high-gain and low-gain amplifiers. The output from the high-gain amplifier is sent to a discriminator with a threshold set to a level of ∼1/4 PE. The output from the low-gain amplifier is sent to a discriminator where the threshold is set to a level of ∼5 PE. Whenever the signal crosses the low (0.25 PE) or the high (5 PE) threshold, a logic pulse is generated with width equal to the length in time that the signal remained above the threshold. Figure 3.6 illustrates the dual threshold technique. This figure is taken from Joe McCullough's thesis (McCullough, 2001).

As can be seen in Figure 3.6, signals with pulse height between 0.25 and 5 PEs generate "2-Edge" pulses, and signals with greater than 5 PEs generate "4-Edge Pulses." The percentage of PMT signals that are 2-Edge and 4-Edge pulses is

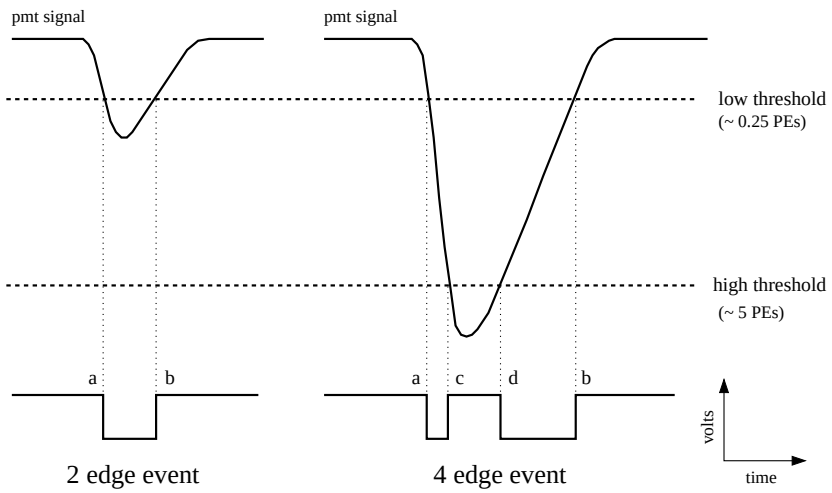

Figure 3.6: Figure showing a conceptual drawing of the dual TOT method and the logic pulses that result from the technique. This figure is taken from Joe McCullough's thesis (McCullough, 2001). Shown are the cases where only the low threshold is exceeded and where both thresholds are exceeded.

$\sim$65% and $\sim$28% respectively. The sum does not total 100% because pulses exist with anywhere from 1 to 16 edges. An edge finding algorithm is applied to all combinations, which assigns either 2 or 4 edges to these pulses. Once the number of edges is found the number of PEs can be calculated. The width of the logic pulse, time-over-threshold, is approximately proportional to the logarithm of the number of PEs. Therefore, using the notation shown in Figure 3.6, the following relation of TOT to PEs is found:

$$\Delta t = t_b - t_a \propto ln(N_{PEs}) \qquad \text{2 edge event}$$
$$\Delta t = t_d - t_c \propto ln(N_{PEs}) \qquad \text{4 edge event}$$

Occasionally, pulses are found with very large low TOT values, and no high TOT values. This can result in an erroneously large pulse height to be returned. Therefore, these events are assigned a maximum possible low TOT and corresponding PE value. The time of the PMT hit is determined to be the time that the PMT pulse passed its highest threshold.[3] In the case of large pulses, this is the high-threshold. However, the pulse must have been above the high-threshold for some time before this is used. For small pulses, the time that the low-threshold was exceeded is utilized as the arrival time. This method of determining the arrival time eliminates the effects of prepulsing.

[3]The arrival time at each PMT is corrected for the finite rise time of the pulse which varies with pulse height.

3.2.5 Trigger

An output of the custom-made electronics boards is also used for the trigger of Milagro. For each PMT signal that crosses the low-threshold, the corresponding electronics channel generates a logic pulse 200 ns wide and 25 mV in amplitude. The analog sum of all these fixed width pulses is sent to a discriminator. If the analog sum is higher than the threshold setting, Milagro is considered to have triggered, and the information from the event is processed. Therefore, the trigger for Milagro is a simple multiplicity trigger. The trigger rate for Milagro versus the number of PMTs required in coincidence is shown in Figure 3.7 As can be seen in the figure, the trigger rate is comprised of two components. At low PMT multiplicity values, the rate is very large and decreases exponentially until about 40 PMTs are required. After this, a second component of the rate is found. This component also decreases exponentially, but at a different rate. The first component is from single muons, which typically fail the angular reconstruction, and the second component is from EAS and are generally successfully reconstructed. Since a lower threshold increases the sensitivity of Milagro to gamma-initiated EAS, particularly those at low energies, the multiplicity required was chosen so that the trigger rate was as large as possible, but did not exceed the level which the data acquisition system could handle ($\sim$2 kHz). Although the exact value of the threshold was varied in order to keep the trigger rate at a constant value,[4] the typical trigger threshold chosen is $\sim$55 PMTs hit within the 200 ns coincidence window.

3.2.6 DAQ

After the trigger criteria from Milagro have been met, the timing information from the PMT pulses are digitized by TDC modules. The time of each triggered event is recorded using the output of a GPS clock. These data, after digitization, are read out by a FASTBUS Smart Crate Controller (FSCC). The data are then transferred to a pair of dual-ported VME memory modules where they are written into the memory boards by the FSCC over a VSB bus. A multi-CPU computer then reads the data from the memory boards over the VME bus. This computer then processes the data. The processing consists of calibrating the data, reconstructing the incident direction of the EAS, and determining a parameter that is utilized for identifying the nature of the primary particle. After the data have been processed, the parameters found from the reconstruction are then recorded to DLT tape. In addition to storing the processed data, selected raw data are

[4] The trigger rate for a certain threshold varies in Milagro due to meteorological effects, light leaks, PMT deaths, etc.

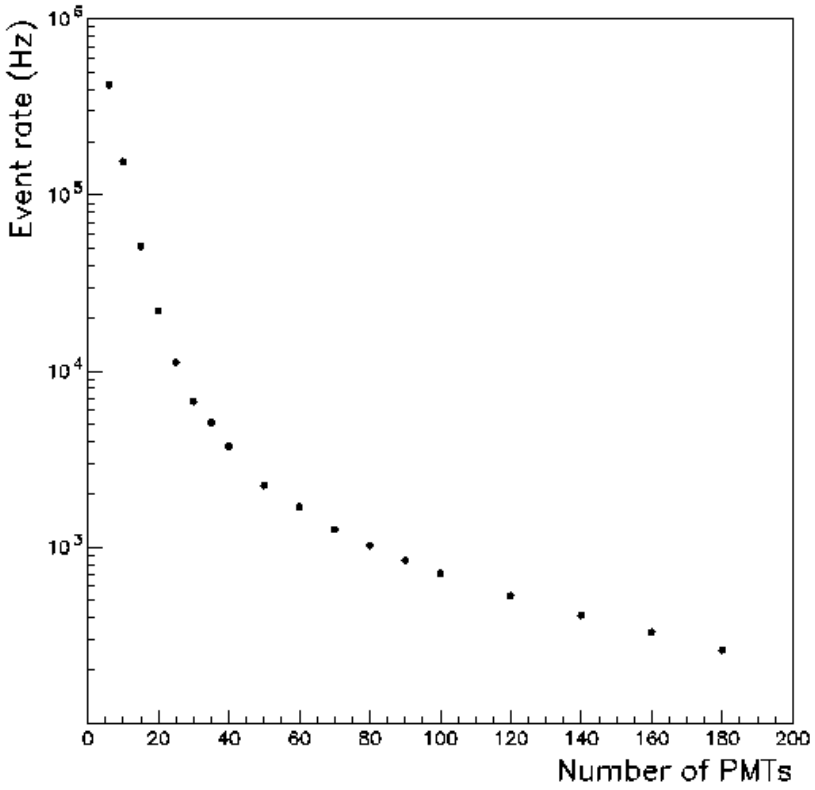

Figure 3.7: Figure showing the trigger rate of Milagro versus the number of top layer PMTs required in the multiplicity trigger (McCullough, 1999).

also saved. Only a limited amount of the raw data can be saved as the raw data rate of Milagro is of order $\sim$50 TB a year. While the selection criteria evolved during data taking, raw data were saved for events initially reconstructed within $\pm$10 degrees in declination of various objects of interest. These objects include the Crab Nebula, the Sun, the Moon, Mrk 501 (at times), and Mrk 421 (at times). Additionally, raw data are saved for showers that pass a loose background rejection criterion, and for showers that possess the characteristics of single hadrons (Yodh, 2001). Finally, Milagro is notified when other detectors observe a gamma-ray burst (GRB). As the location of the GRB is often poorly determined, all raw data from 1/2 hour before through 2 hours after the detected GRB are also saved. These data are archived and can be reprocessed using improved algorithms at a later date.

3.2.7 Monitoring

Since numerous environmental effects can dramatically alter the performance of Milagro, a separate computer is set up to record information from various sensors. This information includes, but is not limited to, the trigger rate, dead time, temperature of various components, individual PMT rates, voltages and currents, water temperature and depth, water filtration system status, as well as meteorological information. These data are archived to computer disk, allowing for in-depth analysis of the detector performance at any chosen time. Further, human monitoring is also performed by a physicist on shift. Any anomalies, as well as difficulties with the detector, are noted and fixed by this person when possible.

3.3 Calibration

As previously discussed the raw data from Milagro consists of a series of times corresponding to discriminator edges. This raw edge information must be converted to relative arrival times of the photons at the PMTs, as well as the pulse height recorded by those PMTs. While the time that each PMT was hit is known, it must be corrected for 2 effects. The first correction is for electronic slewing and is required because the analog PMT pulses have a finite rise time. A large pulse will cross a threshold more quickly than a smaller pulse. Therefore, a timing correction that is a function of pulse height is applied to eliminate this effect. The second timing correction applied accounts for fixed timing offsets between PMT channels. While in principle these offsets should be the same for each PMT, this is not the case due to different operating voltages for each PMT. Finally, the TOT value for each channel needs to be converted to a number of photoelectrons. These corrections and conversions are performed by a software algorithm using appropriate constants determined during calibration runs. In these calibration runs, light from a fast, pulsed laser is sent to a set of diffusing balls in the pond which distribute the light in the pond isotropically. An optical switch allows for one ball at a time to be illuminated. Further, a filter wheel allows for the intensity of the laser pulse to be varied. Analysis of the calibration data allows for the various corrections and conversion constants to be determined individually for each PMT. An ADC is utilized simultaneously during calibration data taking which allows for the conversion of TOT to PEs to be established. The charge resolution of the TOT method is approximately $\sim$10% for most pulse heights. A notable exception to this is the region where the low-TOT is at high values, but before the high-threshold is crossed. Due to the effects of late light in the low-TOT measurement, the charge resolution increases with pulse height to a value of $\sim$35%. After the

high-threshold is crossed the resolution immediately returns to the nominal ∼10% value.

3.4 Event Reconstruction

After the PMT pulses have been calibrated for a given event, the data are then ready to be reconstructed using fast software algorithms. The requirement that the reconstruction algorithms be fast is a result of the high data rate in Milagro. Further, only a small number of parameters are calculated in the reconstruction because of time as well as data size constraints. Although the rate of triggered events is high, every event satisfying the trigger condition for Milagro is reconstructed to determine its characteristics. These traits include the incident direction of the shower plane, the core location, and the nature (hadronic or electromagnetic) of the shower.

The relative arrival times at which the individual PMTs in Milagro are struck by Cherenkov light produced by the secondary particles in the shower front are used to reconstruct the incident direction of the primary gamma-ray. Figure 3.8 shows an event display from Milagro which illustrates this. The timing fit from the top layer is shown by the plane. The distribution of light in the top layer is shown by the green squares, which are proportional in size to the number of PEs in the struck PMT. The event shown in Figure 3.8 has an atypically large number of hit PMTs.

The first step in reconstructing an event is to determine the location of the shower core. After the core is located, a shower front sampling correction is applied. This timing correction accounts for the effect that on average, the larger the pulse height detected by a PMT, the earlier the measured arrival time, and is due to the shower plane having a finite thickness. Another timing correction is then applied to account for the curvature of the shower front. After these corrections are performed, the incident direction of the shower front is determined by a weighted least squares (χ^2) fit to a plane. Figure 3.9 shows a conceptual drawing of how Milagro fits the direction of the incident EAS taken from Joe McCullough's thesis (McCullough, 2001). After the direction is determined, a parameter related to the nature of the primary particle is calculated to perform background rejection.

The information resulting from this event reconstruction can then be used in a search for TeV emission from candidate objects. As previously discussed, only tubes from the top layer of 450 PMTs are utilized to find the incident direction of the EAS, and only tubes from the bottom layer of 273 PMTs are used to perform background rejection.

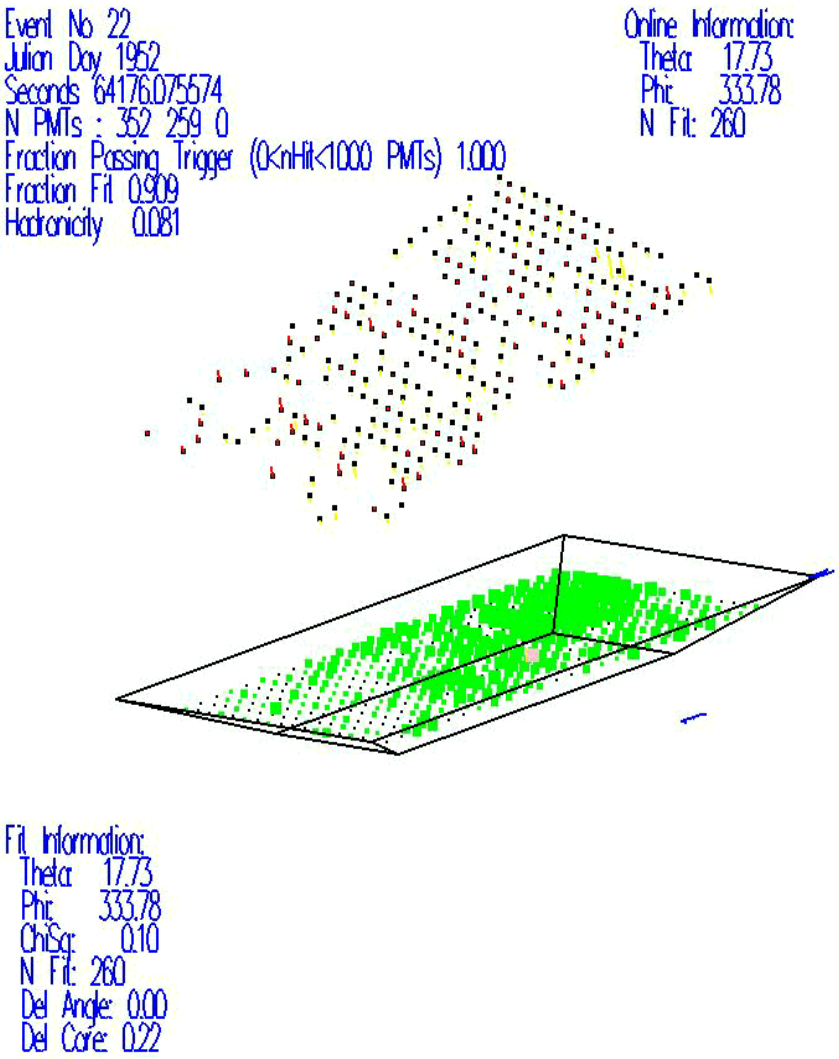

Figure 3.8: An event display for an air shower event in Milagro. The timing fit from the top layer is shown by the plane. The distribution of light in the top layer is shown by the green squares, which are proportional in size to the number of PEs in the struck PMT. This event has an atypically large number of hit PMTs.

3.4.1 Core Fit

The first step in analyzing the calibrated information from a triggered event in Milagro is to determine where the core of the incident EAS is located. Initially, the core location is found from a weighted sum of the locations of the all the hit

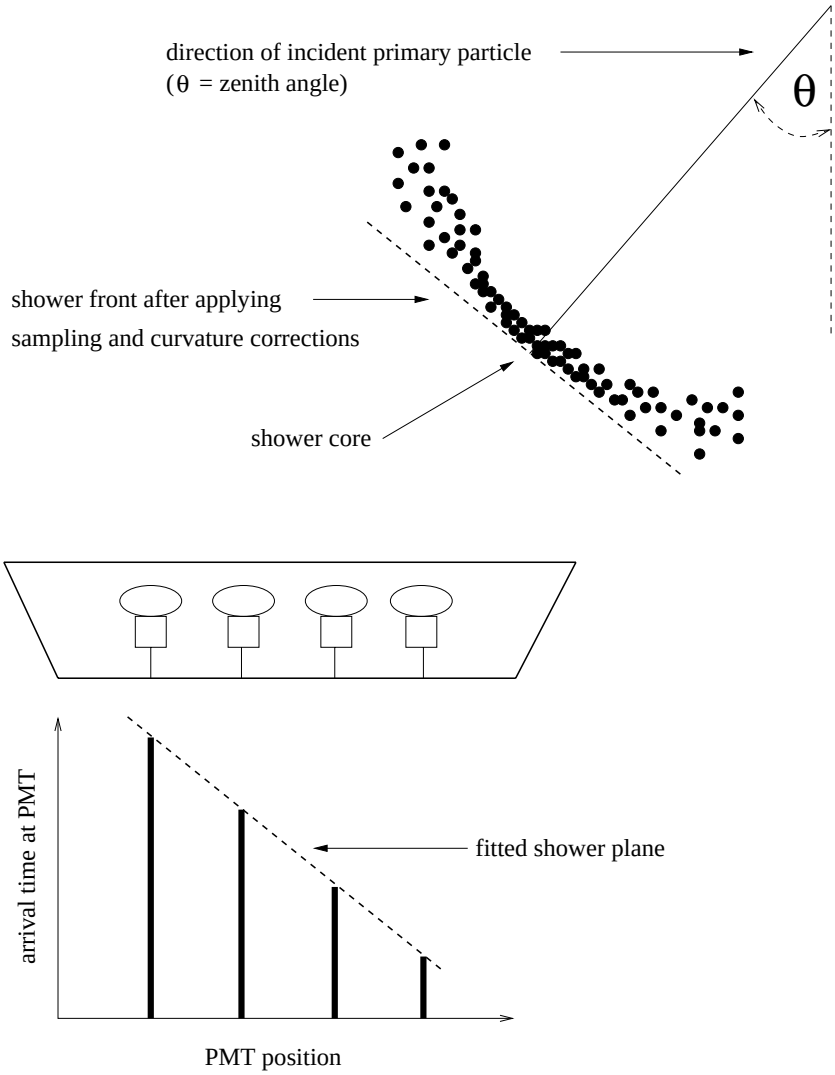

Figure 3.9: Figure showing a conceptual drawing of how Milagro reconstructs the incident direction of the EAS (McCullough, 2001). The drawing is not to scale.

top layer PMTs. This provisional core location is given by:

$$x_{core} = \frac{\sum_i \sqrt{PE_i} \times x_i}{\sum_i \sqrt{PE_i}} \qquad y_{core} = \frac{\sum_i \sqrt{PE_i} \times y_i}{\sum_i \sqrt{PE_i}} \ , \tag{3.1}$$

where PE_i is the number of PEs detected by a PMT whose coordinates are given by x_i and y_i. After the provisional values of x_{core} and y_{core} are found, new values are determined only using PMTs that fall within a triangle along the direction

given by the first fit. After these new values are found, the algorithm then determines the number of PEs per PMT versus distance from the center of the pond for PMTs falling within a smaller triangle along the direction given by the second fit. A function of the form $a+br^2$ is then fit to this information. The results of this fit are then utilized to determine if the core was located on or off the Milagro pond. If the core is found to be off the pond, the reconstructed core location is placed 50 meters from the center of the pond in the direction indicated from the x and y locations found in the second sum. The value of 50 meters is used because Monte Carlo simulations indicate that this value results in the best agreement on average with the true core location. When the core is determined to be on the pond, the previous sum is repeated for a third time, using only PMTs within 8 meters of the second core position. Figure 3.10 shows the fit core locations of EAS that trigger Milagro. The majority ($\sim$84%) of triggered EAS cores are reconstructed off the pond. This is expected, given that the typical EAS is significantly larger than the Milagro detector. The effects of the asymmetry in the pond size can also be seen in Figure 3.10, where fewer cores are reconstructed off the long sides of the pond. The overall performance of this core fitter[5] is discussed in Section 3.6.1.

3.4.2 Shower Front Sampling Correction

After the location of the shower core has been found, a timing correction, known as the sampling correction, is applied to the data. This correction is required, because on average the larger the pulse height detected by a PMT, the earlier the measured arrival time. This effect is the result of the shower front having a finite thickness.[6] The sampling correction is derived from the distribution of timing residuals for each PMT resulting from fits to the shower plane. The timing residual, t_χ, whose average magnitude is strongly dependent on pulse height, is the difference between the PMT and fit shower-plane timing. Figure 3.11 shows the distributions of t_χ for various pulse height ranges, with and without the sampling correction applied in their generation. The value for t_χ is determined in such a way that negative values correspond to late light. As can be seen in Figure 3.11, application of the sampling correction, which is pulse height

[5]Prior to December 15, 2000, a core fitter that only placed cores on the pond was utilized. This algorithm determined the core position in 1 step using an equation similar to Eq. 3.1, except that PE_i is substituted for $\sqrt{PE_i}$ in the equations. Further, the sum was only performed over 9 tubes in a 3x3 grid centered on a specific PMT. This PMT was one of the 3 brightest PMTs in the top layer, the choice of which was determined by which of the 3 had the largest total sum of PEs in the neighboring 8 PMTs. The relevant data and interval over which this is true is discussed in Chapter 4.

[6]There is also an electronic effect (slewing) which is similar but is accounted for in the calibration.

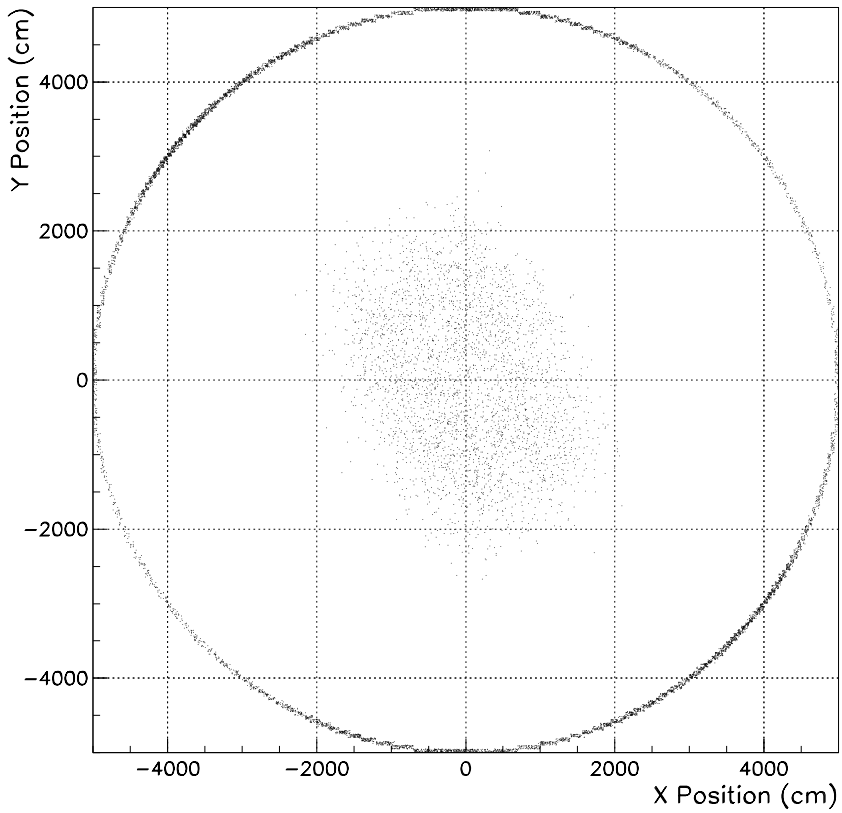

Figure 3.10: Figure showing the distribution of the fit position of the shower cores in EAS which trigger Milagro.

dependent, shifts the peaks of the t_χ distributions to zero, which corresponds to being on time. For large PE values and small PE values, the peaks of the distributions are no longer early and late respectively. The peaks are shifted, instead of the average, because shifting the average would correct too much for the effect since the distributions are strongly non-Gaussian and characterized by a long tail of late light.

The sampling correction is determined in an iterative manner. First, t_χ distributions are generated from fits with no sampling correction applied for various ranges of pulse heights. The peaks of these distributions are found and the values fit as a function of PEs. The function is then applied as a sampling correction and new t_χ distributions are generated. The peaks of these distributions are found and the values fit to a function of PEs. This function is added to the initial function, and the process is repeated with each successive step adding more to the overall correction until it converges. The exact correction applied in Milagro adds Δt to

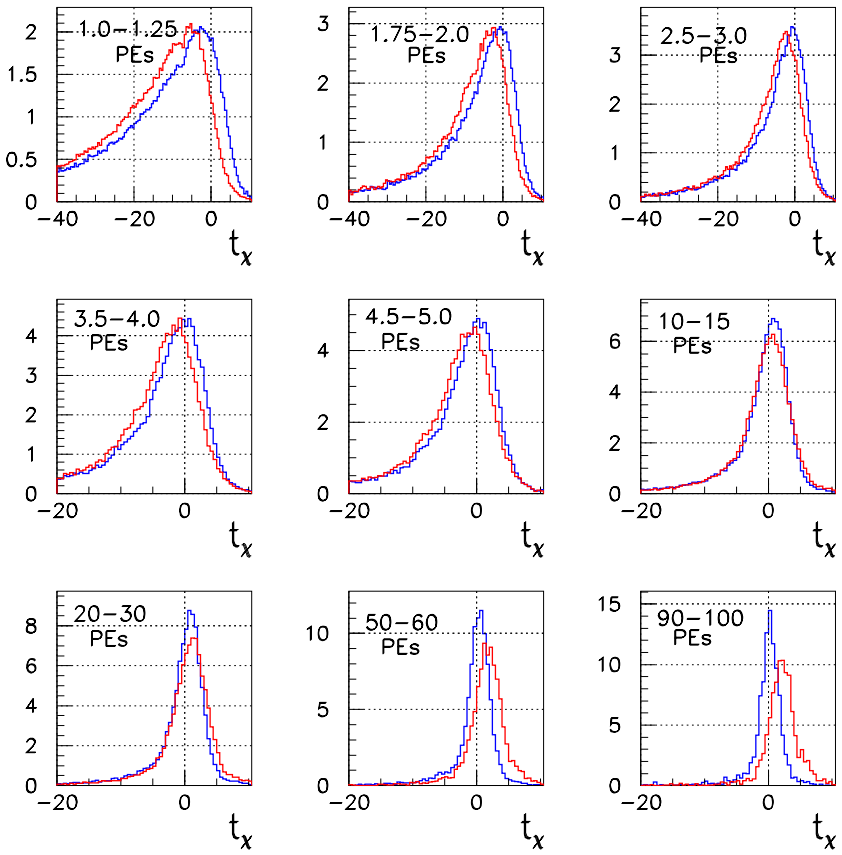

Figure 3.11: Figure showing the distribution of timing residuals (t_χ) for various pulse height ranges. The distributions are shown with (blue) and without (red) the sampling correction applied in the reconstruction of Monte Carlo simulations of gamma-ray showers.

the time of each PMT hit, where Δt is defined as:

$$\Delta t = -5.238667 + 7.514049 \times P - 7.42357 \times P^2 + 5.54304 \times P^3 \qquad (3.2)$$
$$-1.84982 \times P^4 + 0.22202 \times P^5 \ ,$$

where $P = log_{10}(PE)$.

Data were used to determine this correction, which when applied during the reconstruction of Monte Carlo simulations of gamma-ray showers results in the improvement of the average angular resolution of Milagro. It should also be noted that, in principle, the sampling correction should also depend on the distance of the PMT to the shower core. Unfortunately, the core is poorly located by Milagro. Therefore, the distance of the PMT to the shower core is not used in the

sampling correction as it does not yield any improvement in the angular resolution of Milagro.

3.4.3 Shower Front Curvature Correction

After the sampling correction is applied, another timing correction is applied to the data to account for the curvature of the shower front. This correction, known as the curvature correction, is required because, as previously discussed, the incident direction of an EAS in Milagro is determined by a weighted least squares (χ^2) fit of the shower front to a plane. Since the EAS incident on Milagro are not planar, but more approximately a cone with apex at the shower core, correcting for the curvature results in a better quality fit. Although fitting the shower front to a parabola would eliminate the need for a curvature correction, the equations to be solved in such a fit are not closed form, which results in the algorithms being slow and difficult to implement. Further, the lateral extent of Milagro is much smaller than the front of a typical EAS, which would result in a fit to a parabola to be of poor quality. Therefore, instead of a parabolic fit, a curvature correction is applied and the resulting shower front is fit to a plane for speed and simplicity. This curvature correction accounts for the slope of the cone, measured from the shower core, and is 0.07 ns for every meter a hit PMT is distant from the fit shower core.[7] A linear correction, instead of a more complicated form (*e.g.* parabolic), is utilized because any potential improvements from a more complicated format are eliminated due to the location of the shower core being not well determined by Milagro. The value of the curvature correction is found from Monte Carlo studies, which also indicate that the angular resolution of Milagro improves using this correction.

3.4.4 Direction Reconstruction

After the sampling and curvature corrections have been applied to the data, the incident direction of the shower front is determined by a weighted least squares (χ^2) fit to a plane. The χ^2 is minimized with respect to the arrival time of the shower plane and two directional cosines. This results in the equations having closed form, allowing for quick determination of the fit parameters. Although the equations are closed form, the overall process of finding the incident direction is iterative. This is because cuts, that change with each successive iteration, are applied on which PMTs are utilized in the fitting process.

[7] Prior to December 15, 2000, a curvature correction of 0.04 ns/m was utilized in the reconstruction. The relevant data and interval over which this is true is discussed in Chapter 4.

In fitting the shower front to a plane, each PMT hit is assigned a weight depending on its pulse height. The weights are determined using the RMS values of the t_χ distributions for a given pulse height range. Given that different weights and sampling corrections each result in different t_χ distributions, both the sampling correction and weights are determined simultaneously. The value of the weight for each PMT used is $1/\sigma^2$, where σ is given by the following equation:

$$ln(\sigma) = 2.5267 - 0.5217 \times log_{10}(PE). \tag{3.3}$$

As previously discussed, the procedure of fitting the shower front to a plane is iterative in a manner that applies successively different cuts on which PMTs are utilized. Initially, only PMTs hit with greater than 2.25 PEs are used in the fit. After this initial fit is performed, PMTs with a large contribution to the χ^2 are removed, and the plane is fit again. This process continues, with successively harder cuts on the individual χ^2 contributions. After the fit is performed with hardest cut on the individual χ^2 contribution, PMTs with smaller pulse heights are then allowed in the fitting procedure, provided their χ^2 contribution is small. The plane is then re-fit, and the process of removing tubes with large contributions to the χ^2 is repeated. The pulse height cut is relaxed in several stages from the initial cut of 2.25 PEs. The successive cuts are 1.75 PEs, 1.25 PEs, 0.75 PEs, and finally 0.5 PEs. It should be noted that PMTs which are removed from the fit in one stage of the iterative process, can be utilized later if the fit plane changes such that the PMT once again passes the selection requirements. A consequence of the fitting procedure is a strong dependence of the angular resolution on the number of PMTs participating in the fit (N_{fit}). Approximately 90% of the events which trigger Milagro are fit successfully by this method. The remaining triggered events that fail the angular reconstruction algorithms are generally associated with single muons passing through the detector at nearly horizontal angles and single unaccompanied hadrons.

3.4.5 Background Rejection

The final stage of the reconstruction of an EAS in Milagro enables background rejection to be performed. The ability to differentiate gamma-ray induced EAS from the more numerous cosmic-ray induced EAS is crucial for TeV observatories. In order to perform this rejection, subtle differences between the two types of showers must be exploited. EAS induced by hadronic particles contain many more muons and hadrons than those induced by gamma-rays of comparable energy. Monte Carlo simulations show that $\sim$77% of proton initiated showers contain a muon or hadron that enters Milagro, while only $\sim$5% of gamma-ray induced showers contain a muon or hadron that enters the pond. The other major difference

is that the showers induced by gamma rays have a much smoother distribution of particles than those initiated by hadronic particles of comparable energy, which are more laterally dispersed and contain many small sub-showers with particles of higher energies.

In Milagro, the bottom layer of 273 PMTs located at 6 m depth is used to identify the species of primary particle in an EAS. The top 6 m of water effectively absorbs almost all the electrons and positrons in the air showers. Therefore, only penetrating particles such as muons, hadrons, and very energetic electromagnetic particles reach the bottom layer. These penetrating particles will illuminate the PMTs which they pass close to with large amounts of Chereknov light. Cherenkov light produced by the absorbed electrons and positrons also reaches the bottom layer since the water in Milagro has a $\sim$13 m attenuation length. However, most of the Cherenkov light radiated by the electrons and positrons is produced at low water depths, resulting in the intensity of the Chereknov light from these particles being small once it spreads out over the bottom layer of PMTs. Therefore, hadronic events can be identified by searching for bright, compact clusters of light in the bottom layer, while gamma-ray initiated showers can be identified because they illuminate the bottom of the detector uniformly, with small hits.

A parameter, X_2, which exploits these differences and can be used to differentiate between the two types of showers is defined as:

$$X_2 = \frac{N_{B\geq 2PEs}}{PE_{maxB}}\,, \tag{3.4}$$

where $N_{B\geq 2PEs}$ is the number of PMTs in the bottom layer with more than 2 PEs, and PE_{maxB} is the maximum number of PEs in any PMT in the bottom layer. Using this definition, bright, compact clusters of light which result in a small number of PMTs hit with large pulse heights, yield small values of X_2. Alternatively, showers that uniformly illuminate the bottom PMTs with small hits give large values of X_2. Therefore, hadronically initiated showers typically have small values of X_2, while gamma-ray initiated showers typically have large values of X_2. Figure 3.12 shows the percentage of events retained versus X_2 cut for Monte Carlo gamma-ray showers, Monte Carlo proton showers, and data. This cut keeps only events with X_2 greater than some value.

As can be seen in Figure 3.12, there is a clear difference between Monte Carlo gamma-ray showers and Monte Carlo proton showers. Further, the data matches the Monte Carlo proton distribution reasonably well, as expected, since the data consists mainly of proton initiated showers. However, there is a significant divergence between the data and proton distributions at values of $X_2 \geq 2.5$. This discrepancy is likely due to low statistics in the proton simulations and data at high values of X_2, the absence of heavier nuclei in the simulations, and problems

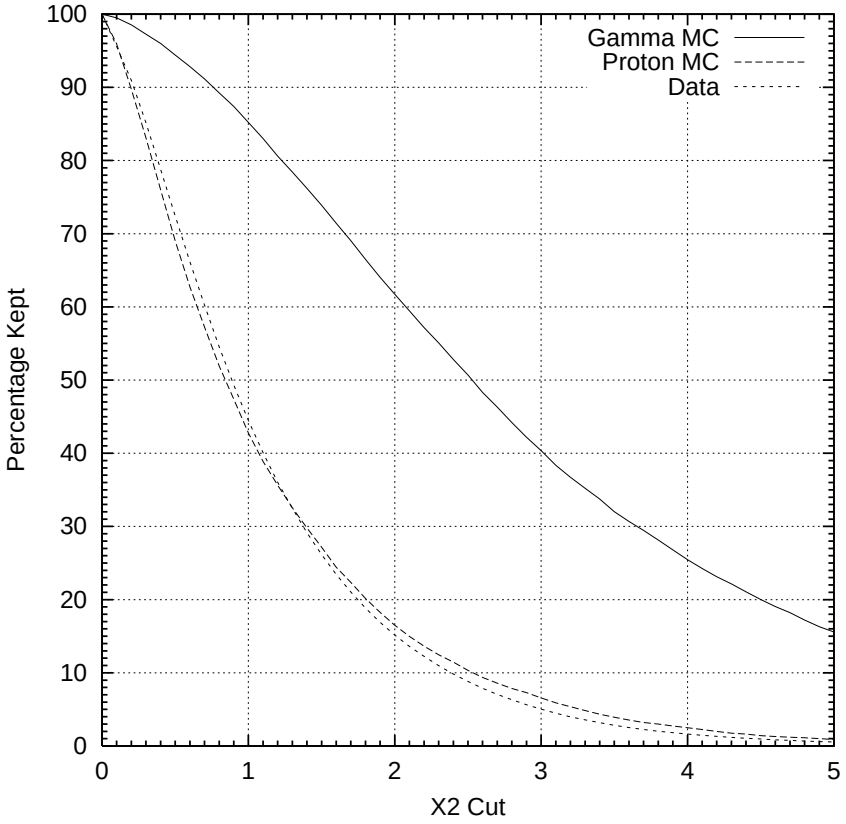

Figure 3.12: Percentage of events retained versus X_2 cut for Monte Carlo gamma-ray showers, Monte Carlo proton showers, and data. This analysis selects events with $X_2 \geq 2.5$.

with the pulse height calibration in the region where low TOT is large, but before the high TOT values exist ($\sim$5 PEs). While some discrepancy in the distributions exists, it is clear that a cut keeping only events with X_2 greater than some value will result in an increase in sensitivity. Calculation of X_2 is the last step of the reconstruction.

The relative increase in sensitivity expected for a given selection criterion is given by Q (for "quality"), which is defined as:

$$Q = \frac{\epsilon_\gamma}{\sqrt{\epsilon_p}}\,, \tag{3.5}$$

where ϵ_γ is the efficiency for retaining gamma-ray showers (signal events), and ϵ_p is the efficiency for retaining proton showers (background events). Figure 3.13 shows the expected Q from Monte Carlo simulations versus X_2 cut. The Q rises rapidly

until a cut of $X_2 \geq 2.5$ is reached, after which the Q rises only slightly. Therefore, a cut keeping only events with $X_2 \geq 2.5$ is chosen to perform background rejection. This cut is selected because the distribution of showers passing the X_2 cut for data and proton showers diverge at higher values of a cut, as well as because only a minor gain in sensitivity is found at larger values for the cut. This cut is expected to retain $\sim$51% of gamma-ray events, and only $\sim$10% of proton events. This results in an expected improvement in sensitivity by a factor of $\sim$1.6.

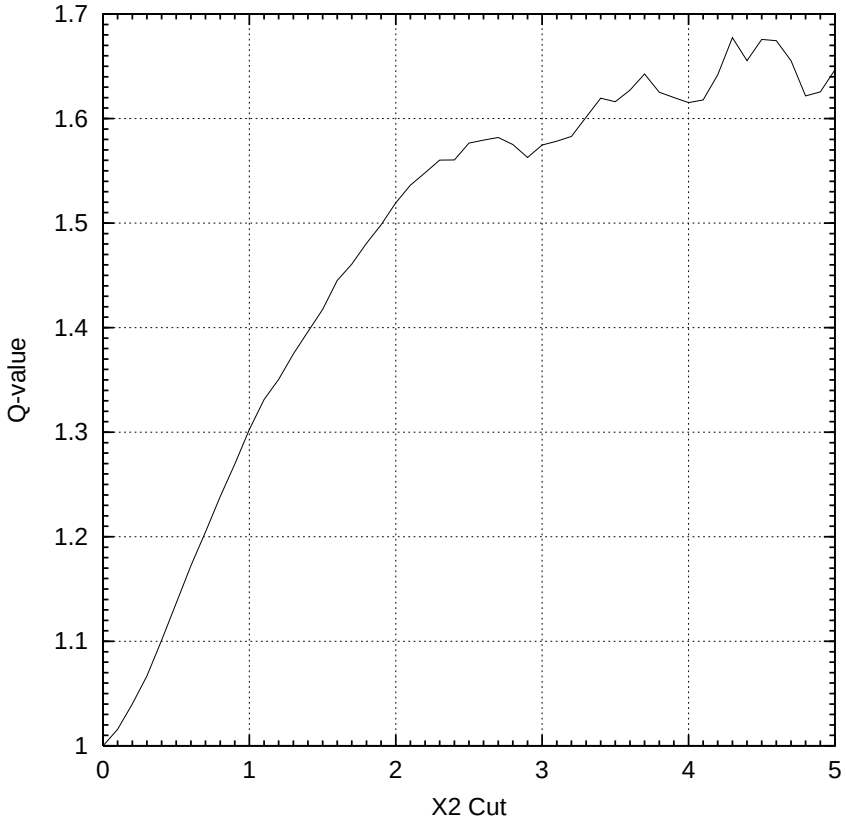

Figure 3.13: Relative Q versus X_2 cut from Monte Carlo simulations.

As the energy dependence of the X_2 cut can have a significant effect on the sensitivity of Milagro to TeV point sources, this effect was explored (Sinnis, 2001). Analysis of fraction of events passing the X_2 cut for various energy bins shows that the X_2 cut uniformly affects protons regardless of the energy of the primary particle. This is not the case for gamma-ray events, where the cut preferentially keeps showers from higher energy primaries. While this could prove advantageous for sources with a hard spectrum, this does not affect the sensitivity to a source with a spectral index similar to that of the Crab. Further, for sources with a

spectrum significantly softer than that of Crab, this would reduce the overall effectiveness of the cut.

3.5 Simulations

Simulating the response of Milagro to EAS is a two step process. In the first stage, the EAS are simulated by a software package known as CORSIKA (Heck et al., 1998). The CORSIKA simulation of an EAS begins with the first interaction of the primary particle in the upper atmosphere, then proceeds to track the subsequent interactions of the secondary particles, eventually propagating the resulting EAS to ground level. All of the secondary particles reaching ground level (the altitude of Milagro) are then input into a detector simulation. This detector simulation represents the second stage of the simulating the response of Milagro to EAS, and is performed using a software package known as GEANT (GEANT C.P.L, 1994). The GEANT package propagates the input secondary particles from CORSIKA through a model of the detector. All the interactions, hadronic and electromagnetic, for both the charged particles, as well as the input photons, are simulated by GEANT. These interactions include the production of Cherenkov light and δ-rays within the detector.

To generate enough statistics for a reasonable analysis of the performance of Milagro, millions of CORSIKA showers were generated for use by GEANT. These showers were generated over an energy range of 100 GeV to 100 TeV, with zenith angles ranging from 0 to 45 degrees "in a manner which represents equal particle fluxes from all solid angle elements of the sky and a registration by a horizontal detector arrangement" (Knapp and Heck, 1997). A falling differential power law energy spectrum is assumed for the CORSIKA showers. The spectral index utilized in the simulations is $\alpha = 2.4$ for gamma-ray primaries, and $\alpha = 2.7$ for proton primaries. The showers from proton primaries were used to simulate the isotropic cosmic-ray background.

The GEANT package then took the resulting CORSIKA showers and randomly shuffled the core position over a circle of 1000 m radius centered on the pond. After propagating the secondary particles through the detector model, the output of the GEANT simulations is similar to the calibrated data format of Milagro. In this sense, each PMT that was hit by at least 1 photon (including the effects of the quantum efficiency and time jitter of the PMT) had the number of PEs and arrival time saved to a file which could be readily analyzed by the standard software algorithms. The trigger condition was set at ≥ 55 top layer PMTs hit, which is equivalent to the approximate hardware trigger in Milagro. Overall, $\sim 2 \times 10^7$ gamma-ray initiated showers were thrown, resulting in $\sim$48,000 triggers,

and $\sim 2 \times 10^7$ proton initiated showers were thrown resulting in $\sim$60,000 triggers.

The presence of dead PMTs alters the results of the simulations slightly. Although this is true, the effect of dead PMTs is small in its effects on the quantities presented later in this chapter, therefore the performance of Milagro is quantified in this chapter using an ideal simulation where all the PMTs are operational.[8] Since many assumptions are made in the Monte Carlo simulations, comparison of the results to data is important. Numerous quantities exist for which distributions are useful for this comparison. These parameters include the zenith angle, number of tubes hit in both layers, PEs (maximum and overall) in both layers, N_{fit}, t_{chi}, and Δ_{EO} (an angular resolution parameter discussed in Section 3.6.2). Analysis of the distributions of these parameters show that the data is in reasonable agreement with the Monte Carlo proton simulations. Therefore, the Monte Carlo simulation of Milagro is considered to be accurate.

3.6 Milagro Performance

The performance of Milagro is evaluated in this section using the Monte Carlo sample previously discussed. Although, the quantities presented in this section are believed to be reasonable indicators of the behavior of Milagro, there are many issues yet to be thoroughly understood in the simulations. These include the estimation of the relative fraction of scattering and absorption in the water, the estimation of the amount of reflection at the various detector surfaces, and the effects of meteorological conditions at the site. Another issue results because there is presently no electronics simulation for Milagro. Therefore, the effects of inaccuracies in PMT calibrations are not included. While these issues need to be resolved, the detector performance is believed to be reasonably well understood.

The response of Milagro to gamma-ray initiated EAS utilizing the best available reconstruction algorithms is presented in this section. The values presented are for all showers that pass the trigger condition, are successfully reconstructed, and pass the various cuts ($N_{fit} \geq 20$ and $X_2 \geq 2.5$) applied to the data discussed in Chapter 4. While the response to proton showers is important, the results are not discussed because these showers should be randomly distributed on the sky in an isotropic manner. Thus, any angular resolution effects are not important for the background determination.

[8] The presence of dead PMTs is easily included. However, the number of dead PMTs varied during data taking making an exact simulation of the effects difficult. Therefore, dead PMTs are not incorporated in this chapter. A "typical" scenario with $\sim$50 dead PMTs is used in the determination of the flux values reported and is discussed in Chapter 5.

3.6.1 Core Resolution

The angular resolution of Milagro depends strongly on the ability to locate the core of an EAS. This is because random inaccuracies in the location of core result in an improper curvature correction being applied, causing a tilt in random directions of the fit shower plane. This naturally degrades the resolution of the detector. Unfortunately, the core location is poorly reconstructed by Milagro. This is due in part to the fact that the core of an EAS is poorly defined. However, the majority of the difficulty in accurately reconstructing the location of the core is the result of the lateral extent of Milagro being significantly smaller than a typical EAS. Therefore, a relatively small fraction of the particles are detected in many of the EAS on which Milagro triggers, resulting in the poor accuracy of core reconstruction. The distribution of the difference in fit core location and true core location, ΔR, is shown for Monte Carlo gamma-ray showers in the top plot of Figure 3.14. The median ΔR is 44 m.

Since Milagro is smaller than the EAS on which it triggers, the resolution of the core finding algorithm depends on whether the core is truly located on or off the pond. Simulations indicate that $\sim$13.5% of the gamma-ray showers that trigger Milagro have their actual core located on the pond, with the remaining $\sim$86.5% located off the pond. The distribution of ΔR for cores which are truly on or off the pond (middle), as well as those whose cores are fit on or off the pond (bottom), is shown in Figure 3.14.

The median ΔR for showers with their core truly on and off the pond is 21 m and 52 m respectively.[9] While this would appear to imply that angular resolution for showers fit on the pond is better than showers that are fit off the pond, this is not the case. This is because the median ΔR for showers with their core fit on and off the pond is 52 m and 41 m respectively, which implies that showers with their core fit off the pond have a slightly better angular resolution (which is the case). This is the result of the inability of the core fitter to determine accurately whether or not the core of an EAS was truly on or off the pond. The fitter finds that $\sim$4.7% of the gamma-ray showers have their core on the pond when they actually are, and $\sim$11.5% have their core on the pond when they actually are not. Further, $\sim$8.7% of the gamma-ray showers are fit off the pond when they are actually on. The remaining $\sim$75% are fit off the pond when they actually are.

[9]The core fitter can only place a shower at most 50 m from the center of the pond. Thus, for showers that are truly on the pond, the core has a maximum amount which the fit location can be off, which is not the case for showers truly off the pond.

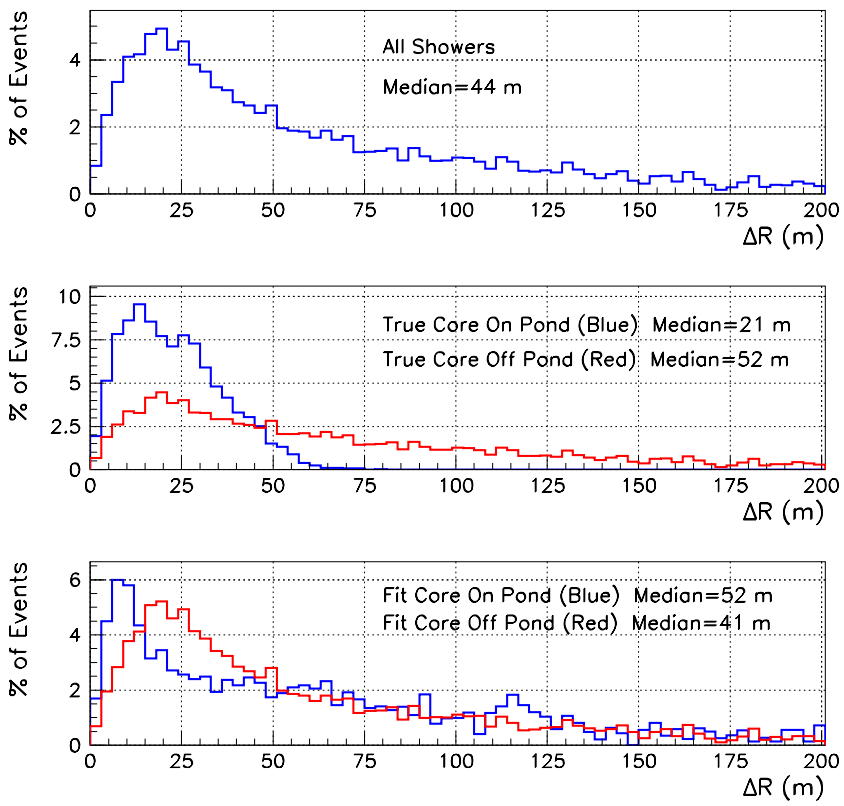

Figure 3.14: Figure showing the distribution of the difference, ΔR, between the true core position and the reconstructed position for Monte Carlo gamma-ray showers. Shown are the distribution of all showers (top), for showers with the core truly on or off the pond (middle), and for showers for which the core is fit on or off the pond.

3.6.2 Angular Resolution

The angular resolution of Milagro can be quantified by two parameters. The first of which, Δ_{angle}, is the space angle difference between the fit direction and true direction (only known for simulated showers) of the shower plane. The second parameter is the space angle difference between fit directions to the shower plane by two independent, interleaved portions of the detector (the detector is divided as light and dark squares of a chessboard) referred to as Δ_{EO}. This latter parameter is not sensitive to systematic errors, such as those due to core location errors, but can be calculated for actual data. It is expected that Δ_{EO} is about twice the overall angular resolution in the absence of systematic effects (Alexandreas et al., 1992). Because of this, minimization of the Δ_{EO} distribution was utilized

to optimize the χ^2 fitter.

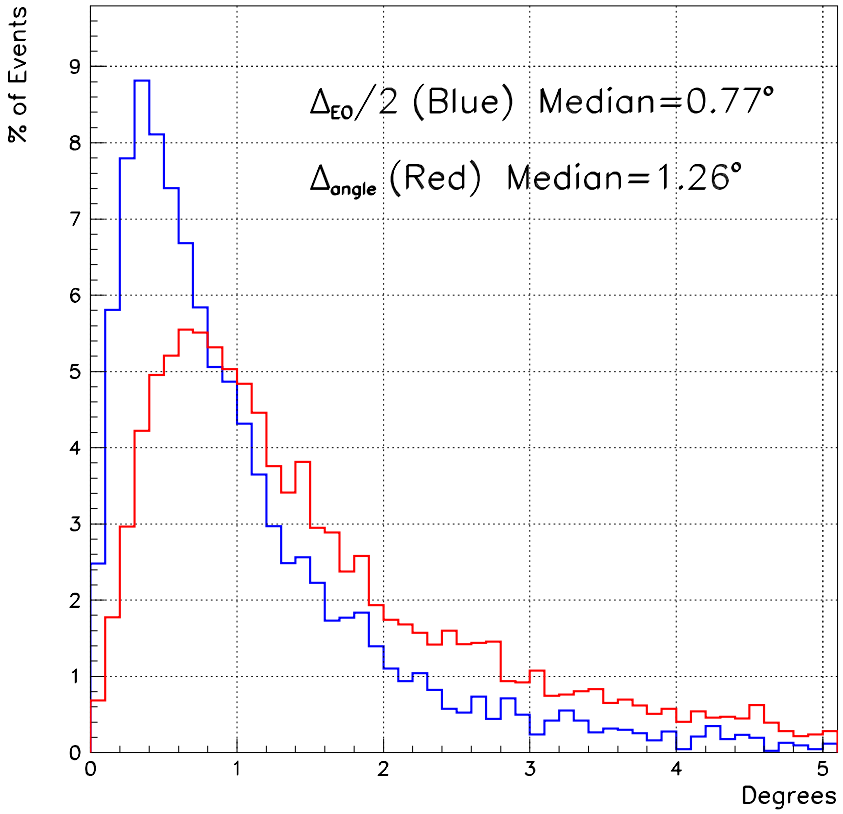

Figure 3.15: Figure showing the distribution of Δ_{angle} (red) and $\frac{\Delta_{EO}}{2}$ (blue) for Monte Carlo gamma-ray showers.

The distribution of Δ_{Angle} and $\frac{\Delta_{EO}}{2}$ for Monte Carlo gamma-ray showers is shown in Figure 3.15, which shows that the angular resolution of Milagro is non-Gaussian and characterized by a tail of poorly reconstructed showers. Table 3.1 shows the median Δ_{angle} and $\frac{\Delta_{EO}}{2}$ values for all gamma-ray showers, as well as those with the core truly on and off the pond, and for those with the core fit on and off the pond.

As can be seen in Table 3.1 the median $\frac{\Delta_{EO}}{2}$ is significantly less than the median Δ_{angle}. Since $\frac{\Delta_{EO}}{2}$ is independent of core location errors, this shows that the difficulties in accurately reconstructing the core location comprise a significant portion of the error in the angular reconstruction. Further, Table 3.1 shows that showers with the core truly on the pond are reconstructed significantly better than showers with the core truly off the pond, as implied by the better median ΔR reported earlier. However, the opposite is true, although the effect is not as

	All Showers	True Core On Pond	True Core Off Pond	Fit Core On Pond	Fit Core Off Pond
Med. Δ_{angle}	1.26°	0.80°	1.40°	1.40°	1.24°
Med. $\frac{\Delta_{EO}}{2}$	0.77°	0.52°	0.83°	0.74°	0.78°

Table 3.1: Table showing the median Δ_{Angle} and $\Delta_{EO}/2$ for Monte Carlo gamma-ray showers, as well as the dependence of the angular resolution on true and fit core location.

significant, for showers where the fit core location is on the pond versus off the pond. Therefore, the fit location of the core cannot be used to identify showers which are reconstructed better and should be treated differently[10] in a search for TeV gamma-ray emission.

The manner in which the plane is fit results in a strong dependence of the angular resolution on the number of PMTs participating in the fit, N_{fit}. Figure 3.16 shows the mean value of Δ_{angle} and $\frac{\Delta_{EO}}{2}$ versus N_{fit}. As can be seen the mean values of both parameters are less as N_{fit} increases. Because of this trend, only showers whose value of N_{fit} is greater than 19 are used in the analysis.

3.6.3 Effective Area

The effective area of Milagro represents the detector's collection efficiency as a function of several parameters. For Milagro, the effective area is a function of both energy and zenith angle, θ. The effective area, A_{eff}, is defined as:

$$A_{eff} = \frac{N_{pass}}{N_{throw}} \times A_{throw} \, , \tag{3.6}$$

where N_{throw} is the number (large) of showers simulated, A_{throw} is the area, normal to the incident direction of the primary particle, over which the showers were thrown, and N_{pass} is the number of showers that trigger the detector, are successfully reconstructed, pass the cuts applied to the data, and fall within the source bin used for analysis.[11] Figure 3.17 shows the effective area of Milagro for gamma-ray showers, as a function of energy for all zenith angles thrown. As can be seen the effective area increases dramatically, from almost zero at 100 GeV,

[10] The bin size used in the analysis, discussed in Chapter 4, depends on the angular resolution. Thus, if one set of showers were systematically reconstructed better, a more complex method for determining the bin size would be merited.

[11] This is discussed in Chapter 4.

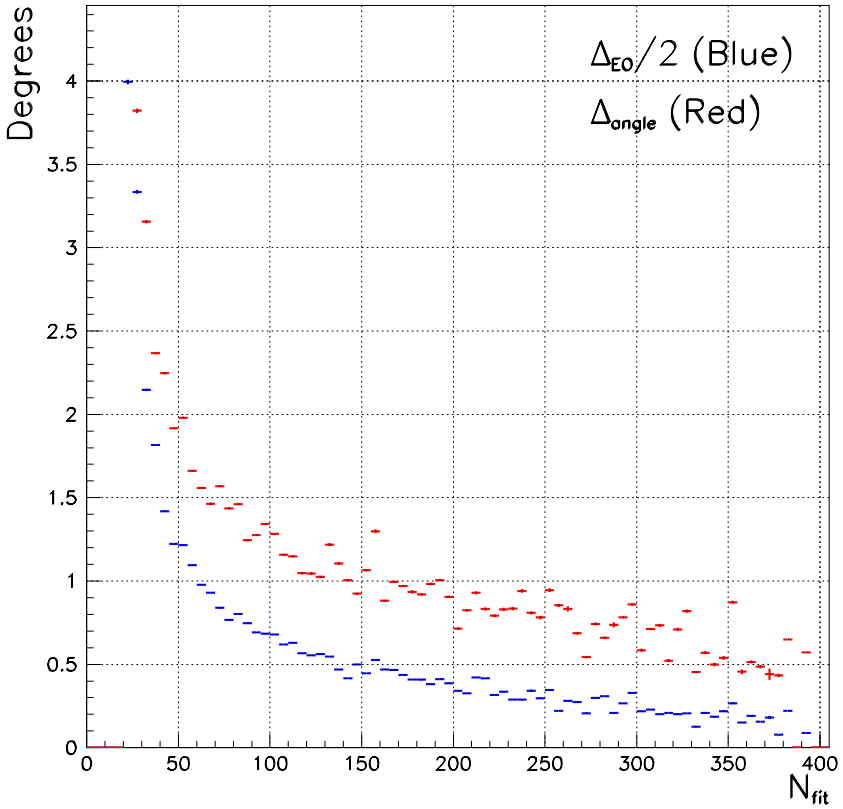

Figure 3.16: Figure showing the mean Δ_{angle} (red) and mean $\frac{\Delta_{EO}}{2}$ (blue) versus N_{fit} for Monte Carlo gamma-ray showers.

up to about 25,000 m^2 at 20 TeV. After 20 TeV, the effective area is essentially constant.

The sensitivity of Milagro is strongly dependent on the zenith angle exposure of the source. The zenith angle dependence of the effective area for gamma-ray showers over the energy range 100 GeV to 100 TeV is shown in Figure 3.18. The figure shows that Milagro is most sensitive to showers near zenith, with approximately constant sensitivity out to zenith angles of 20 degrees, after which the effective area drops off dramatically. As discussed in Chapter 4, a cut on the data is applied keeping only showers with fit zenith angle less than 45 degrees, because of this drop off in sensitivity.

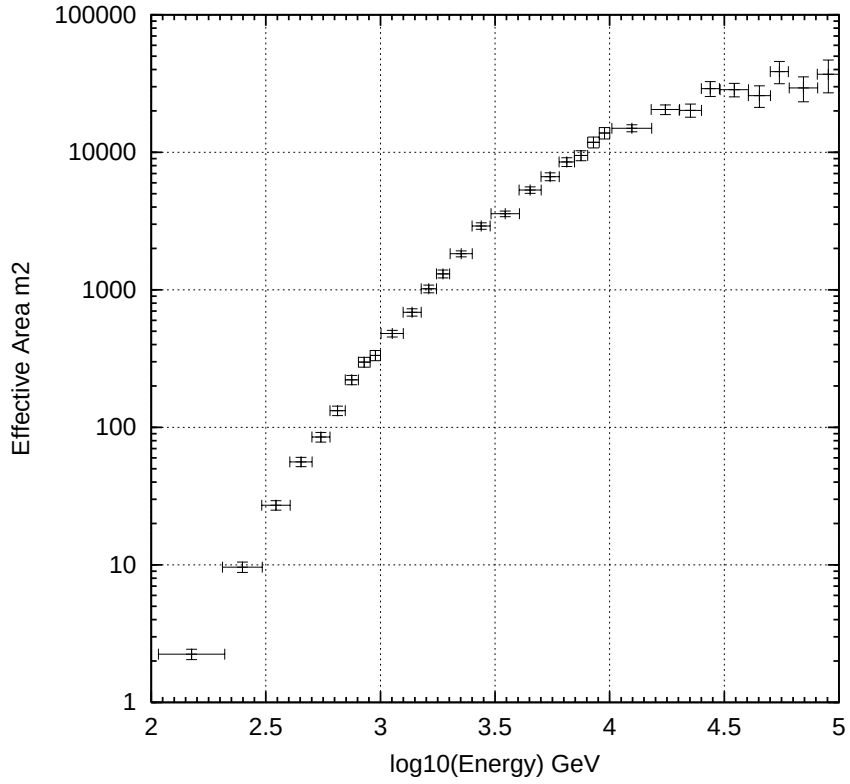

Figure 3.17: The effective area of Milagro versus energy for Monte Carlo gamma-ray showers. Each point represents the contributions from all zenith angles ranging from 0 to 45 degrees, as would be appropriate for an isotropic diffuse gamma-ray source.

3.7 Energy Resolution

Unfortunately Milagro has a very poor energy resolution. One reason for this is random variations in the propagation of the EAS to and through Milagro, which can cause two showers with similar primary type, zenith angle and energy to appear vastly different in the detector. Various factors contribute to the differences including: the number of particles reaching the ground in an EAS due to differences in the height of the first interaction as well as the types and variations of secondary interactions, and the detection of Cherenkov photons in the water. The large differences in appearance that can arise between two similar EAS make the energy determination very poor. Another problem results because the lateral extent of Milagro is much smaller than the typical width of an incident EAS. This causes problems for showers with cores located both on and off the pond.

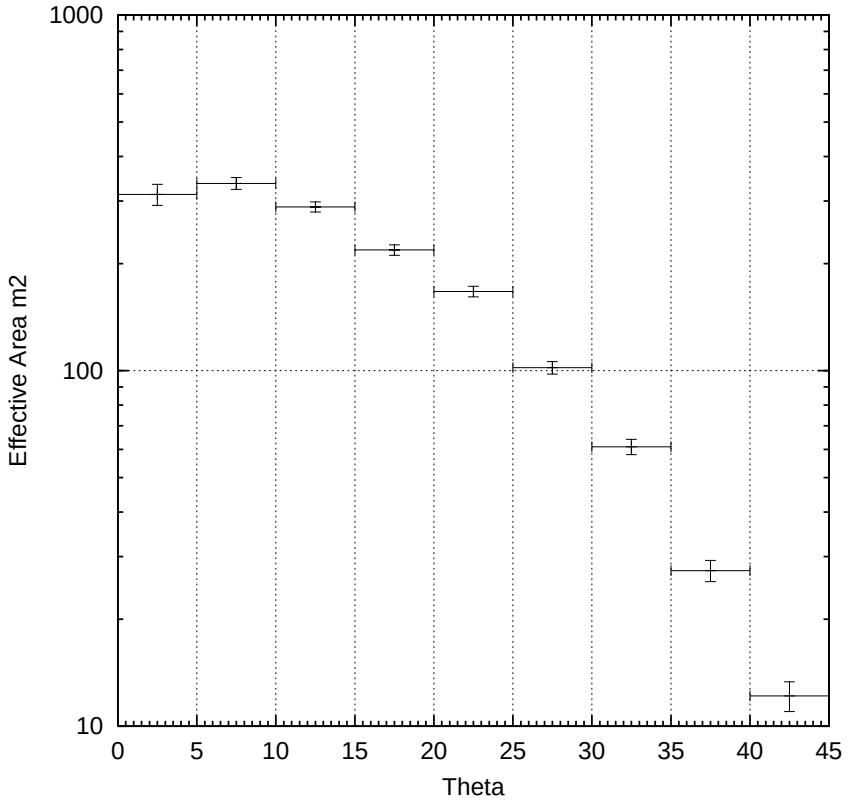

Figure 3.18: The effective area of Milagro versus zenith angle for Monte Carlo gamma-ray showers. Each point represents the contributions from all energies ranging from 100 GeV to 100 TeV.

For showers with their core located on the pond, the energy determination is poor because the whole shower is not imaged. Although a low energy shower has fewer particles, if the core lands on the pond virtually all the PMTs in Milagro are hit because of the relatively small size of Milagro. A high energy shower, which has many more particles, naturally hits most of the PMTs when the core is on the pond as well. Thus, if most of the PMTs are hit in the pond it is difficult to determine if the shower had low or high energy, although the average pulse height detected by the PMTs will generally be larger for a higher energy shower.

For showers with their core located off the pond, the poor energy resolution is the result of inaccuracies in the determination of the core location that results from the relatively small size of Milagro. Without an accurate determination of the core location, it is impossible to determine if the incident EAS was a low energy shower with a core located near the pond, or if the incident EAS was a high energy shower with a core located further away. Therefore, it is virtually

impossible to determine if an incident EAS resulted from a low or high energy primary without accurate knowledge of the core location. Thus, Milagro has a very poor energy resolution.[12]

Because of the poor energy resolution of Milagro, no information as to the differential spectrum of an observed source can be determined. Although true, the median energy of gamma-ray showers from a source which triggers the detector can be quantified with reasonable accuracy from the expected energy dependence of the Milagro response. This value varies for an individual source because of the strong zenith angle and energy dependence of the effective area of Milagro. A method for determining the median energy for a individual source is discussed in Section 4.4.2. The value for each source observed is reported where appropriate.

3.8 Milagro Physics Goals

As it maintains the advantages of a typical EAS array, Milagro serves as a high duty-cycle, all-sky monitor in the VHE regime. This allows for a wide range of physics topics to be addressed. Along with the focus of the thesis (a search for TeV emission from the Crab Nebula and selected AGN), Milagro is presently being used to:

- Survey the Northern sky for steady and episodic sources.
- Search for emission from GRBs over the energy range 100 GeV to 20 TeV.
- Search for diffuse emission from the Galactic plane.
- Search for TeV cosmic antiprotons, as well as to calibrate the energy response of the detector, using high significance observations of the cosmic-ray moon shadow.
- Search for WIMPS annihilating in the vicinity of the Sun.
- Search for evaporating primordial black holes.
- Search for >5 GeV particles from the Sun.
- Measure the primary proton spectrum using single hadrons.
- Measure the composition of cosmic rays above 50 TeV in conjunction with a set of wide aperture atmospheric-Cherenkov telescopes called "WACT."

[12]The lateral extent of Milagro is being extended with detectors known as outriggers. These outriggers will greatly enhance the ability of Milagro to accurately locate the core of an EAS, which will correspondingly dramatically improve the energy resolution.

Chapter 4

Analysis and Data Set

The analysis for Milagro is similar to that of other VHE observatories in that it consists of looking for a relatively small excess of events above the more numerous cosmic-ray background in any given direction. In this sense, any results from Milagro must be expressed statistically. However, before one can express any results, one must decide how to look at the data, what cuts to apply, a method to determine the background, as well as how to statistically interpret any excess or deficit found. Any result, regardless of the statistical significance, can then be converted into a physically meaningful quantity such as a flux value or upper limit from the source. This chapter details the analysis used for interpreting reconstructed data from Milagro, as well as a description of the data set analyzed.

4.1 Binned Analysis

4.1.1 General Definition and Motivation

As the number of events coming from a VHE gamma-ray point source is small compared to the background level and the angular resolution of the Milagro detector is finite ($\sim$0.75 degrees), the data must be grouped in order to be interpreted. First, the data, whether they be signal or background, are placed into maps based on the direction, in right ascension (RA) and declination (δ), of the reconstructed event. Data from the signal and background maps are placed into round angular bins. This step would not be necessary in the absence of a background as an infinitely large bin would keep all the signal events. However, the background is very large compared to the signal. Therefore an infinitely large bin would contain too much background and effectively wash out any signal. Further, the excess from all other possible sources would be included as well. Clearly, an optimal bin size must be determined so that a bin centered on a point source will retain as

little of the background as possible, while keeping the largest fraction of signal events associated with the source falling in the bin. This optimal bin size will, on average, maximize the expected significance of any signal, and is related to the point spread function of Milagro. In this sense, a larger bin size would indicate a worse angular resolution. As round bins were chosen to account for the nature of the point spread function, which is uniform in the declination and RA directions, the search for an optimal bin size is effectively a search for an optimal bin radius.[1]

4.1.2 Optimal Bin Size and Cuts

In the presence of a large number of events, as is the case with Milagro, the optimal source bin is a round angular bin centered on the source with an angular radius given by:

$$r = 1.58 \times \sigma \, , \tag{4.1}$$

where σ is the rms projected angular resolution of the detector. However, a problem exists with determining the optimal bin radius using Eq. 4.1, in that it assumes the detector has an angular resolution that is characterized by a Gaussian. This is not the case for Milagro, where the projected angular resolution of the detector is a sharply peaked, non-Gaussian distribution of events characterized by a long tail of poorly reconstructed events. This long tail causes the rms projected angular resolution to be too large. Therefore the standard formula for determining an optimal bin radius does not apply. Instead, one must determine the optimal bin size using Monte Carlo simulations. This is performed using the distributions of Δ_{angle}, a parameter expressing the space angle difference in degrees between the reconstructed and true direction of the air shower, from the gamma-ray simulations for Milagro. It is assumed that any signal will have a point spread function characterized by this distribution. Figure 4.1 shows the Δ_{angle} distribution of gamma showers passing the background rejection criteria described in Chapter 4. Additionally, the angular resolution of Milagro is a strong function of the number of tubes participating in the fit, N_{fit}. Therefore, a cut keeping only showers with N_{fit} greater than some value eliminates poorly reconstructed showers. As can be seen from Figure 4.1, an N_{fit} cut changes the Δ_{angle} distributions, therefore the optimal bin size and N_{fit} cut must be determined simultaneously.

The following logic is applied to determine the optimal bin size. Applying an N_{fit} cut to the data naturally reduces the number of events in the background. The percentage of events passing various N_{fit} cuts can be seen in Figure 4.2. However, for the signal, an N_{fit} cut improves the quality of the point spread

[1] A square bin with the same angular area is easier to implement and only slightly inferior (Alexandreas et al., 1993).

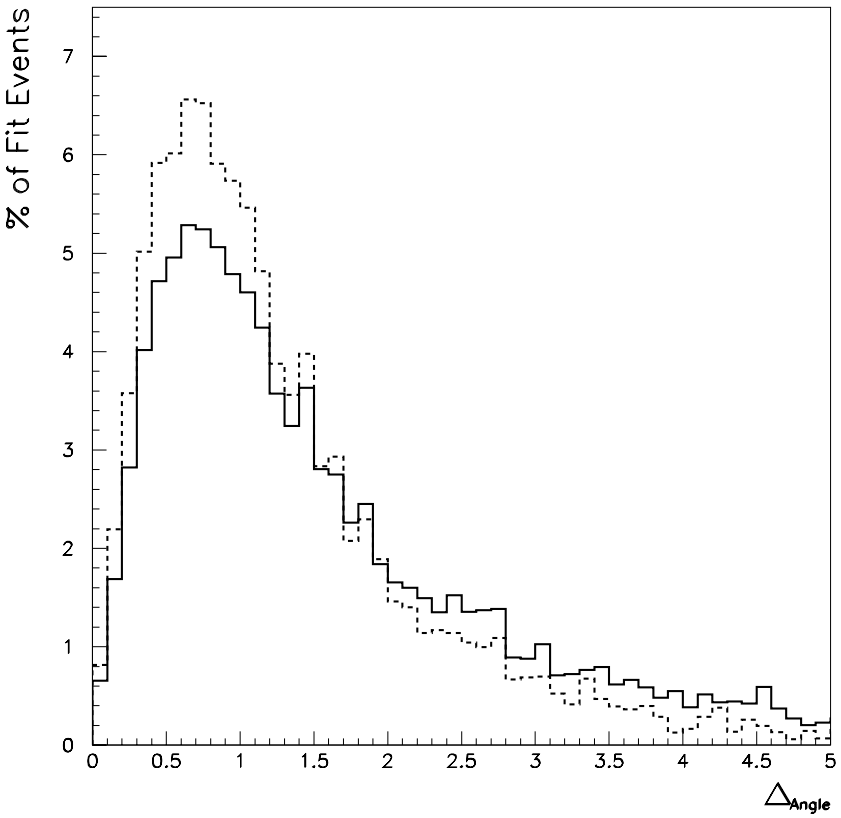

Figure 4.1: Distribution of Δ_{angle} for Showers Passing the X_2 cut. The solid line represents all fit events with $N_{fit} \geq 20$, and the dashed line represents all fit events with $N_{fit} \geq 50$.

function. Therefore, a cut would presumably toss out poorly reconstructed events from the signal. Since most of these events would not have fallen into the signal bin, this allows for a gain in sensitivity as the N_{fit} cut primarily reduces the number of background events. Further, only a small fraction of events are poorly reconstructed, thus one can reduce the bin size and not lose many signal events while removing a significant fraction of the background. As the background is locally flat, the effect of decreasing the bin size is purely geometrical on the number of background events. The fraction of background events kept is proportional to the ratio of the bin areas. For example, a bin of half the original radius only keeps a quarter of the background events retained by the original bin. Decreasing the bin size ultimately results in a gain in sensitivity until some point is reached where too large a fraction of the signal events is thrown out. Figure 4.3 shows the percentage of events that fall within a certain bin radius for various N_{fit} cuts.

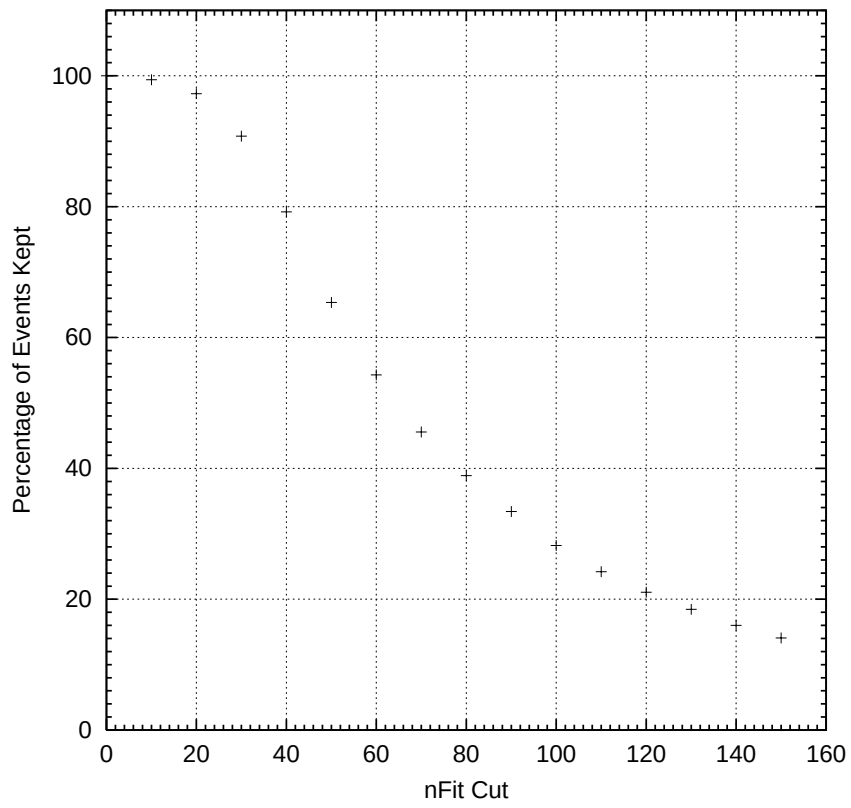

Figure 4.2: Percentage of events retained versus N_{fit} cut.

To express the improvement in sensitivity, Q, the relative factor by which the sensitivity improves, is defined (*cf.* Equation 3.5):

$$Q = \frac{\epsilon_{signal}}{\sqrt{\epsilon_{background}}}\,, \tag{4.2}$$

where ϵ_{signal} is the relative fraction of the signal events kept and $\epsilon_{background}$ is the relative fraction of the background events kept. Using these definitions:

$$\epsilon_{signal} = \frac{N(X,r)}{N(X_\circ,r_\circ)}\,, \tag{4.3}$$

where $N(X,r)$ is the number of gamma-ray events with $N_{fit} \geq X$ and having $\Delta_{angle} \leq r$ with r defined as the bin radius, and

$$\epsilon_{background} = \frac{N(X)}{N(X_\circ)} \times \frac{\pi r^2}{\pi r_\circ^2}\,, \tag{4.4}$$

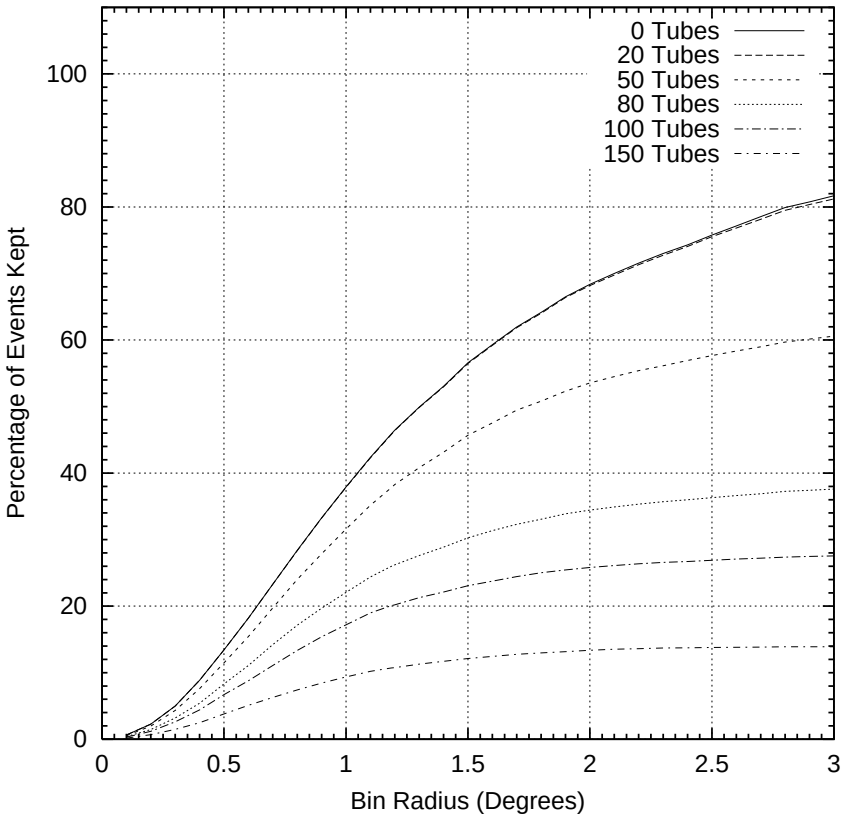

Figure 4.3: Percentage of events retained versus bin radius for various N_{fit} cuts. The 0 Tubes and 20 Tubes curves are almost indistinguishable.

where $N(X)$ is the number of cosmic-ray events with $N_{fit} \geq X$. Substituting Equations 4.3 and 4.4 into Eq. 4.2, Q becomes:

$$Q = \frac{N(X,r)}{N(X_\circ, r_\circ)} \times \sqrt{\frac{N(X_\circ)}{N(X)}} \times \frac{r_\circ}{r}\,. \tag{4.5}$$

For this study, the reference point chosen was $r_\circ = 1.1848$ and $X_\circ = 20$, the final values used in the analysis. The radius of 1.1848 degrees corresponds to the same area as a square bin with 2.1 degree sides.[2]

The relative Q values versus bin size for various N_{fit} cuts are shown in Figure 4.4. The effect of an N_{fit} cut improving the angular resolution can be seen

[2]Clearly the precision of this study doesn't warrant so many significant figures. The value was chosen for comparison to other collaborators using square bins with 2.1 degree sides. A value of $r = 1.2$ degrees would be more appropriate, and the value will be referred to elsewhere as 1.2 degrees.

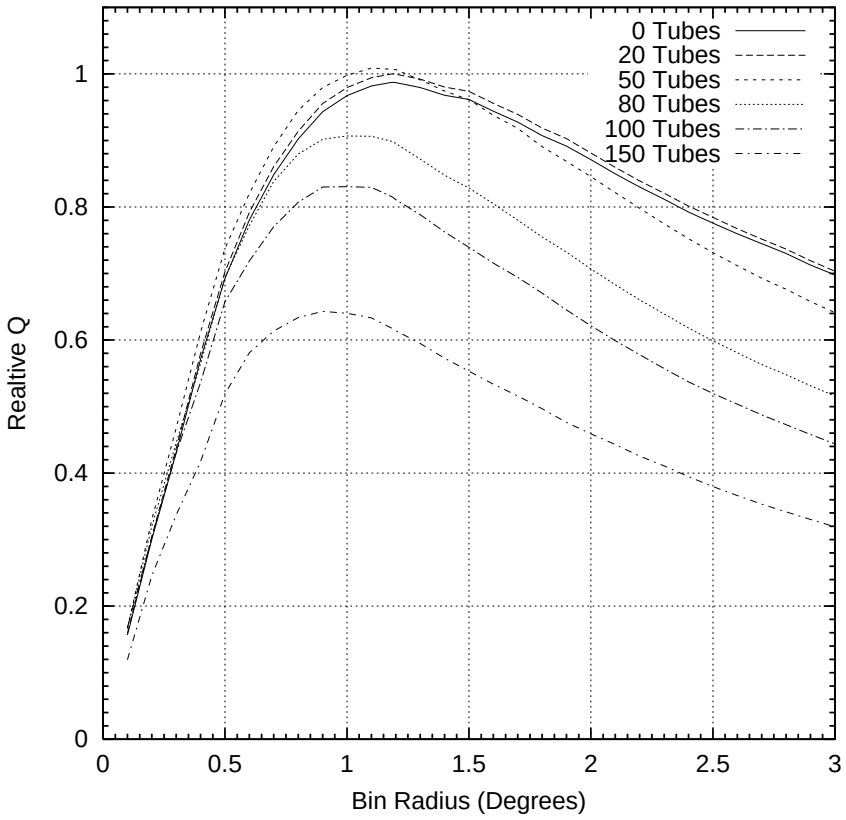

Figure 4.4: Relative Q versus bin radius for various N_{fit} cuts. The Q is relative to the value for the expected significance from the bin radius and N_{fit} cut used in the final source analysis.

in the decrease of the optimal bin radius, represented as the peak in the relative Q curve, for a harder cut. Since the variations in the relative Q are small for $0 \leq N_{fit} \leq 50$, the value of 20 was chosen. This eliminates the showers with the poorest reconstruction, while erring on the side of caution as a significant decrease in expected significance can be seen for large N_{fit} cuts. From the curve corresponding to only events having $N_{fit} \geq 20$, the optimal bin size is 1.1848 degrees radius. The expected significance is optimized using these values, although the maximum is sufficiently flat in these parameters that exact values are not important. These values keep $\sim$46% of the signal events.

As described earlier a cut keeping events with the parameter, $X_2 \geq 2.5$, is applied to the data to perform background rejection. All told $\sim$23% of the signal events are expected to remain in the optimal bin after these cuts. Another cut keeping events with zenith angle, θ, less than 45 degrees is also applied to the data.

This is done because the angular resolution of the detector degrades significantly at higher zenith angles and because no effective areas were determined for showers beyond this zenith angle value. Since each source traverses a different path in local coordinates, it is difficult to quantify the fraction of signal events excluded by this cut. Overall this cut keeps $\sim$94% of the reconstructed events with $X_2 \geq 2.5$ and $N_{fit} \geq 20$. The optimal bin size study was performed using only events passing both the X_2 and zenith angle cuts.

4.2 Background Determination Technique

Any search for gamma-ray emission from TeV point sources is made difficult by the large number of background events coming from isotropic cosmic rays. In light of this one must take great care in selecting a method to estimate the number of background events coming from the direction of a possible source. This is due to the fact that emission from a source would appear as a relatively small excess of events above the background coming from the direction of the source. If one errs in the estimation of the background, it could result in the spurious appearance of a signal, or the washing out of any real signal. Many estimation techniques are typically plagued by a lack of a reasonable method to account for the strong dependence of detection efficiency in local coordinates, as well as any time variations in the overall event rate. A good background estimation technique would thus utilize information from the same regions in the local sky, as well as have a built in method to account for changes in the overall event rate. Such a technique is presented in (Alexandreas et al., 1993), which estimates the expected number of background events utilizing the actual data, and shall be referred to as "time sloshing."

4.2.1 Time Sloshing

Time sloshing is built on the assumption that any signal is at most a minor perturbation of the overall event distribution and works as follows. The right ascension, declination, and time for all reconstructed events passing the data cuts are stored in a buffer that spans 2 hours of data. For each event in the buffer, one creates multiple simulated events by utilizing the time of other events taken at random from this buffer. A simulated event is generated by calculating a new value for the right ascension by shifting the right ascension (15 degrees/hour) of each real event by the time difference between that event and one chosen at random from the buffer. The declination of the simulated event remains unchanged. By using events in the same declination band as the the source bin, one can ensure

that regions of the sky used to determine the background level traverse the same regions in local coordinates as the source bin. Further, this method ensures that the event's local zenith and azimuth angles are kept fixed, as only the time is changed. Clearly events that are not in the source bin, those with the same declination but different RA, traverse the same point in the sky at different times. However this should not be problematic as this method recognizes that while the overall event rate may vary, the dependence of the detection efficiency on local angles tends not to vary over short periods of time. Time sloshing clearly accounts for variations in the event rate, including interruptions in data collection, because the background events have the same time distribution as the real events. By using times from at least 10 "fake" events per real event the statistical error on the background can be kept sufficiently small. For this study 15 "fake" events per real event were chosen. By generating 15 fake events per real event the number of events in the background bin is naturally 15 times too large. Clearly then the expected number of background events, N_B is:

$$N_B = \frac{N_{slosh}}{15}\,, \tag{4.6}$$

where N_{slosh} is the number of events in the background bin.

4.2.2 Source Contamination

Unfortunately due to computational difficulties, events from the source bin are used to estimate the background level. If a weak signal is present, this results in a slight overestimate of the true background, ultimately leading to an underestimate of the signal strength. While a small effect, a correction can be made to account for this problem. The logic of this correction is as follows: Any simulated background event initially drawn from a certain area of the 2 hour buffer can fall into the signal bin. This area is a rectangle of length 30 degrees ($2hrs \times 15degrees/hour$) in the RA direction and width twice the radius in degrees, r, of the signal bin ($\pm r$) in the declination direction. The total area is $A_1 = 30 \times 2 \times r$. The true number of background events expected, N_{Bcorr}, should exclude events initially drawn from within the signal bin which has area, $A_S = \pi r^2$. Thus only events in the buffer from an area, $A_{BG} = A_1 - A_S = 30 \times 2 \times r - \pi r^2$, should be used in the background estimation. Therefore, the expected number of background events calculated by time sloshing can be written as:

$$N_B = \frac{A_{BG} \times N_{Bcorr} + A_S \times N_{on}}{A_1} = \frac{A_{BG} \times N_{Bcorr} + A_S \times N_{on}}{(A_{BG} + A_S)}\,, \tag{4.7}$$

where N_{on} is the number of events in the signal bin. Rearranging Eq. 4.7, yields the equation for the true number of background events expected:

$$N_{Bcorr} = \frac{(30 \times 2 \times r \times N_B - \pi r^2 \times N_{on})}{(30 \times 2 \times r - \pi r^2)} \,. \tag{4.8}$$

By changing the variables to an excess, Δ, where $\Delta = N_{on} - N_B$, the corrected excess, Δ_{corr}, is:

$$\Delta_{corr} = N_{on} - N_{Bcorr} = \frac{60}{60 - \pi r} \times \Delta = 1.066 \times \Delta \,. \tag{4.9}$$

Clearly this correction will increase the value of an excess, increase the magnitude of a deficit, and do nothing in the case of no excess.

4.3 Significance Determination

After one has estimated the background and binned the data, one has a value for the number of events in the bin centered on the source for both the signal and background maps. Using these values one can then convert the excess or deficit of signal events over background events into a statistical significance. This is done using the method of Li and Ma (Li and Ma, 1983). This method states that the significance, S, is:

$$S = \sqrt{2} \sqrt{N_{on}\, ln \left(\frac{(1+\alpha)}{\alpha} \frac{N_{on}}{\Sigma} \right) + N_{off}\, ln \left((1+\alpha) \frac{N_{off}}{\Sigma} \right)} \,, \tag{4.10}$$

where $\Sigma = (N_{on} + N_{off})$, and N_{off} is the number of events in the background bin given by:

$$N_{off} = \frac{N_{Bcorr}}{\alpha} \,. \tag{4.11}$$

In both equations, α is the ratio of signal to background exposure. As stated earlier the area from which the true background is drawn is $A_{BG} = 30 \times 2 \times r - \pi r^2$. The signal is from an area, $A_S = \pi r^2$. Therefore α is:[3]

$$\alpha = \frac{\pi r^2}{(30 \times 2 \times r - \pi r^2)} = \frac{\pi r}{(60 - \pi r)} = 0.06614 \,. \tag{4.12}$$

This method of calculating the significance of an observed excess is based on the method of maximum likelihood ratio test and generates significance distributions

[3] As can be seen, α appears in Eq. 4.9 as well.

that are more consistent with Gaussian probabilities than significance equations derived from Poisson statistics. This equation is valid as long as the number of signal and background events are not too small (*i.e.* $N > 10$). Although this method is more correct, in this study it yields approximately the same results as when the significance, S, is determined by:

$$S = \frac{\Delta_{corr}}{\sqrt{\sigma^2_{N_{on}} + \sigma^2_{off}}} = \frac{\Delta_{corr}}{\sqrt{N_{on} + \alpha\, N_{Bcorr}}}\,. \tag{4.13}$$

4.4 Flux Determination and Upper Limits

4.4.1 Flux Value

After a source has been detected with high statistical significance, it is then possible to use the measured excess to determine an average flux from that source. The integral flux is the average number of photons arriving from a source per unit area per unit time, and is given by the equation:

$$I = \int_{E_t}^{E_c} \frac{dN}{dE}\, dE\,, \tag{4.14}$$

where E_t is some threshold energy, E_c is some cutoff energy and $\frac{dN}{dE}$ is the differential gamma-ray flux. The differential gamma-ray flux is defined as the number of particles from a source striking a given surface per unit energy per unit area per unit time. Since sources in very high energy astrophysics typically have a power law spectrum, this is often expressed as:

$$\frac{dN}{dE} = I_o \left(\frac{E}{E_o}\right)^{-\alpha}\,, \tag{4.15}$$

where I_o is the differential flux normalization, $E_\circ$ is the energy at which the flux is normalized, and α is the spectral index of the source, which is assumed to be constant over the period of the search. Using the measured excess of events,[4] Δ, it is possible to calculate $I_\circ$, since

$$\Delta = \int_{E_t}^{E_c} \int_{t_{start}}^{t_{stop}} \frac{dN}{dE}\, A_{eff}(E, \theta(t))\, dt\, dE\,. \tag{4.16}$$

[4]From this point on Δ refers to the number of excess events corrected for signal contamination in the background estimation, formerly referred to as Δ_{corr}

Substituting Eq. 4.15 into Eq. 4.16, yields:

$$\Delta = \int_{E_t}^{E_c} \int_{t_{start}}^{t_{stop}} I_o \left(\frac{E}{E_o}\right)^{-\alpha} A_{eff}(E, \theta(t))\, dt\, dE\ . \tag{4.17}$$

The effective area was calculated in bins of both energy and zenith angle, θ, such that for every 5 degree bin in θ, from 0 to 45 degrees, the effective area is calculated for 31 bins of energy. Further, the time in seconds that each observed source spent at certain zenith angles is also calculated in 5 degree θ bins. Thus the value of A_{eff} is treated as a constant for some interval of theta or energy. Utilizing this to pull the various terms out of the integrals, as well as that an integral can be broken into parts and summed, Eq. 4.17, becomes:

$$\Delta = \frac{I_\circ\, E_\circ}{(-\alpha+1)} \sum_{i=0}^{8} t(\theta_i) \sum_{j=0}^{30} A_{eff}(\theta_i, E_j) \left[\left(\frac{E_{t_j}}{E_\circ}\right)^{-\alpha+1} - \left(\frac{E_{b_j}}{E_\circ}\right)^{-\alpha+1}\right]\ , \tag{4.18}$$

where $t(\theta_i)$ is the time that the source spent at zenith angles in the bin θ_i, and $A_{eff}(\theta_i, E_j)$ is the effective area for the appropriate zenith angle bin θ_i and energy bin bounded by E_{b_j} and E_{t_j}. Clearly one can rearrange Eq. 4.18 to solve for the differential flux normalization, $I_\circ$. However, the value that is typically reported is the integral flux, I, which after combining Equations 4.14 and 4.15 is given by:

$$I = \int_{E_t}^{E_c} I_o \left(\frac{E}{E_o}\right)^{-\alpha} dE = \frac{I_\circ\, E_\circ}{-\alpha+1} \left[\left(\frac{E_c}{E_\circ}\right)^{-\alpha+1} - \left(\frac{E_t}{E_\circ}\right)^{-\alpha+1}\right]\ , \tag{4.19}$$

where E_t is the generally the median energy of observation, and E_c is the cutoff energy which is assumed to be 100 TeV in this study.[5] For the Crab Nebula the integral flux is commonly reported with $E_t = 1$ TeV.

4.4.2 Median Energy

The integral flux is often reported as using the integral above the median energy of observation, E_{med}. Further, the differential flux normalization is typically normalized to this value. The purpose of using the median energy in the determination of these quantities is that it reduces the effects of the choice of spectral index utilized. As the value of the spectral index is often assumed or not well determined, this is important in ensuring that an accurate flux value is calculated. Therefore, the method for determining the median energy must be discussed.

[5] This is essentially the same as no cutoff!

Since each candidate position traverses a different portion of the local sky, E_{med} varies for individual sources. This is because the effective area of Milagro depends strongly on zenith angle. In principle calculating E_{med} should be a simple process, where gamma-showers would be simulated with the desired energy spectrum and appropriate local angle distribution. The energy of successfully reconstructed events, which pass the analysis cuts and fall into the source bin, could then be placed in a histogram and the median calculated. However, the amount of time required to simulate enough showers to have reasonable statistics for each source is prohibitive. Therefore, an alternative, equivalent method is used.

Since the effective area as a function of zenith angle and energy ($A_{eff}(E,\theta)$), as well as the desired energy spectrum (α) and appropriate zenith angle exposure for an individual source ($t(\theta)$), is known, Eq. 4.18 can be utilized to calculate E_{med}. This is because E_{med} is defined as the energy below which half of the excess events, Δ, were detected. Using arbitrary values for $I_\circ$ and $E_\circ$, if the energy cut off in Eq. 4.18 were reduced from the original value of 100 TeV, keeping all the other quantities the same, the calculated excess would be reduced. This is because the only thing that changed in the overall calculation is the energy integral (sum), which is reduced. In this scenario, there exists a smaller cut off energy at which the energy integral is half the original value, resulting in half the excess to be calculated. This cut off energy is by definition E_{med}. Therefore, the initial step in determining the median energy of observation for an individual source is to calculate an excess using arbitrary values for $I_\circ$ and $E_\circ$, with the appropriate spectrum and zenith angle exposure, and a cut off energy of 100 TeV. The next steps involve reducing only the cut off energy until the resulting excess calculated is half the original value. This cut off energy is E_{med}. Clearly this method only depends on the effective area, exposure, and assumed spectrum, which is important since $I_\circ$ and $E_\circ$ have no bearing on E_{med}.

4.4.3 Upper Limit

Although a detection of high statistical significance for a source is clearly desirable, a non-detection can still yield something scientifically meaningful. For the non-detection of a source, one can calculate an upper limit on the source flux. This is the value that the source flux must have been less than, at some confidence level, in order for it to have not been detected. For this study any upper limit will be quoted at the 90% confidence level. The calculation of an upper limit is similar to the flux calculation, except, one substitutes for Δ an upper limit, N_{90}, on the number of detected events in Eq. 4.18. Specifically, N_{90} is how large the actual excess arriving from the source could be, at the 90% confidence level, given the excess that was measured. This value accounts for the possible statistical

fluctuations in the background level.

The value for N_{90} is calculated following the method of Helene(Helene, 1983). Since the number of events in Milagro is large, this method will be employed under the assumption that the number of photons detected from a source follows a Gaussian distribution. This distribution is centered on the measured value for the excess, Δ, and has $\sigma = \sigma_\Delta$, where σ_Δ is the statistical error on the measured excess. As a negative number of events coming from a source is non-physical, any measurement yielding such a value is the result of a statistical fluctuation in the background. Thus the only physically allowed result is where the number of counts coming from a source is greater than zero. Therefore, there is an area under the postulated Gaussian which represents the physically allowable space. One can numerically calculate this area, and using this result determine what 90% of that physically allowed area is. Once this value has been determined, one can numerically calculate the x-ordinate that corresponds to having 90 percent of the physically allowed area below it. This value is N_{90}.

The method of determining N_{90} is illustrated for the case of $\Delta = -500$ and $\sigma_\Delta = 730$ in Figure 4.5. In this example $\sim$24.7% of the area under the Gaussian is above $x = 0$ and is considered the physically allowed space. The x-ordinate that corresponds to having 90% of the physically allowed area, $\sim$97.5% of the total area, below it is at $x = \Delta + 1.96\sigma_\Delta$, leading to $N_{90} = 935$. Using N_{90} calculated in this manner one can then rearrange Eq. 4.18 to determine the differential flux normalization, and then use Eq. 4.19 to solve for the 90% confidence limit on the integral flux from that source.

4.5 The Data Set

4.5.1 Reconstructed Data History

The Milagro detector has been acquiring processed data since June 19, 1999. While designed to operate nearly continuously, there have been several lengthy interruptions in the data taking due to the Cerro Grande fire,[6] a DAQ computer breakdown, a tape library death, and several scheduled PMT repairs. Figure 4.6 shows the duty cycle of Milagro for the length of the data set analyzed, as well as when these major interruptions occurred. The data set ends on January 28, 2002, for a total length of 955.29 days (2.62 years). During this time Milagro was operational during 734.89 days, however some of the data from the detector is flawed for a variety of reasons. Examination of the experimental logbook, as

[6]The fire did not affect Milagro directly, but LANL required operation of the detector to be ceased for the duration of the fire.

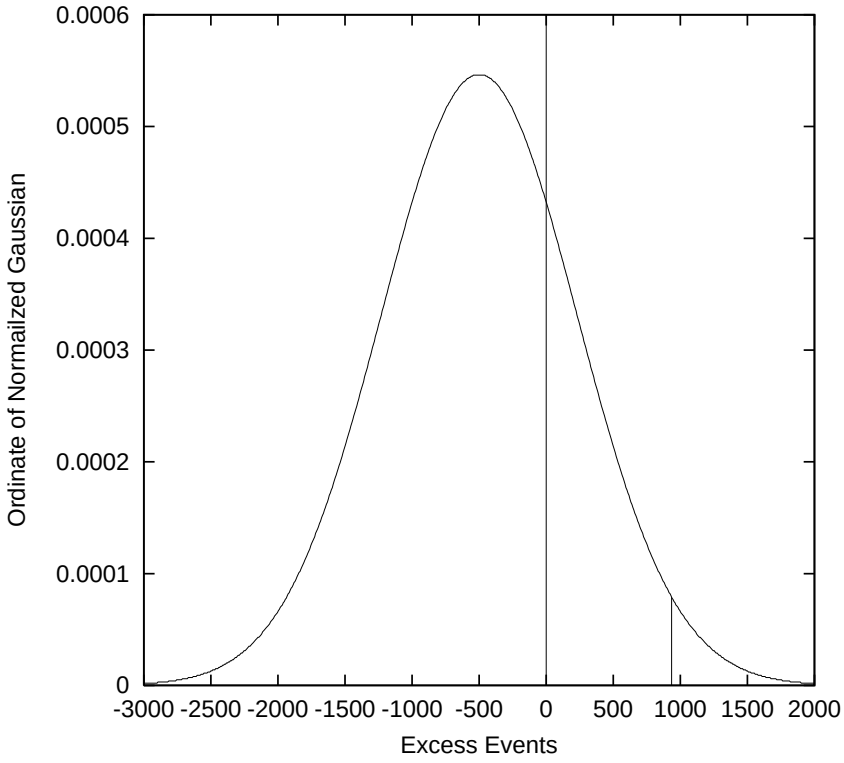

Figure 4.5: Illustration to clarify N_{90} calculation. A Gaussian distribution of excess events for which there is a deficit of -500 ± 730, which results in a value for $N_{90} = 935$. The area under the curve above $x = 0$ corresponds to the physically allowed space. The rightmost line represents the value for N_{90}, below which 90% of the physical area is contained.

well as a trial processing of the data enabled the identification of this data which accounts for a total of 18.70 days of operation. This data was removed from the data set,[7] leading to an effective uptime of 716.19 days (1.96 years) or ∼75% duty cycle. Table 4.1 shows a breakdown of the time for Milagro operations. The remaining downtime for Milagro is due to power outages, special data runs, and upgrades. If one removes the time that Milagro was scheduled to be down for PMT repairs, the operational and useful duty cycles for Milagro are ∼87% and ∼85% respectively.

The rate at which the experiment has been running is not set to some predetermined optimal value, but rather set to a level which the data acquisition

[7]Some of the data may be usable for short term analysis, if needed. However, since these runs represented a small fraction of the overall number of events, they were removed to ensure the data quality.

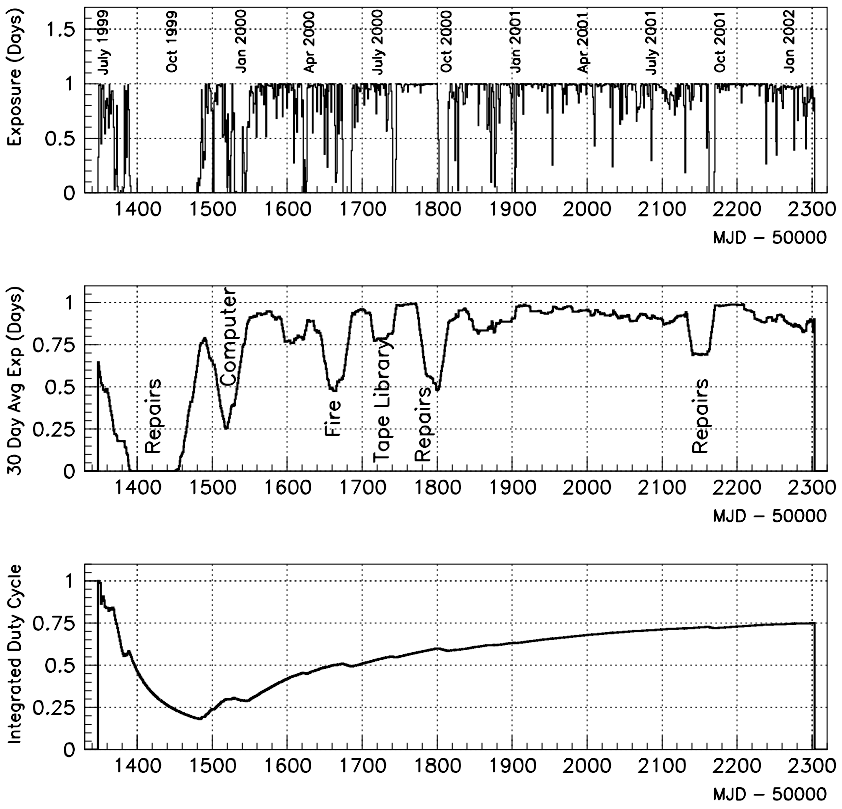

Figure 4.6: Figure showing the daily duty cycle (top), 30-day average duty cycle (middle), and integrated duty cycle (bottom) for Milagro.

Category	**Days**	% **of Total**
Good Data	716.2	75.0
Bad Data	18.7	2.0
PMT Repairs	108.0	11.3
Cerro Grande Fire	12.1	1.3
Computer Fix	9.4	1.0
Tape Lib. Fix	5.1	0.5
Other	85.8	9.0

Table 4.1: Breakdown of Milagro operation.

system can handle. Initially the Milagro detector was only able to operate at a trigger rate of $\sim$1 kHz due to this limitation. After significant efforts to upgrade the data acquisition system, the experiment can currently handle a rate of $\sim$2

kHz. Milagro has been running nearly continuously at this high rate, typically ranging from 1500 to 2000 Hz, since January, 2000. Figure 4.7 shows the daily and cumulative average rates of triggers and successfully processed data for Milagro during this 2.62 year period. As can be seen there are significant daily variations generally due to experimental conditions at the site, as well as overall trends in the event rate. However, on average the rates during this study are fairly stable. The cumulative average rate of triggers, reconstructed events, and events passing the data cuts[8] during this study is 1385 Hz, 1229 Hz, and ~90 Hz respectively. All told the "good" data from this data set contains 8.57×10^{10} events satisfying the Milagro trigger condition. Of these events, 7.57×10^{10} were usable in that they were successfully reconstructed and did not possess any errors in the reconstructed parameters.

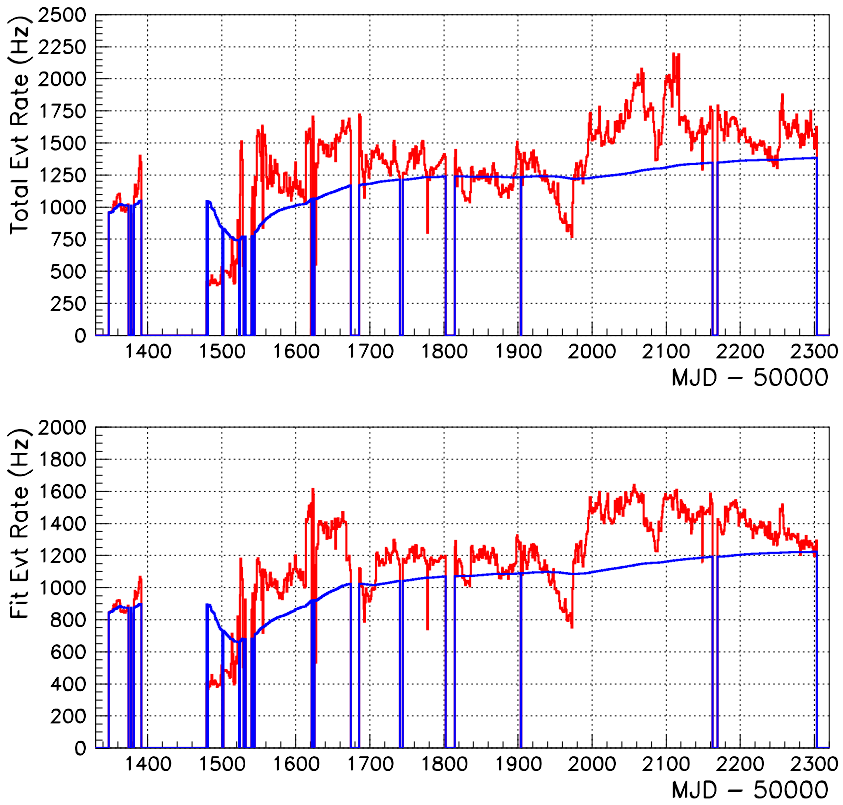

Figure 4.7: Figure showing the daily and cumulative average trigger rates (top) and usable event rates (bottom) for Milagro.

[8]This value is an approximation utilizing the percentage of reconstructed events that pass the data cuts (~7.3%).

4.5.2 Algorithm Improvements

As the understanding of the detector has increased, the online event reconstruction has undergone many changes. While many of these are relatively minor, two of these have resulted in large increases in the detector's sensitivity. The first, occurring on July 20, 2000, involved implementing the background rejection algorithm online. As discussed earlier, Monte Carlo simulations indicate that the use of this algorithm, a cut on X_2, leads to an expected increase in sensitivity by a factor of 1.6. A new core reconstruction algorithm and curvature correction, implemented on December 15, 2000, constitutes the second major change. Monte Carlo simulations show that this change should result in an additional increase in sensitivity by a factor of 1.4. An additional change includes an improvement in the PMT calibration of Milagro installed on June 7, 2001. While it is difficult to quantify the effect of the calibration changes, due to a lack of an electronics simulation, it is expected that they would both affect the hadron rejection and, to a lesser extent, the angular reconstruction of Milagro. Any data processed online before the implementation of any of these changes would not have the corresponding improvements. However as discussed in Chapter 4, raw data initially reconstructed in the direction of the Crab Nebula exists. This includes all data when the Crab was higher than a zenith angle of 45 degrees in the sky with a fit declination within 10 degrees of the Crab. The existence of raw data allows for the data to be re-reconstructed using the best algorithms and calibrations available. The results of this reprocessing are used for the study of the Crab Nebula.

4.5.3 AGN Study Subset

Unfortunately, only limited raw data exists for events initially reconstructed in the vicinity of the candidate AGN. This does not allow for the re-reconstruction of the data for these sources using these improved techniques. Thus, the online processed data must be used. A consequence of utilizing the online reconstructed data for this study is that one must combine data processed with varying algorithms possessing different levels of sensitivity. Further, it will be shown later that the use of the background rejection technique results in the detection of the Crab Nebula with high significance, whereas it is not found without this technique. Therefore, the Milagro data set from July 20, 2000, when the X_2 parameter became a part of the online reconstruction, through January 28, 2002, is searched for TeV emission from the candidate AGN. This time period includes the large flare of Mrk 421 in early 2001, as reported by HEGRA, Whipple, and the RXTE all-sky monitor.

The subset of data for which the AGN were studied consists of 558.00 days

(1.53 years) of data taking. During this time Milagro was operational for 506.75 days. After the flawed data, as discussed previously, which represents 7.49 days worth of exposure, is removed, the effective exposure is actually 499.26 days (1.37 years) and corresponds to an active duty cycle of 90%. This value is much higher than that of the entire data set due to the installation of UPS crates to power the electronics, which eliminated downtime due to brief power outages. Another reason involves improvements in the pace and methods of PMT repairs. The total down time for the scheduled PMT repairs totals 18.76 days, which amounts to only ∼3.4% of the data interval compared to ∼11.3% previously. The operational and useful duty cycle during times which the detector was scheduled for running are ∼94% and ∼93% respectively. Figure 4.8 shows the duty cycle for Milagro during this interval.

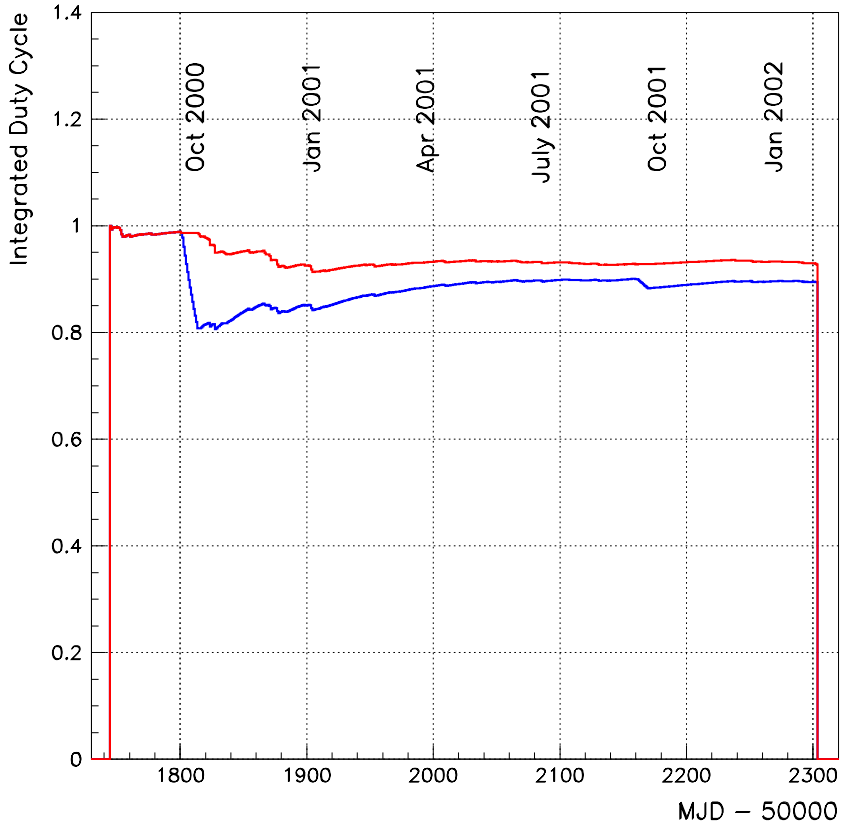

Figure 4.8: Figure showing the integrated duty cycle for the AGN study subset of data, with (blue) and without (red) including the scheduled downtime for PMT repairs.

Overall, the sample for which the AGN are studied consists of 6.288×10^{10}

events satisfying the Milagro trigger condition. Of these events, 5.616×10^{10} are usable in that they were successfully reconstructed and did not possess any errors in the reconstructed parameters. From this, a total of 4.09×10^{9} events pass the data cuts and are analyzed. This corresponds to 7.3% of the usable events. The daily and cumulative average rate of triggered, reconstructed, and analyzed events during this interval can be seen in Figure 4.9. The cumulative average rate of Milagro triggers, reconstructed events, and analyzed events during this interval is 1458 Hz, 1302 Hz, and 94.8 Hz respectively. These rate averages are higher than that of the overall sample, reflecting the improvement in the DAQ system's capabilities.

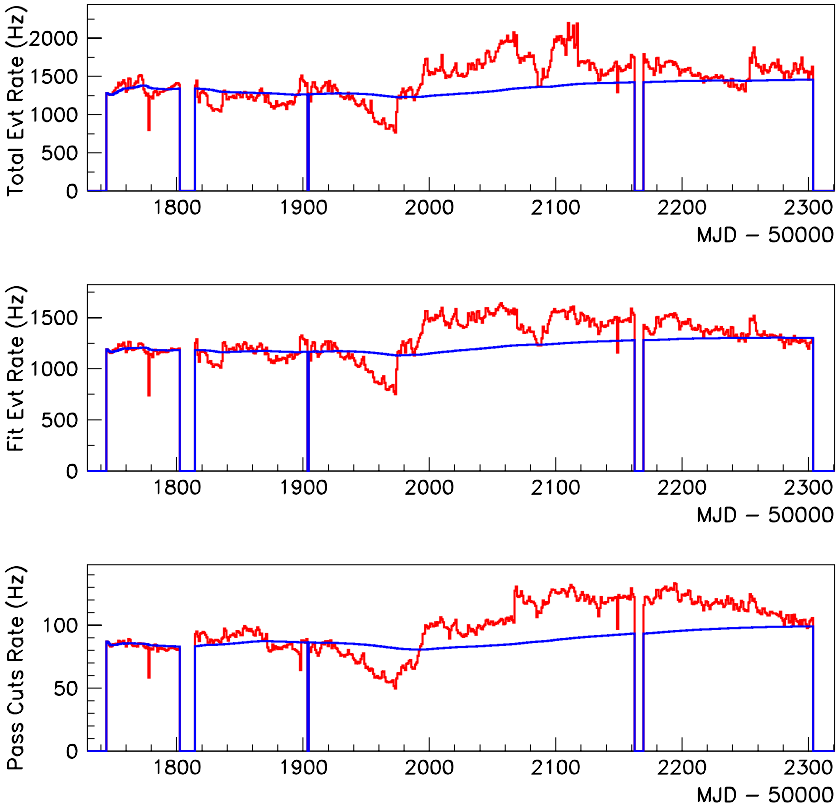

Figure 4.9: Figure showing the daily and cumulative average trigger rates (top), fit event rate (middle), and rate of events passing the data cuts (bottom) for the AGN study subset of data.

4.5.4 Time Scales of Analysis

A search for appreciable excess in the direction of the Crab Nebula is performed for the length of the entire data set (1.96 years of exposure). This search is done utilizing the re-reconstructed Crab data until the online and reprocessing analysis are equivalent, after which the online processed data is used. While a detection of the Crab Nebula is of moderate scientific interest given that Milagro utilizes a new technique for observing TeV gamma-ray sources, it would not be revelation of a new source. Therefore, any observations of the Crab at TeV energies would be a confirmation of detections by a wide variety of generally more sensitive instruments. While only confirming previously accepted detections, studying the Crab is of interest, because one can utilize the information from the detection to ensure that Milagro is operating as expected. Further, it provides a direct indication of the sensitivity of the detector to a steady TeV point source. Studies of the Crab can also be useful to determine if Milagro is a reliable instrument. For this reason, a short-term time scale analysis is performed for the Crab on 11 time scales of 1, 3, 5, 7, 10, 14, 21, 30, 50, 100, and 150 days. Since the TeV flux from the Crab is constant with no observed flaring behavior, this is not done to search for flares from the Crab. Rather, if no flaring behavior is observed for the Crab Nebula on any of these timescales, one can safely assume that the detector is behaving in a stable manner. After studies of the Crab have elucidated that Milagro works, how sensitive the detector is, and that it operates in a stable manner, one can then trust the instrument for use in the study of the candidate AGN as well as in a search for as yet unidentified TeV sources.

A search for appreciable excess from each of the 27 AGN is performed for the length of the entire AGN data set (1.37 years), as well as for the 11 aforementioned timescales. The online reconstructed data is utilized for this search. As mentioned previously, the first parts of the online reconstructed data do not utilize the improved software algorithms or PMT calibration. Therefore this search is initially less sensitive. As comparisons to observations of the Crab Nebula are important, the use of online processed data rather than re-reconstructed data dictated that the same studies be performed for the Crab over this data set as well. An important difference in the analysis of the smaller time scales is that for the Crab it is used to show that the detector is stable, where for the AGN the purpose is to find flaring behavior.

It is important to note that the large number of time scales analyzed is not ideal. This is because the total number (11) represents a large oversampling in time, which results in extra trials that need to be accounted for in the statistical analysis of any excess found on a short-term time scale. It has been shown that an ideal time scale search would be where the interval increased by a factor of $\sim$3

(Biller, 1996). In this sense, a search of only 5 time scales, 1, 3, 10, 30, and 100 days in length would have been most efficient. While this is not disputed, the expected level of sensitivity for Milagro, as well as uncertainties surrounding the techniques employed, dictated a more thorough analysis of the results. Therefore the time was oversampled to ensure nothing unexpected occurred. Naturally, if some short-term flare had stood out, the inefficient number of time scales would reduce the overall significance of the finding. This could in principal create a statistical dilemma, however the oversampling does not change the general conclusions of this study, and the results from the search on all 11 time scales are reported.

Chapter 5

Results for the Crab Nebula

Having been observed with high significance by many different instruments in the TeV energy range, the Crab Nebula has become the standard reference for VHE gamma-ray astronomy. Emission from the Crab is characterized by a flux that is constant in time and has been seen to energies beyond 20 TeV with no evidence for a cut-off in the source's power law spectrum. These qualities make it a useful object to determine whether or not a new observatory works, whether its operation is stable in time, how sensitive the instrument is, as well as an indicator for how well the analysis techniques perform. This chapter shows that Milagro has successfully observed TeV emission from the Crab Nebula, that the detector operates in a stable manner, and that the choice of analysis techniques, cuts and bin size are reasonable. The sensitivity of the instrument is also indicated. The flux of TeV photons above 1 TeV from the direction of the Crab Nebula is determined, compared to the results from other instruments, and any discrepancies explained in this chapter as well.

5.1 Overall Results

Milagro has successfully observed TeV gamma-ray emission from the Crab Nebula during the duration of the data set analyzed. As discussed previously this encompasses 2.62 years worth of mostly re-reconstructed data with a duty cycle of $\sim$75% corresponding to 1.96 years of actual exposure. During this interval, $N_{on} = 1,640,210$ events were observed in the bin centered on the position of the Crab Nebula. Given an N_{on} value of this size, the corrected number of background events expected from the time sloshing technique is $N_{Bcorr} = 1,634,036$. This corresponds to an excess of 6174 ± 1322 events, or a significance calculated by Eq. 4.10 of 4.7σ. Figure 5.1 shows a sky map of observed significance for the region

surrounding the Crab Nebula. The size of the angular bin used, a circle with a radius of 1.2 degrees, is shown on the map for the bin centered on the position of the Crab. As the significances on this map are calculated on a 0.05×0.05 degree grid, neighboring bins are highly correlated. Therefore, this image does not represent the actual distribution of events on the sky, but rather shows the effects of the finite resolution of the Milagro detector.[1] As can be seen the choice of bin size is reasonable since the "spot" falls within the source bin shown on the plot. Further, the point of maximum significance, 5.7σ, is reasonably close to the position of the Crab ($\sim$0.3 degrees "southwest" on the plot). One does not expect the point of maximum significance to be at the true position of a source due to statistical fluctuations and resolution effects. The observations that the spot falls within the source bin and that the point of maximum significance is reasonably close to the source position, allows for the reasonable assumption that the observed excess is from the Crab Nebula.

The calculated significance implies a sensitivity to a source given by the following equation:

$$\sigma_{exp} = \sigma_{obs} \times \sqrt{\frac{t_{exp}}{t_{total}}}, \tag{5.1}$$

where σ_{exp} is the significance expected for the chosen time interval of t_{exp}, and σ_{obs} is the observed significance for the total time interval t_{total}. Since $\sigma_{obs} = 4.7$ for $t_{total} = 1.96$ years for the Crab Nebula, this implies a sensitivity of 3.4σ per ideal year of exposure. However, the actual value expected for a year of observation will be slightly less than this as the duty cycle for Milagro currently is $\sim 95\%$.

5.2 Time Scale Analysis

While it is well known that the TeV flux from the Crab Nebula is constant in time, a time scale analysis of the excess events detected by Milagro from the direction of the Crab Nebula is performed. This study is not undertaken with the hypothesis that the TeV flux from the Crab Nebula actually varies in time. Instead, the purpose is to show that the detected excess of events from the Crab is accumulated in a manner that is consistent with being constant in time. While this would not reveal anything unknown about the TeV flux from the Crab, it would allow for the assertion that Milagro has operated in a stable manner with constant sensitivity over the entirety of the data set. As this has important ramifications

[1] The angular extent of the Crab is such that it can be considered a point source given the resolution of Milagro.

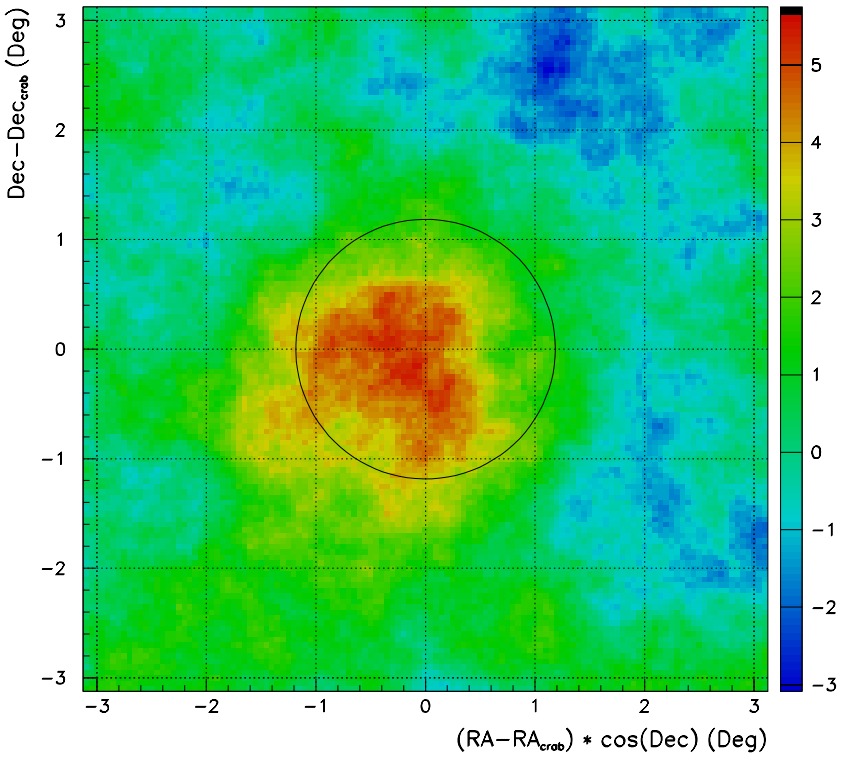

Figure 5.1: Sky map of observed significance for the region centered on the Crab Nebula for the time period from June 19, 1999, to January 29, 2002. Neighboring points are highly correlated due to overlapping bins. The circle represents the bin size used for the analysis and is centered on the position of the Crab Nebula. The significance at the position of the Crab Nebula is 4.7σ.

in any search for TeV gamma-ray emission from known or unknown sources with Milagro, a time scale analysis of the Crab signal is therefore warranted.

Utilizing the actual daily exposure of Milagro along with the expected significance for that cumulative exposure given by Eq. 5.1, one can view how the significance was accumulated versus what is expected for a constant signal. This is shown in Figure 5.2. As this is a plot of cumulative significance, neighboring points are highly correlated. Further, the expected significance is approximated. This is because only the total exposure for each particular day is considered, where the actual position in the sky of the Crab is ignored. Given that the effective area for Milagro depends heavily on zenith angle, as well as the presence of a zenith angle cut in the data, this is problematic for short time scale evaluations. While the expected significance is only an approximation, the value should be reasonably accurate after a few accumulated days since the zenith angle effects of down time would eventually average out. Although somewhat biased by correlation effects, clearly there are a larger number of points observed above the significance expected from the final excess, than those that are below expectation. This may indicate that the final significance quoted may in fact be low by a few tenths of a sigma due to statistical fluctuations. Outside of this systematic trend, which is a very minor effect, the data are statistically consistent with expectations for a constant signal. Therefore, the assumption can be made that Milagro has operated in a stable manner for the duration of the data set.

Due to the previously mentioned systematic trend, as well as the importance of showing that Milagro operates in a stable manner, a more thorough analysis is warranted to determine if the signal was acquired at a rate consistent with being constant. Therefore the time variance of the Crab signal is analyzed utilizing two methods, which shall be referred to as the "maximum deviation method" and the "all possibility method." Each of these methods analyzes the emission from the Crab Nebula on smaller time scales than the whole and determines whether or not emission on these smaller time scales significantly deviates from a constant level over time. If no significant variations are observed, then it can be assumed that the detector is operating in a stable manner. This in turn would indicate that the sensitivity of Milagro is unchanging in time.[2]

For each method, the excess events from a particular source are binned on various time scales. A bin is generated for the appropriate time period beginning on each day during the data set. Since the time scales range from 1 day to 150 days in length, neighboring bins are correlated with the exception of the 1

[2]Due to the evolution of analysis techniques this is not in fact true. However, the data utilized to analyze the Crab was consistently reconstructed with the same, best-available algorithms. Therefore, this statement can be made.

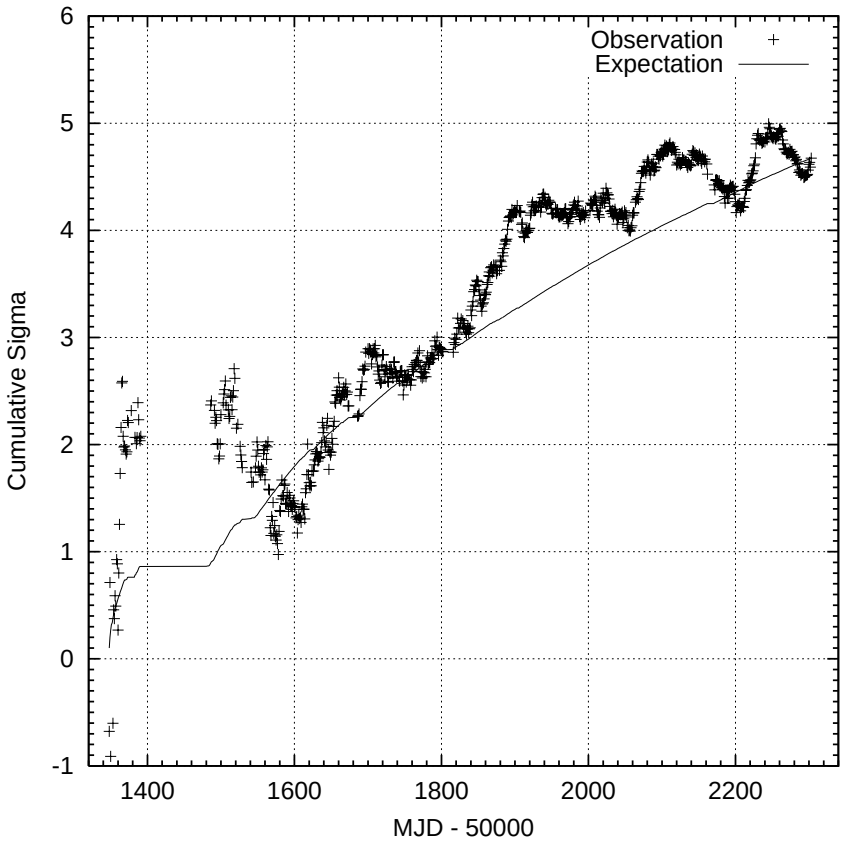

Figure 5.2: This figure shows how the significance observed for the bin centered on the Crab Nebula accumulated versus time. Also shown is what would be expected for a constant signal given the sensitivity implied by this observation and the true exposure of each date. Neighboring points are highly correlated.

day time scale. Therefore a set of independent bins must be decided upon for interpretation. For a time scale of N days, there are N different choices, with no a priori reason to believe that any one is more characteristic of the behavior of the detector than another. If only one particular choice is analyzed, it might miss significant variations which straddle two bins. Thus, 2 methods were chosen to analyze the short-term information. While each method possesses strengths and weaknesses, if both yield consistent results, then it is assured that the time scale analysis can be trusted.

The first method simply identifies the bins which are maximally deviant in significance, in both increasing and decreasing directions, from what is expected for each time scale and then performs a statistical interpretation of these points. Therefore this method simply chooses the scenario in which one is most likely to conclude that there was a singular variation over time in a given interval. If no significant deviations are found, then it can be assumed that the excess of events was accumulated in a manner that is consistent with being constant in time. This method is the maximum deviation method. Although useful for setting a limit on the level of fluctuations, this method only analyzes the largest fluctuations and is not indicative of the average behavior of the detector. Therefore another method, the all possibility method, of analyzing the time variance of the signal is performed. This method analyzes each possible set of independent bins to determine how consistent that set, as a whole, is with being constant. The set of independent bins with the most average behavior is then identified from all the possibilities on a particular time scale. The results from this set are then chosen for use in interpretation of whether or not the signal was accumulated in a manner that is consistent with being constant. If the results from all time scales are shown to be consistent with being constant, then the assumption can be made that there were no statistically significant time variations in the acquired excess.

5.2.1 Maximum Deviation Method

The time bins which deviate from the expected significance for a particular time scale by the largest amount in both the increasing and decreasing directions are identified for all 11 timescales from 1 to 150 days. After the bins of maximum and minimum significance are found for each time scale, analysis is performed to determine if the variation from expectation is statistically significant. A plot of rolling significance allows for the identification of the appropriate time bin with the maximum deviation from the expected level. In such a plot, the significance of the number of excess events detected is calculated for the appropriate time bin beginning on the date of the point. Neighboring points for the time scales longer than 1 day are highly correlated. Figure 5.3 shows the rolling significance for the

bin centered on the Crab Nebula for the 10, 30 and 100-day time scales. Plots of the rolling significance for the 8 remaining time scales are in Appendix A.

Utilizing information from these plots to determine the stability of the signal from the Crab versus time can be difficult due to the aforementioned correlations. Although the bin of maximum deviation is at some significance level, one must take into account that a large number of bins were examined, increasing the likelihood that a more extreme deviation would be found. The minimum number of bins that must be accounted for is the number of independent bins of the same length in time that are allowed over the whole data set. For example, a 1000 day data set can have up to 11 independent 100 day bins, where the bin of maximum deviation would only represent one of those. However, the minimum number of independent bins only represents the lower limit on the number of bins (trials) that must be accounted for. In actuality, the number of trials is higher than this value because of the correlated bins that were examined. Unfortunately, the exact number of trials is difficult to determine. Therefore, the bin of maximum deviation is only corrected for the minimum number of independent bins. To perform this correction, the probability that the maximum observed deviation would be found in a sample of some number of independent observations, assuming a Gaussian distribution of probabilities, is calculated. The significance of this probability is an upper limit on the statistical significance of the most extreme fluctuation, and the actual statistical significance will be smaller.

Table 5.1 shows the maximum significance of excess events found in any time bin for all 11 analyzed time scales, as well as the ideal expected significance for that time scale given the final result from Eq. 5.1,[3] and the significance of the deviation from this expected value. Also shown is the number of independent time bins possible, which represents the lower limit on the number of trials, and the significance of the deviation after accounting for the minimum number of trials. As mentioned previously this is the upper limit on the trials corrected significance of the deviation.

As can be seen in Table 5.1, none of the time bins with the most extreme deviation in increasing significance from that which is expected for a constant signal are statistically significant after accounting for the minimum number of trials. Even the most extreme case, an upper limit of 2.1σ for the 5-day time scale, is not significant. The significance of this upper limit is further reduced because the number of time scales analyzed needs to be accounted for. Since 11 timescales were analyzed, the probability that a 2.1σ effect would be found given 11 attempts needs to be determined. This significance is only 0.9σ. Even if a

[3]As the exposure during any interval varies, this is only an approximation, and is in fact slightly overestimated due to the duty cycle of Milagro (typically $\sim$95%).

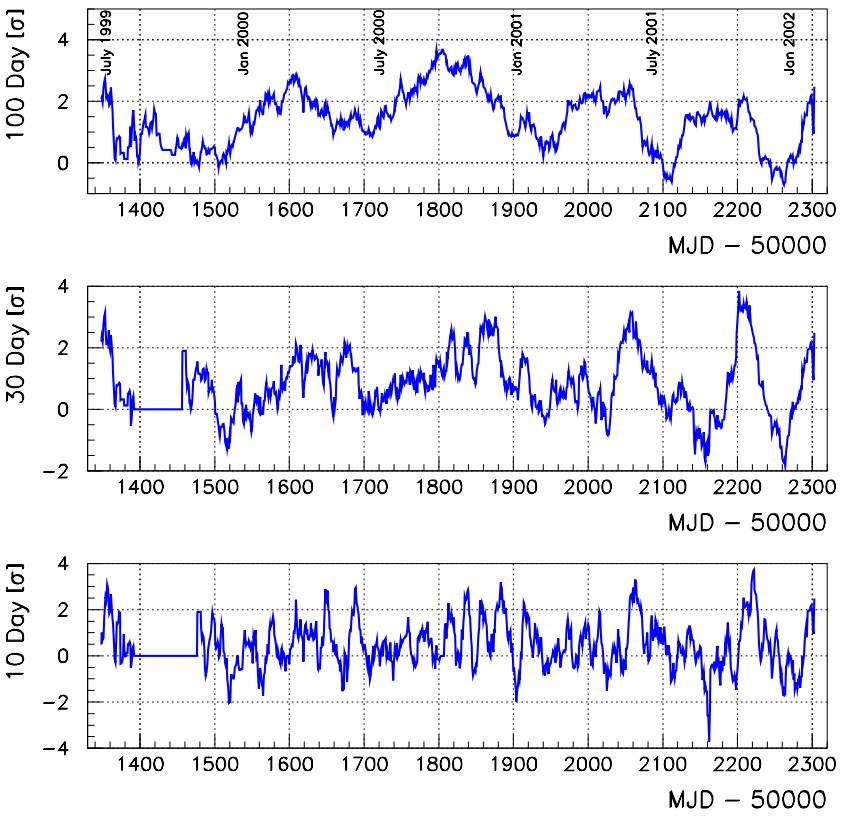

Figure 5.3: This figure shows the rolling significance of the excess found at the position of the Crab Nebula for the 10, 30, and 100-day time scales. Entries are plotted according to the *first* day of the interval. Neighboring points are correlated.

Time Scale (Days)	σ **Obs.**	σ **Exp.**	σ **of Deviation**	**No. of Ind. Bins**	**Corrected** σ **of Deviation**
150	3.7	2.1	1.6	7	0.4
100	3.7	1.8	1.9	10	0.7
50	3.5	1.2	2.3	19	0.9
30	3.8	1.0	2.9	31	1.6
21	4.1	0.8	3.2	44	1.9
14	3.8	0.7	3.1	64	1.6
10	3.7	0.6	3.2	89	1.5
7	3.6	0.5	3.1	126	1.3
5	4.1	0.4	3.7	175	2.1
3	3.6	0.3	3.3	286	1.1
1	3.3	0.2	3.2	770	0.1

Table 5.1: Significance of the maximum deviation from the expectation in the direction of increasing significance for various time scales. Apparent mathematical discrepancies are due to rounding. The corrected σ of deviation represents the upper limit on the significance of the deviation. The actual statistical significance is smaller.

method were employed to reduce the oversampling in time to a more ideal value as discussed in Chapter 4 (Biller, 1996), *i.e.* use 1, 3, 10, 30 and 100-day bins only, the upper limit on the significance of the most extreme case found on these 5 time scales, 1.6σ for the 30-day time scale, would only be 0.6σ upper limit after accounting for the 5 time scales. Therefore, this method shows that no extreme deviations from what is expected for a constant signal occurred in the temporal accumulation of excess events from the Crab Nebula.

Table 5.2 shows the same results with the exception that the analysis is performed on the minimum significance found for any time bin in all 11 analyzed time scales. While the results appear to be more extreme, the maximum deviation method is flawed in this case. The upper limit on the significance of the most extreme case, that of the 10-day time scale, is 3.1σ. After accounting for the 11 time scales, this is actually a 2.3σ effect. If the number of time scales (oversampling in time) were reduced by only analyzing the 5 previously discussed, this is still the most extreme effect, which after accounting for the 5 time scales is 2.6σ. While not a confirmation of variation in the detected excess, this probability merits further investigation. As it turns out, the maximum deviation method is flawed in the case of analyzing the bin of minimum significance. This is primar-

ily due to detector down time. For example, the detector may have only been operational for a few hours during a 10 day time period. This causes a problem because the significance that one would expect over a few hours is essentially none. Therefore, the deviation from expectation is overestimated. This is the case: the bin of minimum significance found for almost all of the time scales is exactly the same and occurs on the date before the 3rd tube repair. The exposure during this time bin is only a few hours, before a break of $\sim$10 days. Thus the smallest time scales have the exact same results for minimum significance. In fact all of the bins of minimum significance have less than 50% exposure, allowing for an overestimate of the expected significance. Unfortunately, removing all of the bins with low exposures is difficult. Thus, utilizing the maximum deviation technique in the case of minimum significance is flawed and a poor indication of the stability of the sensitivity of Milagro.

Time Scale (Days)	σ **Obs.**	σ **Exp.**	σ **of Deviation**	**No. of Ind. Bins**	**Corrected** σ **of Deviation**
150	-0.2	2.1	2.3	7	1.4
100	-0.6	1.8	2.4	10	1.4
50	-1.4	1.2	2.7	20	1.4
30	-1.8	1.0	2.8	31	1.4
21	-2.0	0.8	2.8	43	1.3
14	-2.7	0.7	3.3	64	1.9
10	-3.7	0.6	4.3	89	3.1
7	-3.2	0.5	3.7	126	2.1
5	-3.2	0.4	3.6	175	1.9
3	-3.2	0.3	3.5	286	1.5
1	-3.2	0.2	3.4	770	0.7

Table 5.2: Significances of the maximum deviation from the expectation in the direction of decreasing significance for various time scales. Apparent mathematical discrepancies are due to rounding. The corrected σ of deviation represents the upper limit on the significance of the deviation. The actual statistical significance is smaller.

No statistically significant variations were found in the most extreme cases of short time scale bins of excess events. Therefore, the limit on the level of fluctuations in the excess found by this method demonstrates that it is safe to assume that Milagro has behaved in a stable manner. While this method does not explore the average behavior of the detector, no particular bin truly stood

out. Therefore, even if one had chosen the maximally deviant bin for use in the evaluation of the stability, one would have been led to the conclusion that the excess was accumulated in a manner that was consistent with being constant.

5.2.2 All Possibility Method

This method examines the fractional excess detected by Milagro binned on various time scales. As mentioned previously, for a given time scale there are a number of independent ways to bin the data. In this method each variation of independent bins of the fractional excess versus time is examined. The data for the given variation are fit to a constant, and the χ^2 from the fit is found. Using this value, along with the number of degrees of freedom in the fit, the probability (P) that, if the experiment were repeated, a single measured value of χ^2 would be greater than the one determined, is calculated. A distribution of the probability values is then generated for a particular time scale from the fits to all the possible variations of independent bins. Figure 5.4 shows the resulting probability distributions generated for the 9 largest time scales.

The distributions shown in Figure 5.4 are reasonable, with no major deviations occurring. As this is the case, the median probability is therefore a useful indicator of how consistent the temporal distribution of the excess, on average, is with being constant. Thus, the median probability is determined for each time scale and used to evaluate any possible variations in the detector's sensitivity. Table 5.3 shows the median probability and corresponding reduced χ^2 resulting from a fit of the fractional excess versus time to a constant for all possible variations of independent bins on the 11 time scales.

As can be seen from Table 5.3 the median probability values resulting from χ^2 fits to the fractional excess versus time are consistent with being constant for the longer time scales ($\geq$30 days). The fits on shorter time scales become less consistent with being constant as the time scale is decreased. While undesirable, this is reasonable since the disagreement is generally not large and a number of effects can contribute to short term changes in sensitivity. These include a variable number of dead PMTs in the detector, reflectivity changes at detector surfaces due to variations in environmental conditions (*e.g* a thin sheet of ice or large air bubbles under the cover), changes in the amount of overburden (water on the cover), and dramatic short term changes in the the trigger rate shown in Figure 4.7. A more thorough analysis which incorporates these effects, as well as other possible contributions, would be required to demonstrate that the short term sensitivity of Milagro behaves in a reasonable manner. As the focus of the results presented in this thesis is for time scales of at least 150 days, this analysis is not performed. Therefore the all possibility method shows that the

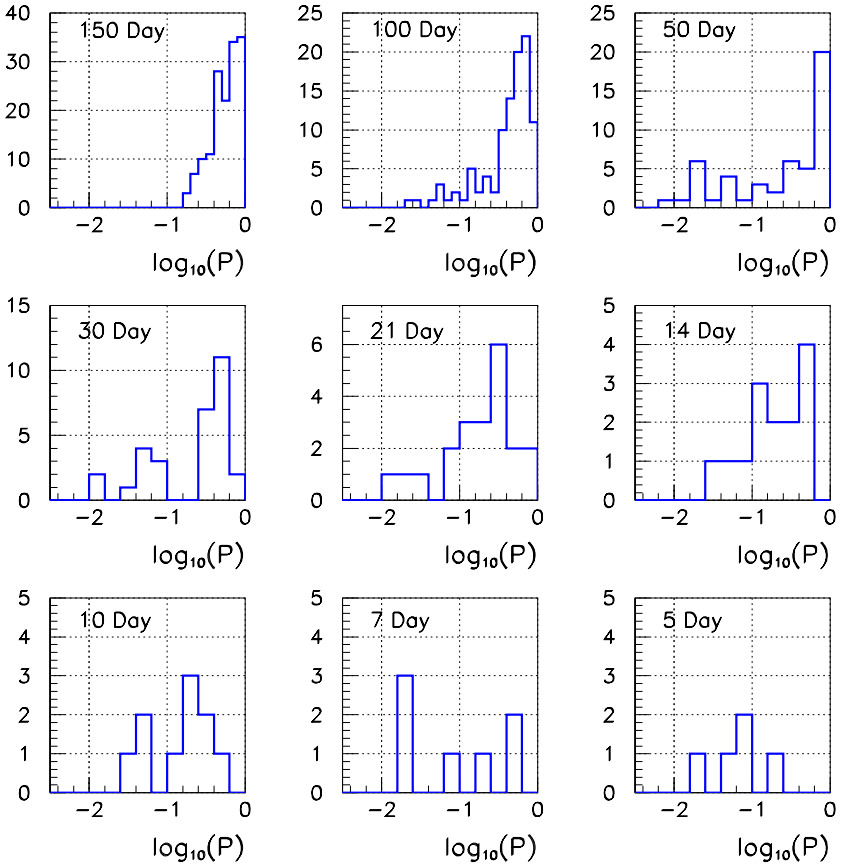

Figure 5.4: This figure shows the distribution of probability values calculated from the χ^2 resulting from fits to all the possible sets of independent bins of the fractional excess versus time from the Crab Nebula. The distributions are for the 9 largest time scales analyzed.

Time Scale (Days)	Reduced χ^2	Degrees of Freedom	Median Probability	Median Fit Excess Value
150	0.76	6	0.60	0.00402±0.00073
100	0.92	10	0.52	0.00421±0.00079
50	1.03	17	0.42	0.00384±0.00086
30	1.06	29	0.38	0.00402±0.00086
21	1.17	42	0.21	0.00414±0.00090
14	1.12	62	0.24	0.00401±0.00089
10	1.14	86	0.18	0.00406±0.00089
7	1.20	122	0.08	0.00399±0.00092
5	1.17	169	0.07	0.00388±0.00091
3	1.12	272	0.08	0.00375±0.00089
1	1.10	769	0.02	0.00337±0.00088

Table 5.3: Table showing the median probability and the corresponding reduced χ^2 resulting from fits to all possible sets of independent bins of the fractional excess versus time for 11 different time scales.

signal from the Crab Nebula was accumulated in a manner that is consistent with being constant in time for the relevant time intervals. To further illustrate this, Figure 5.5 shows the fractional excess versus time for the 30-day time scale. The choice of independent bins is the one which corresponds to the median probability. Also shown in the plot is the fit constant. As can be seen there are no points which vary dramatically from the fit constant, as expected from the reported χ^2 value. Plots of the fractional excess versus time for the remaining 10 time scales are found in Appendix A.

The maximum deviation method, the all possibility method, and analysis of the cumulative significance versus time, all indicate that the temporal behavior of the observed excess of events from the direction of the Crab Nebula is consistent with being constant in time (at least for time scales $\geq$30 days). Thus, the statement that the detector has behaved in a stable manner can be made. As this is expected, it shows that Milagro is a reliable instrument for use in the search for TeV gamma-ray emission.

5.3 Detailed Analysis

While the optimal values for the data cuts and bin size used in the analysis are determined a priori, the use of the Crab as a indication of how the detec-

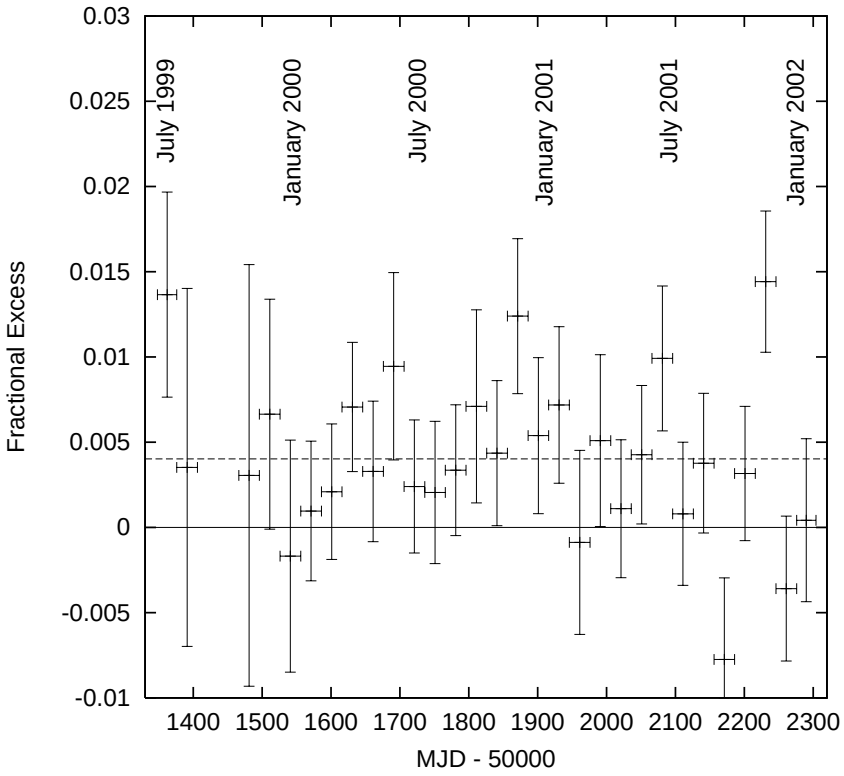

Figure 5.5: This figure shows the fractional excess versus time from the Crab Nebula for the 30-day time scale. The choice of independent bins is the one which corresponds to the median probability. The dashed line represents the constant that was fit to this set of bins.

tor performs begs the question of whether these values were determined properly. Therefore, an analysis of the behavior of the excess detected from the Crab Nebula versus X_2 cut, bin size, N_{fit} cut, and zenith angle is performed.[4] Should the excess behave as expected, it will further demonstrate that Milagro can provide scientifically meaningful results from the Crab Nebula as well as from other sources.

5.3.1 Performance of Background Rejection Technique

As the detection of any source at TeV energies relies heavily on the ability to reject the more numerous cosmic ray background events, an evaluation of how the background rejection technique, the X_2 cut, performs is merited. This is especially important as significant variations are seen in the percentage of data events passing the X_2 cut at high X_2 values when compared to predictions from the Monte Carlo simulations. Since the X_2 cut is not completely understood in the Monte Carlo simulations, the first question to be addressed is what happens to the Crab signal without utilizing it.

Without the X_2 cut, 13,703,349 events are found in the bin centered on the Crab, yielding an excess above the expected background level, corrected for signal contamination, of 3268 ± 3822 events or 0.9 sigma. Therefore, Milagro has not detected emission from the Crab Nebula without use of the background detection technique. Although this is not entirely unexpected, it does indicate some problems with the understanding of the Crab signal. As can be seen the number of excess events is actually smaller than the 6174 ± 1322 found with the X_2 cut. The X_2 cut chosen should reduce the number of excess events by a factor of $\sim$2, not increase it. Further, this means that the Q value found for the X_2 cut is $5.5^{+\infty}_{-3.2}$ whereas a value of 1.6 is expected. Although the disagreement with expectations is not severe (1.2σ), it is clear that the performance of the background rejection parameter is not completely explained by the Monte Carlo simulations. Given this, an exploration of how the observed Crab signal behaves as the X_2 cut is varied was undertaken. Figure 5.6 shows the observed excess of events in the bin centered on the Crab Nebula versus the X_2 cut utilized. As a cut of some value retains all the same events passing a cut of a higher value, neighboring points are correlated. Also shown in Figure 5.6 is the number of excess events predicted by Monte Carlo simulations. The predicted value is normalized in such a way that the prediction at a cut of $X_2 \geq 2.5$ is what was measured. Therefore all expectations are relative to this value. As can be seen in the figure the number of excess events detected from the Crab is low compared to predictions for small values of

[4] A similar analysis is performed on the signal detected from Mrk 421 in Appendix C.

the X_2 cut, while in agreement for the higher values of the cut. It should be noted that there are relatively poor statistics for the predictions at higher X_2 values. Thus some modest disagreement may be expected in this regime. Further, the large error bars on the points with the low X_2 values as well as the correlations may make the disagreement in the plot appear worse than actual.

Figure 5.7 shows the significance observed from the Crab Nebula versus the X_2 cut utilized. Also shown is that which would be predicted given the expected Q-value from Monte Carlo simulations. Again the expectations are normalized in such a manner that the value measured at $X_2 \geq 2.5$ is exactly correct. Clearly the predictions don't match the measured values well. At high X_2 values this is likely a result of poor statistics in the simulation, but for the low values the effect is currently unexplained. Therefore, the statement can be made that the background rejection technique works, but is not well simulated. However, as only one source is utilized to make this statement, no clear conclusions can be drawn as to why this occurs.

5.3.2 Performance Versus Bin Size

Given that the Monte Carlo simulations of the performance of the X_2 cut do not match well, exploration of how the Crab signal behaves for other cuts is undertaken. Shown in Figure 5.8 is the excess events observed from the Crab Nebula versus bin size. As a bin of smaller radius is completely contained by a bin of larger radius, neighboring points are correlated. The solid line in Figure 5.8 is the predicted number of excess events. This value is determined using the percentage of events that should fall within the source bin, given the chosen data cuts, according to Monte Carlo simulations. The curve is normalized in a manner that the value measured at the bin size, $r = 1.1848°$, is exactly what is predicted. As can be seen there is agreement with the prediction from simulations. Therefore the conclusion can be drawn that the Monte Carlo simulations predict the angular resolution of the detector reasonably.

Figure 5.9 shows the observed significance of the Crab Nebula versus bin size with and without the X_2 cut. Also shown are the Monte Carlo predictions normalized so that they agree with with the measurement at the bin size used for the analysis. It should be noted that the dependence on bin size of the significance without the X_2 cut is different than the dependence with it. This is because the average angular resolution of showers not passing the X_2 cut is slightly better. This does yield a different optimal bin size, but the overall difference is not large. While the predictions from Monte Carlo simulations match the measured values when the X_2 cut is applied, they match poorly in the absence of an X_2 cut. This may indicate that some anomalous behavior is occurring with the Crab signal

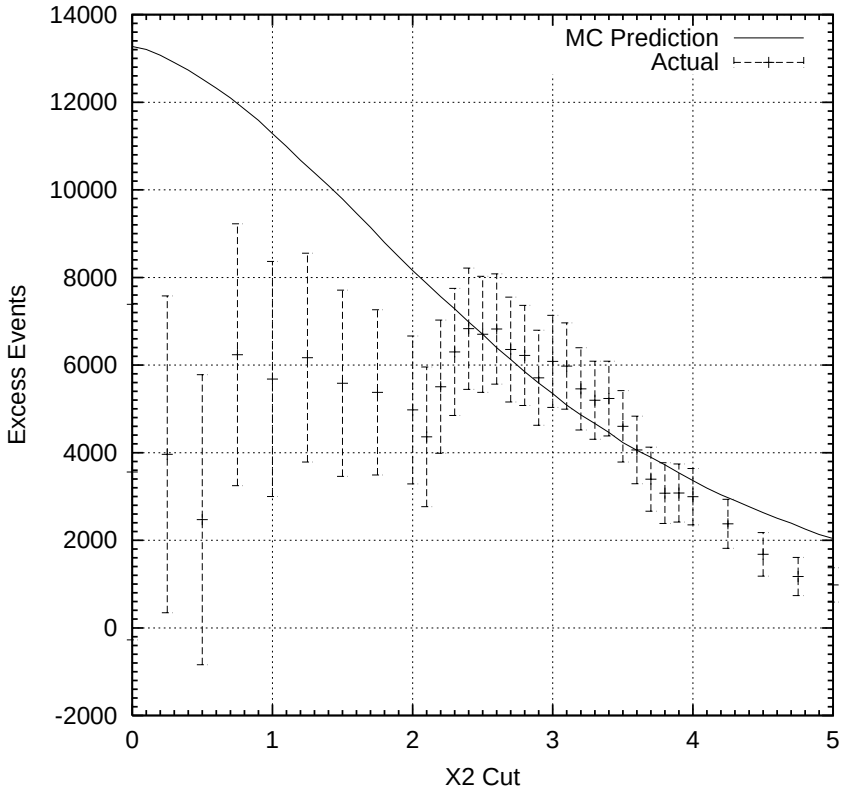

Figure 5.6: Plot of the excess events observed in the bin centered on the true position of the Crab Nebula versus X_2 cut. Neighboring points are correlated. The solid line represents the expected behavior from the Monte Carlo simulation normalized to the value of the excess measured with a cut keeping only events with $X_2 \geq 2.5$.

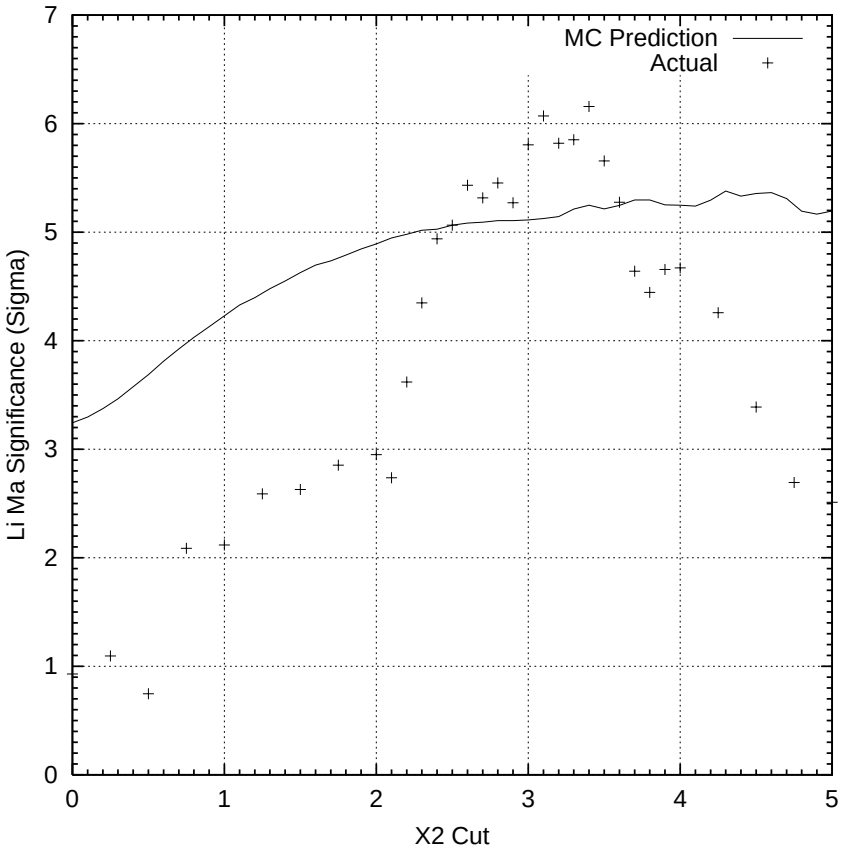

Figure 5.7: Plot of the significance observed in the bin centered on the true position of the Crab Nebula versus X_2 cut. Neighboring points are correlated. The solid line represents the predicted behavior from Monte Carlo simulation normalized to the value measured at $X_2 \geq 2.5$.

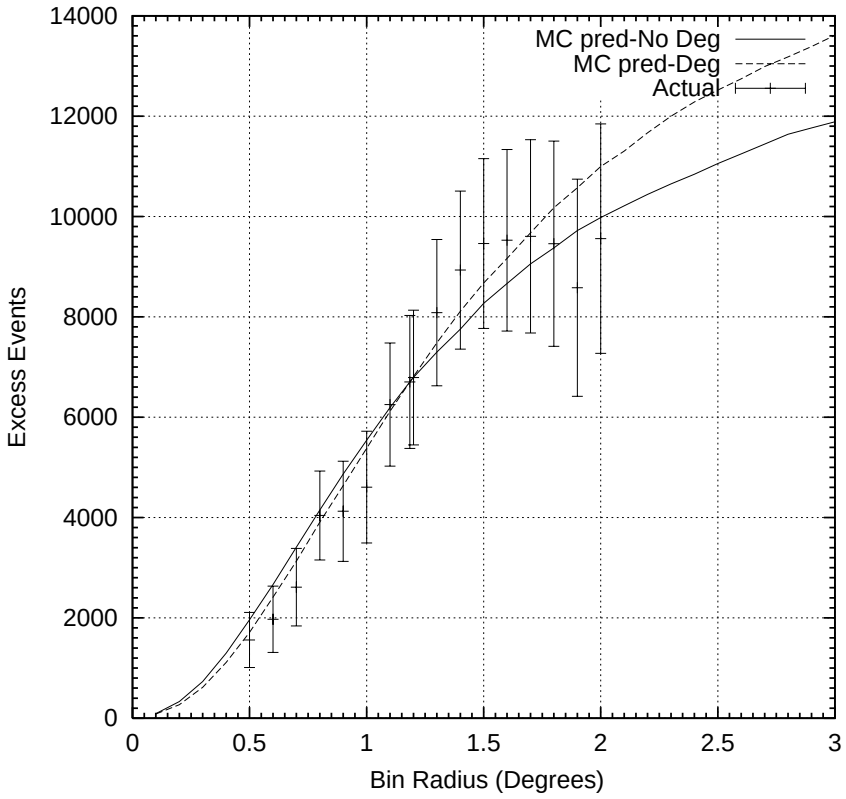

Figure 5.8: Plot of the excess events observed in the bin centered on the position of the Crab Nebula versus bin size. Neighboring points are correlated. The solid line represents the expectations from Monte Carlo simulation normalized to agree with the results at the bin radius used in the analysis, $r = 1.1848°$. The dashed line represents the expectations from Monte Carlo simulations, also normalized to agree with the results at $r = 1.1848°$, if the angular resolution was systematically degraded by 20% from the original prediction (explained later in this subsection).

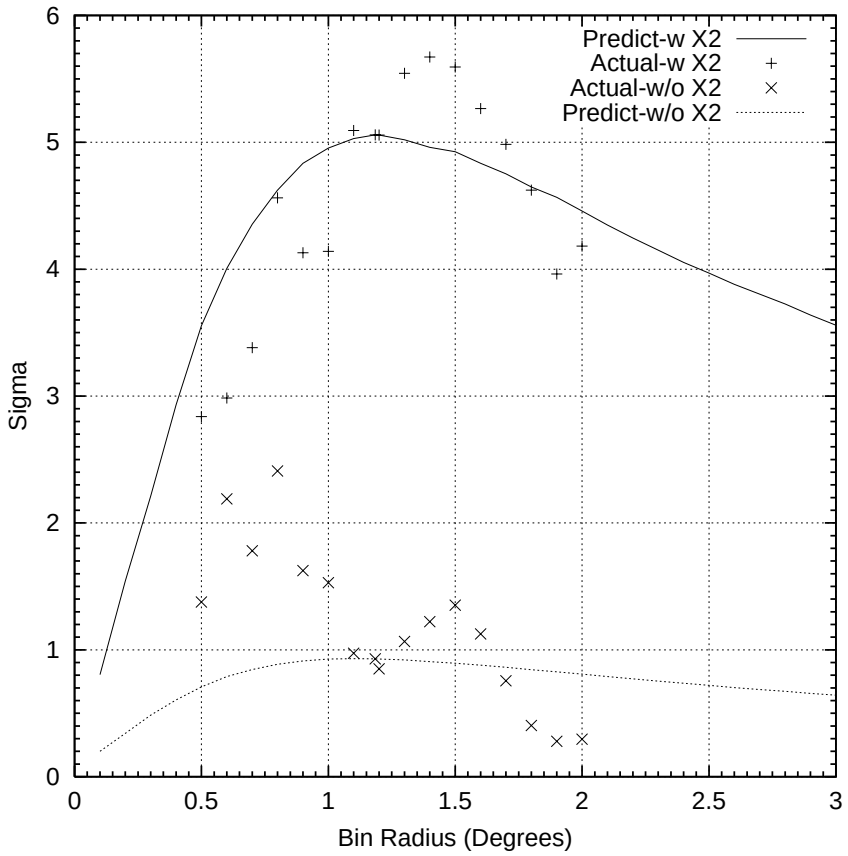

Figure 5.9: Plot of the significance observed in the bin centered on the true position of the Crab Nebula versus bin size. Shown are results with and without utilizing the X_2 cut. Neighboring points are correlated. The expected significance is shown by the solid lines, normalized in a manner that the prediction at $r = 1.1848$ agrees perfectly with what was measured.

when no cut is applied, although more source detections need to be examined to make a firm conclusion regarding this.

Although the bin size dependence of the actual number of excess events retained, as well as the significance observed from the Crab Nebula, is in statistical agreement with what is predicted from Monte Carlo simulations, a minor systematic trend is observed. It is clear from Figure 5.8 that at small bin size values the number of excess events observed is low compared to predictions. Further, at higher values for the bin size the number of excess events observed is consistently high compared to predictions. While this effect is overstated by the correlations in the plot, it is suggestive that the actual resolution of the detector may in fact be underestimated. If this were the case the optimal bin size would be larger than the simulations indicated, which would result in a larger excess and significance to be found for the Crab. A worse angular resolution would also change the shape of the predicted curves. The dashed line in Figure 5.8 shows the predicted curve that results if the difference in true direction and reconstructed direction, Δ_{angle}, were made 20% worse for every reconstructed event in the Monte Carlo simulations (a simple approximation which degrades the angular resolution). This curve is also normalized in a manner such that it agrees with the measured value at r=1.1848°. While the original predicted curve is in statistical agreement with what is measured, the curve which represents the prediction with a worse angular resolution matches the measured values even better. Therefore there is motivation for the statement that the Monte Carlo simulations predict the angular resolution to be too good.[5] As will be discussed in Section 5.5.3, this can have an effect on the value determined for the flux from the source.

5.3.3 Performance Versus N_{fit} Cut

Figure 5.10 shows the detected significance from the Crab Nebula versus N_{fit} cut for various bin sizes. Since a high N_{fit} cut improves the angular resolution of the detector, the optimal bin size is smaller at larger values. For almost all bin sizes the significance is approximately constant for cuts up to 40 tubes participating in the fit. After a cut of 50 tubes the significance clearly drops off. This is in agreement with the predictions from Monte Carlo simulations and indicates the the chosen N_{fit} cut of 20 PMTs is reasonable. This plot also shows that for bin sizes of 1.4 to 1.6 degrees radius, the significance found is higher than that found for the nominally optimal bin size of 1.2 degrees, for N_{fit} cuts of up to 100 PMTs

[5]This same systematic trend, discussed in Appendix C, is seen in the analysis of the signal from Mrk 421.

participating in the fit.[6] This provides motivation that the bin size may be too small, which would be justified if the Monte Carlo simulations predicted to good an angular resolution for the detector.

5.3.4 Performance Versus Zenith Angle

Figure 5.11 shows the excess of events detected from the Crab Nebula for various zenith angle bins. As can be seen the bulk of the detected excess comes from zenith angles of less than 30 degrees. No excess events are seen with zenith angles of less than 10 degrees due to the path in local coordinates that the Crab Nebula traverses. This is in agreement with the predicted effective area which shows that Milagro is most sensitive at small zenith angles.

5.4 Crab Nebula Flux Determination

While no spectral information about the Crab can be ascertained from the detected signal due to the fact that the energy resolution of Milagro is very poor, a scientifically meaningful result, the flux of TeV photons, can be calculated. This is done using an assumed spectral index dictated by the results of detections from other observatories.

In order to calculate the flux from the Crab, the zenith angle exposure of Milagro to the Crab must be determined. This is empirically calculated in the following manner: For every integer second that Milagro was operational, the zenith angle of the Crab was determined. Using this value of the zenith angle, the time that the Crab spent in the corresponding 5 degree zenith angle bin was incremented by 1 second. The cumulative exposure is calculated by performing this operation during analysis of the entire Milagro data set studied. It is expected that these results are accurate to a few seconds in time and therefore errors in the calculated exposure are not large. While the exposure is accurate in the actual length of time Milagro was operational, it does not account for the dead time of the Milagro detector while reading out triggered events. During the running of Milagro, the dead time was typically $\sim$6%. Assuming that the dead time affects the exposure in a uniform manner, a simple correction that multiplies the time exposure of Milagro to the Crab initially calculated by 0.94 will account for this. The zenith angle exposure to the Crab, corrected for dead time, is shown in Figure 5.12.

[6] This behavior is also seen in the detected signal from Mrk 421 and is discussed in Appendix C.

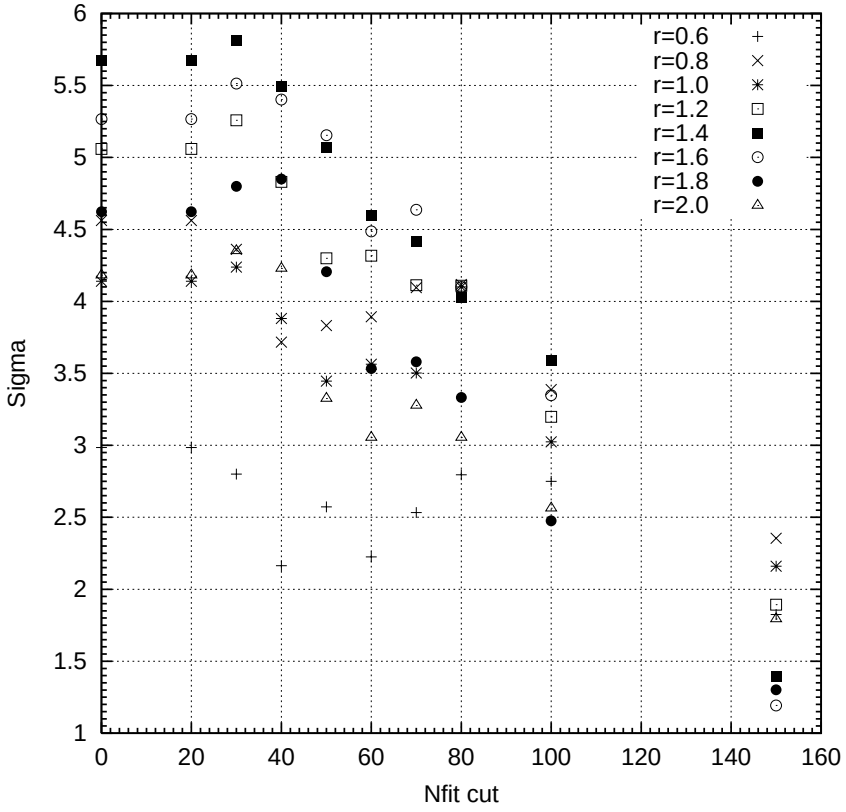

Figure 5.10: Plot of the significance observed in the bin centered on the true position of the Crab Nebula versus N_{fit} cut for various bin sizes. Neighboring points are correlated.

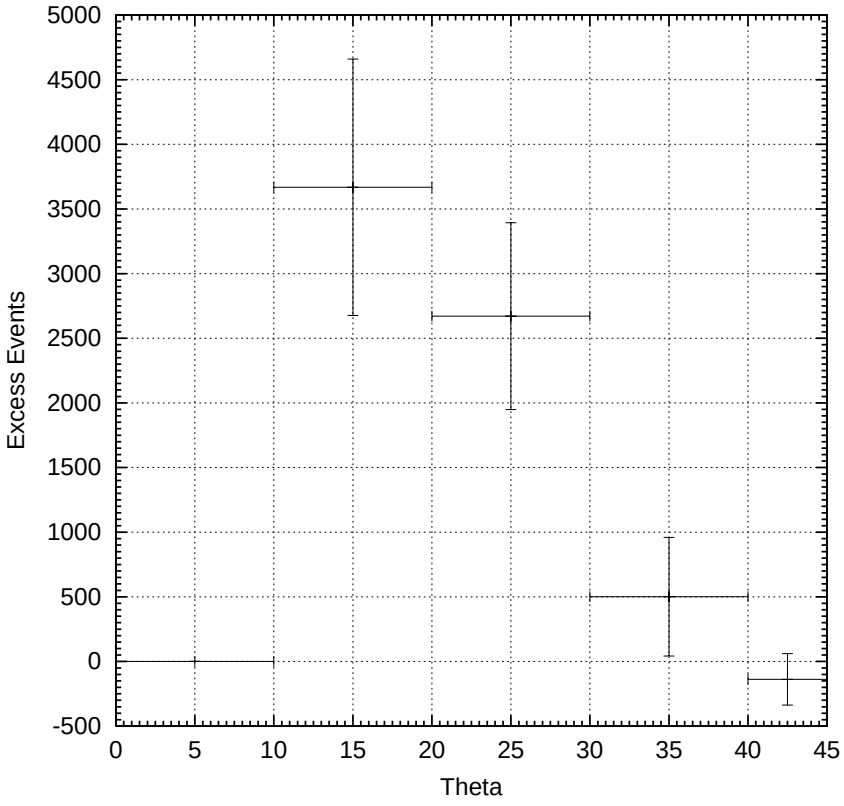

Figure 5.11: Plot of the excess events observed in the bin centered on the true position of the Crab Nebula versus zenith angle (θ). For comparison, Figure 5.12 shows the exposure of the Crab Nebula versus zenith angle bin.

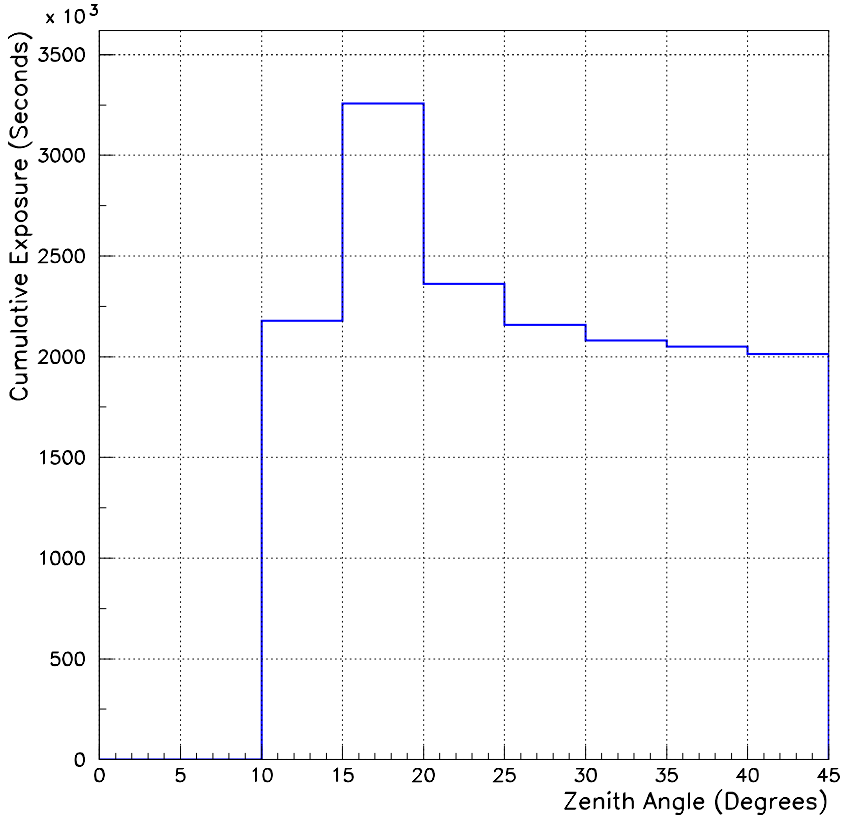

Figure 5.12: Plot of the dead-time-corrected cumulative time exposure versus actual zenith angle position of the Crab Nebula during data taking. The values shown are the amount of time that the actual position of the Crab in local coordinates was within the zenith angle bin indicated during Milagro data taking. The values agree within <1% of what would be theoretically predicted from the total cumulative exposure of Milagro. The minor differences are a result of the effects of down time in the detector.

Before the flux from the Crab can be calculated the effect of dead PMTs in Milagro needs to be accounted for in the effective area. The effective area of Milagro shown in Chapter 3 is ideal in that the simulations utilized did not account for the effect of dead PMTs. Therefore, it is not used for calculating flux values from the Crab. Unfortunately, the effects of the dead PMTs are difficult to simulate exactly because their deaths occurred on different dates and the dead tubes were eventually replaced at varying times. However, general statements can be made as to the effects of dead PMTs. To do this effective areas were calculated with a typical number ($\sim$50) of the PMTs inoperational in both layers. Since the positions of the individual dead PMTs varied, every 16th tube in the detector (48 total) was made inoperational while simulating the effective area of the detector. While this would not account for any detector asymmetries caused by dead tubes in groups, it serves as a useful approximation for the effect of dead PMTs. For this approximation all values such as X_2, Δ_{angle}, N_{fit}, etc. were recalculated not utilizing the inoperational PMTs during the generation of the new effective area. Further, the dead tubes are directly accounted for in the trigger, where $\geq$55 operational top layer PMTs hit is required. The bin size and data cut values are not changed in determining the effective area. Figure 5.13 shows the effective area as a function of energy with and without the 48 dead PMTs accounted for. As expected, the effective area is less when the dead PMTs are accounted for. All effective areas shown and utilized in this thesis have the typical number of dead PMTs incorporated in their generation.

Utilizing the excess of events detected from the Crab Nebula of $\Delta = 6174 \pm 1322$ events, and the cumulative zenith angle exposure of Milagro to the Crab shown in Figure 5.12, along with the effective area for Milagro shown in Figure 5.13, the differential flux normalization, $I_\circ$, for the Crab Nebula is calculated. The energy to which the flux is normalized, $E_\circ$, is the median energy of observed events for the Crab Nebula of 3 TeV. This value is determined utilizing the methods discussed in Section 4.4.2. The value selected for the spectral index in this analysis is $\alpha = 2.59$. Since $I_\circ$ is normalized to the median energy of observation, the exact choice of spectral index is small in its effect on the differential flux normalization as long as it is reasonable. Using Eq. 4.18 the differential flux normalization calculated for the Crab Nebula is $I_\circ = (1.27 \pm 0.27) \times 10^{-12}$ TeV^{-1} cm^{-2} s^{-1}. This results in a integral flux given by Eq. 4.19 above the median energy of 3 TeV of $(2.53 \pm 0.54) \times 10^{-12}$ cm^{-2} s^{-1} for a spectral index of $\alpha = 2.49$, and $(2.38 \pm 0.51) \times 10^{-12}$ cm^{-2} s^{-1} for a spectral index of $\alpha = 2.59$.[7]

[7] These results do not include systematic errors. The two spectral indices correspond to those found for the Crab Nebula by HEGRA (Aharonian et al., 2000) and Whipple (Hillas et al., 1998) respectively.

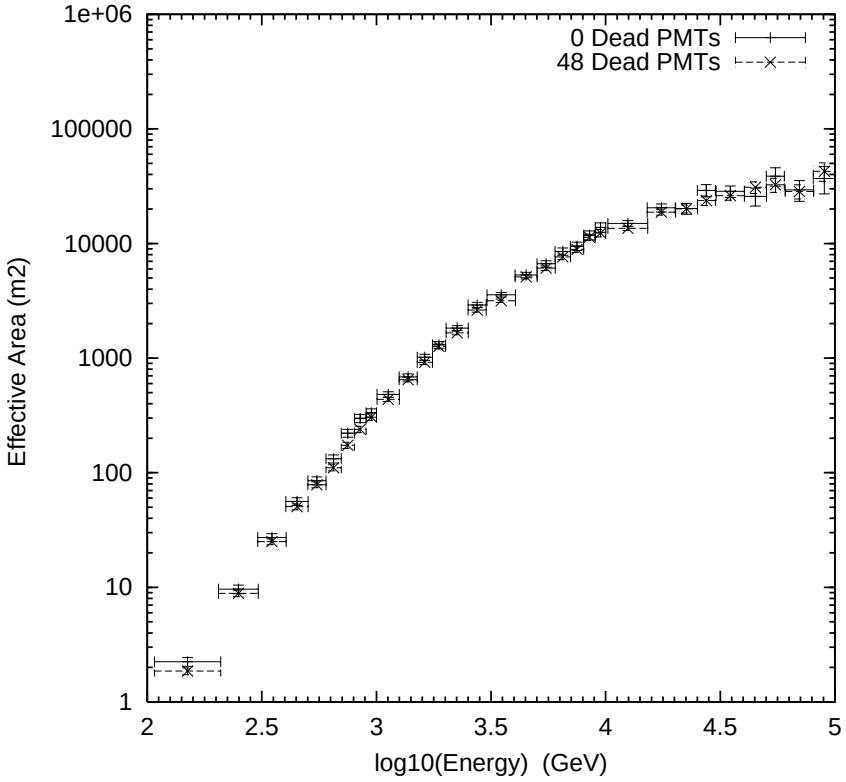

Figure 5.13: Plot of the effective area versus energy for the case of no dead PMTs present as well as for the case of a typical number of dead PMTs (48 total) present. As can be seen the presence of dead PMTs reduces the effective area slightly. The effective area with the typical number of dead PMTs incorporated is utilized during the calculation of all reported flux values.

5.5 Systematic Errors in the Milagro Flux Determination

Examination of Eq. 4.18 shows that there are three variables that enter into the final flux determination. These variables are the time exposure, the effective area and the observed excess. Due to systematic errors in the values utilized in calculating the flux, the results quoted in the previous section may not be entirely accurate. In this section, possible systematic errors in the three variables are motivated and their effects explored.

5.5.1 Systematic Error in the Exposure

The first variable is the time exposure of Milagro to the Crab Nebula. To verify that the exposure shown in Figure 5.12 was proper, the ideal exposure of Milagro to the Crab Nebula for 1 day was calculated theoretically for each bin. The results were then multiplied by the total exposure of Milagro in days, adjusted for detector dead time, and compared to the results shown in Figure 5.12. The agreement was found to be within less than 1 percent. Such small deviations are expected as the exposure for Milagro is not ideal due to detector down time.

Although the exposure is calculated accurately, a source of systematic error arises in the reported flux results from the detector dead time correction. The dead time in Milagro was not always 6% as it varied with the trigger rate. This variation is difficult to account for exactly. However, the overall variation typically is no greater than $\sim$2%. Therefore, the size of the effect of systematic errors in the time exposure on the integral flux is no greater than $\sim$2%. Clearly, the contribution of systematic errors in the exposure is small.

5.5.2 Systematic Errors in the Effective Area

There are many issues with the Monte Carlo simulations than can cause the effective area to differ from that which is utilized. These include, but are not limited to, the number of dead tubes simulated, the model of the detector trigger threshold chosen, and the effect of the background rejection technique. Further, the statistical error in the effective area, $\sim$3%, contributes to the systematic error in the calculated flux.

Dead PMTs

The effective area utilized assumes a detector in which 48 PMTs were not operational. Since the number of dead PMTs varied during data taking, the effect

of different numbers of the dead PMTs is explored. To do this new effective areas were generated for varying numbers of dead PMTs (25, 74 and 95) in Milagro in the same manner described in Section 5.4 (*i.e.* removing every 32nd, 10th, and 8th PMT). The effect of no dead PMTs is also evaluated. Utilizing the appropriate effective areas, new integral fluxes[8] above 1 TeV were calculated [9] using the spectral index of $\alpha = 2.59$. Table 5.4 shows the integral flux results. Since the actual number of dead PMTs was almost always between 25 and 75, the size of the systematic error in the flux that results from estimating the number of dead PMTs is $\sim$+7/-3%. Clearly, variations in the number of dead PMTs only results in a small effect on integral flux.

Fraction of Dead PMTs	**Number Dead**	$I(\geq 1\,TeV)$ $\times 10^{-12}$ **cm**$^{-2}$ **s**$^{-1}$	**Increase (%)**
None	0	12.5 ± 2.7	-8.8
1/32	25	13.3 ± 2.8	-2.9
1/16	48	13.7 ± 2.9	0.0
1/10	74	14.6 ± 3.1	6.6
1/8	95	15.3 ± 3.3	11.7

Table 5.4: Table showing the integral flux greater than 1 TeV from the Crab Nebula from the Milagro results utilizing the spectral index of α =2.59. These results show the general effects of varying numbers of dead PMTs. The case of every 16th PMT inoperational (48 total) is used in the standard analysis.

Trigger Threshold Model

In the Monte Carlo simulations the detector trigger threshold is modeled. If this were inaccurate, it would affect the effective areas and correspondingly the integral flux reported. For all of the previous analysis a threshold of 55 top layer PMTs hit was chosen for the threshold in the Monte Carlo simulations, as this is the approximate threshold utilized in the electronic trigger of Milagro. This value is reasonable because the results of simulations with this trigger threshold match the data fairly well. Unfortunately the exact threshold that should be used in the simulation is difficult to determine. This is because the threshold was

[8]The calculation of new fluxes is much simpler than comparing the effective areas which depend on both zenith angle and energy.

[9]Since the integral flux from the Crab is often reported above 1 TeV, the systematic errors on this result (as opposed to above the median energy of observed events inferred of 3 TeV) are explored.

varied during data taking to keep the trigger rates essentially constant, providing uncertainty as to the exact value utilized. Therefore the effects of various trigger thresholds are explored to see how they contribute to the integral flux reported. Since it is highly unlikely that the threshold was not between 40 and 70 tubes during Milagro operations, effective areas were recalculated for thresholds of 40, 50, 60, and 70 tubes.[10] Table 5.5 shows the integral fluxes calculated using the different effective areas determined for the various trigger thresholds. These values were calculated using the spectral index of $\alpha = 2.59$. As can be seen the effect of varying the trigger threshold is small. From this study it is estimated that the size of the systematic error on the integral flux that results from the modeling of the trigger threshold is $\sim$5%.

Threshold (No. PMTs)	$I(\geq 1\,TeV)$ $\times 10^{-12}$ **cm**$^{-2}$ **s**$^{-1}$	**Change** (%)
40	12.7 ± 2.7	-7.3
50	13.3 ± 2.8	-2.9
55	13.7 ± 2.9	0.0
60	14.2 ± 3.0	+3.6
70	15.5 ± 3.3	+13.1

Table 5.5: Table showing the integral flux greater than 1 TeV from the Crab Nebula from the Milagro results utilizing the spectral index of $\alpha = 2.59$. These results show the effects of varying the trigger threshold in the Monte Carlo simulations. The threshold chosen for the standard analysis is 55 PMTs.

Background Rejection Effects

As discussed in Section 5.3.1, the behavior of the background rejection parameter, X_2, is not well simulated for Milagro. This statement is based on the observed performance of an X_2 cut on the Crab Nebula signal. Therefore the effects of not utilizing the X_2 cut were explored in relation to its effects on the reported integral flux from the Crab. To do this, the effective area for Milagro was generated in the absence of an X_2 cut. This effective area is higher by a factor of $\sim$2 than the values with the X_2 cut. Using the detected excess of 3268 ± 3822, this results in an integral flux above 1 TeV of $(3.4 \pm 4.0) \times 10^{-12}$ cm^{-2} s^{-1}. Although the excess is a non-detection, this value is the flux implied by the excess. This integral flux is generated for the spectral index of $\alpha = 2.59$. The value without use

[10] The bin size and data cuts were unchanged in the effective area determinations.

of the X_2 cut is substantially lower than the baseline result previously reported of $(13.7 \pm 2.9) \times 10^{-12}$ cm^{-2} s^{-1}. This provides some indication that something anomalous is occurring in the observations of the Crab Nebula without use of the X_2 cut. Therefore, the conclusion that the X_2 cut is not well simulated for Milagro must be verified using the detections of other sources. However, the uncertainties in the simulation of the X_2 cut also contribute to the systematic error on the reported flux. To estimate the contribution, effective areas were generated for an X_2 cut of 2.0 and 3.0. Using the excess from the Crab for these X_2 cuts shown in Figure 5.6, as well as the corresponding effective area, the integral flux was calculated. Comparison to the baseline result previously mentioned shows that the integral flux is 35% smaller with an X_2 cut of 2.0, and 26% larger with an X_2 cut of 3.0. Therefore the contribution to the systematic error from this simulation of the X_2 cut is +26%/-35%.

5.5.3 Systematic Error in the Predicted Angular Resolution

Although the Monte Carlo simulations assume that the PMTs in Milagro are perfectly calibrated, in reality this is not the case. An imperfect PMT calibration along with the likely presence of PMT hits not associated with the detected shower from single muons, light leaks, late light resulting from reflections within the detector, and the like, as well as possible errors in the curvature correction would degrade the angular resolution of the detector from that which is predicted by the Monte Carlo simulation. Unfortunately, the amount of degradation is difficult to quantify exactly, although it is expected that the Monte Carlo simulation will generally predict the resolution of the detector to be too good. If the angular resolution is worse than predicted, the effective area would be smaller, as the number of events falling into the signal bin is reduced. This effect would increase the calculated integral flux. Although this is true, if the angular resolution were known to be worse, a larger bin size would be used in the analysis retaining a larger number of the events. This larger bin size would lead to an increase in the effective area because of the higher percentage of events retained, thereby reducing the reported integral flux. As discussed earlier, this possible larger bin size is somewhat motivated by the higher detected significances at larger bin sizes, as shown in Figure 5.9, which suggest that the selected bin size is too small. To first order, these effects largely offset each other in terms of the effective area. However, the number of excess events detected would increase with the larger

bin size as shown in Figure 5.8.[11] As can be seen, an increase in bin size of ∼20% increases the excess by ∼40%. This increased excess, utilizing the same effective areas, would correspondingly increase the value for the differential flux normalization, as well as the integral flux, since $I_\circ$ is directly proportional to the detected excess.

To illustrate this effect, a simple approximation which degrades the angular resolution was made and the effects explored. For each Monte Carlo gamma-ray shower that passed the angle fitter, the difference between the true direction and fit direction, Δ_{angle}, was made a constant percentage worse. The optimal bin size and N_{fit} cut analysis were performed again with the degraded resolution. The resulting optimal bin size is shown in Table 5.6 for various amounts of degradation. For each case the ideal N_{fit} cut is 40 PMTs. Utilizing the appropriate value for the bin size, along with the corresponding degraded angular resolution, the effective area was determined for each case. The effective area for each variation in the amount of degradation is shown in Figure 5.14. As can be seen the different cases are indistinguishable, confirming that the effective area remains unchanged.

The excess of events detected from the direction the Crab Nebula with these new optimal bin sizes were found and shown in Table 5.6. Utilizing the spectral index of $\alpha = 2.59$, the integral flux above 1 TeV is determined for these new excess values and appropriate effective areas.[12] The results are shown in Table 5.6. As can be seen, the integral flux increases as the resolution is degraded until values of degradation of 30% or more, after which the flux is consistent within errors. While these results are suggestive of a systematic effect in the angular resolution, the increase in integral flux could be solely from opening up the bin size. To see if this is the case, the effective areas were calculated using the bin size indicated by analysis utilizing the degraded resolution, while keeping the resolution unchanged (no degradation). Using these effective areas as well as the results from the analysis of the Crab excess, new integral fluxes were calculated and are shown in Table 5.6. Although the effect is smaller, an increase in the integral flux from only opening up the bin size is also seen. Again, the values are consistent within errors of being the same for the largest bin sizes. No increase would be found if the Monte Carlo simulations correctly predicted the angular resolution. Although a higher significance, excess, and flux is found at larger bin

[11] The higher excess and significance at larger bin sizes is also seen in the detection of Mrk 421 and is discussed in Appendix C.

[12] For the standard analysis, that of no degradation, the N_{fit} cut is increased to 40 PMTs to keep the cut consistent. Monte Carlo simulations, detailed in the previous chapter, predict that this should have a negligible effect on the significance found, which is the case. The flux is calculated with the appropriate effective area and is consistent with the result using an N_{fit} cut of 20 PMTs.

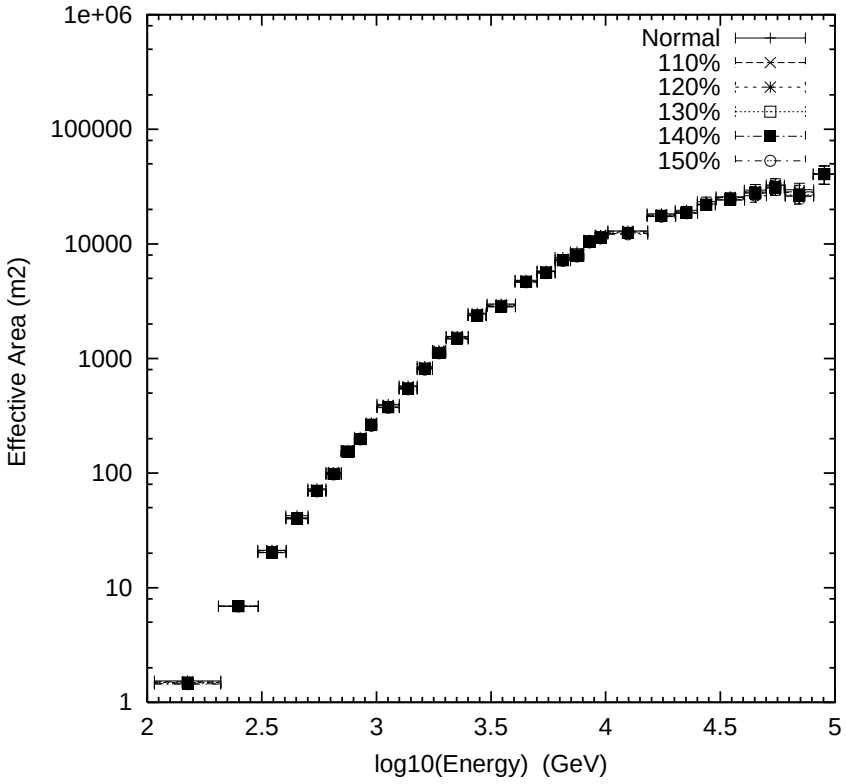

Figure 5.14: Plot of the effective area versus energy utilizing the degraded angular resolution as well as the optimal bin size and N_{fit} cut determined for those degraded resolutions. As can be seen the values are indistinguishable.

sizes, the integral flux is further increased when it is assumed that the resolution is degraded. This effect is illustrated in Figure 5.15, where the integral fluxes, are shown versus bin size with and without the angular resolution being degraded in the determination of the effective areas.

Degrade (%)	**r**	**Excess Events**	σ	**Degradation** $I(\geq 1\,TeV)$ $\times 10^{-12}$ **cm**$^{-2}$ **s**$^{-1}$	**No Degradation** $I(\geq 1\,TeV)$ $\times 10^{-12}$ **cm**$^{-2}$ **s**$^{-1}$
0	1.2°	5725 ± 1183	4.8	13.8 ± 2.9	13.8 ± 2.9
10	1.3°	6596 ± 1284	5.1	16.1 ± 3.2	14.8 ± 2.9
20	1.4°	7619 ± 1387	5.5	18.8 ± 3.4	16.1 ± 2.9
30	1.5°	8749 ± 1490	5.9	21.8 ± 3.7	17.6 ± 3.0
40	1.6°	8608 ± 1594	5.4	21.7 ± 4.0	16.6 ± 3.1
50	1.7°	8886 ± 1698	5.2	22.5 ± 4.3	16.5 ± 3.2

Table 5.6: Table showing optimal bin size, r, determined using an angular resolution, degraded by the indicated percentage, in the Monte Carlo simulations. Also shown are the values of the excess detected from the Crab Nebula using these bin sizes and their corresponding ideal N_{fit} cut of 40 PMTs. The integral flux greater than 1 TeV from the Crab Nebula for these excess values, utilizing the spectral index of $\alpha = 2.59$, is also shown for the cases where the predicted angular resolution of Milagro is ("Degradation") and is not ("No Degradation") increased by the constant percentage in the determination of the effective area.

Clearly the results of degrading the predicted angular resolution and reanalyzing the data with the new optimal bin size dictated by this have a substantial effect on the final result. As this is a significant and plausible effect, it is hypothesized that the Monte Carlo simulations predict too good an angular resolution of Milagro, resulting in too low an integral flux. The flux becomes approximately independent of bin size for bins larger than 1.4° or 1.5°, suggesting a degradation of 20–30% in the data. While plausible, independent confirmation that the angular resolution is in fact worse from another analysis is required for these flux values to be reported as the final results. Therefore, the results of this study are only suggestive and indicate a systematic error on the calculated integral flux of $\sim$45% in the increasing direction.

5.5.4 Systematic Error in the Absolute Energy Scale

A systematic error arises in the integral flux determined from the uncertainty in the absolute energy scale of Milagro. The differential flux normalization calculated

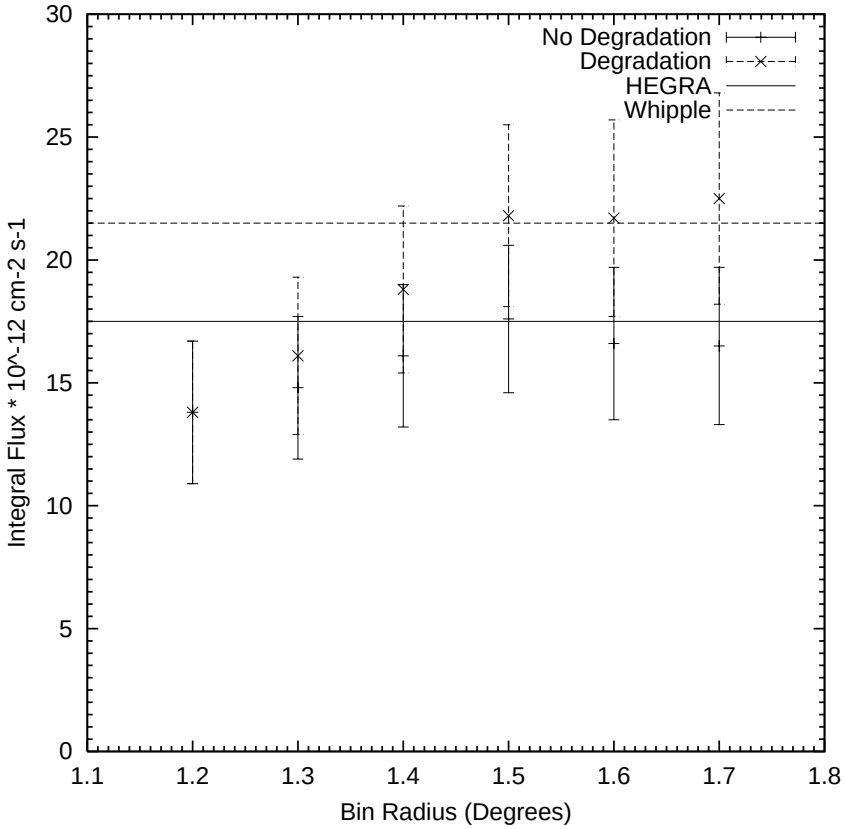

Figure 5.15: Plot of the integral flux greater than 1 TeV from the Crab Nebula versus bin size, with and without degradation in the angular resolution utilized in the effective area determination. The points represent the values determined using the HEGRA spectral index of $\alpha = 2.59$. Each of the points are $\sim$5.5% lower if the Whipple spectral index of $\alpha = 2.49$ is used instead. The bin radii shown correspond to the optimal bin sizes determined by an analysis utilizing the degraded resolution. The case of 1.2 degrees corresponds to the optimal bin with no degradation, 1.3 degrees to 10% degradation, 1.4 degrees to 20% degradation, 1.5 degrees to 30% degradation, 1.6 degrees to 40% degradation and 1.7 degrees to 50% degradation. For comparison, the solid line represents the value reported by HEGRA of $(17.5 \pm 3.2) \times 10^{-12}$ cm^{-2} s^{-1}. The dashed line represents the value reported by Whipple of $(21.5 \pm 4.3) \times 10^{-12}$ cm^{-2} s^{-1}.

for the Crab is normalized to 3 TeV. If what the simulations refer to as 3 TeV is actually 2.7 TeV or 3.3 TeV, a large systematic error arises. The absolute energy scale can be determined using the displacement of the cosmic ray moon shadow (Wascko, 2001). A preliminary estimate of the energy scale from the Moon shadow observed by Milagro indicates the median cosmic ray energy of 640 ± 70 GeV (Samuelson, 2002). This value is in agreement with the results of simulations which predict a median proton energy of 690 GeV. However, the statistical error (11%) in the median cosmic ray energy contributes a +35%/-24% error to the determination of the integral flux.

5.5.5 Total Systematic Error

The effects of all the previously mentioned systematic errors combine. All the estimated individual contributions are added in quadrature, with the exception of the effect of the degraded angular resolution resulting in a total systematic error of $\pm 45\%$. Once the effect of a possible degraded resolution is included, by adding it in quadrature with the previous total, the total systematic error is +65%/-45%.

5.6 Comparison of Crab Flux to Other Observations

Since the Crab Nebula has been successfully observed by many other instruments in the energy range to which Milagro is sensitive, it is useful to compare the results reported from those instruments. What is generally reported is the differential flux normalization and spectral index of the Crab from the detection by a particular instrument. This makes comparison complicated since the energy to which the flux is normalized varies as the median energy of observation by those instruments differs. Therefore, the integral flux above a certain energy is generated from the reported differential flux normalization for detections by 4 instruments. These are Whipple (Hillas et al., 1998), HEGRA (Aharonian et al., 2000), CANGAROO (Tanimori et al., 1998b), and Tibet (Amenomori et al., 1999). Since the integral flux from the Crab Nebula is typically reported above 1 TeV, it is calculated from this value up to 100 TeV for the respective spectral index reported by the other instruments using Eq. 4.19. The reported differential flux normalization, spectral index, median energy, as well as the resulting integral flux values are shown in Table 5.7. Table 5.8 shows the values generated from the observations by Milagro utilizing the same spectral index of the detections by other instruments, as well as how those values compare. As can be seen in the tables, the results for Milagro are lower than those reported by the other instruments,

but, with the exception of Tibet, within the errors. Therefore, the observations of the Crab Nebula by Milagro are consistent with expectations, meaning that the flux obtained by Milagro for other sources can be considered accurate.

Instrument	$I_\circ \times 10^{-12}$ **TeV**$^{-1}$ **cm**$^{-2}$ **s**$^{-1}$	$E_\circ$ **(TeV)**	α	**I(≥1 TeV)** $\times 10^{-12}$ **cm**$^{-2}$ **s**$^{-1}$
HEGRA	$27.9 \pm 0.2 \pm 5$	1.0	2.59±0.06	17.5 ± 3.2
Whipple	$32.0 \pm 1.7 \pm 6$	1.0	2.49±0.07	21.5 ± 4.3
CANGAROO	0.201 ± 0.036	7.0	2.53±0.18	18.0 ± 5.3
Tibet	4.61 ± 0.90	3.0	2.62±0.17	50.6 ± 10.7

Table 5.7: Table showing the differential flux normalization, energy to which the flux was normalized (median energy), spectral index, and calculated integral flux greater than 1 TeV from the Crab Nebula as detected by various instruments sensitive to TeV gamma-rays.

Comparison Instrument	α	**I(≥1 TeV)** $\times 10^{-12}$ **cm**$^{-2}$ **s**$^{-1}$	**Ratio** $\frac{I_{Milagro}}{I_{Comparison}}$	**Deviation** σ
HEGRA	2.59	$13.7 \pm 2.9\ ^{+8.9}_{-6.2}$	0.78	0.4
Whipple	2.49	$13.0 \pm 2.8\ ^{+8.5}_{-5.9}$	0.61	0.9
CANGAROO	2.53	$13.3 \pm 2.8\ ^{+8.6}_{-6.0}$	0.74	0.5
Tibet	2.62	$13.4 \pm 2.9\ ^{+8.7}_{-6.0}$	0.28	2.6

Table 5.8: Table showing the integral flux greater than 1 TeV from the Crab Nebula from the Milagro results utilizing the spectral index determined by various instruments. For comparison, the ratio of integral fluxes reported and the significance of the disagreement is shown as well.

Comparing the results of other instruments to the increased flux using a degraded angular resolution, is also useful in determining how much the angular resolution is degraded from the predictions of Monte Carlo simulations. As can be seen in Figure 5.15, the integral flux is in good agreement with the value from HEGRA of $(17.5 \pm 3.2) \times 10^{-12}$ cm^{-2} s^{-1}, for values of the degradation between 10% and 20%. Comparison with the integral flux from Whipple of $(21.5 \pm 4.3) \times 10^{-12}$ cm^{-2} s^{-1} shows that better agreement is reached at values for the degradation of about 30%. This observation further strengthens the case that the angular resolution is predicted to be too good by the Monte Carlo simulations.

5.7 Crab Results for AGN Study Subset

As mentioned in Chapter 4, the 27 selected AGN are studied over a different interval in time than the Crab. This is due to the lack of the ability to perform the background rejection technique in the data reconstructed online for the first year of Milagro data taking. Further, improvements to the detector's sensitivity were made during the AGN study. The improvements are the result of changes in the online reconstruction algorithms (factor of $\sim$1.4 increase in sensitivity expected), as well as the PMT calibration (expected improvement cannot be quantified). Since raw data existed for the Crab Nebula, this data was re-reconstructed using these improvements. There is no corresponding raw data from the AGN. Therefore, the previously discussed analysis of the Crab should not be used as an indicator of the sensitivity of Milagro during this interval. For a direct comparison, the Crab Nebula must be analyzed utilizing the same information (online reconstruction) as the AGN study. This will enable statements as to the sensitivity and overall quality of the AGN study. As mentioned in Chapter 4, the AGN data set is 558.0 days in length, with a duty cycle of 90%, corresponding to an effective exposure of 499.3 days. The improved version of the reconstruction algorithms were installed after the first 125.5 days of exposure, and the improved PMT calibration is utilized after the initial 289.5 days of exposure.

5.7.1 Overall Results

During the 499.3 days of exposure, 1,011,921 events were observed in the bin centered on the Crab Nebula. After determining the corrected number of background events expected in the signal bin, this corresponds to an excess of 3484 ± 1039 events or 3.4σ. This result implies a sensitivity to the Crab during this data set, given by Eq. 5.1, of 2.9σ per year of ideal exposure(100% duty cycle). This sensitivity is less than the previously reported result of 3.4σ per year due to the upgrades in the reconstruction algorithms and PMT calibration utilized to study the Crab, and not due to any differences in the analysis technique. The same time scale analysis previously discussed of the excess versus time from the Crab Nebula was performed over the AGN study data set as well, the results of which indicate that the excess from the Crab Nebula is accumulated in a manner that is consistent with being constant in time for time scales longer than 100 days. Therefore, any analysis of the AGN data set can be considered stable in time.

5.7.2 Comparison of Reconstruction Methods

As comparison of the online data set to the re-reconstructed data set is useful for many reasons, the results from the Crab Nebula for both the online reconstruction and re-reconstruction are analyzed. The effects of the re-reconstruction are shown for the whole AGN data set, as well as 2 interesting sub-intervals during this time in Table 5.9. The first sub-interval is the portion of the data set prior to the improved core location algorithm and the different curvature correction being installed. The second is the interval immediately following the first, which utilizes the improved core location algorithm and different curvature correction, but is prior to the use of an improved PMT calibration online. After the installation of the improved PMT calibration, the online reconstruction is equivalent to the re-reconstruction, and no comparison is necessary. As can be seen, utilizing the re-reconstructed data for analysis on the Crab Nebula results in a higher significance being found. This verifies the claims that the changes in the algorithms improved the sensitivity of Milagro. The results show that the improvement in significance comes from the use of the new core fitting technique and different curvature correction, whereas the effect of the new PMT calibration[13] actually decreases the significance slightly, although the decrease in significance in the second interval is statistically insignificant. While this information is helpful in demonstrating the effects of the re-reconstruction, the 2 sub-intervals are short in length, which does not allow for strong conclusions to be drawn.

Reconstruction Differences	**Exposure (Days)**	**Online Significance**	**Re-reconstructed Significance**
Core Finder, Curvature Corr., Calibrations	125.5	2.2σ	3.3σ
Calibrations	164.0	1.8σ	1.5σ
None	209.8	1.9σ	1.9σ
Various	499.3	3.4σ	3.8σ

Table 5.9: Table showing the effects of re-reconstructing the raw data from the direction of the Crab Nebula. The 499.3 day exposure represents the entirety of the AGN study data set.

[13]The effect of re-reconstructing, using the improved PMT calibration, a small set of raw data from Mrk 421 is discussed in Appendix C. For reasons provided in the discussion, this re-reconstructed data are not used in any of the analysis.

5.7.3 Crab Flux Determination

Utilizing the detected excess and cumulative zenith angle exposure, shown in Figure 6.13, of the Crab Nebula during the AGN study interval, the differential flux normalization of the Crab Nebula during this data set is found to be $(1.11 \pm 0.33\ ^{+0.72}_{-0.50}) \times 10^{-12}$ TeV^{-1} cm^{-2} s^{-1} from Eq. 4.18. The differential flux is normalized to the median energy of 3 TeV with a spectral index of $\alpha = 2.59$ reported by HEGRA. As mentioned previously, the choice of spectral index has an insignificant effect on the differential flux normalization as it is normalized to the median energy. This is true as long as the spectral index is reasonably close to the value chosen for the integral flux determination. The resulting integral flux above 1 TeV, is determined to be $(12.0 \pm 3.5\ ^{+7.8}_{-5.4}) \times 10^{-12}$ cm^{-2} s^{-1}. The same systematic errors (+65%/-45%) discussed in Section 5.5.5 are included in these results. The measured flux is lower than the value determined using the re-reconstructed data over a longer time interval, which was reported earlier to be $(13.7 \pm 2.9\ ^{+8.9}_{-6.2}) \times 10^{-12}$ cm^{-2} s^{-1}. While lower than the previously reported result, this value is still in statistical agreement with what was determined earlier. Further, the effects of the Monte Carlo simulations predicting the angular resolution to be better than actual, are likely more severe in the AGN study than in the re-reconstructed data for the Crab because the improved PMT calibration was not available for the initial 58% of the exposure in this sample. While the effects are impossible to simulate, it is expected that a calibration that is of lower quality would degrade angular resolution further.

Although an improved version of the reconstruction algorithms was installed after the initial 25% of exposure in this data set, the effects are not the reason for the discrepancy between the Crab flux reported from the entirety of Milagro data taking and the AGN study. This is because the different effective area of the initial fraction of the data sample was accounted for. As previously discussed, the changes implemented after the first part of the data, an improved core fitter and different curvature correction, resulted in an increase in sensitivity by a factor of $\sim$1.4. To account for this, the effective area was generated for the less sensitive reconstruction and utilized accordingly. Figure 5.16 shows the effective area versus energy for both versions of the reconstruction. As can be seen the effective area is less for the initial reconstruction algorithms as expected. The final 75% of the exposure in the AGN data set were reconstructed with the same improved algorithms used in the re-reconstruction of the data from the Crab Nebula. Therefore, the effective area for the improved algorithms is utilized for this part of the data. To account for the different effective areas, the sum over time in Eq. 4.18 is broken into 2 parts, each utilizing the the appropriate effective areas and exposures.

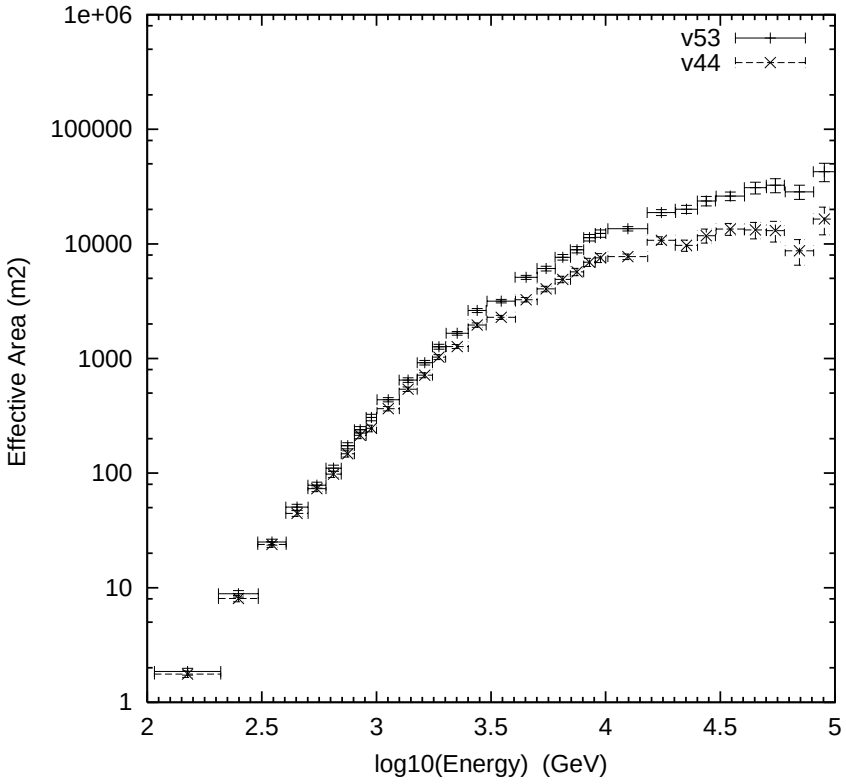

Figure 5.16: Plot of the effective area versus energy for both versions of the online reconstruction algorithms. As can be seen the values utilizing the improved algorithms (v53) are higher than those with the initial algorithms (v44).

Chapter 6

Results of Search for TeV Gamma-Ray Emission from Selected AGN

Several AGN have been detected at TeV energies by a variety of observatories. The emission from these objects is highly variable and characterized by flaring behavior, where the flux increases dramatically on small time scales. The high duty cycle (∼95%) and wide aperture (∼2 sr) of Milagro allow for the detection of flaring behavior associated with TeV AGN, even during daytime transits. This chapter presents results of a search for TeV emission from 27 candidate AGN with Milagro. The AGN Mrk 421 was detected in this search with Milagro during its flare in 2001. A detailed analysis of the signal from Mrk 421, including the measured flux value during this flare, is presented. Upper limits on the flux are found for the non-detected AGN and compared to other published values when possible. These upper limits are shown to be consistent with expectations for AGN previously detected at TeV energies, competitive with those from other observatories, and useful for constraining models of TeV AGN.

6.1 Overall Results

A search for emission from 27 selected AGN was performed using Milagro. These AGN were selected as likely candidates to be sources of TeV photons using criteria described in Chapter 2. As discussed in Chapter 4, the data interval during which the search was performed is 558.0 days in length, where Milagro operated with a duty cycle of 90%, giving an effective exposure of 499.3 days. While some motivation was provided in Chapter 5 for increasing the bin size utilized in the

analysis, the standard analysis was performed on the position of each of the 27 candidate AGN. This consists of using a round source bin of 1.2 degrees radius, and data cuts keeping only events with $N_{fit} \geq 20$, $X_2 \geq 2.5$, and fit zenith angle, $\theta \leq 45$ degrees. As discussed in Chapter 5, the Crab Nebula was observed by Milagro with a significance of 3.4σ during this time using this standard analysis. Further, it was shown using the detected signal from the Crab, that the detector operated in a stable manner during this time period. Having addressed the general sensitivity and stability of the study, the results are presented.

Figure 6.1 shows a histogram of the detected significance at the position of each of the candidate AGN. As can be seen in the figure, only one of the AGN, Mrk 421, was detected by Milagro during this interval. The distribution of the 26 remaining significances reasonably follows the distribution that would be expected, with $\sim$2/3 (58%) of the significances being found within $\pm 1\sigma$, and the remainder being less than $\pm 2.2\sigma$.

Although the detection of Mrk 421 is strong, the fact that a search for an excess was performed at the positions of 27 AGN needs to be addressed. Therefore, the probability that a 4.0σ effect would be observed in 27 attempts, assuming a Gaussian distribution of probabilities, must be calculated. This trials corrected significance is 3.1σ. Therefore it can be stated that Milagro detected Mrk 421 during the data interval studied, while no significant excess was found for the other 26 AGN. Table 6.1 shows the detected excess and significance of that excess in the bin centered on the positions of each of the 27 AGN. An interesting note is that 2 of the 3 highest significances, not including Mrk 421, come from AGN, Mrk 501 and 1ES2344+514, which have been detected previously by other TeV observatories. While this suggestive that Milagro may be seeing the TeV emission from these sources, the level of significance found is well below that which can be claimed as a detection. On the other hand, 1ES1426+428 was observed by Whipple (Horan et al., 2002) and HEGRA (Aharonian et al., 2002a) to have flared at TeV energies during the data interval analyzed, yet the significance found is among the smallest of all the AGN observed.

6.2 Mrk 421

6.2.1 General Results

Since Mrk 421 was detected in the sample of AGN, a thorough analysis of the excess is performed. During the time interval studied, $N_{on} = 1,406,842$ events were observed in the bin centered on the position of the Mrk 421. The corrected number of background events expected from the time sloshing technique

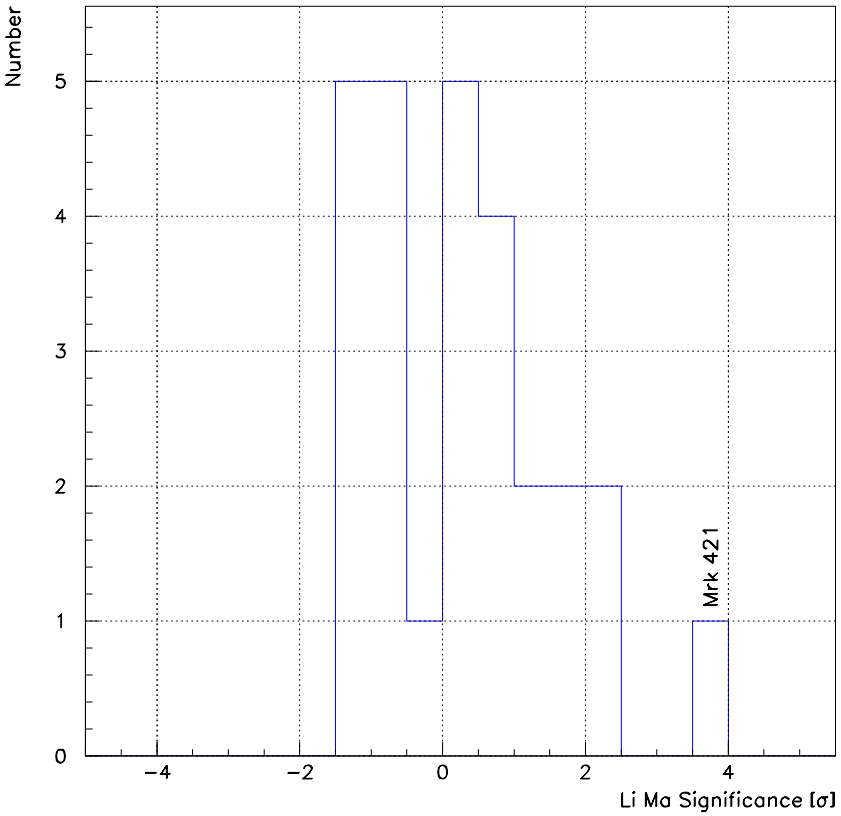

Figure 6.1: Distribution of significance found in the bin centered on the position of each of the 27 candidate AGN.

Nominal Coordinates	Name	Class	z	Excess	Sig. σ
1101+384	Mrk 421	XBL	0.031	4855 ± 1225	4.0 σ
1426+428	1ES	XBL	0.129	-1382 ± 1211	-1.1 σ
1652+398	Mrk 501	XBL	0.034	2197 ± 1230	1.8 σ
1959+650	1ES	XBL	0.048	-199 ± 758	-0.3 σ
2344+514	1ES	XBL	0.044	2411 ± 1088	2.2 σ
0033+595	1ES	XBL	0.086	-1167 ± 903	-1.3 σ
0110+418	RGB	XBL	0.096	1468 ± 1220	1.2 σ
0152+017	RGB	XBL	0.080	516 ± 487	1.1 σ
0153+712	RGB	XBL	0.022	-380 ± 577	-0.7 σ
0214+517	RGB	XBL	0.049	14 ± 1086	0.0 σ
0314+247	RGB	XBL	0.054	-665 ± 1090	-0.6 σ
0656+426	RGB	XBL	0.059	-1545 ± 1213	-1.3 σ
1133+704	Mrk 180	XBL	0.046	-327 ± 608	-0.5 σ
1532+302	RGB	XBL	0.064	-962 ± 1180	-0.8 σ
1610+671	RGB	XBL	0.067	164 ± 702	0.2 σ
1727+502	I Zw 187	XBL	0.055	-613 ± 1116	-0.5 σ
1741+196	1ES	XBL	0.083	2105 ± 981	2.1 σ
2321+419	1ES	XBL	0.059	-1228 ± 1215	-1.0 σ
2322+346	RGB	XBL	0.098	2205 ± 1220	1.8 σ
0010+106	III Zw 2	FSRQ	0.090	651 ± 752	0.8 σ
0138+398	B2	FSRQ	0.080	-1417 ± 1228	-1.2 σ
0321+33	B2	FSRQ	0.062	91 ± 1216	0.1 σ
1413+436	RGB	FSRQ	0.090	142 ± 1202	0.1 σ
2209+184	PG	FSRQ	0.070	837 ± 955	0.9 σ
1219+285	W Comae	RBL	0.102	129 ± 1147	0.1 σ
1807+698	3C371	RBL	0.051	377 ± 622	0.6 σ
2200+420	BL Lac	RBL	0.069	609 ± 1212	0.5 σ

Table 6.1: Table showing the detected excess and significance of that excess for the bin centered on the positions of all the 27 candidate AGN.

is $N_{Bcorr} = 1,402,288$. This corresponds to an excess of 4855 ± 1225 events, or a significance calculated by Eq. 4.10 of 4.0σ. Using Eq. 5.1, with $\sigma_{obs} = 4.0$ for $t_{total} = 1.37$ years, the observed significance implies a sensitivity of 3.4σ per ideal year of exposure. Given the flaring nature of Mrk 421, this is not a reasonable statement as it implies a constant flux from the source over a full year. Although unrealistic, the sensitivity implied does elucidate the strength of the Mrk 421 signal in the data set and is useful for comparison to the strength of the signal from the Crab Nebula during this time (2.9σ per year from the comparable analysis as described in Section 5.7). As can be seen the emission from Mrk 421 is detected at a higher level of significance than the Crab during this time. This does not necessarily imply a higher average flux over the length of the data set as the zenith angle exposure of these sources in Milagro, shown in Figure 6.13, differs dramatically.

6.2.2 Time Scale Analysis

Given the highly variable nature of the flux from AGN at TeV energies, a time scale analysis of Mrk 421 is undertaken to determine if the excess was accumulated in a manner that is consistent with being constant over the data set, or if the majority of it was accumulated in some short interval. Utilizing the actual daily exposure of Milagro along with the expected significance for that cumulative exposure given by Eq. 5.1, one can view how the significance was accumulated versus what is expected for a constant signal. This is shown in Figure 6.2. As this is a plot of cumulative significance, neighboring points are highly correlated. Further, the expected significance is approximated. This is because only the total exposure for each particular day is considered, where the actual position in the sky of the Mrk 421 is ignored. Given that the effective area for Milagro depends heavily on zenith angle, and the presence of a zenith angle cut in the data, using the total exposure for a given day can be problematic for short time scale evaluations. While the expected significance is only an approximation, the value should be reasonably accurate after a few accumulated days since the zenith angle effects of down time would eventually average out.

As can be seen in Figure 6.2, the cumulative excess observed does not agree well with what is expected for a constant signal in the early part of the data set. The level of significance found for Mrk 421 is essentially none for the first 150 days, after which a sharp increase is observed for the next 150 days, followed by a period where the significance increases slightly for the remainder of the data set. This suggests that Mrk 421 was relatively quiet for much of the data set, but experienced a flare during part of the data interval studied. This flaring notion is supported by the observations from several other TeV observatories which showed

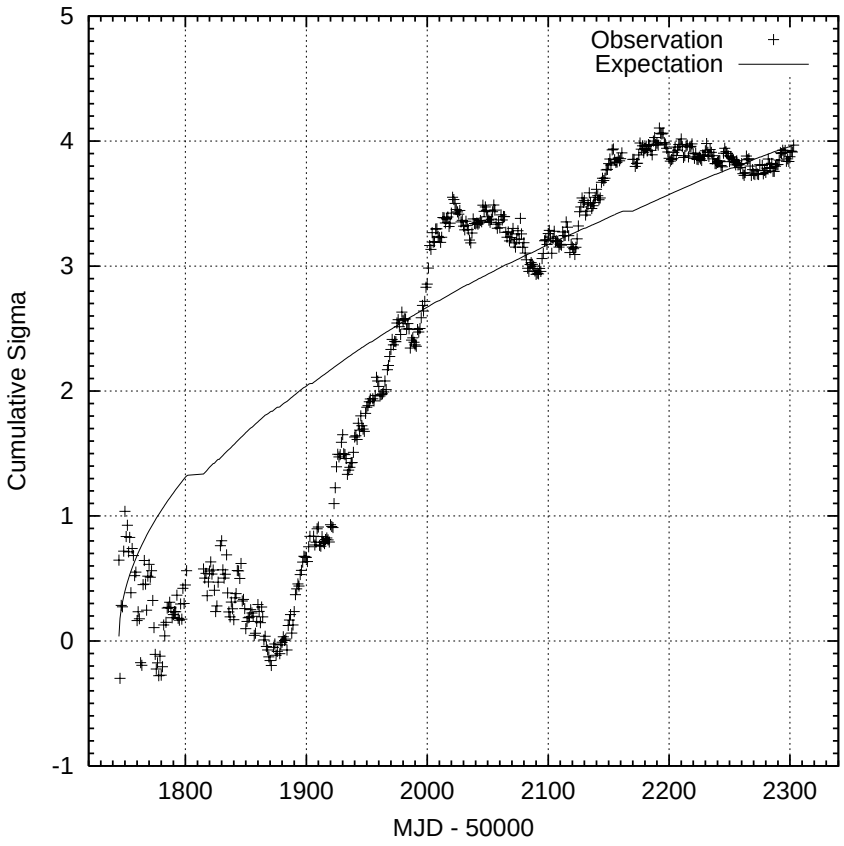

Figure 6.2: This figure shows how the significance observed for the bin centered on Mrk 421 accumulated versus time. Also shown is what would be expected for a constant signal given the sensitivity implied by this observation and the true exposure of each date. Neighboring points are highly correlated.

that Mrk 421 did experience a flare during the time period studied. An interesting note is that the cumulative significance increases dramatically at almost the exact same time that an improved core fitter and curvature correction were installed in the online reconstruction (MJD 51894). As discussed previously, these changes were expected to increase the sensitivity of Milagro by a factor of 1.4. Although interesting, the variable nature of the emission from Mrk 421 makes it impossible to state whether these changes directly affected the increase in significance.

Given that observations of Mrk 421 by other observatories showed that it experienced a flare during the data interval, as well as the behavior shown in the cumulative significance plot, a more thorough study of how the excess from Mrk 421 was accumulated versus time was performed. The maximum deviation method, as well as the all possibility method, discussed in Chapter 5, were used to analyze the temporal behavior of the excess found at the position of Mrk 421.

Maximum Deviation Method

Figure 6.3 shows a rolling significance plot for the bin located at the position of Mrk 421 for the 10, 30, and 100-day time scales. Plots of the rolling significances for Mrk 421 on the other 8 time scales are found in Appendix B. From these plots the bins of maximum significance were found for each of the 11 time scales analyzed. The maximum deviation method was not performed for the case of the maximal deviation in the direction of minimum significance. This is because the maximum deviation found, regardless of direction, on all 11 time scales was always in the direction of increasing significance, and because it was shown in Chapter 5 that the method was flawed in the case of decreasing significance. Therefore, the maximum deviation method in essence becomes a flare search from the position of Mrk 421. By analyzing the time bin of maximum significance, the best case scenario for having observed a short-term flare is studied. Table 6.2 shows the maximum significance of excess events found in any time bin for all 11 analyzed time scales, the expected significance for that time scale given the final result from Eq. 5.1,[1] and the significance of the deviation from this expected value. Also shown in the table is the number of independent time bins possible, which represent the minimum number of trials that need to be accounted for in the statistical interpretation of the significance of the deviation. The table also shows the upper limit on the significance of the deviation. This value is an upper limit because only the minimum number of trials are used in the interpretation. The number of trials which should be accounted for is larger than the number of independent bins, because every bin is examined resulting in the actual significance of the

[1] As the exposure during any interval varies, this is only an approximation, and is in fact slightly overestimated due to the duty cycle of Milagro (typically $\sim$95%).

deviation being less than the upper limit indicated. However, the exact number is difficult to determine due to correlations.

Time Scale (Days)	σ **Obs.**	σ **Exp.**	σ **of Deviation**	**No. of Ind. Bins**	**Corrected** σ **of Deviation**
150	5.0	2.2	2.8	5	2.3
100	4.7	1.8	2.9	7	2.2
50	3.7	1.3	2.4	12	1.3
30	3.7	1.0	2.7	20	1.5
21	3.5	0.8	2.6	28	1.2
14	3.7	0.7	3.1	41	1.7
10	3.7	0.6	3.1	57	1.6
7	3.5	0.5	3.1	79	1.4
5	3.4	0.4	3.0	112	1.2
3	3.6	0.3	3.3	181	1.4
1	2.9	0.2	2.7	531	-1.0

Table 6.2: Significances of the maximum deviation from the expectation in the direction of increasing significance for various time scales. Apparent mathematical discrepancies are due to rounding.

While the maximum significance found in some of the longer time scales appear to suggest Milagro could isolate when the flaring behavior observed from Mrk 421 occurred, this is not the case. As can be seen in Table 6.2, none of the time bins with the most extreme deviations in increasing significance from that which is expected for a constant signal are statistically significant after accounting for the number of independent bins in the data sample. Even the most extreme case, an upper limit of 2.3σ for the 150 day time scale, is not significant. This upper limit is further reduced because the number of time scales analyzed needs to be accounted for. Since 11 timescales were analyzed, the probability that a 2.3σ effect would be found given 11 attempts is only 1.2σ. Even if a method were employed to reduce the oversampling in time to a more ideal value as discussed in Chapter 4 (Biller, 1996), i.e. use 1, 3, 10, 30 and 100-day bins only, the most extreme deviation, and upper limit of 2.2σ, for the 100 day time scale would only be 1.5σ after accounting for the 5 time scales. Further, the results represent the most likely possibility of having observed a flare. Naturally if a more average selection of time bins were chosen, the results would be even less significant. Therefore, this method implies that the excess of events from the Mrk 421 is accumulated in a manner consistent with being constant in time. To verify that this assertion

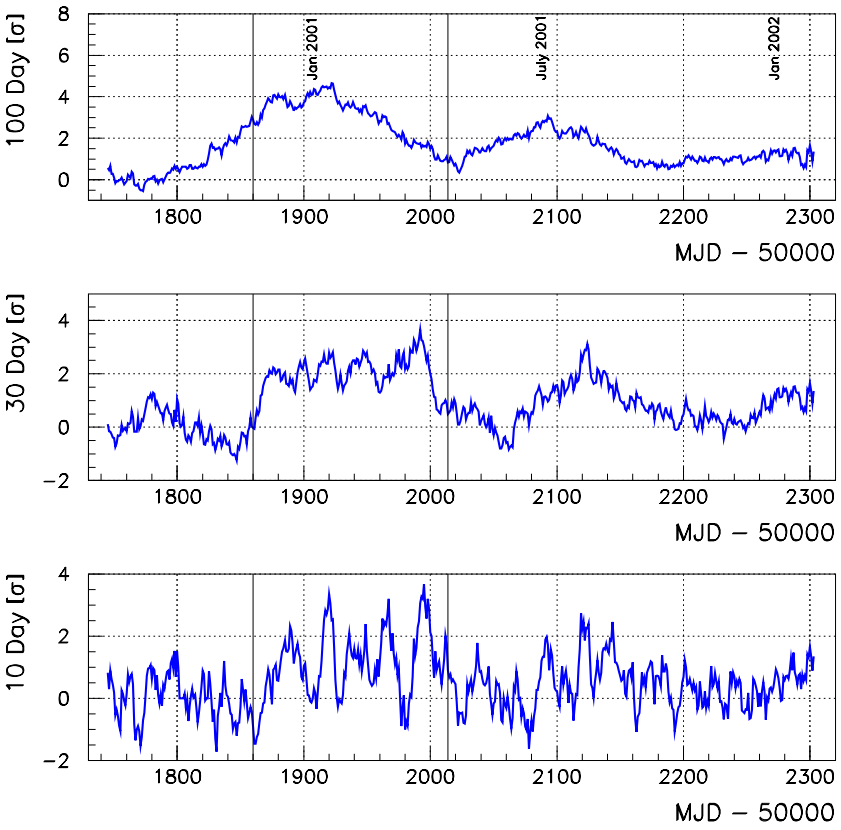

Figure 6.3: This figure shows the rolling significance observed at the bin centered on Mrk 421 versus time for the 10, 30, and 100-day time scales. Entries are plotted according to the *first* day of the interval. Neighboring points are correlated. The 2 vertical solid lines indicate the duration of the flaring period of Mrk 421 as identified using information from the RXTE all-sky monitor. The method for identifying this flaring period is discussed in Section 6.3.1.

is true, the all possibility method discussed in Chapter 5 was also employed to analyze the temporal behavior of the excess from Mrk 421.

All Possibility Method

In this method, the fractional excess versus time observed from Mrk 421 was binned on 11 time scales and analyzed. Since there are a number of ways to independently bin the fractional excess versus time, each variation was studied. For all 11 time scales, the data for each set of bins were fit to a constant and a χ^2 value generated. Figure 6.4 shows the fractional excess versus time from Mrk 421 binned on the 30-day time scale. Plots of the fractional excess versus time for the other 10 time scales are found in Appendix B. The value of the fit constant is shown by the dashed line in each of the figures.

From the resulting χ^2 values for all the possible variations of independent bins, a distribution of corresponding probabilities was generated for each time scale and is shown in Figure 6.5. As can be seen in the figure, the distributions are reasonable. As this is the case, the median probability is therefore a useful indicator of how consistent the temporal distribution of the excess, on average, is with being constant. Therefore, the median χ^2_{red} value is determined for each time scale. This value is characteristic of the most average fit of all the possibilities, and is therefore considered to be the best indicator of the general behavior of the data.

Table 6.3 shows the median probability and corresponding reduced χ^2 resulting from a fit of the fractional excess versus time to a constant for all possible variations of independent bins for each of the 11 time scales. The set of independent bins chosen for Figure 6.4 is the one that corresponds to the median χ^2 probability. As can be seen from the table the median probabilities resulting from fits to the fractional excess versus time are consistent with being constant for all time scales less than 30 days with the exception of the 1 day time scale. As discussed in the previous chapter, stability is not expected on some of the smaller time scales. Minor inconsistencies with constant behavior are found on the 3 largest time scales, suggesting that a flare did occur. However, the significance of these inconsistencies does not allow for the conclusive statement that Mrk 421 experienced a short term (compared to the length of the study) flare during the AGN study. Therefore the signal from the Mrk 421 should be considered to have accumulated in a manner that is consistent with being constant in time.

The methods of analyzing the temporal behavior of the observed excess of events from the direction of the Mrk 421, show no inconsistencies with it being accumulated in a manner that is constant in time. While this is the case, each method is suggestive that a flare did occur on some of the longer time scales (50,

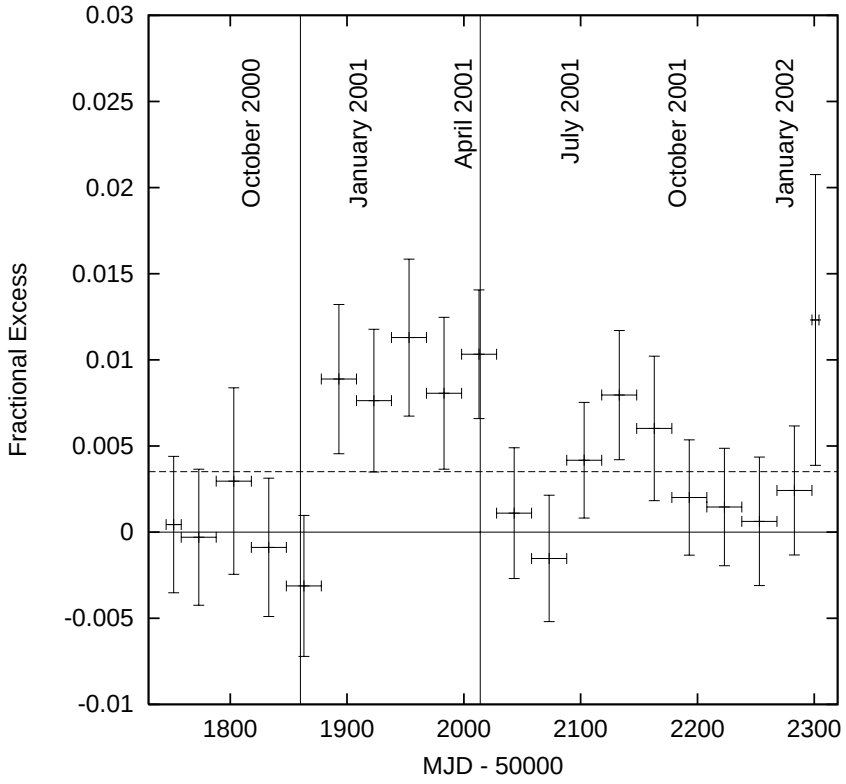

Figure 6.4: This figure shows the fractional excess observed at the position of Mrk 421 versus time for the 30-day time scale. The dashed line is the value resulting from a fit of this information to a constant. The choice of independent bins corresponds to the median χ^2 probability. The 2 vertical lines indicate the duration of the flaring period of Mrk 421 as identified using information from the RXTE all-sky monitor. The method for identifying this flaring period is discussed in Section 6.3.1.

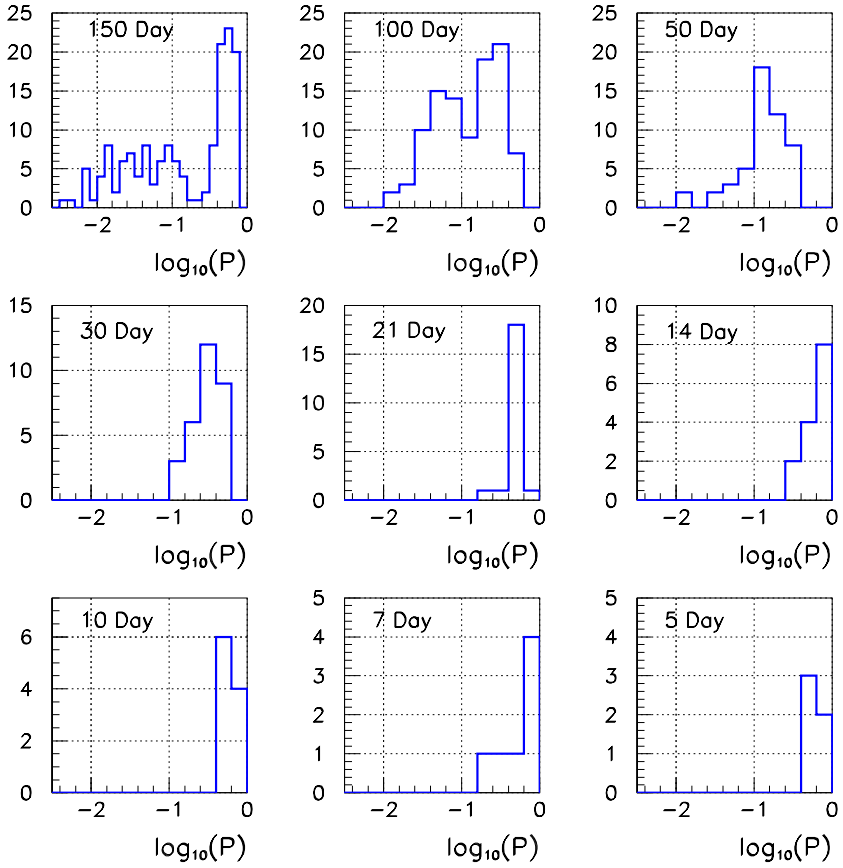

Figure 6.5: This figure shows distribution of probabilities calculated from the χ^2 resulting from fits to all the possible sets of independent bins of the fractional excess versus time from the Crab Nebula. The distributions are for the 9 largest time scales analyzed.

Time Scale (Days)	Reduced χ^2	Degrees of Freedom	Median Probability	Median Fit Excess Value
150	1.49	4	0.20	0.00352±0.00106
100	1.59	6	0.15	0.00359±0.00111
50	1.46	11	0.14	0.00351±0.00106
30	1.14	19	0.30	0.00351±0.00095
21	0.98	27	0.49	0.00365±0.00088
14	0.90	40	0.65	0.00365±0.00086
10	0.96	56	0.56	0.00367±0.00088
7	0.91	78	0.70	0.00363±0.00086
5	0.96	111	0.61	0.00363±0.00088
3	0.98	180	0.56	0.00353±0.00089
1	1.08	530	0.10	0.00318±0.00094

Table 6.3: Table showing the median probability and the corresponding reduced χ^2 resulting from fits to all possible sets of independent bins of the fractional excess versus time for 11 different time scales.

100, 150 days) within the data set. This is verified by observations from other TeV observatories which show Mrk 421 to be dim at TeV energies for parts of the data set, and very bright during other parts. Unfortunately the sensitivity of Milagro is too low to isolate when such a flare occurred in Mrk 421. This only allows for the statement that Milagro observed the recent flare of Mrk 421 during the data set studied, but could not reliably indicate exactly when the TeV flux from Mrk 421 increased dramatically from its quiescent level.

6.3 RXTE Flare Interval for Mrk 421

6.3.1 Identification of the Flare Interval

While emission from Mrk 421 was observed in the Milagro data, it is known from the results of other instruments that the source was not bright in the TeV regime for the full duration of the data set studied. Unfortunately, the results of the time scale analysis of the excess observed from Mrk 421 are only suggestive that a flare occurred within the time interval studied. Due to low statistics, no information can be ascertained from the Milagro data elucidating when the flux, in the TeV energy range, from Mrk 421 increased dramatically. Although this is the case, the results from another instrument can be used to isolate when the source's

flux increased, as well as when the emission returned to the normal quiescent level. After identifying a flare interval, a more sensitive analysis of the emission from Mrk 421 and the response of Milagro to it can be performed.

This flare interval is identified using results from the RXTE all-sky monitor, sensitive to x-rays in the energy range from 2 to 10 keV. The belief that information from this instrument is a useful indicator of the TeV behavior of Mrk 421 stems from observations that flares in the x-ray energy regime have been seen to correlate with those at TeV energies with little or no time delay between the onsets (Buckley, 1999). Therefore, the information about Mrk 421 from this instrument was downloaded from the web site (http://xte.mit.edu) and analyzed. As the RXTE all-sky monitor records data from a particular source in 90 second intervals, known as dwells, only the information from when Mrk 421 was within the field of view of the Milagro detector was utilized. For this study, the field of view of Milagro is defined as when the source's position in local coordinates had a zenith angle, θ, less than 45 degrees. This definition is used because of the cut in the analysis keeping only events with $\theta \leq 45$ degrees in the Milagro data.

Figure 6.6 shows one-day average count rate information from the all-sky monitor for a 6 year period. As can be seen the rate is fairly steady for the bulk of this time period except for parts of 1998, and the period between late 2000 and early 2001. To quantify this statement, Table 6.4 shows the results from a χ^2 fit of this data to a constant for each year of data taking by RXTE, as well as for the whole data set. Given the variable nature of emission from AGN, it is not expected that the count rate will be constant. However, the constant resulting from the fit is a weighted average value for the year, and is therefore a useful indicator of the count rate expected on a typical date. Further, the reduced χ^2 gives information as to which years the AGN was more variable in its x-ray flux.

As can be seen in the table, 1998, 2000, and 2001 are years in which Mrk 421 is more active than in other years. Therefore, the results from 1999 were used as a baseline for the RXTE results in the quiescent state. The term baseline is defined in this case as the average count rate expected in the quiescent state on any given day from the RXTE instrument. Figure 6.7 shows the RXTE one-day average count rate from Mrk 421 for the length of the Milagro data set analyzed in this study. Also shown is the baseline determined by fitting the one-day average count rate in 1999 to a constant.

Using the baseline as the one-day average count rate that one would expect to observe from Mrk 421, the significance of the deviation in the average count rate actually observed is calculated for each date of during Milagro data set analyzed. This significance is shown in Figure 6.8 As can be seen there are more points with positive significance than negative. This is not unexpected as the level of emission is higher during this time than in 1999. To identify the flare interval

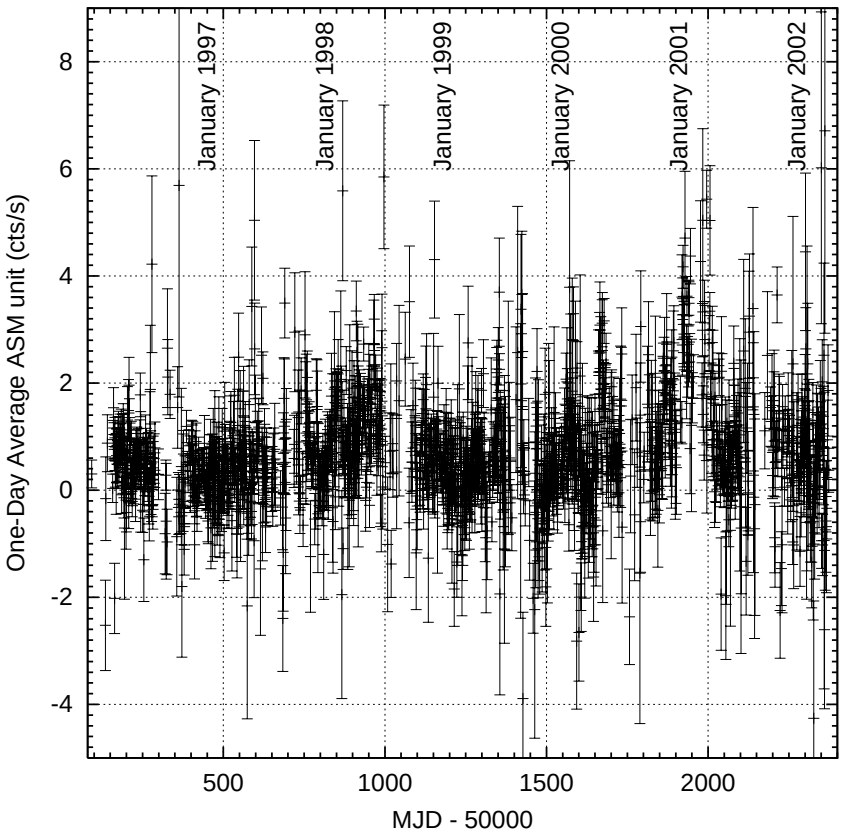

Figure 6.6: This figure shows the 1-day average count rate observed from Mrk 421 by the RXTE all-sky monitor. Only dwells occurring when Mrk 421 was within the field of view of Milagro, $\theta \leq 45$, are utilized in the count rate determination.

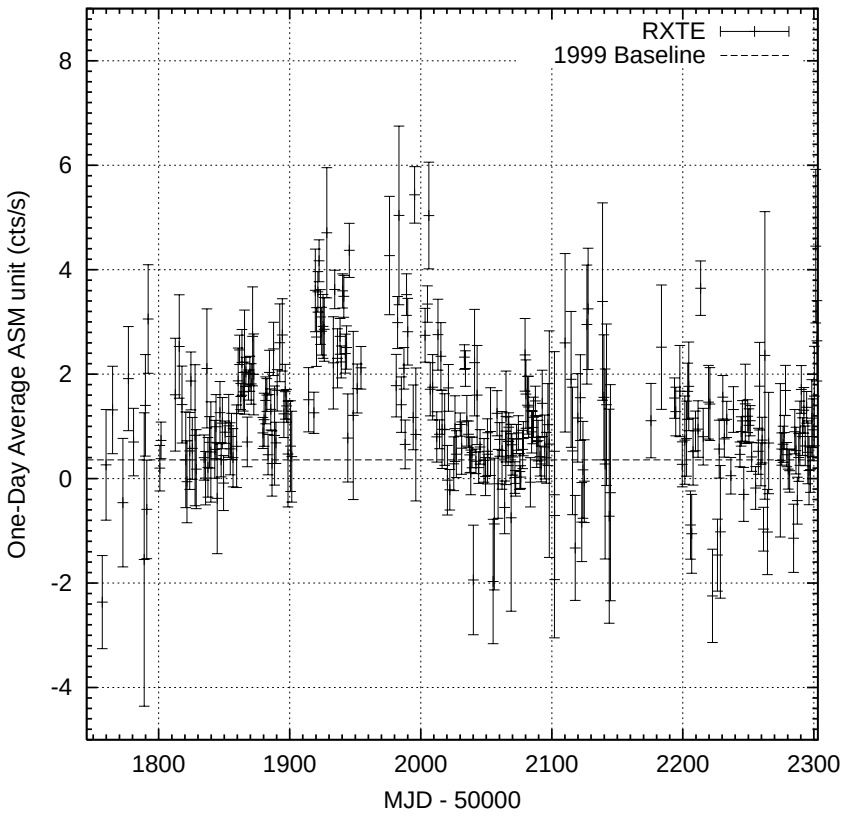

Figure 6.7: This figure shows the 1-day average count rate observed from Mrk 421 by the RXTE all-sky monitor for the duration of the Milagro data set analyzed (7/20/2000 to 1/29/2002). Only dwells occurring when Mrk 421 was within the field of view of Milagro, $\theta \leq 45$, are utilized in the count rate determination. Also shown is the baseline determined from the 1999 RXTE data.

Year	χ^2_{red}	D.O.F.	Fit Value
1996	2.1	184	0.464±0.036
1997	2.1	244	0.466±0.032
1998	3.2	237	0.929±0.043
1999	2.0	255	0.358±0.039
2000	3.3	241	0.863±0.050
2001	6.2	180	1.117±0.084
2002	1.8	85	0.639±0.076
ALL	3.4	1432	0.658±0.019

Table 6.4: Table showing the results from fits to a constant of the 1-day average count rate from the RXTE all-sky monitor. The fits are performed for each year of data taking, as well as the whole data set, utilizing only the information from when RXTE was in the field of view of Milagro.

to be studied by Milagro, only the data points with significance greater than 3σ were considered. Figure 6.9 shows this information for the duration of the Milagro data set analyzed. It is clear from this figure that the flare begins in the RXTE instrument on MJD 51860 and approximately ends around MJD 52014. These dates correspond to November 12, 2000, and April 15, 2001, respectively, and are shown by the vertical lines in the plot. As can be seen there are a few points beyond the stated end of this flare with significance greater than 3σ. However, the density of these points in time is sufficiently small that they are not included in the flare interval. This said, if one views the cumulative significance plot shown earlier in Figure 6.2, it is clear that the significance continues to increase slightly after the end of the flare interval identified. These remaining points above 3σ beyond the end of the flare suggest that this is a real effect and not that of statistical fluctuations.

While it would seem more appropriate to utilize information from instruments sensitive to the same energy range as Milagro for identification of this flare interval, their observations of Mrk 421 are limited. Although this is the case, information from atmospheric Cherenkov telescopes, such as HEGRA, can be used to help in the determination of the flare interval. Shown in Figure 6.10 is the preliminary significance observed by HEGRA from Mrk 421 versus time as reported on their website (http://www-hegra.desy.de/mrk-421). While the data do not begin until after the start of the flare indicated by RXTE,[2] it is clear that Mrk 421 is bright at TeV energies during the suggested flare interval. The end of the flare in Mrk 421 is

[2]Published data from Whipple begin even later.

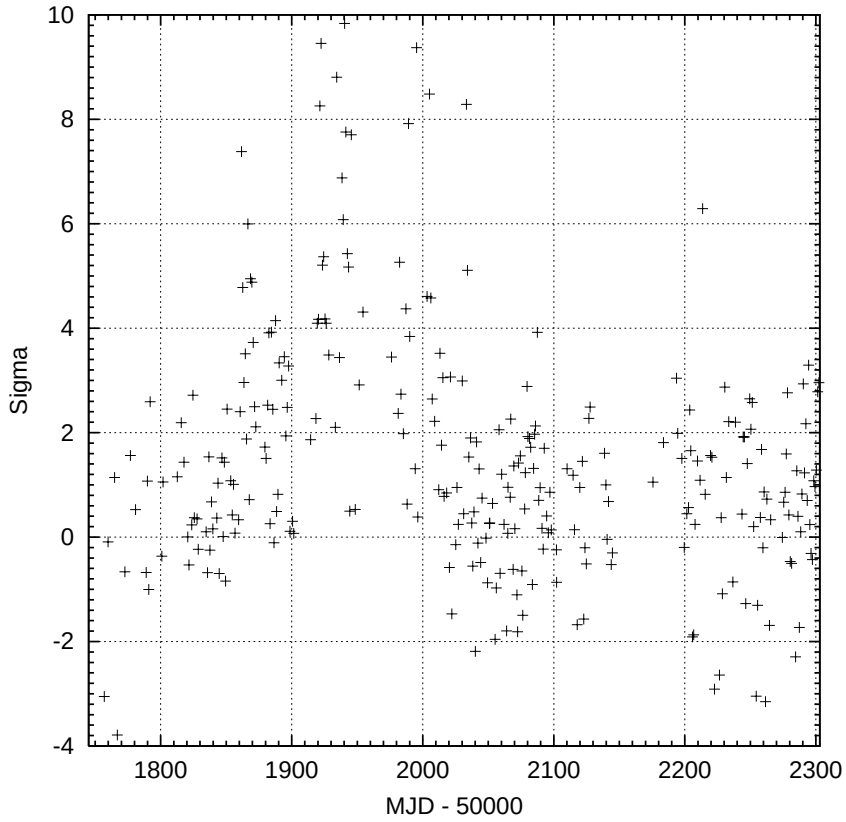

Figure 6.8: This figure shows the significance of the deviation of the 1-day average count rate observed from Mrk 421 by the RXTE all-sky monitor from the baseline determined from the 1999 RXTE data. Only dwells occurring when Mrk 421 was within the field of view of Milagro, $\theta \leq 45$, are utilized in the count rate determination. The data shown corresponds to the information gathered during the period of the Milagro data set analyzed (7/20/2000 to 1/29/2002).

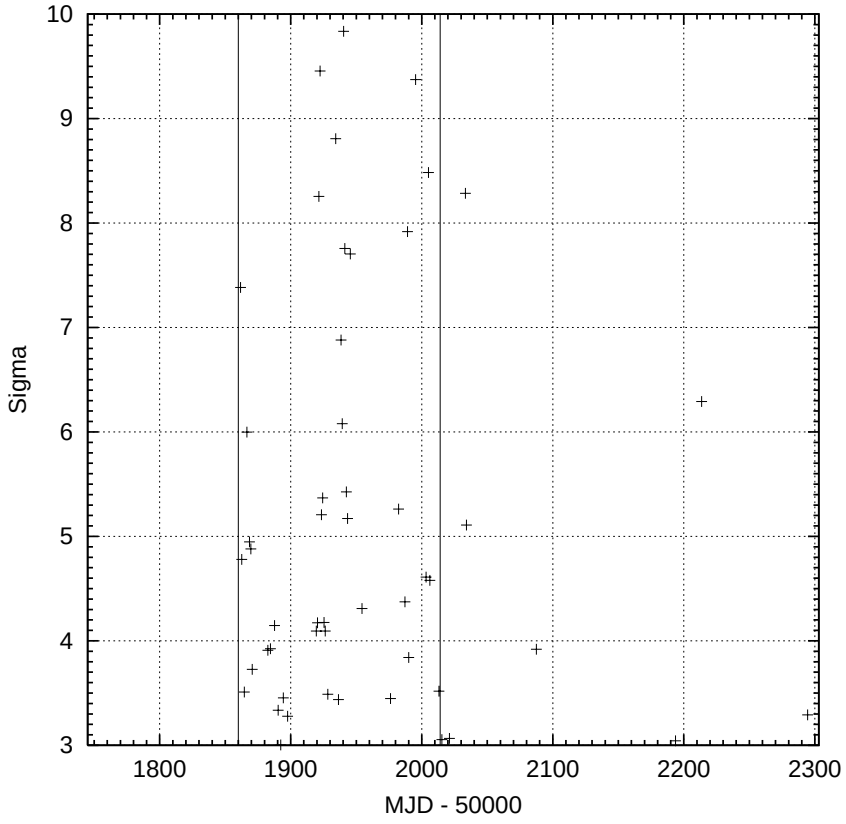

Figure 6.9: This figure shows a close up view of the significance of the deviation of the 1-day average count rate observed from Mrk 421 by the RXTE all-sky monitor from the baseline determined from the 1999 RXTE data. Only dwells occurring when Mrk 421 was within the field of view of Milagro, $\theta \leq 45$, are utilized in the count rate determination. The data shown corresponds to the information gathered during the period of the Milagro data set analyzed (7/20/2000 to 1/29/2002). The solid vertical lines correspond to the flare interval identified from the RXTE information.

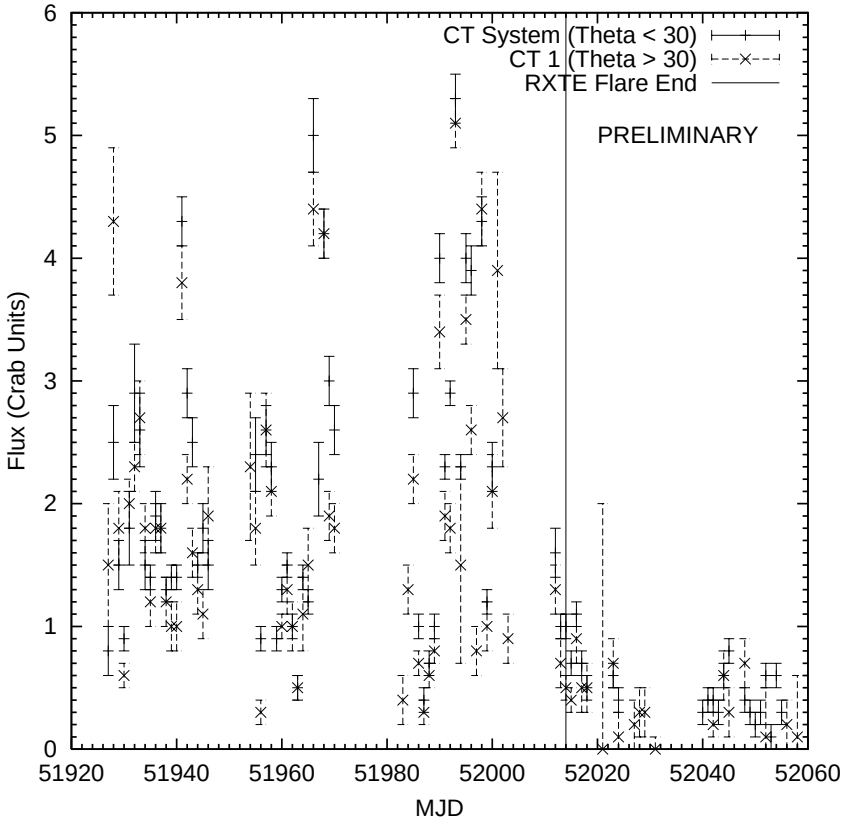

Figure 6.10: This figure shows the preliminary significances versus time of observations by HEGRA from Mrk 421 in early 2001. The vertical line corresponds to the end of the flare state in Mrk 421 as determined from RXTE all-sky monitor data.

seen in the HEGRA data as well. The observed end agrees with that determined from the RXTE instrument, shown as the vertical line in Figure 6.10, providing further evidence that the flare interval identified by RXTE is useful for a detailed study of Milagro data.

6.3.2 Results from Milagro during the RXTE Flare Interval

The flare interval identified utilizing RXTE data is 154.0 days in length, during which Milagro operated with an average duty cycle of 92%, leading to a effective exposure of 141.6 days. Analyzing information from this time shows that $N_{on} = 328,124$ events were observed in the bin centered on the position of Mrk 421. The corrected number of background events expected in the source bin is $N_{Bcorr} = 325,561$, resulting in an excess of 2563 ± 591 events, or 4.3 sigma. The calculated significance implies a sensitivity to Mrk 421 during this interval, using $\sigma_{obs} = 4.3$ for $t_{total} = 0.39$ years in Eq. 5.1, of 7.0σ per ideal year of exposure (100% duty cycle). This sensitivity would imply that Mrk 421 was in a flare state for a year, which is not the case. However, it is useful to compare the level of emission observed by Milagro to its detection of the Crab (2.9σ per ideal year during the entire AGN study). It is also interesting to note that the maximum significance found at the position of Mrk 421 on a 150-day time scale, 5.0σ, begins only 12 days after the start of the flare as indicated by RXTE.

Figure 6.11 shows a sky map of observed significance for the region surrounding Mrk 421 during the flare interval. The size of the angular bin used, a circle with a radius of 1.2 degrees, is shown on the map for the bin centered on the position of Mrk 421. As the significances on this map are calculated on a 0.05×0.05 degree grid, neighboring bins are highly correlated. Therefore, this image does not represent the actual distribution of events on the sky, but rather shows the effects of the finite resolution of the Milagro detector. As can be seen the choice of bin size is reasonable since the "spot" falls within the source bin shown on the plot. Further, the point of maximum significance, 5.0σ, is reasonably close to the position of the Mrk 421 ($\sim$0.3 degrees east on the plot). Naturally, it is not expected that the point of maximum significance will be located be at the true position of a source due to statistical fluctuations and resolution effects. However, these 2 observations allow for the reasonable assumption that the detected excess is from Mrk 421.

Figure 6.12 shows how the significance for Mrk 421 accumulated during the flare interval identified by the RXTE all-sky monitor, as well as how it accumulated for the duration of the Milagro AGN study. As can be seen the bulk of

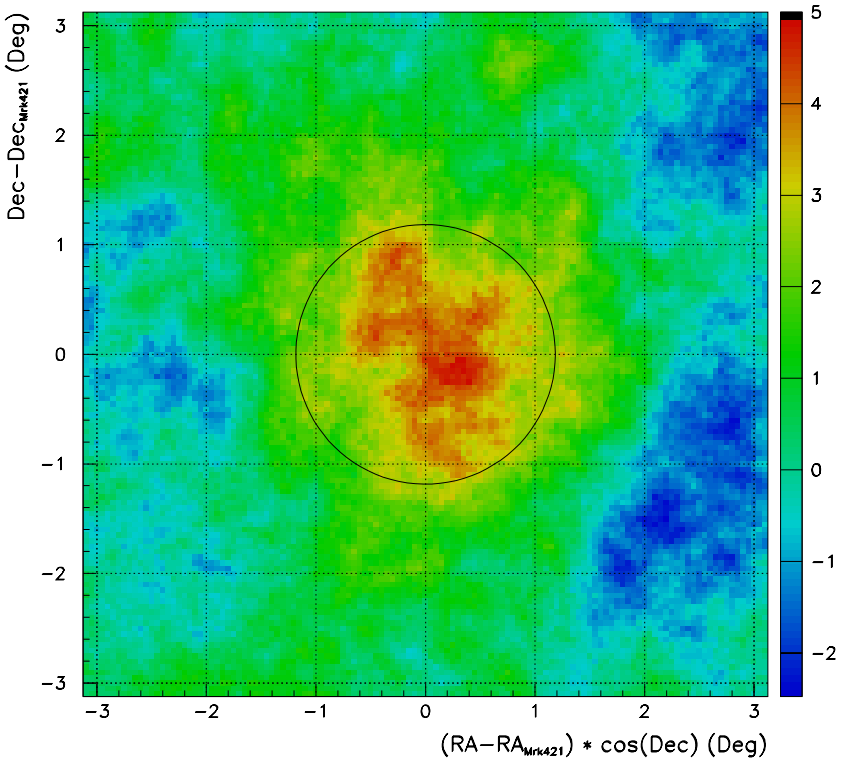

Figure 6.11: Sky map of observed significance for the region centered on Mrk 421 for the flare interval identified with RXTE data (November 12, 2000, to April 15, 2001). Neighboring points are highly correlated due to overlapping bins. The circle represents the bin size used for the analysis and is centered on the true position of Mrk 421. The significance observed at the position of Mrk 421 is 4.3σ.

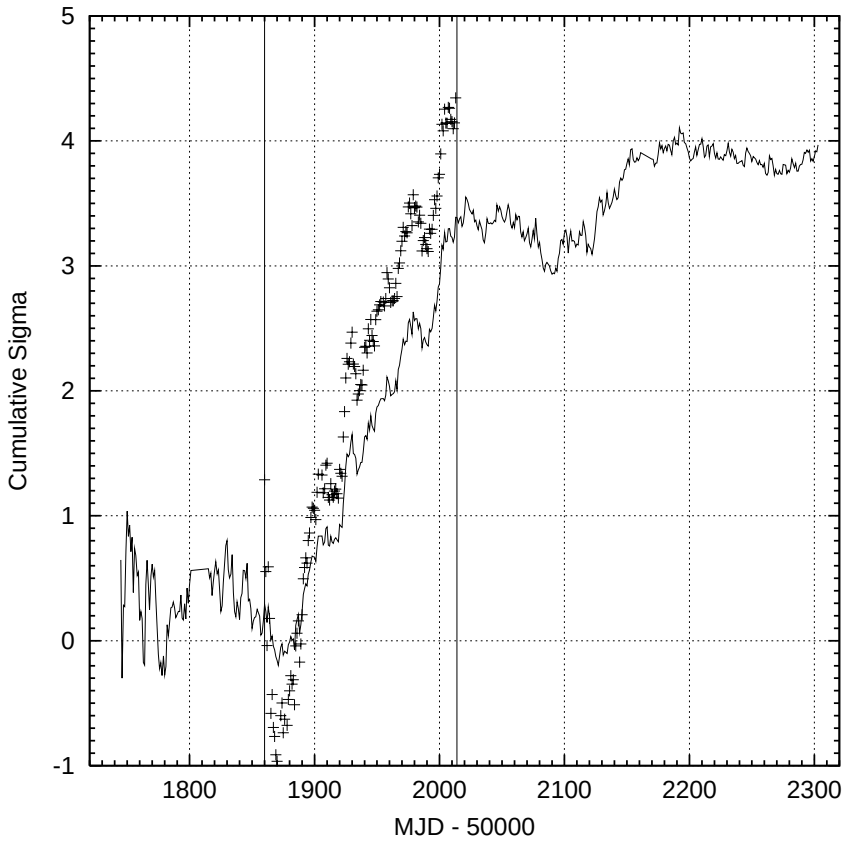

Figure 6.12: Plot showing how the significance accumulated versus time for Mrk 421 during the flare interval as indicated by RXTE. The solid vertical lines represent the start and end of this 154.0 day interval. Also shown is how the significance at the position of Mrk 421 accumulated during the entire length of Milagro data taking analyzed. The date 1910 represents January 1, 2001.

the significance accumulated by Milagro occurs during this time. What can also be seen in this figure is that for the first month of the flare interval, virtually no significance accumulated at the position of Mrk 421. While interesting, this does not conclusively show that there is a time lag between the onset of the flare in the x-ray regime and the TeV regime. Further, the period of time prior to MJD 51894 was reconstructed with less sensitive algorithms as discussed in Chapter 4. This may in part explain the lack of significance initially accumulated during the flare interval.

A detailed analysis of the signal from Mrk 421 during the RXTE flare interval, similar to that performed for the Crab in Section 5.3, is provided in Appendix C.

6.4 Flux from Mrk 421

Since Mrk 421 was detected in a search over the length of the data set as well as during the smaller flare interval indicated by the RXTE all-sky monitor, the average integral flux is calculated for both periods of time. Observation by other experiments have shown that the flux from this object varied dramatically in both its magnitude as well as its differential spectrum over the course of the data set (Aharonian et al., 2002b). While the spectrum was measured for a time period from November 2000, until May 2001, this does not encompass the majority of the data set. However, the duration of the RXTE flare is fully contained by these observations. Therefore, different spectral assumptions are used for calculating the integral flux from Mrk 421 during the flare interval and during the whole length of the study.

For the whole length of the AGN study, the integral flux is calculated using an assumed power law spectrum with no cutoff. Using the cumulative zenith angle exposure to Mrk 421 adjusted for detector dead time shown in Figure 6.13, the excess previously reported ($\Delta = 4855 \pm 1225$), and appropriate effective areas,[3] the integral flux is determined for three different spectral indexes. The spectra utilized are those of the Crab Nebula ($\alpha = 2.6$), a softer spectrum ($\alpha = 3.2$), and a harder spectrum($\alpha = 2.0$). Table 6.5 shows, for each spectral index, the inferred median energy of observation, $E_\circ$, the differential flux normalization, $I_\circ$, integral flux greater than median energy ($I(\geq E_\circ)$), as well as the integral flux greater than 1 TeV ($I(\geq 1$ TeV$)$). Systematic errors (+65%/-45%) determined in Section 5.5 are not included in the table. These include the possible effect of an angular resolution worse than the Monte Carlo simulations indicate, which would

[3]Since two versions of the online reconstruction, with different levels of sensitivity, were utilized during observations, two different effective areas need to be utilized. This is discussed in Section 5.7.3.

increase the flux reported from Mrk 421 as well as the Crab.

α	**Median Energy (TeV)**	**I$_\circ$ x 10^{-12} (cm^{-2} s^{-1} TeV^{-1})**	**I ($\geq E_\circ$) x 10^{-12} (cm^{-2} s^{-1})**	**I($\geq$1 TeV) x 10^{-12} (cm^{-2} s^{-1})**
2.6	2.5	1.7 ± 0.4	2.6 ± 0.6	11.3 ± 2.5
2.0	6.0	0.23 ± 0.06	1.3 ± 0.3	8.2 ± 2.1
3.2	1.0	21.9 ± 5.5	9.9 ± 2.5	9.9 ± 2.5
Cutoff	1.75	9.5 ± 2.4	5.1 ± 1.3	14.3 ± 3.6

Table 6.5: Average flux results from Mrk 421 for the entire data set. Table showing the inferred median energy of observation ($E_\circ$), average differential flux normalization ($I_\circ$), integral flux greater than the median energy (I($\geq E_\circ$)), and integral flux greater than 1 TeV (I($\geq$1 TeV)) measured for Mrk 421 using 4 different spectra. The differential flux normalization, $I_\circ$, is normalized to the median energy. The errors on $I_\circ$ and the integral flux quoted are propagated from the statistical error on the detected excess. Power law spectra of the indicated index, α, are used in the determination of the values with the exception of the cutoff entry which refers the result found using a spectrum of the form in Eq. 6.1 with $\alpha = 2.19$ and $E_{cut} = 3.6$.

Clearly the value of the spectral index utilized does not have much affect on the overall result for the integral above 1 TeV. For comparison, the integral flux greater than 1 TeV from the Crab Nebula was measured to be $(13.7 \pm 2.9) \times 10^{-12}$ cm^{-2} s^{-1}. As can be seen in the table, the average integral flux over the length of the data set from Mrk 421 is comparable to that of the Crab Nebula. This is true regardless of the differential spectrum chosen. The results in Table 6.5 also show that the integral flux determined using a spectrum of the form shown in Eq. 6.1 only slightly increases the integral flux above 1 TeV from values attained using a simple power law.

The differential spectrum for Mrk 421 was measured by HEGRA with data taken during the flare interval identified using data from RXTE (Aharonian et al., 2002b). Their results found the spectrum to have an exponential cutoff present. A differential spectrum of the form:

$$\frac{dN}{dE} = I_\circ \left(\frac{E}{E_\circ}\right)^{-\alpha} e^{-\frac{E}{E_{cut}}} , \tag{6.1}$$

fit the HEGRA data much better than a fit with a simple power law form. From the fit, the spectral index was determined to be, $\alpha = 2.19 \pm 0.02 \pm 0.04$. The

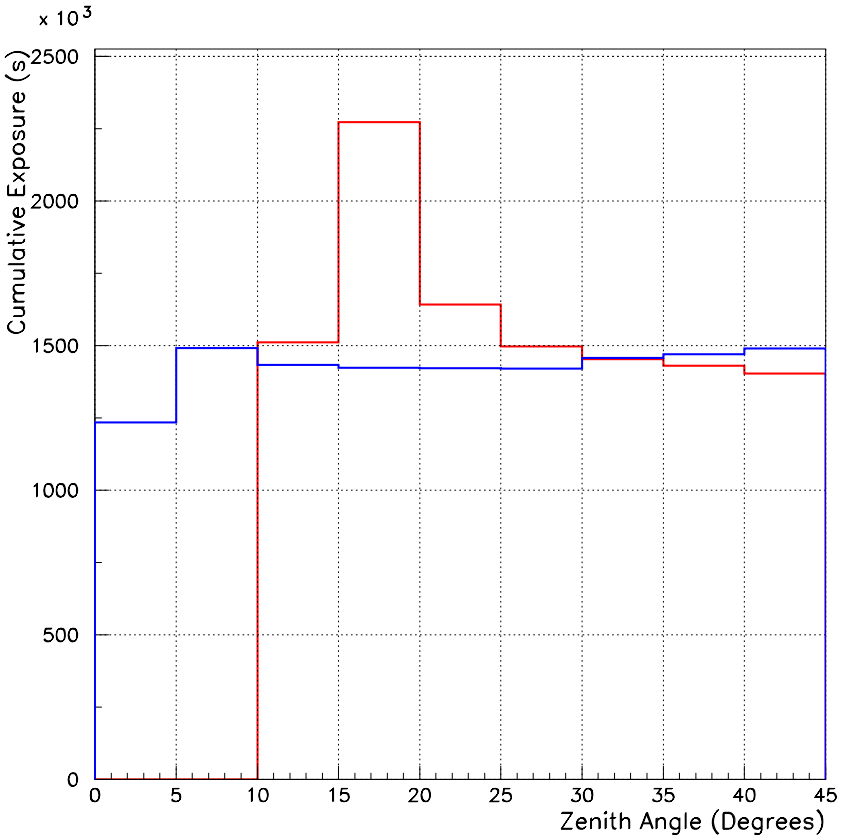

Figure 6.13: Figure showing the cumulative time exposure of Mrk 421 (blue) versus zenith angle bin for the length of the AGN study. Also shown for comparison is cumulative time exposure of the Crab Nebula (red).

cutoff energy was determined to be, $E_{cut} = 3.6^{+0.4\ +0.9}_{-0.3\ -0.8}$ TeV. While the HEGRA results also showed the differential spectrum to change slightly during the data set, a spectrum of this form was used in the calculation of the integral flux from Mrk 421 reported. HEGRA found the integral flux greater than 1 TeV to be $(41.9 \pm 0.4 \pm 4) \times 10^{-12}$ cm^{-2} s^{-1} using these values. Whipple determined a similar spectrum from Mrk 421 during this time (Krennrich et al., 2001). Their results, which are consistent with the HEGRA values, indicate a spectral index of $\alpha = 2.14 \pm 0.03$ and a cutoff energy of $E_{cut} = 4.3 \pm 0.3\ ^{+1.7}_{-1.4}$ TeV. No flux values were reported for this spectrum in their publication.

To determine results for Milagro, Eq. 4.18 and Eq. 4.19 were modified to account for the different form of the spectrum. The relevant integrals were numerically calculated. The average integral flux determined with Milagro for the flare interval identified using RXTE, using Eq. 6.1 as the form of the differential spectrum, with the spectral index and cutoff energy reported by HEGRA, is $(26.0 \pm 6.0) \times 10^{-12}$ cm^{-2} s^{-1}. This result[4] is ~62% of the value reported by HEGRA. The difference between values determined by Milagro and HEGRA is not surprising. This is because the flux from Mrk 421 was highly variable during the RXTE flare interval. The value from HEGRA utilizes 255 hours of data taken from November 2000, to May 2001. As Milagro operates continuously the exposure to this source is much larger. Therefore, the value from Milagro represents the integral flux averaged over considerably more time. As this is the case, it is reasonable to expect the result to differ. Further, the same systematic errors described in Section 5.5 are applicable to the result from Mrk 421. This includes the possible systematic effect of the predicted angular resolution. As discussed in Section 5.5.5, the total systematic error estimated for the integral flux is +65%/-45%. Therefore, the integral flux for Mrk 421 determined by Milagro is not in disagreement with the value from HEGRA when the systematic errors are accounted for.

The Crab Nebula was only measured with a significance of 1.1σ during the RXTE flare interval which is not above the level for which a detection can be claimed. Therefore, this value can not be used to compare to the flux from Mrk 421 during this time. Using the results from the length of Milagro data taking, $(13.7 \pm 2.9) \times 10^{-12}$ cm^{-2} s^{-1}, the average flux greater than 1 TeV detected from Mrk 421 during the RXTE flare interval is about twice that of the Crab.[5]

[4]The integral flux is 2% lower using the Whipple values.

[5]This is true, even when the possible systematic effect of the angular resolution predicted by the Monte Carlo simulations is accounted for.

6.5 Undetected AGN

As discussed previously, no significant excess was found from the positions of the other 26 AGN selected for study with Milagro. While unfortunate, this was not entirely unexpected for 10 of the candidate AGN. This is because RXTE all-sky monitor data for the time interval during which the Milagro study was performed did not indicate flaring behavior at x-ray energies for these AGN. Observations are reported on the RXTE website (http://xte.mit.edu) for the following 10 candidate AGN: Mrk 501, 1ES2344+514, 1ES1426+428, 3C371, BL Lac, RGB0214+517, Mrk 180, 1ES1741+196, 1ES1959+650, and 1ES2321+419. The same technique utilized to isolate the flare of Mrk 421 for analysis by Milagro was performed on these AGN. Virtually no data existed for any of the AGN where the 1 day average count rate from these sources deviated by more than 3.0σ from the base line established for them. Since TeV and x-ray flares are often correlated, the lack of any significant findings in the x-ray data made it likely that there would be none in the TeV.

6.5.1 Time Scale Analysis

Although no significant excess was found for the duration of the data set analyzed from the positions of the other 26 AGN, a time scale analysis was performed for each of them. The hypothesis of this analysis is that while the AGN may not have been bright at TeV energies over the length of the data set, they may have been for some fraction of it. If a particular AGN had been bright enough for a brief period of time, the significance detected, on some shorter time scale, would be large enough to be significant after statistically accounting for the number of trials. Both the maximum deviation method and the all-possibility method were employed to study the excess found on smaller time scales for each of the AGN. While nothing significant was found, the results are reported.

Maximum Deviation Method

Table 6.6 shows the maximum significance found for each of the AGN for each of the 11 time scales analyzed. When interpreting the maximum significance found for a particular time scale, a number of trials must be accounted for. The minimum number of trials is the number of independent bins allowed in the data set which is shown in the bottom row of the table. The maximum significance found on any time scale for all of the AGN is 4.0σ for the 21-day interval. After accounting for the number of independent bins of this length in the sample, 28, this is a 3.1 sigma upper limit. The fact that 26 AGN were analyzed also needs

to be accounted for. The probability of getting a 3.1 sigma effect in 26 trials is 2.0 sigma, which is not significant without even considering the number of time scales searched. After accounting for the number of time scales (11) examined the significance is only 0.8σ. Therefore, the maximum significance found from any of the AGN after accounting for the number of trials is not statistically significant. As this represents the most likely probability that a flare from any of these AGN was observed with Milagro, no significant excess was detected from any of these 26 AGN on any time scale.

All Possibility Method

Although the maximum deviation method did not indicate flaring behavior present in any of the remaining 26 AGN, the all-possibility method was also utilized to study the temporal behavior of the excess from each of these AGN on the 11 time scales. This is because while 1 individual bin may not have been significant, a combination of multiple independent bins with high significance would not be found in the previous technique. Such a combination of bins could be indicative of flaring behavior in the AGN. Therefore, all the possible variations of independent time bins of the fractional excess were fit to a constant for all 11 time scales. From the resulting χ^2 values, distributions of the corresponding probabilities were generated, and the median probability determined for each AGN on each of the 11 time scales. The distribution of all the probabilities found for each AGN is shown in Figure 6.14 for 9 of the 11 time scales examined. The reduced χ^2 corresponding to the individual median probabilities are shown in Table 6.7.

As can be seen all but one of the χ^2 probabilities shown are consistent with being constant. This value is from the fit to the 1-day time scale bins of the fractional excess observed from 1ES1741+196, which is shown in the table to have a reduced χ^2 of 1.30, corresponding to the median probability, for 530 degrees of freedom.[6] Some of this disagreement is explained by the fluctuations for the Crab Nebula on the 1-day time scale shown in the previous chapter. Regardless the cause of this poor result was explored because the probability value is a $\sim 4.5\sigma$ effect. As can be seen in Table 6.6, 1ES1741+196 has the largest significance found on the 1-day time scale for any of the AGN analyzed (3.7σ), including Mrk 421. Analysis of each individual point for this AGN shows that the majority of the contribution to the reduced χ^2 comes from 9 points, 7 of which are low by more than 3σ, while the other 2 are $>3\sigma$ high. None of these points had very small exposure times which would allow for extreme effects in the resulting

[6] The actual reduced χ^2 for III Zw 2 is 1.25 (shown as 1.3).

AGN	150	100	50	30	21	14	10	7	5	3	1
1426+428	0.6	0.6	1.2	1.9	2.1	2.9	2.9	2.9	2.9	2.9	3.3
Mrk 501	2.3	2.2	2.5	2.5	2.6	2.7	3.0	3.0	3.2	3.2	3.0
1959+650	1.6	1.9	2.3	2.6	2.7	2.8	2.9	3.2	2.8	2.8	2.4
2344+514	2.6	2.3	2.5	2.8	2.9	2.8	3.1	3.4	3.2	3.1	2.8
0033+595	0.5	0.6	1.5	2.2	2.5	2.8	2.8	2.8	2.8	2.8	3.2
0110+418	2.6	3.2	2.8	3.0	3.1	3.1	3.0	2.9	2.9	3.0	2.6
0152+017	2.1	1.9	2.3	2.4	2.6	2.7	3.0	4.0	3.4	3.8	3.5
0153+712	1.5	1.6	1.8	2.6	2.6	2.4	2.5	2.6	2.7	3.0	3.3
0214+517	1.2	1.9	1.8	2.1	2.2	2.3	2.6	2.3	2.5	2.7	2.9
0314+247	1.9	2.1	2.2	2.1	1.8	1.9	2.6	2.6	2.8	2.7	3.2
0656+426	0.9	1.3	1.9	2.1	2.5	2.7	2.9	2.7	2.9	2.9	2.9
Mrk 180	1.8	2.1	2.6	3.1	2.9	2.6	2.5	2.7	3.7	3.0	3.0
1532+302	2.3	2.0	2.1	2.9	2.9	3.1	2.9	2.8	2.9	2.7	3.2
1610+671	2.1	1.9	2.4	2.1	2.7	3.2	2.9	2.8	2.9	3.0	3.6
I Zw 187	1.8	2.2	2.3	2.4	2.3	2.4	2.5	2.7	2.8	3.3	3.3
1741+196	2.2	2.3	2.9	3.2	3.3	3.5	3.3	3.0	2.9	2.9	3.7
2321+419	0.8	1.2	1.8	2.6	2.7	3.0	3.0	2.7	2.8	3.0	2.7
2322+346	3.4	2.7	3.1	3.2	2.9	3.0	3.0	2.7	3.7	3.3	3.1
III Zw 2	3.0	3.0	3.7	3.6	4.0	3.6	3.6	3.3	3.3	3.0	3.7
0138+398	0.7	1.0	1.7	2.5	2.6	2.6	3.2	3.5	3.4	3.0	3.1
0321+33	1.9	2.0	2.3	2.3	2.2	2.5	2.5	3.1	3.1	3.8	3.1
1413+436	1.9	1.8	2.5	2.4	3.2	2.8	2.5	2.8	2.7	3.3	3.3
2209+184	2.0	2.0	2.3	2.3	2.7	3.1	3.5	3.5	3.6	3.5	2.8
W Comae	1.6	1.9	2.7	2.4	2.7	2.8	2.6	2.7	2.5	2.7	3.0
3C371	1.8	2.0	1.9	1.8	2.4	2.0	2.0	2.4	2.5	2.8	2.5
BL Lac	1.4	2.0	2.8	2.6	2.8	3.0	3.0	3.2	3.1	3.6	3.4
No. Ind. Bins	5	7	12	20	28	41	57	79	112	181	531

Table 6.6: Table showing the maximum significance in standard deviations found on a given time scale for the 26 undetected AGN. The time scales range from 1 to 150 days. The bottom line shows the minimum number of independent bins that must be accounted for in the statistical interpretation of this value.

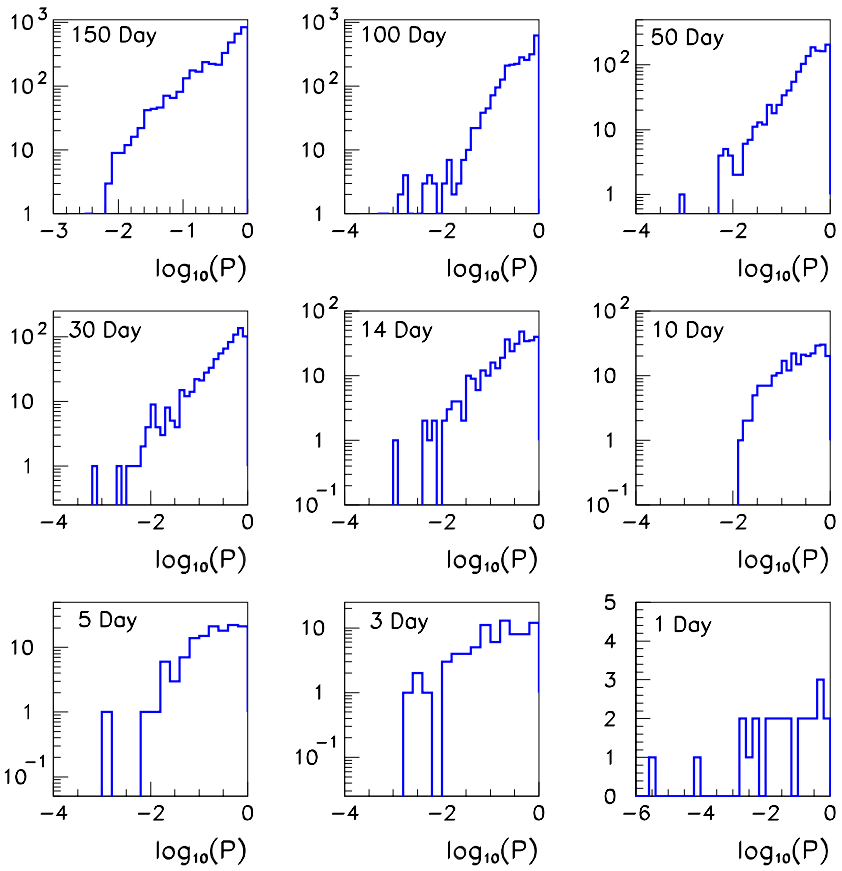

Figure 6.14: Figure showing the distribution of χ^2 probabilities found, for 9 time scales, from fits to all possible sets of independent bins of the fractional excess versus time to a constant for each of the 26 undetected AGN.

AGN	**150**	**100**	**50**	**30**	**21**	**14**	**10**	**7**	**5**	**3**	**1**
1426+428	0.2	0.3	0.6	0.7	0.8	1.1	1.2	1.2	1.2	1.1	1.2
Mrk 501	0.2	0.3	0.7	0.8	0.9	1.1	1.1	1.2	1.2	1.2	1.2
1959+650	1.1	1.1	1.0	1.2	1.2	1.1	1.0	0.9	1.0	0.9	1.0
2344+514	0.8	0.7	0.9	1.0	1.1	1.1	1.0	1.1	1.1	1.1	1.1
0033+595	0.2	0.4	0.5	0.6	0.7	0.8	0.8	0.8	0.9	0.9	1.0
0110+418	1.7	1.7	1.9	1.8	1.6	1.4	1.3	1.2	1.1	1.2	1.1
0152+017	0.5	0.6	0.9	0.8	0.9	0.9	1.0	1.1	1.2	1.2	1.2
0153+712	0.6	0.5	0.7	0.8	1.0	1.0	1.0	1.0	1.0	1.1	1.0
0214+517	0.6	0.6	0.9	0.9	0.8	0.8	0.9	0.9	0.9	0.9	1.1
0314+247	1.9	1.4	1.2	1.1	1.1	1.1	1.1	1.2	1.2	1.1	1.1
0656+426	0.7	1.2	1.1	1.2	1.2	1.2	1.1	1.1	1.0	1.0	1.1
Mrk 180	1.5	1.1	0.9	0.9	0.9	0.9	0.9	1.0	1.0	1.0	1.0
1532+302	1.0	1.2	1.1	1.4	1.3	1.2	1.2	1.1	1.1	1.1	1.1
1610+671	1.7	1.3	1.2	1.3	1.2	1.3	1.3	1.2	1.2	1.0	0.9
I Zw 187	2.3	1.8	1.4	1.2	1.1	1.0	1.0	1.1	1.1	1.1	1.1
1741+196	0.7	0.4	0.9	0.8	0.8	0.9	1.1	1.2	1.2	1.2	1.3
2321+419	0.4	0.8	1.4	1.2	1.2	1.2	1.3	1.2	1.1	1.1	1.1
2322+346	0.8	0.9	0.8	1.0	0.9	1.0	0.9	0.9	1.0	1.0	1.1
III Zw 2	1.0	1.2	1.1	1.2	1.3	1.2	1.3	1.1	1.2	1.2	1.3
0138+398	0.5	0.8	0.9	1.1	1.2	1.2	1.1	1.1	1.1	1.1	1.0
0321+33	0.9	0.8	1.4	1.2	1.1	1.0	1.1	1.1	1.1	1.2	1.2
1413+436	1.8	1.3	1.0	0.8	1.0	1.1	1.2	1.1	1.1	1.2	1.2
2209+184	1.4	1.3	1.1	1.4	1.4	1.3	1.3	1.2	1.2	1.1	1.1
W Comae	0.5	0.7	1.1	1.1	1.3	1.4	1.2	1.1	1.1	1.1	1.1
3C371	0.6	0.7	1.0	0.9	0.9	1.0	0.9	0.9	0.9	1.0	0.9
BL Lac	0.6	0.8	1.1	1.0	1.2	1.2	1.2	1.2	1.1	1.1	1.1
D.O.F	4	6	11	19	27	40	56	78	111	180	530

Table 6.7: Table showing the reduced χ^2 corresponding to the median probability found from fits to a constant of all possible sets of independent bins of the fractional excess versus time for a given AGN on various time scales. The 11 time scales range from 1 to 150 days in length. The bottom line shows the number of degrees of freedom in the fit.

significance. However, the presence of so many points on the low side, with not so many on the high side, insinuates that something odd was occurring, therefore all 9 were removed from the data set. Removing these points from the fit resulted in a reduced χ^2 of 1.1. Therefore, no flaring behavior was observed from 1ES1741+196 on the 1-day time scale. Hence, no significant excess was found from the positions of any of the 26 remaining candidate AGN on any time scale.

6.5.2 Upper Limits

As discussed earlier, no significant excess was found for any of the other 26 candidate AGN on any time scale. While a detection of a source with high statistical significance is clearly desirable, the lack of such a finding can still produce scientifically meaningful results. As discussed in Chapter 4, an upper limit on the integral flux value from a source can be calculated. This value is how "bright" a source could have been, at some confidence level, for it to have remained undetected by Milagro. This value can have significant importance in constraining models of TeV emission from blazars. Further, some of the undetected AGN are known to be sources of TeV photons. If the reported flux from these sources is below the upper limit established by observations with Milagro, the non-detection is in agreement with expectations. This is because it would show that while a certain source is known to emit TeV gamma-rays, it was not bright enough to be detected by Milagro.

To determine the upper limit, the differential flux normalization, $I_\circ$, is calculated by substituting the 90% confidence limit on the number of events from a particular source, N_{90}, for the excess, Δ, in Eq. 4.18. The value to which the flux is normalized is the median energy, E_{med}, expected for events detected by Milagro given the assumed spectrum. This value is determined using the method discussed in Section 4.4.2. Using the median energy makes the choice of differential spectrum involved in the calculation insignificant. This is clearly desirable as the actual spectrum of the undetected sources is for the most part unknown. The value chosen for the determination of $I_\circ$ is that of a source with a differential spectrum similar to that of the Crab Nebula. This spectrum is a power law with spectral index, $\alpha = 2.6$. Once $I_\circ$ has been determined, the value is integrated using Eq. 4.19, and results in an upper limit on the integral flux from the source at the 90% confidence level. The integration is performed from the median energy of observation, E_{med}, up to 100 TeV assuming the same power law spectrum ($\alpha = 2.6$); no spectral cutoff is assumed. The motivation for choosing this spectrum is provided by the spectra determined for AGN detected at TeV energies. Mrk 421 and Mrk 501 are the two most extensively studied AGN at TeV energies. The spectrum found for these objects is a power law with an exponential cutoff

shown in Eq. 6.1. While the spectral index determined by Whipple for Mrk 421 ($\alpha = 2.14$) and Mrk 501 ($\alpha = 1.95$) are harder than the one chosen, the presence of an exponential cutoff in these objects (4.3 TeV and 4.6 TeV respectively) makes the spectra effectively softer. Other AGN observed at TeV energies, 1ES2344+514 and 1ES1959+650, have a measured spectral index consistent with the value chosen ($\alpha = 2.6$). The spectrum determined for 1ES2344+514 is a power law with spectral index, $\alpha = 2.5$ (Catanese et al., 1998). A preliminary analysis of very recent Whipple observations of 1ES1959+650 find the spectrum to be fit by a power law with spectral index $\alpha = 2.4 \pm 0.14$. This detection (13σ) is currently unpublished, but reported on their website (http://egret.sao.arizona.edu). Finally, a soft power law spectrum was found for for 1ES1426+428, $\alpha = 3.55$ (Horan et al., 2002). Since it is not clear which of these objects would be most characteristic of the AGN selected for study, a power law spectrum with spectral index, $\alpha = 2.6$, was chosen as it represents the middle ground. Table 6.8 shows the median energy for Milagro, as well as the upper limits at the 90% confidence level on the number of detected events, differential flux normalization, and integral flux above the median energy for each of the candidate AGN studied by Milagro.

6.5.3 Error on the Upper Limits

Statistical Error

There are two sources of statistical error in the flux upper limits determined. The largest is due to fluctuations in the number of excess events observed from the source. The other is from the uncertainty in determining the number of background events expected. However, the time sloshing technique, discussed in Chapter 4, utilized to estimate the background makes the size of this error small. Regardless of the individual contributions, the determination of N_{90} accounts for the statistical error. Therefore, no statistical error bars are required on the upper limits.

Systematic Error

Although the statistical errors are included in the determination of the flux upper limits, the same systematic errors described in Section 5.5 are applicable to the results. These include the possible systematic effect of the predicted angular resolution. As discussed in Section 5.5.5, the total systematic error estimated for the integral flux is +65%/-45%. Another source of systematic error, not included in this value results from the choice of spectral index. While the value of the spectral index ($\alpha = 2.6$) was chosen, it is not clear that this is correct. Therefore, the upper limit on the integral flux above the median energy shown in Table 6.8

AGN	**z**	N_{90}	**Median Energy** $E_\circ$ **(TeV)**	$I_\circ$ **x** 10^{-13} **(cm^{-2} s^{-1} TeV^{-1})**	**I**$(\geq E_\circ)$ **x** 10^{-13} **(cm^{-2} s^{-1})**
1426+428	0.129	1325	2.5	4.7	7.3
Mrk 501	0.034	3800	2.5	12.9	20.1
1959+650	0.048	1131	6.0	1.5	5.6
2344+514	0.044	3814	3.0	11.5	21.5
0033+595	0.086	940	4.0	2.2	5.5
0110+418	0.096	3114	2.5	10.8	16.8
0152+017	0.080	1182	8.0	2.2	10.9
0153+712	0.022	746	10.0	0.7	4.1
0214+517	0.049	1795	3.0	5.4	10.1
0314+247	0.054	1434	2.5	6.5	10.1
0656+426	0.059	1270	2.5	4.4	6.9
Mrk 180	0.046	821	8.0	0.9	4.6
1532+302	0.064	1443	2.5	5.4	8.4
1610+671	0.067	1261	7.0	1.5	6.3
I Zw 187	0.055	1500	3.0	4.1	7.6
1741+196	0.083	3371	3.0	12.8	24.0
2321+419	0.059	1390	2.5	4.8	7.5
2322+346	0.098	3793	2.5	13.1	20.4
III Zw 2	0.090	1674	5.0	3.6	11.2
0138+398	0.080	1339	2.5	4.5	7.1
0321+33	0.062	2056	2.5	7.2	11.1
1413+436	0.090	2067	2.5	7.4	11.5
2209+184	0.070	2173	3.0	8.8	16.4
W Comae	0.102	1968	2.5	7.8	12.1
3C371	0.051	1282	8.0	1.4	6.7
BL Lac	0.069	2404	2.5	8.4	13.2

Table 6.8: Table showing the redshift, median energy of observation ($E_\circ$), 90% confidence limits of the number of events (N_{90}), differential flux normalization ($I_\circ$), and integral flux above the median energy, $I(\geq E_\circ)$, for each of the candidate AGN not detected by Milagro. A power law spectrum with spectral index $\alpha = 2.6$ and no cutoff is assumed.

was determined for each AGN for spectral indices of $\alpha = 2.0$ and $\alpha = 3.2$. The harder index always results in a larger upper limit (21% greater on average), and the softer index results in a smaller upper limit (48% less on average). Therefore the systematic error on the integral flux upper limit that results from the estimation of the spectral index is +21%/-48%. Adding this in quadrature with all the other contributions to the systematic error results in a total systematic error of $\pm 65\%$ for the upper limit of the integral flux above the median energy shown in the table.

6.5.4 Comparison of Upper Limits

Comparison to Flux in Known Sources of TeV Photons

Some of the undetected AGN are known to be sources of TeV photons. Comparison of the upper limits determined by Milagro to the flux reported from known sources of TeV photons is performed in this section. The results show that the non-detection of these sources is in agreement with expectations.

The blazar, Mrk 501, has been detected by many observatories at TeV energies, including a less sensitive version of Milagro, known as Milagrito (Atkins et al., 1999). The flux from this object has been shown to be highly variable. It is dim at the normal, quiescent level, and very bright during flaring periods. It is during such a flare in 1997 that it was detected by Milagrito. There have been no reports of flaring behavior at TeV energies for Mrk 501 during the time period of observations by Milagro. Therefore the non-detection of it by Milagro is somewhat expected. This is shown using the quiescent level of the integral flux from Mrk 501 in 1995 as reported by Whipple (Quinn et al., 1996). While it is known that the flux from Mrk 501 varies significantly over time, the 1995 level should be a reasonable indicator of the level of flux expected from it during the observations of Milagro. The integral flux reported by Whipple is $(8.1 \pm 1.4) \times 10^{-12}$ cm^{-2} s^{-1}, above a threshold of 300 GeV. Unfortunately no spectral index is quoted in the paper. Using the upper limit on the differential flux normalization for Mrk 501 shown in Table 6.8, the upper limit on the integral flux above 300 GeV is 5.9×10^{-11} cm^{-2} s^{-1}. This value assumes a spectral index of $\alpha = 2.6$. Although there are suggestions in the Whipple paper that a harder differential index of $\alpha = \sim 2.0$ is appropriate, the value from Milagro is then smaller by factor of ~ 2. Regardless, the upper limit reported for Mrk 501, is well above the quiescent flux from Mrk 501. Therefore, it can be stated the Milagro result from Mrk 501, a non-detection, is consistent with expectations.

Emission at TeV energies has also been detected from the blazar, 1ES2344+514, by Whipple (Catanese et al., 1998). During their observations in 1995-1996, a 6σ

excess was observed on one evening. This result implied a integral flux greater than 350 GeV of $(6.6 \pm 1.9) \times 10^{-11}$ cm^{-2} s^{-1}. The observations from 1995-1996, not including the flare, yielded a 4σ excess indicating an integral flux greater than 350 GeV of $(1.1 \pm 0.4) \times 10^{-11}$ cm^{-2} s^{-1}. The spectral index utilized in the Whipple calculations was $\alpha = 2.5$. Using the differential flux normalization shown in Table 6.8, the upper limit on the integral flux above 350 GeV was calculated for Milagro. This value is 6.6×10^{-11} cm^{-2} s^{-1}. Clearly the average level of flux reported from 1ES2344+514 by Whipple is lower than the upper limit from Milagro. Therefore, while no significant excess was observed from 1ES2344+514 by Milagro, this is consistent with expectations. Further the flux reported on the brightest night of observations by Whipple is the same as the upper limit from Milagro. As the value for Milagro is the average result from 499.3 days of exposure, it is likely that Milagro would not have observed even the brightest flare known so far from this object.

The blazar 1ES1426+428 has also been detected by several TeV observatories. During the 2000-2001 observations by Whipple which detected the AGN with a significance of 5.5σ, the integral flux above 280 GeV was observed to be $(2.04 \pm 0.35) \times 10^{-11}$ cm^{-2} s^{-1} (Horan et al., 2002). This value was calculated for a soft power law spectrum of $\alpha = 3.55$. During previous observing campaigns by Whipple this object was not detected and the resulting upper limits are much less than the flux in 2000-2001, indicating that 1ES1426+428 experienced a flare during the observations by Whipple and Milagro. Unfortunately, even though it flared, 1ES1426+428, was not observed to have a significant excess in the Milagro data set analyzed. The resulting 90% confidence limit on the integral flux from this object above 280 GeV, with the same spectrum, is 12.1×10^{-11} cm^{-2} s^{-1}. Clearly the flux reported during this flare is much less than this, which is consistent with the source not being detected by Milagro.

The detection of 1ES1959+650, currently unpublished but reported on the Whipple website (http://egret.sao.arizona.edu), occurred after the end of the data set analyzed in the AGN study. The preliminary flux found had a maximum of 2.5 times that of the Crab. However, it is not clear that this value is appropriate for comparison since represents the largest flux observed on two nights of observation occurring after the end of data set. Therefore, it can not be stated whether the non-detection of 1ES1959+650 is in agreement with expectations. Although the statement can be made that the flux from this blazar could not have been consistently this large during Milagro data taking, or else it would have been detected in this study. Comparison to the upper limit on the flux from this object previously published by Whipple is performed in Table 6.9.

Comparison to Published Flux Upper Limits from Other AGN

Upper limits on the integral flux from some of the candidate AGN are published by the Whipple group (Buckley, 1999). Although the energy threshold is different for the Whipple upper limits, the results from Milagro can be calculated above this threshold and compared. Table 6.9 shows the 99% upper limits on the integral flux above the indicated energy threshold of observations published by Whipple for these candidate AGN. Also shown in the table is the 99% confidence limits from Milagro observations of these objects, as well as the ratio of these values. While the Whipple results are lower, the Milagro results are competitive and therefore useful. Further, this shows that upper limits from Milagro for AGN that do not have upper limits presently published are useful as well. This is especially important as Milagro is capable of simultaneously observing all AGN within its field of view with almost 100% duty cycle. Therefore, useful upper limits can be obtained from the Milagro data for almost all AGN in the northern sky.

AGN	**z**	**Whipple** $E_\circ$ **(TeV)**	**Whipple** $\mathbf{I(\geq E_o)\ x\ 10^{-11}}$ $\mathbf{(cm^{-2}\ s^{-1})}$	**Milagro** $\mathbf{I(\geq E_o)\ x\ 10^{-11}}$ $\mathbf{(cm^{-2}\ s^{-1})}$	$\frac{I_M}{I_W}$
3C371	0.051	0.35	1.9	15.0	7.9
BL Lac	0.069	0.35	0.53	4.6	8.7
W Comae	0.102	0.35	0.59	4.4	7.5
Mrk 180	0.046	0.35	1.1	11.4	10
I Zw 187	0.055	0.5	0.69	2.2	3.2
1ES1741+196	0.083	0.35	0.48	9.8	20
1ES1959+650	0.048	0.35	1.3	8.5	6.5
1ES2321+419	0.059	0.35	1.1	3.0	2.7

Table 6.9: Table showing the redshift, Whipple energy threshold ($E_\circ$), Whipple 99% confidence limits of the integral flux above the threshold, $I(\geq E_\circ)$, Milagro 99% confidence limits of the integral flux above the threshold, $I(\geq E_\circ)$, and the ratio of those upper limits. For the Milagro results, a a power law spectrum with spectral index $\alpha = 2.6$ and no cutoff is assumed.

Comparison of Upper Limits to Predictions

The upper limits from Milagro are competitive with those reported by air-Cherenkov telescopes such as Whipple, making them useful in constraining models of TeV emission. In a recent publication (Constamante and Ghisellini, 2002)

the integral flux above 1 TeV was predicted for AGN (blazars) likely to be sources of TeV photons using two different models. In one model, a synchrotron self-Compton model (SSC), described in Chapter 2, aimed to fit the measured synchrotron component of the spectral energy distribution (SED), was used to predict the inverse Compton spectrum and correspondingly the flux of TeV photons. In the other model, the flux of TeV photons is calculated using a different model thought to describe the average SED of blazars. This model, a slightly modified version of one previously published (Donato et al., 2001), uses the radio luminosity to predict the inverse Compton power. Neither model accounts for the possible absorption of TeV photons by the infrared background radiation. However, the effect is likely to be small since the AGN are close ($z<0.1$). The second model tends (almost always) to predict a larger flux of TeV photons. In many cases the difference is several orders of magnitude. Both models predict fluxes which are in agreement with measurements of already detected TeV sources. Therefore, in order to determine which model is the best indicator of the TeV flux requires comparison of the results from other AGN. This comparison not only sheds light on the underlying phenomena in AGN, but has implications regarding which sources should be selected for observation by TeV observatories with a pointed, small field-of-view and limited duty cycle such as the imaging air-Cherenkov telescopes described in the introductory chapter. Table 6.10 shows the predictions (when available) of each of these models for the integral flux greater than 1 TeV, as well as the 90% upper limit on that flux determined by Milagro.

AGN	**SSC (low E fit) Model I($\geq$1 TeV)**	**Avg. SED Model I($\geq$1 TeV)**	**Milagro 90% Upper Limit I($\geq$1 TeV)**
BL Lac	NA	0.43	0.57
1ES0033+595	0.04	0.48	0.51
RGB0214+517	0.0062	1.43	0.59
Mrk 180	NA	1.93	1.3
I Zw 187	NA	1.23	0.44
1ES1741+196	0.01	0.84	1.4
1ES1959+650	NA	1.74	0.99

Table 6.10: Table showing the predictions of two models for the integral flux greater than 1 TeV from selected AGN, as well as the 90% upper limit on that flux determined by Milagro. The SSC (low E fit) model is the first described, and the Avg. SED Model is the second. The units are 10^{-11} cm^{-2} s^{-1}.

The table shows that the predictions for the integral flux above 1 TeV are significantly below the 90% upper limit determined by Milagro for the first model. The predictions from the second model are above the Milagro upper limit in 3 of the cases. This is true even when the systematic error ($\pm 65\%$) is accounted for. The Milagro upper limit is comparable to the predictions in the remaining 4 cases. Therefore, some evidence is provided by the Milagro observations that the first model is a better indicator of the TeV flux. Although, the results from observations of more AGN are required to make conclusive statements regarding this.

Chapter 7

Conclusions

The Milagro gamma-ray observatory is a unique EAS array which uses a water-Cherenkov technique to continuously monitor the sky for astrophysical gamma-ray emission near 1 TeV. Milagro's large aperture and high duty cycle allow it to serve as an all-sky monitor in the VHE regime, enabling the study of a wide range of physics topics. The results from a study of TeV emission from the Crab Nebula and 27 selected AGN using Milagro are summarized in this chapter. Future improvements to Milagro are also discussed.

7.1 Summary of Results

7.1.1 The Crab Nebula

Since the Crab Nebula is the standard reference for TeV gamma-ray astronomy due to its steady and relatively large flux, the purpose of studying the Crab Nebula was to demonstrate that Milagro functions as expected. In this sense the study was successful. Milagro successfully observed the Crab Nebula during 2.6 years of data taking (2.0 years of exposure). The detected significance (4.7σ) corresponds to a sensitivity to the Crab Nebula of 3.4σ per year of exposure. The signal from the Crab Nebula is observed to be steady in time for time scales longer than $\sim$30 days indicating that the sensitivity of the detector is stable in time. Using the signal from the Crab Nebula, the analysis techniques and data cuts were shown to be reasonable. The integral flux greater than 1 TeV measured by Milagro from the Crab Nebula is low, but in agreement within errors, compared to the flux reported by VHE observatories such as Whipple and HEGRA. As the results of the study of the Crab Nebula at TeV energies demonstrate that Milagro operates in a stable manner with a sensitivity that is both understood and expected from observations

by other observatories, it can be assumed that the results from observations of a variety of astrophysical objects are accurate.

7.1.2 Selected AGN

Several AGN have been detected at TeV energies by a variety of observatories. The emission from these objects is highly variable and characterized by flaring behavior, where the flux increases dramatically on small time scales. Due to the variable nature of these objects, Milagro's ability to continuously monitor the overhead sky, even during daytime transits, makes it well suited for studies of AGN. In the study of 27 selected AGN during 1.5 years of data taking (1.4 years of exposure) with Milagro, Mrk 421 was detected with a significance of 4.0σ (3.4σ per year of exposure). This detection coincides with flaring behavior observed by several other TeV observatories in early 2001. The average flux measured from Mrk 421 during this time is comparable to that of the Crab Nebula. Since it is known that Mrk 421 was not bright at TeV energies during the entire data interval studied, a time scale analysis of the signal from Mrk 421 was performed. The results suggest that the signal from Mrk 421 was not accumulated in a manner that is consistent in time for time scales longer than $\sim$ 50 days. However, the sensitivity of Milagro is too low to isolate exactly when the flare of Mrk 421 occurred. In order to more closely study the response of Milagro to the flare of Mrk 421, an *a priori* flare interval was determined using information from the RXTE all-sky monitor. During this interval of 154 days (142 days of exposure) Mrk 421 was observed with a significance of 4.3σ (7.0σ/year). The flux found from Mrk 421 by Milagro during this flare interval is about twice that of the Crab Nebula and in agreement with the value found by HEGRA. No emission was observed on any time scale from any of the 26 other AGN selected for study with Milagro. Although several (4) of the other AGN selected for study are known to be emitters of TeV photons, the upper limits on the integral flux determined by Milagro are above the flux reported from these objects by other observatories. Thus, the non-detection of these four AGN are consistent with expectations. The upper limits determined for the non-detected AGN are competitive with those established by Whipple and are useful for constraining models of TeV emission in AGN, ruling out at least one model.

7.2 Future of Milagro

Although Milagro has successfully observed TeV gamma-ray sources, two improvements to the detector are currently being implemented. The first is the

deployment of 175 water tanks as Cherenkov detectors, known as "outriggers", surrounding the pond. Use of the outriggers will substantially improve the angular resolution, the gamma-hadron separation, and the energy determination of events that trigger Milagro. The second improvement is the installation of smart triggering processors which will lower the energy threshold of Milagro.

7.2.1 Outriggers

The lateral extent of Milagro is smaller than that of a typical EAS which triggers the detector. This causes much difficulty in determining the core position of the EAS. Knowledge of the core position is important as the shower front of an EAS is curved. As discussed in Chapter 3, this requires application of a correction, which depends on distance to the fit core position, to account for the curvature before the shower front is fit to a plane. Any improper determination of the core position results in the wrong curvature correction being applied, degrading the angular resolution. Inaccurate knowledge of the core position also makes it difficult to distinguish between a low-energy shower hitting the pond and a high-energy shower far away, resulting in a poor energy determination. Finally, the gamma-hadron separation in Milagro can be improved by the proper knowledge of the core position.

In order to increase the lateral extent of Milagro, resulting in a better determination of the core position, 175 individual cylindrical water tanks, 0.91 m in height by 2.4 m diameter, made of black polyethelene and lined in the interior with Tyvek are being deployed. Each of the tanks is filled with water and has an individual PMT facing down from the top, enabling it to function as an individual water-Cherenkov detector capable of measuring the particles in an EAS with high efficiency. The tanks are deployed over a 200 m x 200 m area surrounding the pond as shown in Figure 7.1. Studies show that the outrigger array will increase the sensitivity of Milagro by at least a factor of 2, as well as improving the energy resolution (Sullivan, 2001).

7.2.2 Smart Triggering

The simple multiplicity trigger, discussed in Chapter 3, used during data taking for this thesis limits the low energy reach of Milagro. The DAQ system for Milagro can currently handle a trigger rate of $\sim$2 kHz which is reached at a multiplicity of $\sim$55 top layer PMTs hit within an 200 ns coincidence window. At smaller PMT multiplicities the trigger rate, shown in Figure 3.7, becomes exponentially larger and is higher than the DAQ's ability to read the data out. While the DAQ cannot handle the trigger rate associated with lower multiplicities, Milagro

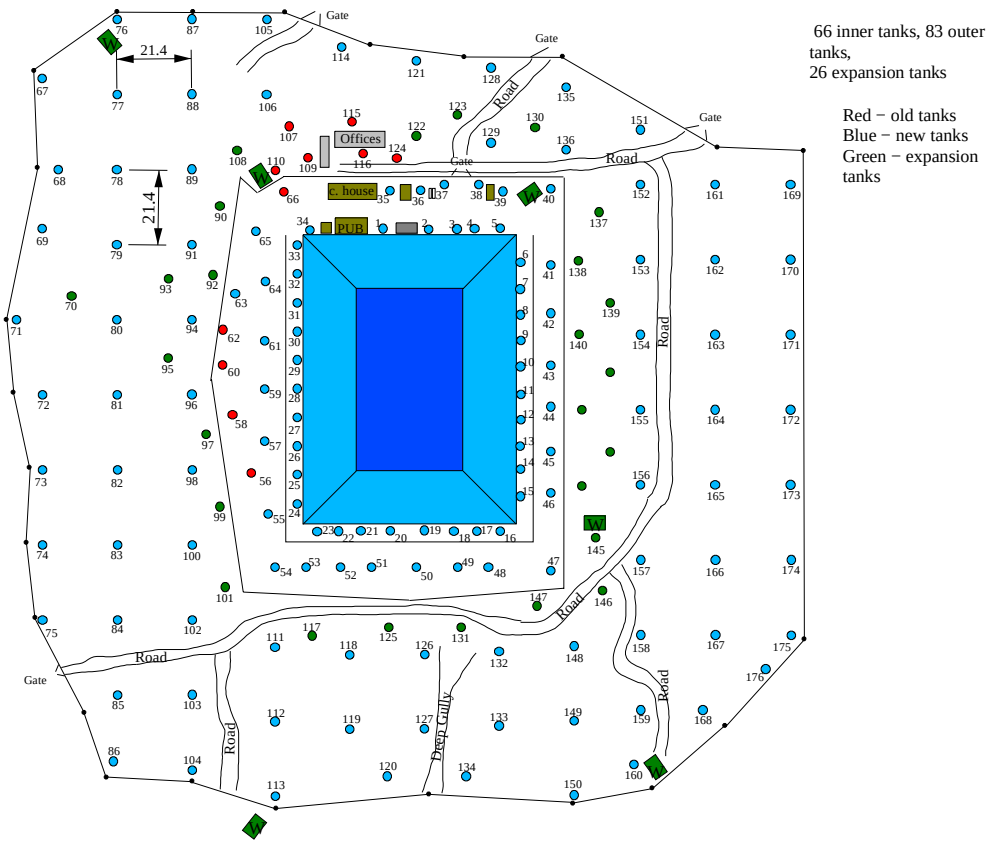

Figure 7.1: Plan for the layout of the outrigger array (Sullivan, 2001). The Milagro pond will be surrounded by ∼170 outriggers.

is capable of reconstructing gamma-ray showers with good angular resolution and high efficiency down to a level of ∼10 PMTs hit. Since the increase in trigger rate is predominantly due to non-shower events such as single muons, rejecting these events allows for the threshold to be reduced. Therefore, custom trigger processors which utilize both the time signature information and muon layer information to perform this rejection and reduce the threshold have recently been installed. This lower trigger threshold results in a lower energy threshold, increasing the sensitivity of Milagro to gamma-ray sources, particularly to those at cosmological distances, where higher energy gamma-rays are attenuated due to interactions with the extragalactic background light.

7.3 Conclusion

Milagro has been operating since June 1999, and has successfully observed two TeV gamma-ray sources. Clearly Milagro should be able to observe similar phenomena with appreciable significance, especially since improvements to Milagro currently being implemented will allow for even more sensitive studies to be performed. This, coupled with the ability of Milagro to observe transient phenomena such as GRBs, demonstrates that Milagro is capable of significant contributions to the field of TeV astrophysics.

Appendix A

Time Scale Plots for the Crab Nebula

This appendix contains figures referred to in Chapter 5. These plots are used in the analysis of the temporal behavior of the observed excess from the Crab Nebula on eleven short-term time scales. The first three figures show the rolling significance for the bin centered on the Crab Nebula for the eight time scales not shown in Section 5.2.1. These were used to identify the appropriate time bin of maximum and minimum significance in the maximum deviation method. In these plots, the significance of the number of excess events detected is calculated for the appropriate time bin beginning on the date of the point. Neighboring points for the time scales longer than 1 day are highly correlated. The remaining ten figures show the fractional excess versus time for the ten time scales not shown in Section 5.2.2. These plots illustrate the all possibility method, which determined that the signal from the Crab Nebula was accumulated in a manner that is consistent with being constant in time for the time scales longer than $\sim$30 days. The choice of independent bins shown is the one which corresponds to the median χ^2 probability. The constant fit to these bins is also shown.

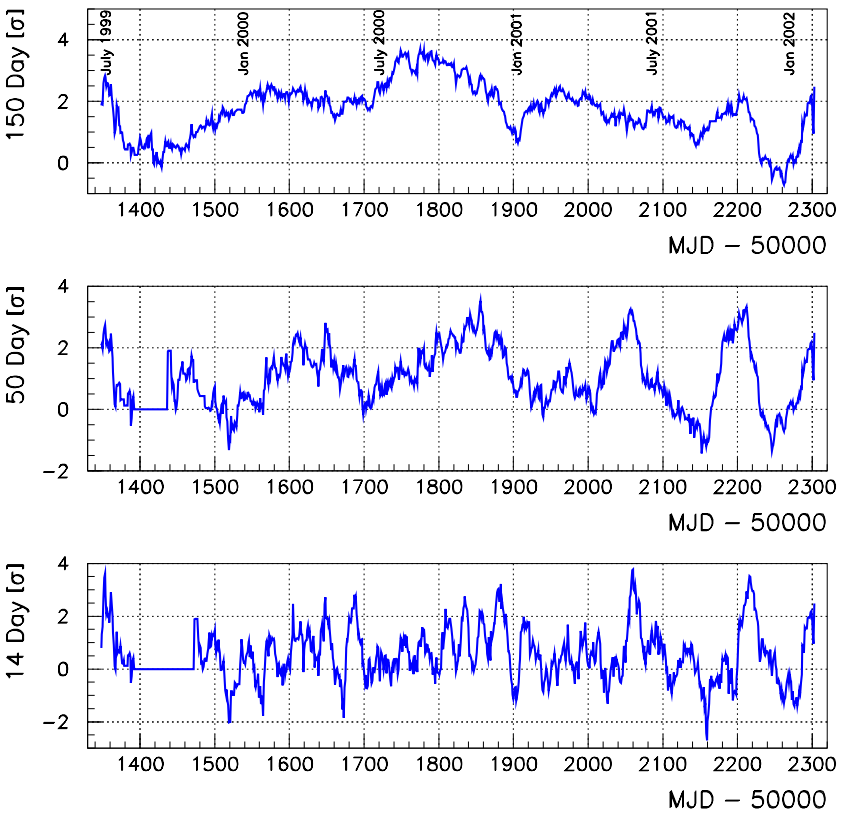

Figure A.1: This figure shows the rolling significance of the excess found at the position of the Crab Nebula for the 14, 50, and 150-day time scales. Entries are plotted according to the *first* day of the interval. Neighboring points are correlated.

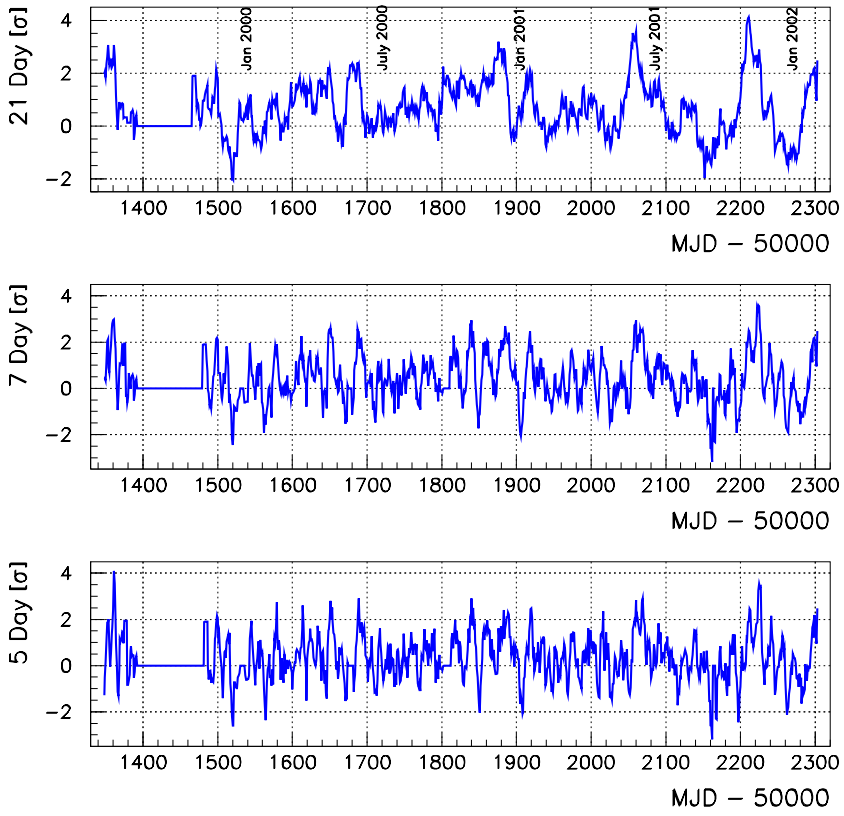

Figure A.2: This figure shows the rolling significance of the excess found at the position of the Crab Nebula for the 5, 7, and 21-day time scales. Entries are plotted according to the *first* day of the interval. Neighboring points are correlated.

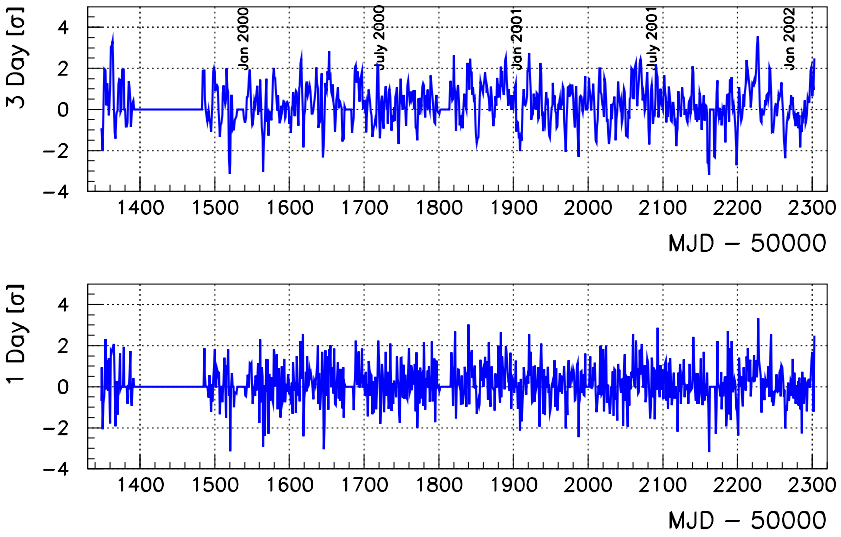

Figure A.3: This figure shows the rolling significance of the excess found at the position of the Crab Nebula for the 1 and 3-day time scales. Entries are plotted according to the *first* day of the interval. Neighboring points are correlated for the 3-day time scale.

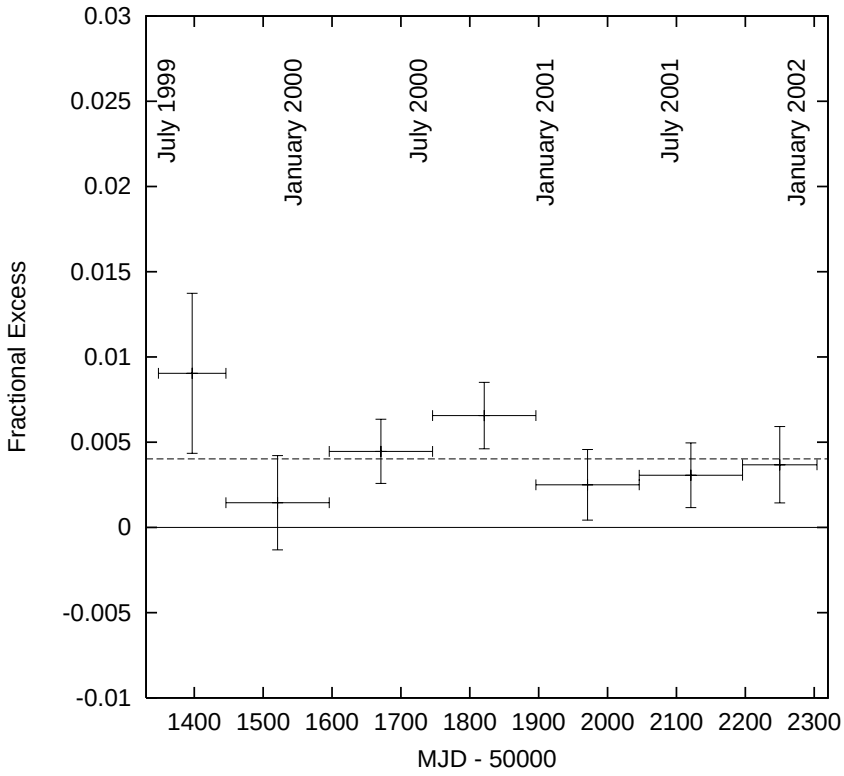

Figure A.4: This figure shows the fractional excess versus time from the Crab Nebula for the 150-day time scale. The choice of independent bins is the one which corresponds to the median χ^2 probability. The dashed line represents the constant that was fit to this set of bins.

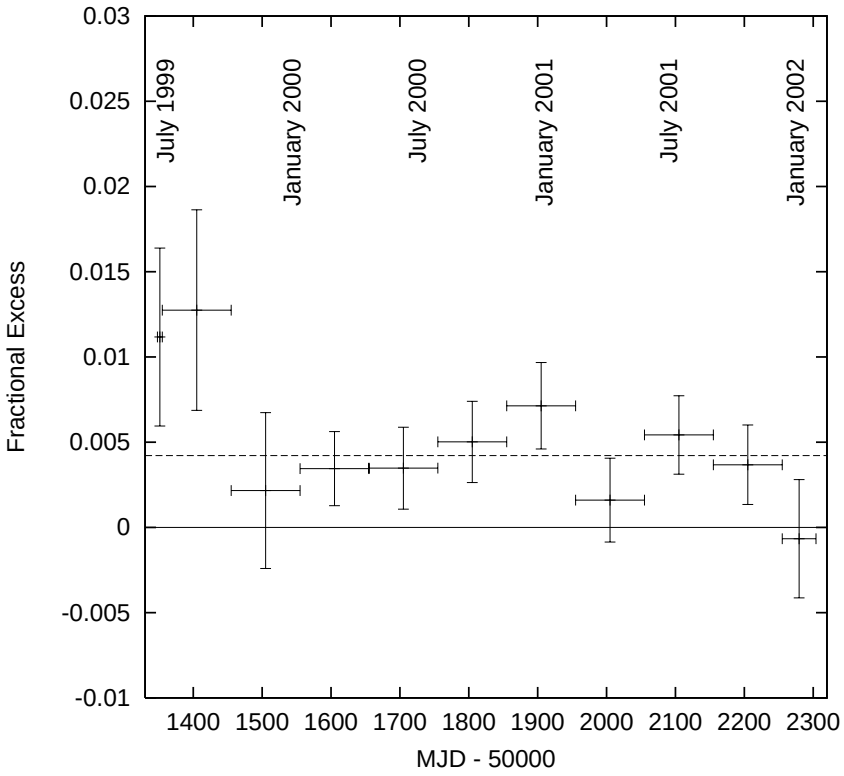

Figure A.5: This figure shows the fractional excess versus time from the Crab Nebula for the 100-day time scale. The choice of independent bins is the one which corresponds to the median χ^2 probability. The dashed line represents the constant that was fit to this set of bins.

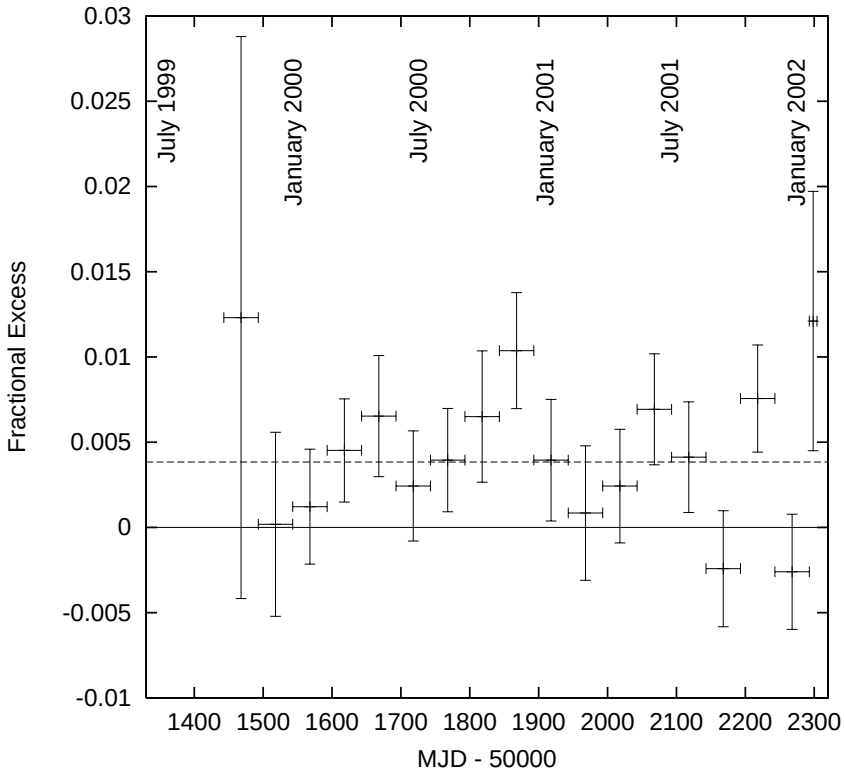

Figure A.6: This figure shows the fractional excess versus time from the Crab Nebula for the 50-day time scale. The choice of independent bins is the one which corresponds to the median χ^2 probability. The dashed line represents the constant that was fit to this set of bins.

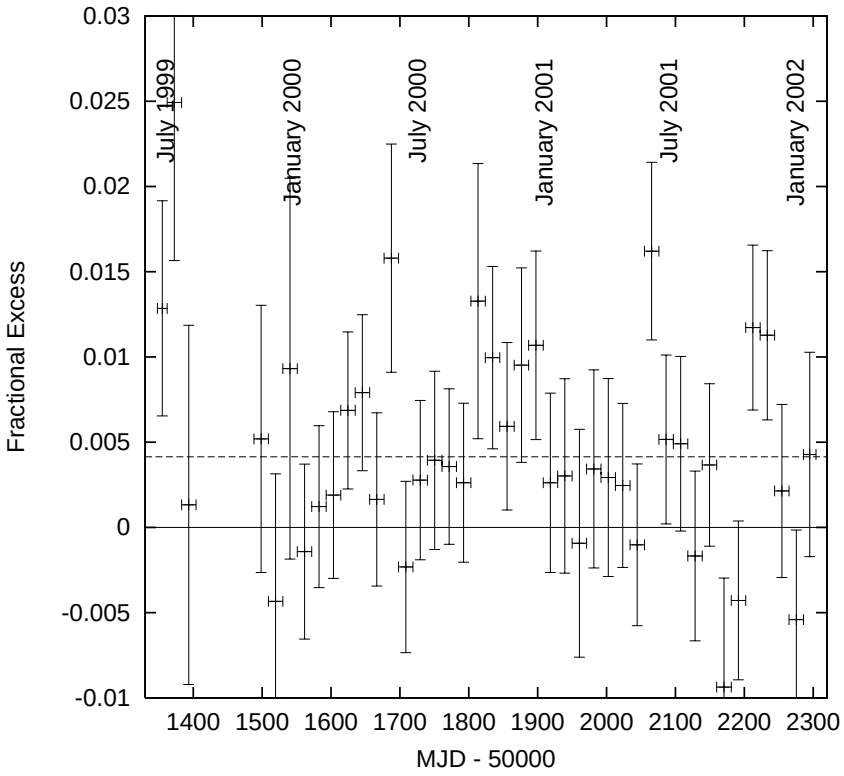

Figure A.7: This figure shows the fractional excess versus time from the Crab Nebula for the 21-day time scale. The choice of independent bins is the one which corresponds to the median χ^2 probability. The dashed line represents the constant that was fit to this set of bins.

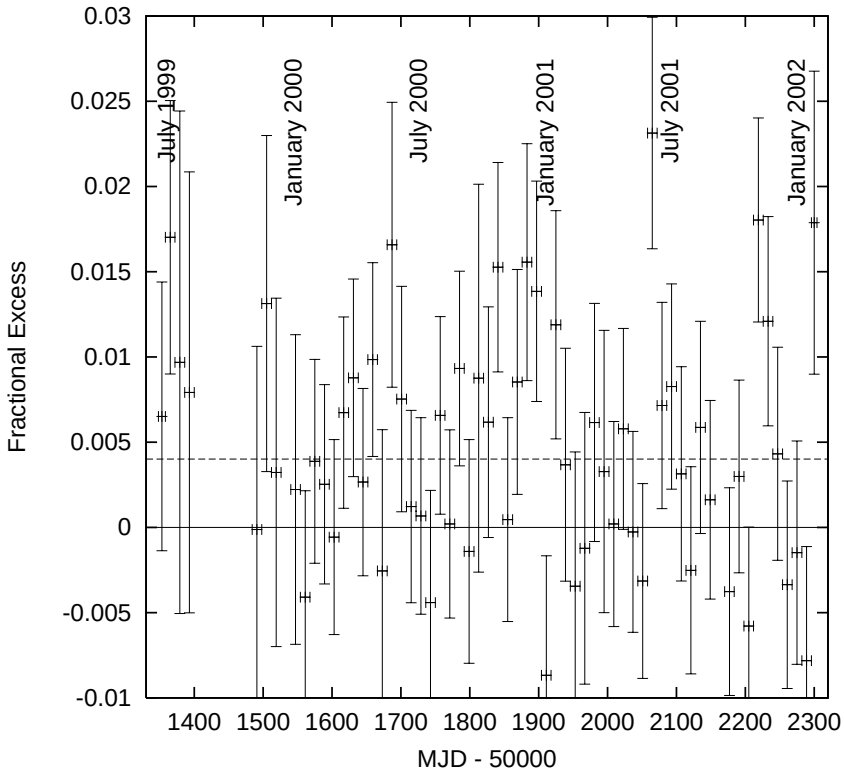

Figure A.8: This figure shows the fractional excess versus time from the Crab Nebula for the 14-day time scale. The choice of independent bins is the one which corresponds to the median χ^2 probability. The dashed line represents the constant that was fit to this set of bins.

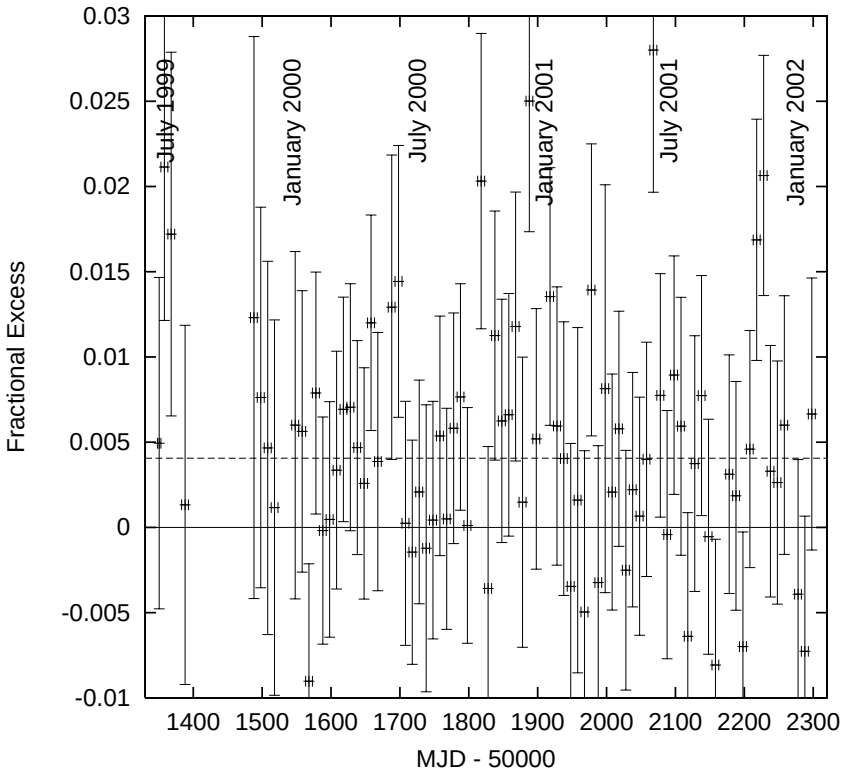

Figure A.9: This figure shows the fractional excess versus time from the Crab Nebula for the 10-day time scale. The choice of independent bins is the one which corresponds to the median χ^2 probability. The dashed line represents the constant that was fit to this set of bins.

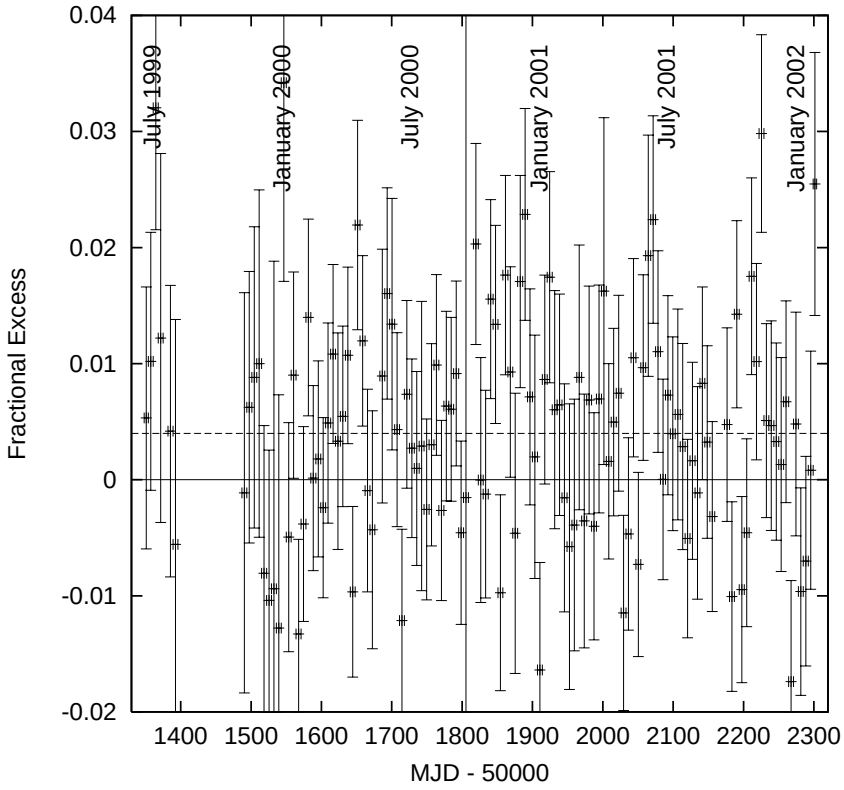

Figure A.10: This figure shows the fractional excess versus time from the Crab Nebula for the 7-day time scale. The choice of independent bins is the one which corresponds to the median χ^2 probability. The dashed line represents the constant that was fit to this set of bins.

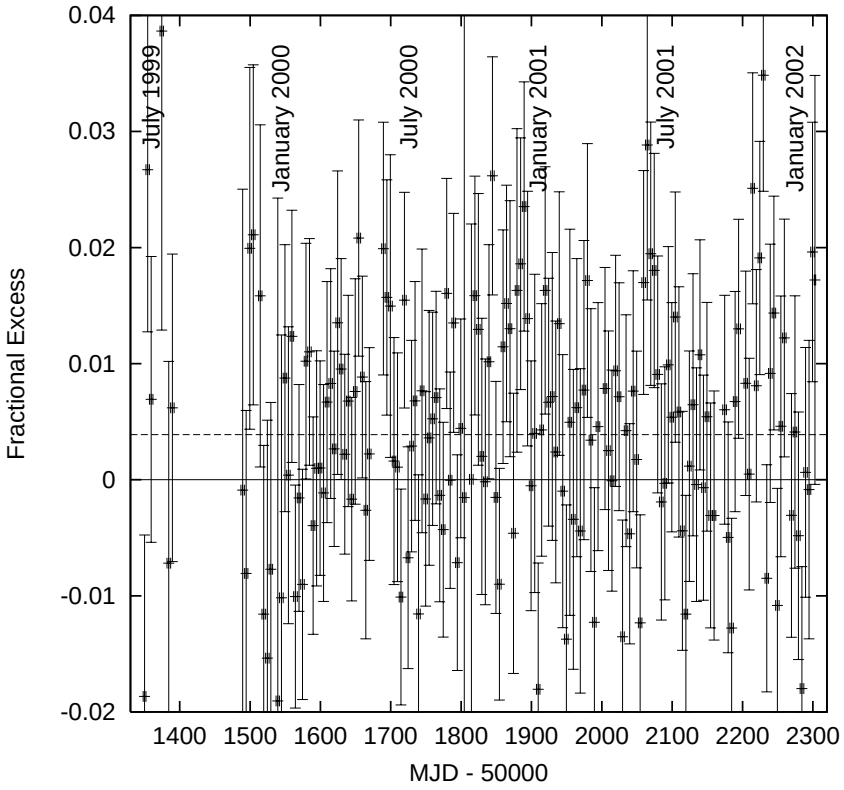

Figure A.11: This figure shows the fractional excess versus time from the Crab Nebula for the 5-day time scale. The choice of independent bins is the one which corresponds to the median χ^2 probability. The dashed line represents the constant that was fit to this set of bins.

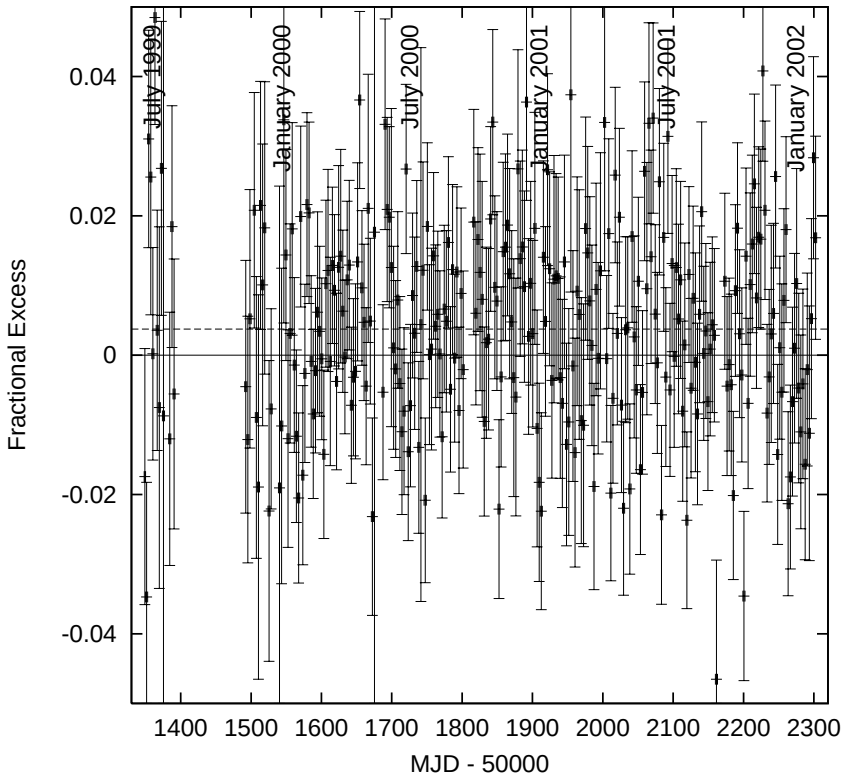

Figure A.12: This figure shows the fractional excess versus time from the Crab Nebula for the 3-day time scale. The choice of independent bins is the one which corresponds to the median χ^2 probability. The dashed line represents the constant that was fit to this set of bins.

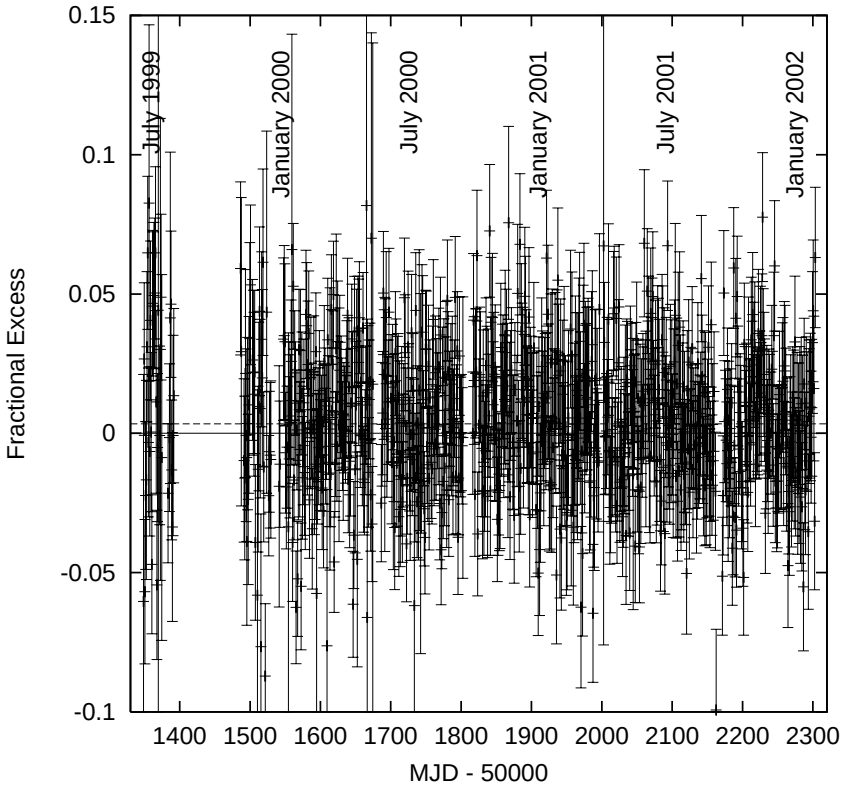

Figure A.13: This figure shows the fractional excess versus time from the Crab Nebula for the 1-day time scale. The choice of independent bins is the one which corresponds to the median χ^2 probability. The dashed line represents the constant that was fit to this set of bins.

Appendix B

Time Scale Plots for Mrk 421

This appendix contains figures referred to in Chapter 6. These plots are used in the analysis of the temporal behavior of the observed excess from Mrk 421 on eleven short-term time scales. The first three figures show the rolling significance for the bin centered on Mrk 421 for the eight time scales not shown in Section 6.2.2. These were used to identify the appropriate time bin of maximum significance in the maximum deviation method. In these plots, the significance of the number of excess events detected is calculated for the appropriate time bin beginning on the date of the point. Neighboring points for the time scales longer than 1 day are highly correlated. The remaining ten figures show the fractional excess versus time for the ten time scales not shown in Section 6.2.2. These plots illustrate the all possibility method, which determined that the signal from Mrk 421 was accumulated in a manner that is consistent with being constant in time for all time scales less than 30 days with the exception of the 1 day time scale. Minor inconsistencies with constant behavior are found on the 3 largest time scales. The choice of independent bins shown is the one which corresponds to the median χ^2 probability. The constant fit to these bins is also shown. In each of the figures the 2 vertical solid lines indicate the duration of the flaring period of Mrk 421 as identified using information from the RXTE all-sky monitor. The method for identifying this flaring period is discussed in Section 6.3.1.

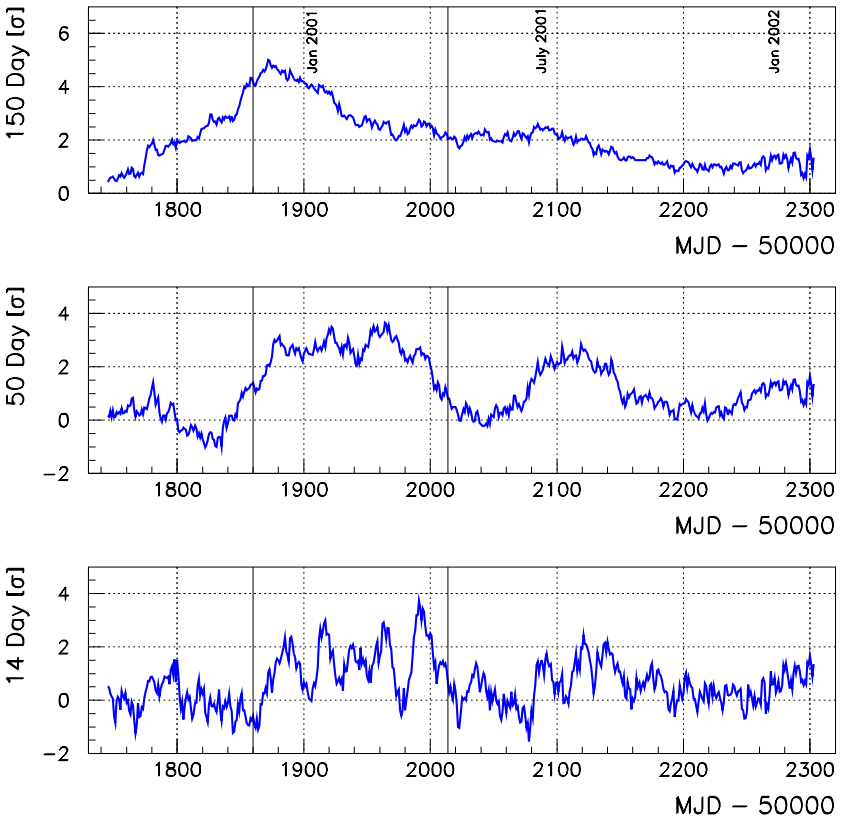

Figure B.1: This figure shows the rolling significance observed at the bin centered on Mrk 421 versus time for the 14, 50, and 150-day time scales. Entries are plotted according to the *first* day of the interval. Neighboring points are correlated. The 2 vertical solid lines indicate the duration of the flaring period of Mrk 421 as identified using information from the RXTE all-sky monitor.

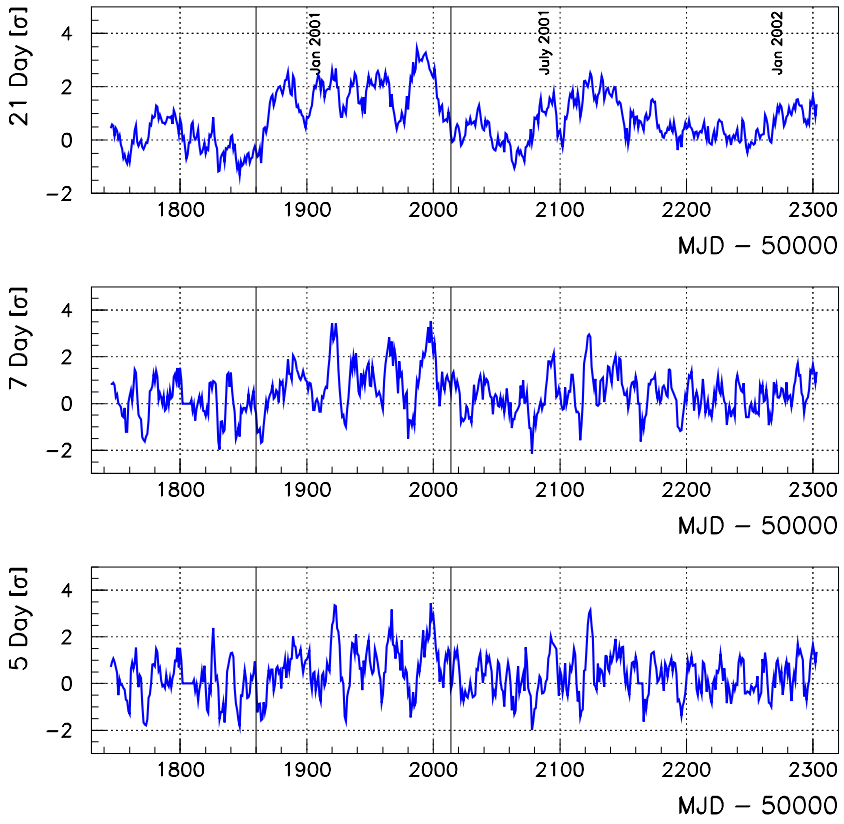

Figure B.2: This figure shows the rolling significance observed at the bin centered on Mrk 421 versus time for the 5, 7, and 21-day time scales. Entries are plotted according to the *first* day of the interval. Neighboring points are correlated. The 2 vertical solid lines indicate the duration of the flaring period of Mrk 421 as identified using information from the RXTE all-sky monitor.

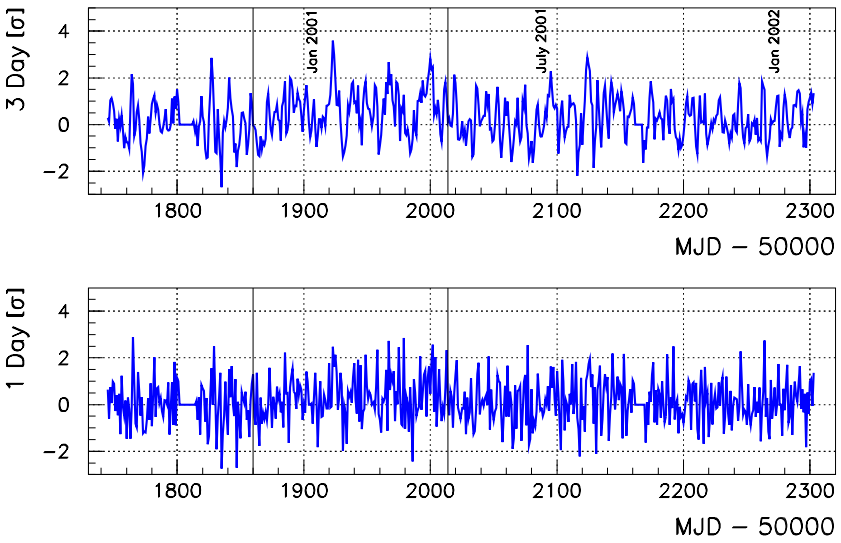

Figure B.3: This figure shows the rolling significance observed at the bin centered on Mrk 421 versus time for the 1 and 3-day time scales. Entries are plotted according to the *first* day of the interval. Neighboring points are correlated for the 3-day time scale. The 2 vertical solid lines indicate the duration of the flaring period of Mrk 421 as identified using information from the RXTE all-sky monitor.

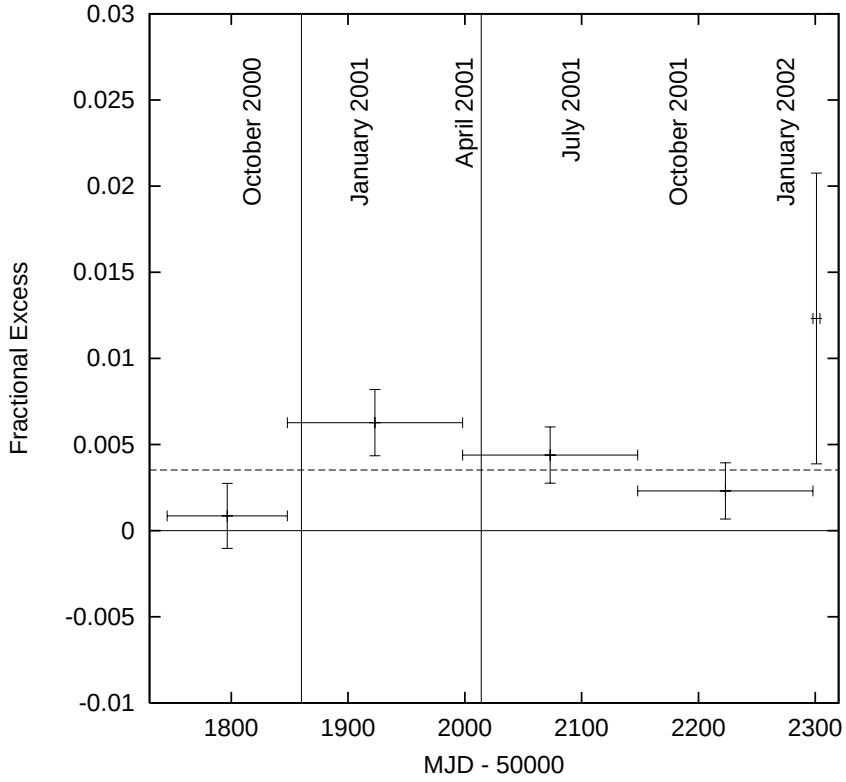

Figure B.4: This figure shows the fractional excess observed at the position of Mrk 421 versus time for the 150-day time scale. The dashed line is the value resulting from a fit of this information to a constant. The choice of independent bins corresponds to the median χ^2 probability. The 2 vertical solid lines indicate the duration of the flaring period of Mrk 421 as identified using information from the RXTE all-sky monitor.

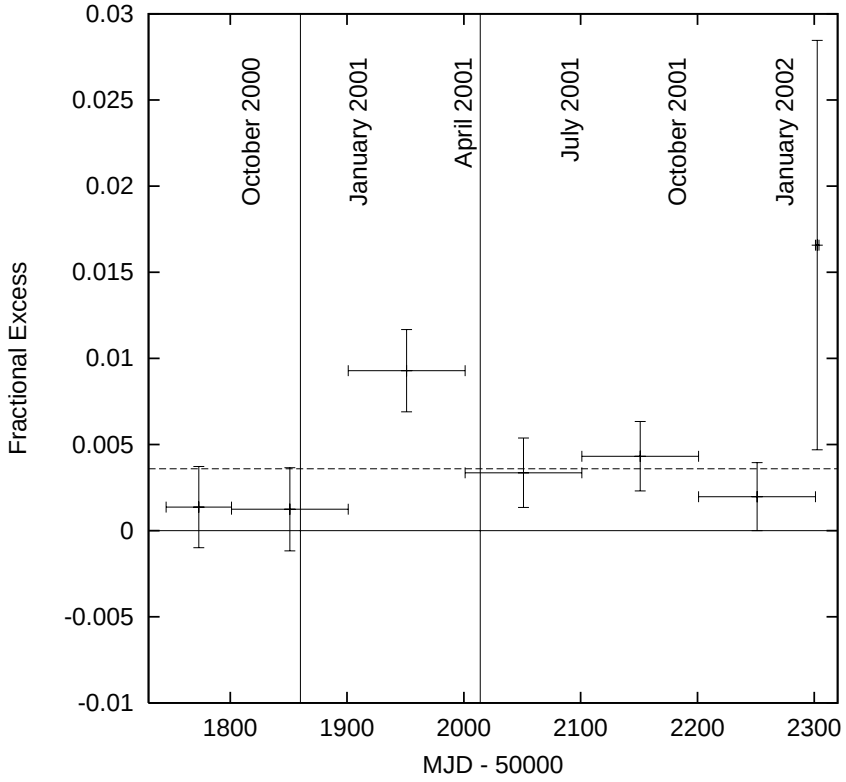

Figure B.5: This figure shows the fractional excess observed at the position of Mrk 421 versus time for the 100-day time scale. The dashed line is the value resulting from a fit of this information to a constant. The choice of independent bins corresponds to the median χ^2 probability. The 2 vertical solid lines indicate the duration of the flaring period of Mrk 421 as identified using information from the RXTE all-sky monitor.

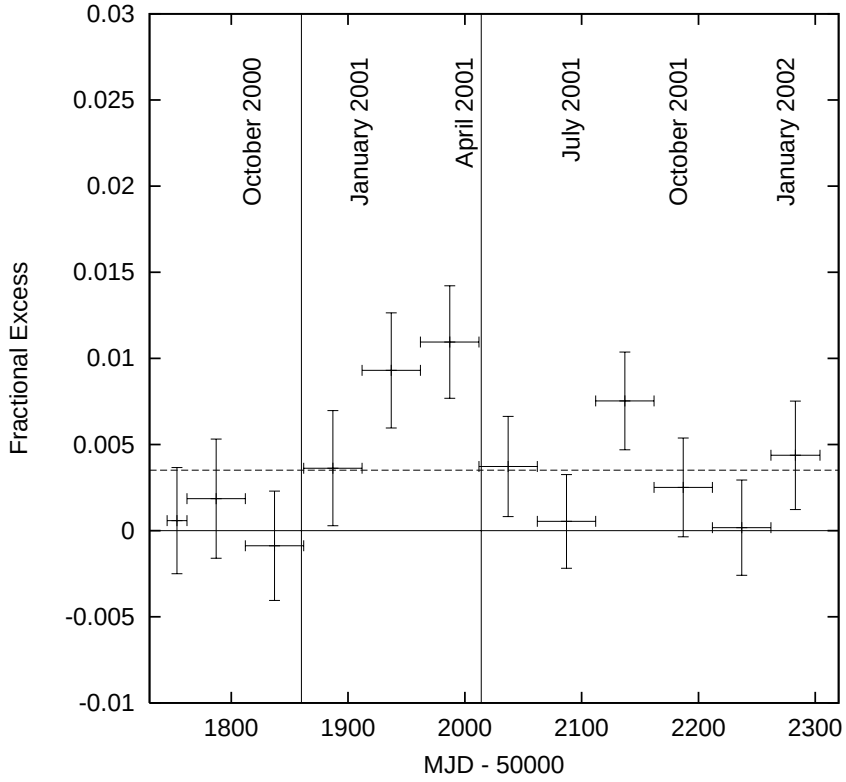

Figure B.6: This figure shows the fractional excess observed at the position of Mrk 421 versus time for the 50-day time scale. The dashed line is the value resulting from a fit of this information to a constant. The choice of independent bins corresponds to the median χ^2 probability. The 2 vertical solid lines indicate the duration of the flaring period of Mrk 421 as identified using information from the RXTE all-sky monitor.

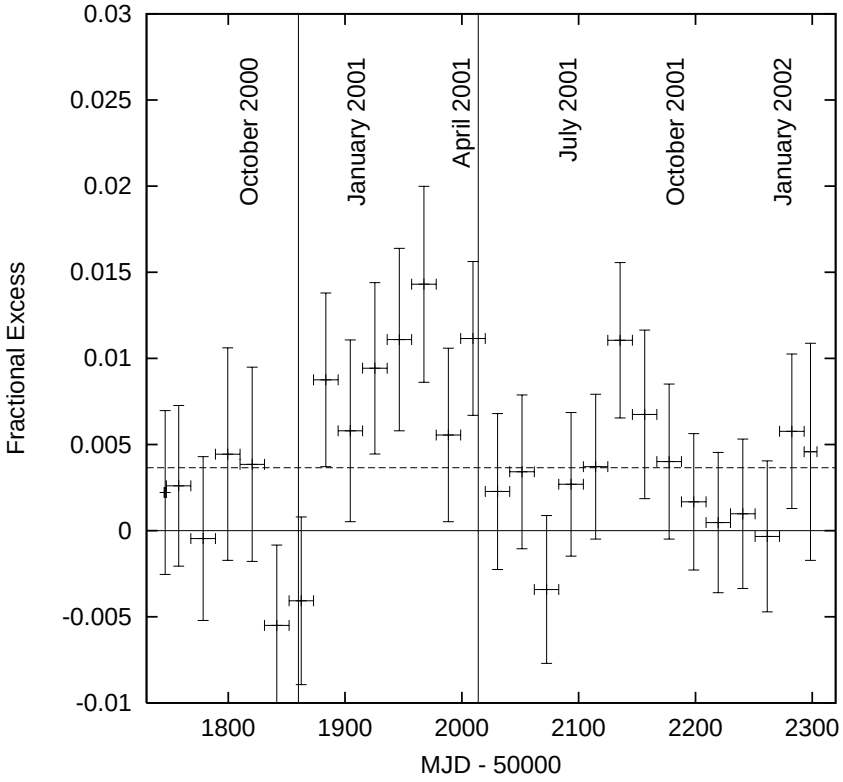

Figure B.7: This figure shows the fractional excess observed at the position of Mrk 421 versus time for the 21-day time scale. The dashed line is the value resulting from a fit of this information to a constant. The choice of independent bins corresponds to the median χ^2 probability. The 2 vertical solid lines indicate the duration of the flaring period of Mrk 421 as identified using information from the RXTE all-sky monitor.

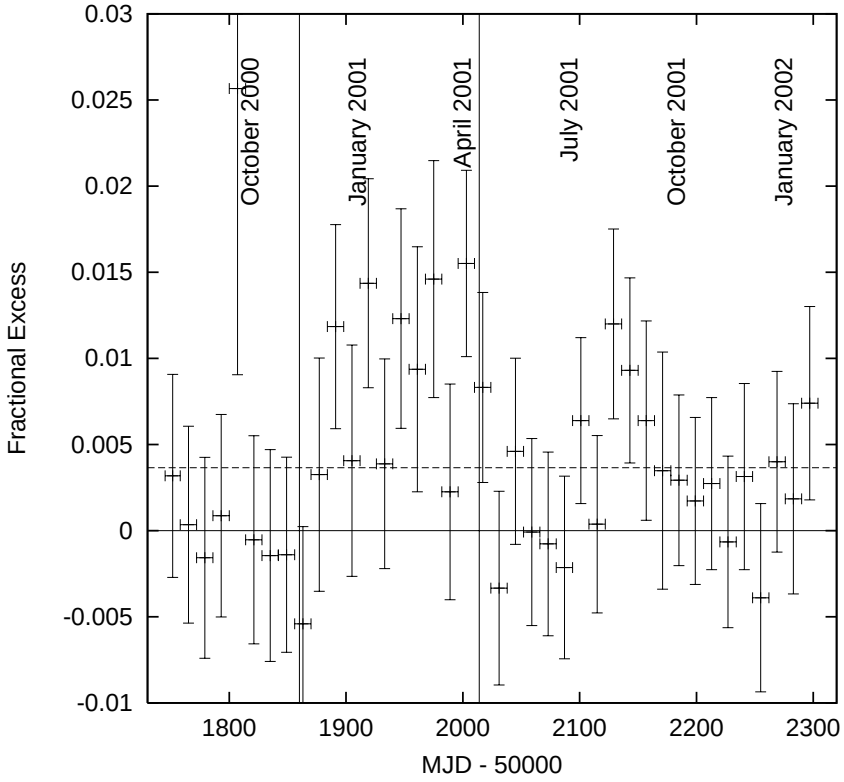

Figure B.8: This figure shows the fractional excess observed at the position of Mrk 421 versus time for the 14-day time scale. The dashed line is the value resulting from a fit of this information to a constant. The choice of independent bins corresponds to the median χ^2 probability. The 2 vertical solid lines indicate the duration of the flaring period of Mrk 421 as identified using information from the RXTE all-sky monitor.

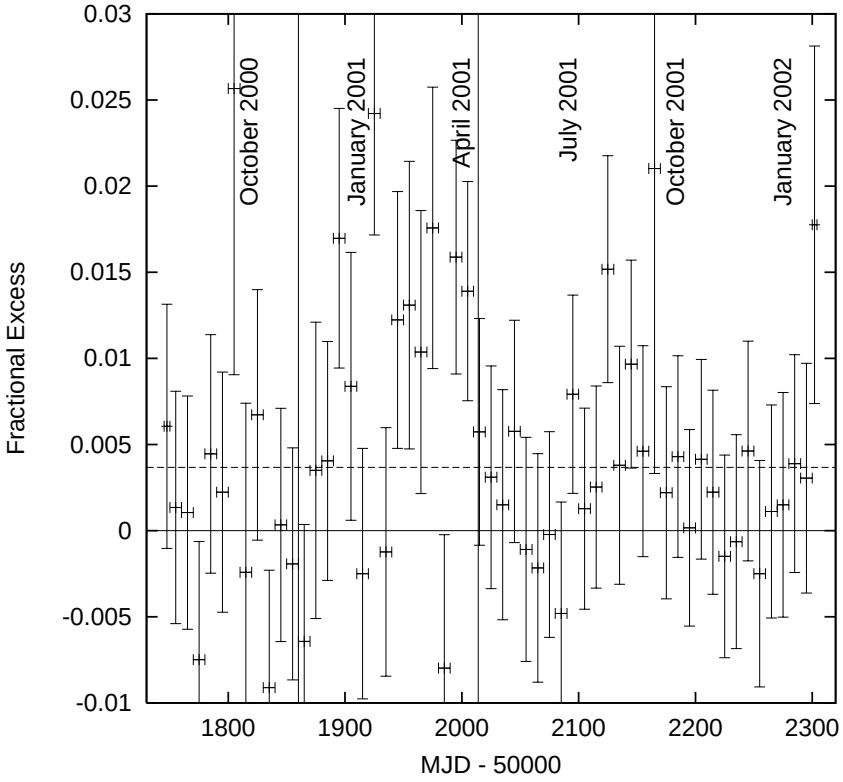

Figure B.9: This figure shows the fractional excess observed at the position of Mrk 421 versus time for the 10-day time scale. The dashed line is the value resulting from a fit of this information to a constant. The choice of independent bins corresponds to the median χ^2 probability. The 2 vertical solid lines indicate the duration of the flaring period of Mrk 421 as identified using information from the RXTE all-sky monitor.

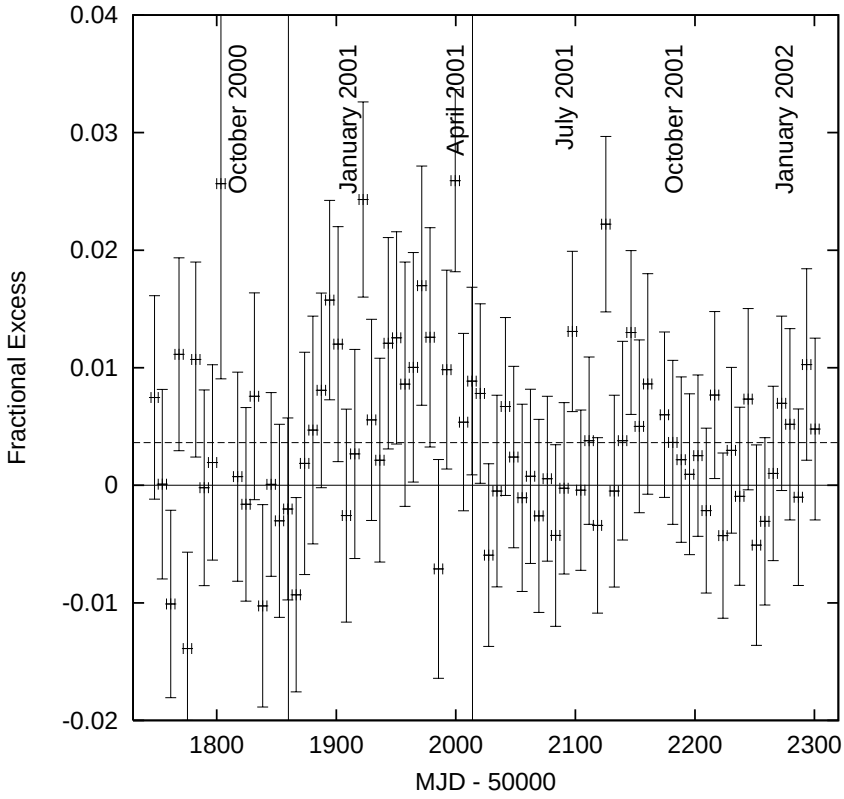

Figure B.10: This figure shows the fractional excess observed at the position of Mrk 421 versus time for the 7-day time scale. The dashed line is the value resulting from a fit of this information to a constant. The choice of independent bins corresponds to the median χ^2 probability. The 2 vertical solid lines indicate the duration of the flaring period of Mrk 421 as identified using information from the RXTE all-sky monitor.

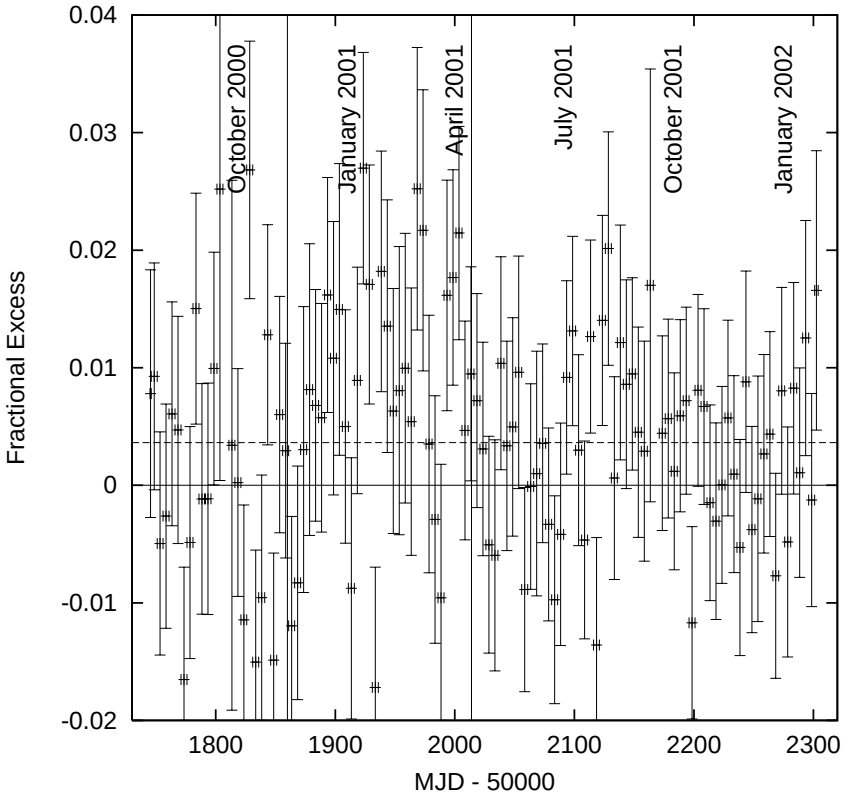

Figure B.11: This figure shows the fractional excess observed at the position of Mrk 421 versus time for the 5-day time scale. The dashed line is the value resulting from a fit of this information to a constant. The choice of independent bins corresponds to the median χ^2 probability. The 2 vertical solid lines indicate the duration of the flaring period of Mrk 421 as identified using information from the RXTE all-sky monitor.

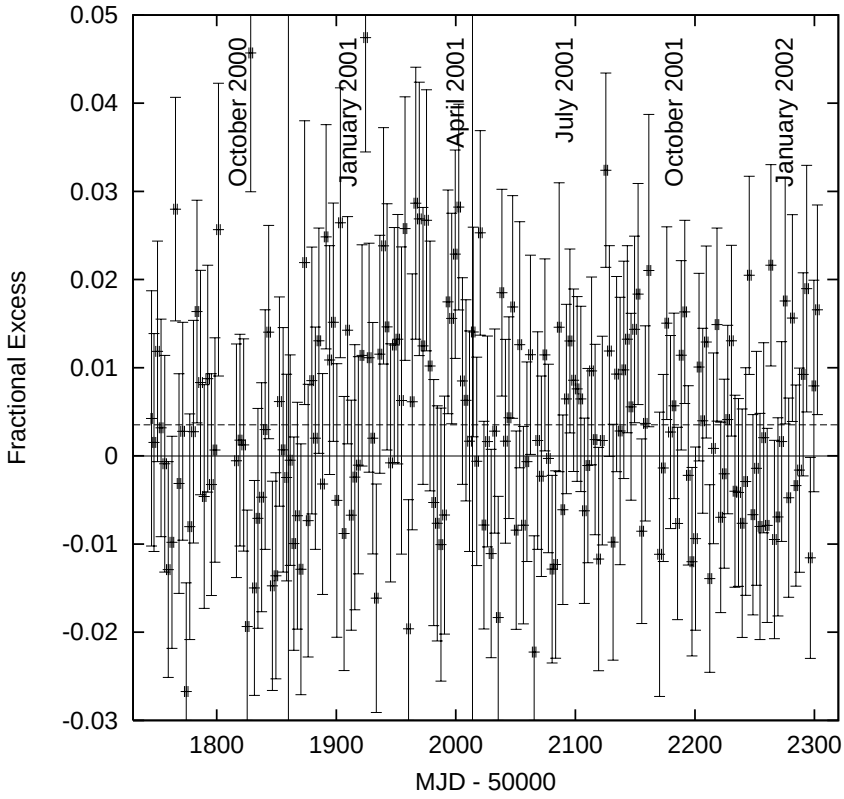

Figure B.12: This figure shows the fractional excess observed at the position of Mrk 421 versus time for the 3-day time scale. The dashed line is the value resulting from a fit of this information to a constant. The choice of independent bins corresponds to the median χ^2 probability. The 2 vertical solid lines indicate the duration of the flaring period of Mrk 421 as identified using information from the RXTE all-sky monitor.

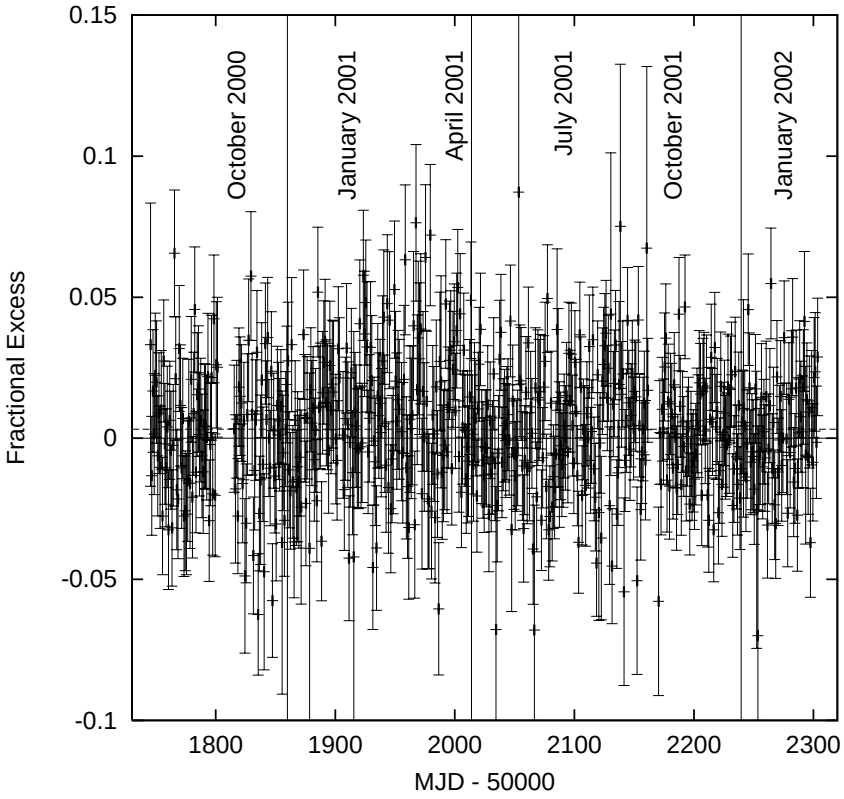

Figure B.13: This figure shows the fractional excess observed at the position of Mrk 421 versus time for the 1-day time scale. The dashed line is the value resulting from a fit of this information to a constant. The choice of independent bins corresponds to the median χ^2 probability. The 2 vertical solid lines indicate the duration of the flaring period of Mrk 421 as identified using information from the RXTE all-sky monitor.

Appendix C

Detailed Analysis of the Mrk 421 Signal

Since the detection of Mrk 421 represents the second source of TeV photons detected by Milagro, the same analysis is performed on the detected excess during the RXTE flare interval as is described for the Crab in Section 5.3. Again, the purpose is to explore how the Milagro detector performs versus expectations. The availability of a second source to make statements about how the analysis performs allows for stronger conclusions to be drawn regarding the techniques.

C.1 Performance of the Background Rejection Technique

As the performance of the background rejection technique, the X_2 cut, did not perform as expected from Monte Carlo simulations on the excess detected from the Crab Nebula, exploration of its effects on the signal from Mrk 421 is undertaken. Without the X_2 cut, 3,416,497 events are found in the bin centered on Mrk 421, yielding an excess above the expected background level, corrected for signal contamination, of 7380 ± 1908 events or 3.9σ. Therefore, Milagro has detected emission from Mrk 421 without use of the background detection technique. As discussed in Chapter 5, this is not the case for the signal from the Crab Nebula. Other dissimilarities are found as well in the performance of the technique. First, use of the X_2 cut does decrease the number of excess events from Mrk 421, as expected. The excess utilizing the X_2 cut, 2563 ± 591, is $\sim$35% of the amount found without it. However, Monte Carlo simulations indicate that the excess should be reduced by 50% using the cut. Though a decrease in events is found, it is somewhat too large, although, given the errors, consistent with the

expectation. Second, the X_2 cut does not enhance the signal from Mrk 421 as much as it did on the Crab Nebula. The Q found for X2 is $1.1^{+0.5}_{-0.4}$ whereas a value of 1.6 is expected. While the Q is in agreement (1.0σ low), it is troubling that the cut performs so well on the Crab (Q=$5.5^{+\infty}_{-3.2}$), and not so well for Mrk 421. This difference (1.4σ) may be the result of spectral differences in the 2 sources, the difference in zenith angles the sources traverse, or even something unexplained. Regardless, it is clear that the background rejection technique is not completely understood.

Given the problems with the understanding of the background rejection technique, further exploration of how the observed Mrk 421 signal behaves as the X_2 cut is varied is undertaken. Figure C.1 shows the observed excess of events in the bin centered on Mrk 421 versus the X_2 cut utilized. As a cut of some value retains all of the events as a cut of a higher value, neighboring points are correlated. Also shown in Figure C.1 is the number of excess events predicted by Monte Carlo simulations. The predicted value is normalized in such a way that the prediction at a cut of $X_2 \geq 2.5$ is what was measured. As can be seen in the figure, the number of excess events detected from Mrk 421 is consistent with predictions for small values of the X_2 cut, while in poor agreement for the higher values of the cut. It should be noted that there are relatively poor statistics for the predictions at higher X_2 cuts. Thus some modest disagreement may be expected in this regime. Further, the correlations may make the disagreement in the plot at high values of the X_2 cut appear worse than actual. Comparing Figure C.1 to Figure 5.6 shows a distinct difference in the behavior of the excess from Mrk 421 and the Crab with the X_2 cut. For the Crab Nebula the excess at low values of the X_2 cut is too small compared to predictions, where it is consistent for Mrk 421. The opposite effect occurs at high values of the X_2 cut where the excess is consistent with predictions for the Crab, and low for Mrk 421. Given these differences it is difficult to evaluate how the background rejection technique truly performs.

Figure C.2 shows the significance observed from Mrk 421 versus the X_2 cut utilized. Also shown is that which would be predicted given the expected Q from Monte Carlo simulations. Again the expectations are normalized in such a manner that the value measured at $X_2 \geq 2.5$ is exactly correct. The predictions don't match the measured values very well. At high X_2 values this is likely a result of poor statistics in the simulation, but for the low values the effect is currently unexplained. What is also clear given the behavior of the significance versus X_2 cut, is that it does not help much in improving the detected significance from Mrk 421. As this is not the case with the Crab Nebula, it is clear that the X_2 cut is not well explained by the Monte Carlo simulations.

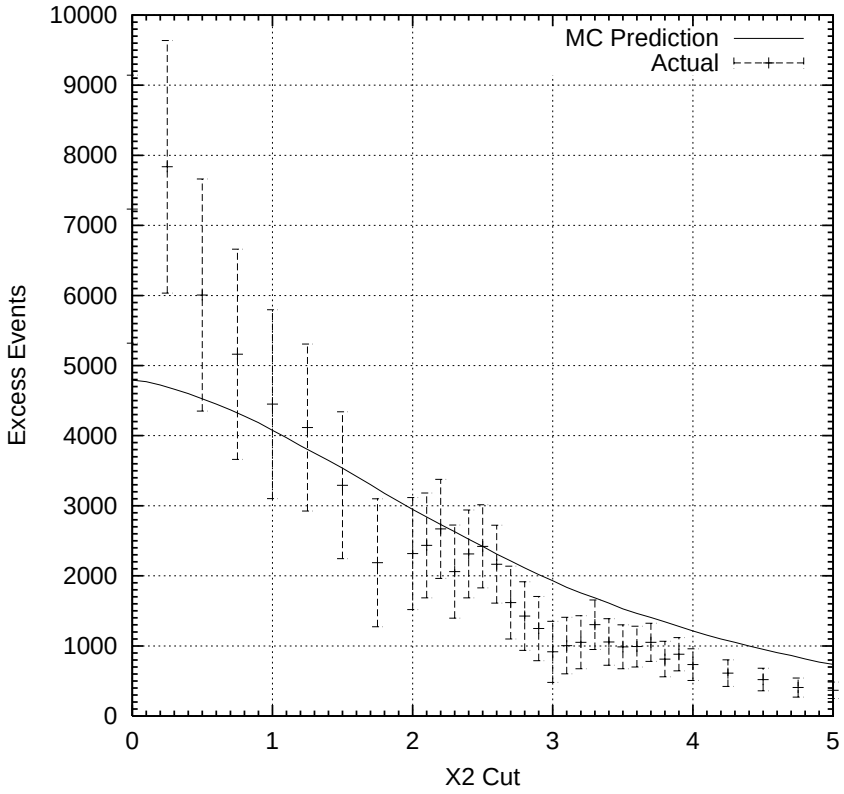

Figure C.1: Plot of the excess events observed in the bin centered on the true position of Mrk 421 versus X_2 cut. Neighboring points are correlated. The solid line represents the expected behavior from the Monte Carlo simulation normalized to the value of the excess measured with a cut keeping only events with $X_2 \geq 2.5$.

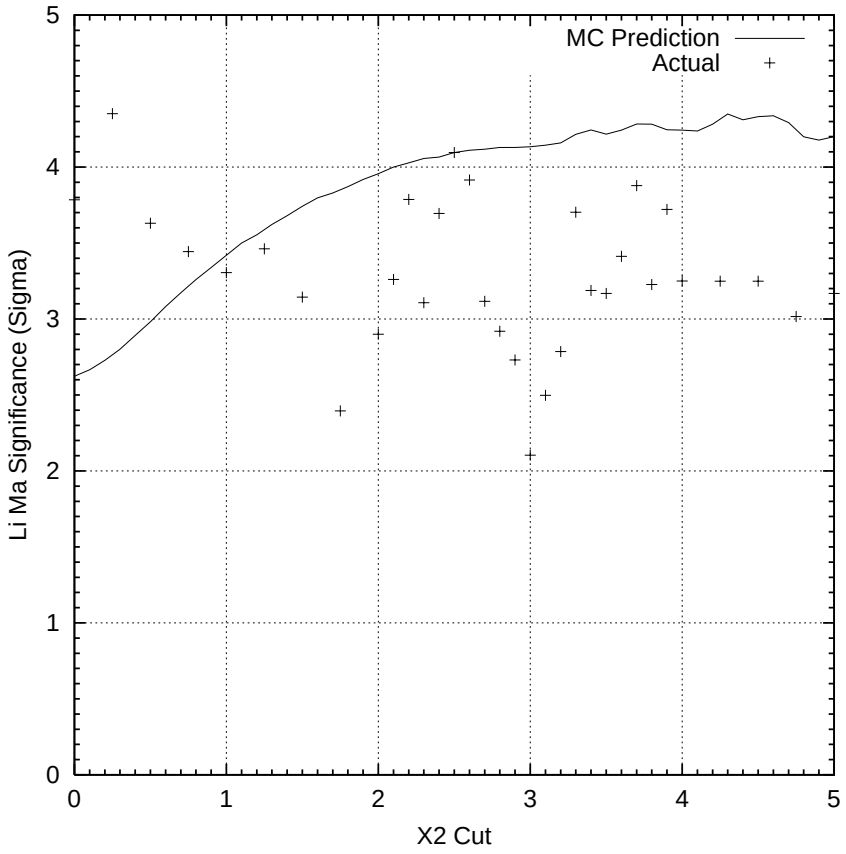

Figure C.2: Plot of the significance observed in the bin centered on the true position of Mrk 421 versus X_2 cut. Neighboring points are correlated. The solid line represents the predicted behavior from Monte Carlo simulation normalized to the value measured at $X_2 \geq 2.5$.

C.2 Performance Versus Bin Size

Given that the performance of the X_2 cut shows different results for the two detected sources and generally does not match the expectations from Monte Carlo simulations very well, exploration of how the Mrk 421 signal behaves for other cuts and analysis parameters is undertaken. Shown in Figure C.3 is the excess events observed from the Mrk 421 versus bin size. As a bin of smaller radius is completely contained by a bin of larger radius, neighboring points are correlated. The solid line in Figure C.3 is the predicted number of excess events. This value is determined using the percentage of events that should fall within the source bin, given the chosen data cuts, according to Monte Carlo simulations. The plot is normalized in a manner that the value measured at the bin size used for the analysis is exactly what is predicted. As can be seen there is agreement with the data and prediction from simulations, as is seen in the behavior of the excess from the Crab Nebula. Given the similar behavior in two sources, the Monte Carlo simulations predict the angular resolution of the detector reasonably. However, the same systematic trend is observed as for the Crab Nebula. Namely, at small bin sizes the number of excess events observed is low compared to predictions, and the number of excess events observed is consistently high compared to predictions at large bin sizes. While this effect is overstated by the correlations in the plot, it is again suggestive that the actual resolution of the detector may in fact be underestimated. As discussed in Section 5.3.2, a worse angular resolution would change the shape of the predicted curve. This is shown by the dashed line in Figure C.3 which is the predicted curve that results when the difference in true direction and reconstructed direction, Δ_{angle}, is made 20% worse for every reconstructed event in the Monte Carlo simulations (a simple approximation which degrades the angular resolution). This curve is also normalized in a manner such that it agrees with the measured value at r=1.1848°. While the original predicted curve is in statistical agreement with what is measured, the curve which represents the prediction with a worse angular resolution matches the measured values even better. Since this same trend is observed in the analysis of the signal from the Crab Nebula, the case that the Monte Carlo simulations predict that the angular resolution of the detector too well is strengthened.

Figure C.4 shows the observed significance of Mrk 421 versus bin size, with and without the X_2 cut. Also shown are the predictions from Monte Carlo simulations with no degradation in the angular resolution. The predicted significance with and without the X_2 cut is similar for bin radii below 1 degree, because the average angular resolution of showers not passing the X_2 cut is slightly better. The predictions from Monte Carlo simulations match the measured values when the X_2 cut is applied for Mrk 421, as they do for the signal from the Crab Nebula.

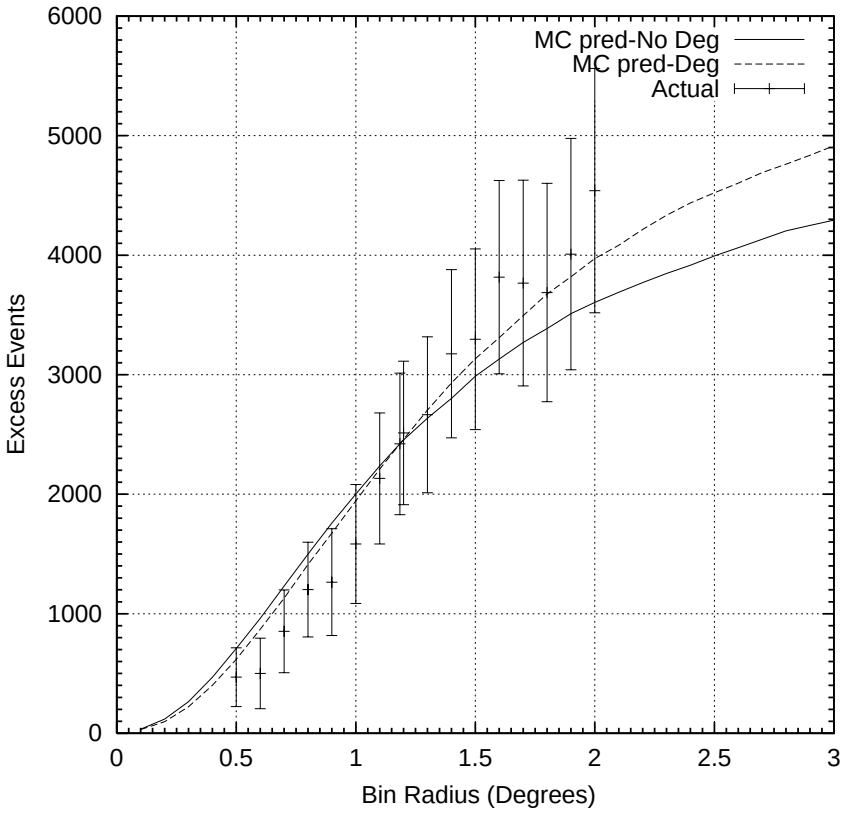

Figure C.3: Plot of the excess events observed in the bin centered on the true position of Mrk 421 versus bin size. Neighboring points are correlated. The solid line represents the expectations from Monte Carlo simulation normalized to agree with the results at the nominally optimal bin radius, $r = 1.1848$. The dashed line represents the expectations from Monte Carlo simulations, also normalized to agree with the results at $r = 1.1848$, if the angular resolution was systematically degraded by 20% from the original prediction.

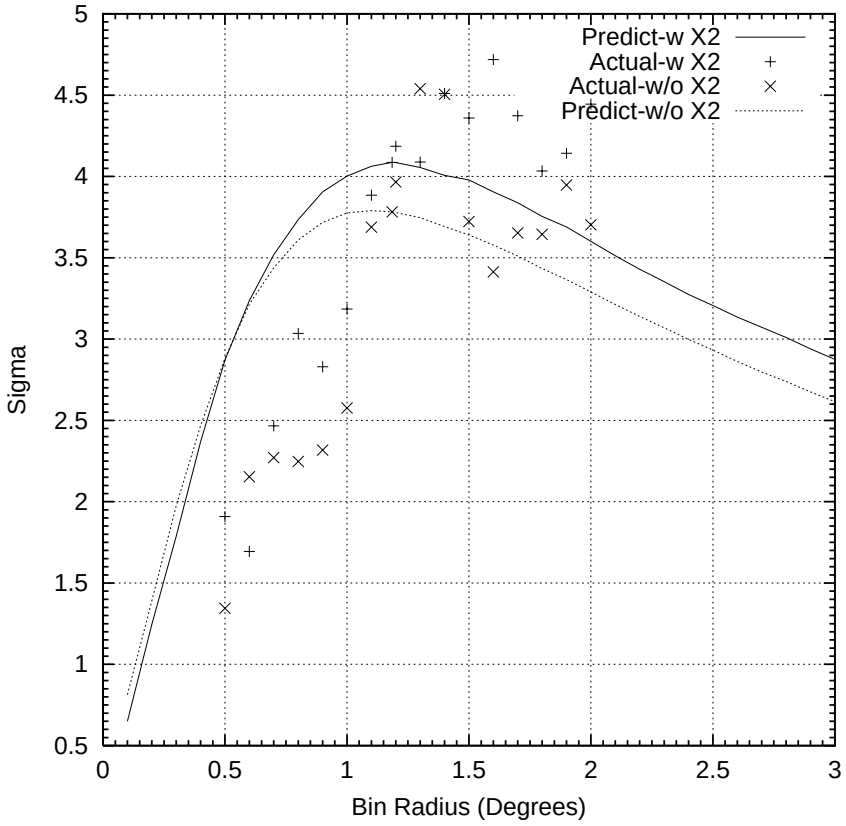

Figure C.4: Plot of the significance observed in the bin centered on the true position of Mrk 421 versus bin size. Shown are results with and without utilizing the X_2 cut. Neighboring points are correlated. The expected significance is shown by the solid lines, normalized in a manner that the prediction at the optimal bin radius, $r = 1.1848$ agree perfectly with what was measured.

The predictions also are not a bad match in the absence of an X_2 cut. This is not the case for the signal from the Crab Nebula, and provides further evidence that something odd is occurring with the observations of the Crab Nebula without utilizing the X_2 cut.

Naturally the better agreement of predictions with measured values of excess events seen when a degraded angular resolution is utilized translates into better agreement of the measured significance with predictions using a worse angular resolution. An angular resolution worse than Monte Carlo simulations predict would result in a larger bin size required to retain an ideal fraction fraction of signal events. Use of a larger bin increases the excess and significance found for Mrk 421, providing further motivation that the angular resolution is worse than predicted. Since degrading the angular resolution in the Monte Carlo also brings the flux measured from the Crab Nebula into better agreement with values from other instruments, there is much evidence that the Monte Carlo simulations predict the angular resolution to be too good.

C.3 Performance Versus N_{fit} Cut

Figure C.5 shows the detected significance from Mrk 421 versus N_{fit} cut for various bin sizes. Since a high N_{fit} cut improves the angular resolution of the detector, the optimal bin size will be smaller at larger values. Therefore, the results from a high N_{fit} cut should be evaluated with a smaller bin size than the 1.2 degree radius utilized in the standard analysis. As can be seen from the plot, for almost all bin sizes the significance is approximately constant for cuts up to 40 tubes participating in the fit. After a cut of 50 tubes the significance drops off for larger bin sizes. For smaller bin sizes, the significance increases slightly with increasing N_{fit} cut, until it drops off at high N_{fit} cuts. This is in agreement with the predictions from Monte Carlo simulations and indicates the the chosen N_{fit} cut of 20 PMTs is reasonable. This plot also shows that for bin sizes of 1.4 to 1.6 degrees radius, the significance found is higher than that found for the bin size of 1.2 degrees, for N_{fit} cuts of up to 100 PMTs participating in the fit. This same behavior is also observed for the Crab Nebula, providing motivation that the bin size may be too small. As discussed earlier, this effect would be justified if the Monte Carlo simulations predict to good an angular resolution for the detector.

C.4 Performance Versus Zenith Angle

Figure C.6 shows the excess of events detected from Mrk 421 for various zenith angle bins. The majority of the detected excess comes from zenith angles of less

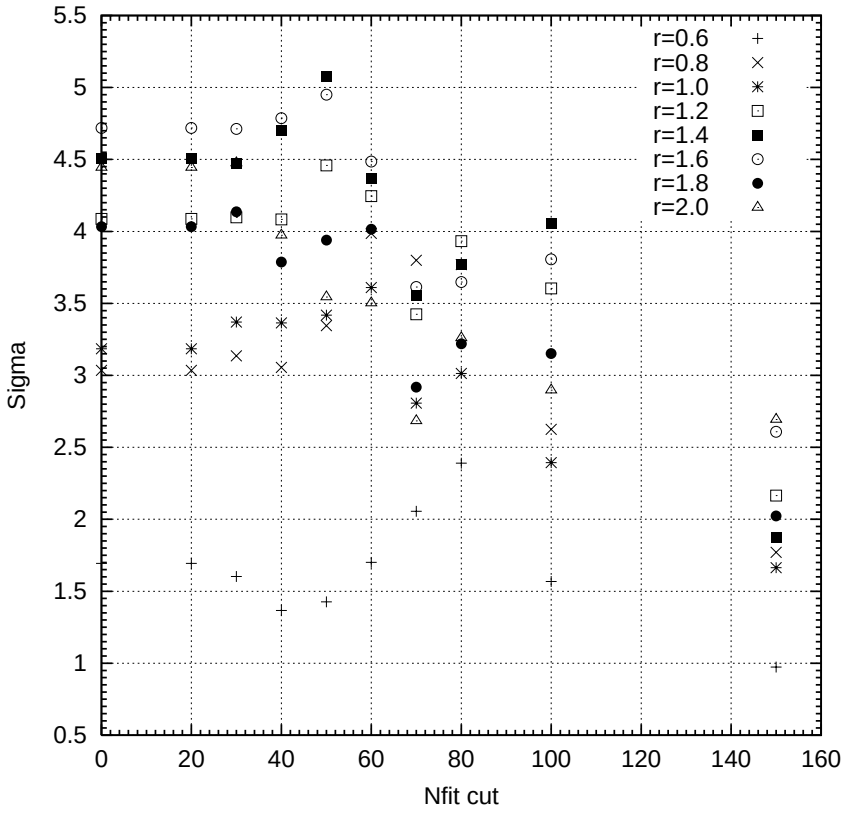

Figure C.5: Plot of the significance observed in the bin centered on the true position of Mrk 421 versus N_{fit} cut for various bin sizes. Neighboring points are correlated.

than 10 degrees. This behavior is different than was observed from the Crab, and is also in slight disagreement with what would be expected. The effective area for Milagro shown in Figure 3.18 is relatively constant out to 20 degrees, after which a decrease is seen. This decrease is not dramatic until zenith angles greater than 30 degrees are reached. Given the exposure shown in Figure 6.13, which is approximately constant for each zenith angle bin, it would be expected that the excess versus theta bin would follow a steady trend downward, which is not the case. Although it should be noted that this disagreement is minor as only 1 point in the plot, $10 \leq \theta \leq 20$ degrees, does not behave as expected. Given that the much of the detected excess from Mrk 421 is at small zenith angles, which is not the case for the Crab Nebula, a θ dependence in the X_2 cut could explain some of the differences observed in the performance of that cut.[1]

C.5 Re-reconstruction Effects

Upon receiving notification that the flux from Mrk 421 had increased dramatically, raw data initially reconstructed in the direction of Mrk 421 was saved to tape. This began on January 22, 2001, some time after the improved core fitter and different curvature correction had been incorporated into the online reconstruction. These raw data were re-reconstructed using the improved PMT calibration. Using this re-reconstructed data, when available, instead of the online reconstructed data did improve the significance of the excess observed from Mrk 421 slightly. The significance detected from Mrk 421 improved from 4.0σ to 4.2σ for the entire duration of AGN study. For the flare interval identified with RXTE data, the significance improved from 4.3σ to 4.5σ. Dramatic increases in the significance were not expected. This is because studies, detailed in Section 5.7.2, showed that the major improvements in the quality of the re-reconstructed data used to analyze the Crab Nebula, as compared to the online data, resulted from the improved core fitting technique and different curvature correction. Since the effects of the re-reconstruction for Mrk 421 were minimal and because their incorporation into the analysis proved difficult, these results are not utilized in the analysis or the determination of the flux from Mrk 421.

[1] This possible dependence was not found when the Monte Carlo simulations were explored. However, low statistics made determination of the ideal cut for various zenith angles difficult. Therefore, a possible zenith angle dependence of the X_2 cut is not ruled out.

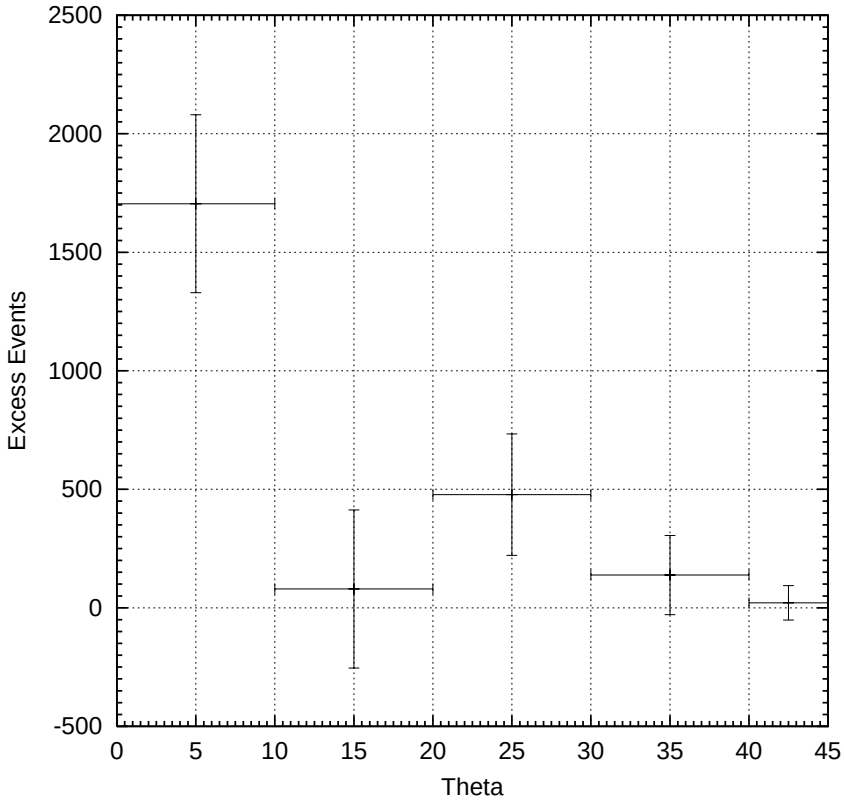

Figure C.6: Plot of the excess events observed in the bin centered on the true position of Mrk 421 versus zenith angle (θ).

Bibliography

Aharonian et al. 2000, *Astrophysical Journal*, **539**, 317

Aharonian et al. 2002a, *Astronomy and Astrophysics*, **384**, L23

Aharonian et al. 2002b, *Astronomy and Astrophysics*, Submitted for Publication

Aid et al. 1995, *Zeitschrift Für Physik C*, **69**, 27

Alexandreas et al. 1992, *Nuclear Instruments and Methods in Physics Research Section A*, **311**, 350

Alexandreas et al. 1993, *Nuclear Instruments and Methods in Physics Research Section A*, **328**, 570

Alexandreas et al. 2000, *Nuclear Instruments and Methods in Physics Research Section A*, **449**, 478

Amenomori et al. 1997, *Proceedings of the* 25^{th} *International Cosmic Ray Conference, Durban*, **5**, 245

Amenomori et al. 1999, *Astrophysical Journal*, **525**, L93

Atkins et al. 1999, *Astrophysical Journal*, **525**, L25

Atkins et al. 2000, *Astrophysical Journal*, **533**, L119

Atkins et al. 2002, *Astrophysical Journal*, Submitted for Publication

Barrau et al. 1998, *Nuclear Instruments and Methods in Physics Research Section A*, **416**, 278

Barrio et al. 1998, *The Magic Telescope, Design Study*, MPI-PhE/98-5

Biller 1996, *Astroparticle Physics*, **4**, 285

Biller et al. 1998, *Physical Review Letters*, **80**, 2992

Borione et al. 1994, *Nuclear Instruments and Methods in Physics Research Section A*, **346**, 329

Buckley 1999, *Astroparticle Physics*, **11**, 119

Catanese et al. 1998, *Astrophysical Journal*, **501**, 616

Catanese and Weekes 1999, *Publications of the Astronomical Society of the Pacific*, **111**, 1193

Cawley et al. 1990, *Experimental Astronomy*, **1**, 173

Chadwick et al. 1999, *Astrophysical Journal*, **513**, 163

Chantell et al. 1998, *Nuclear Instruments and Methods in Physics Research Section A*, **408**, 468

Constamante and Ghisellini 2002, *Astronomy and Astrophysics*, **384**, 56

Daum et al. 1997, *Astroparticle Physics*, **8**, 1

deJager and Harding 1992, *Astrophysical Journal*, **396**, 161

Dermer et al. 1992, *Astronomy and Astrophysics*, **256**, L27

Donato et al. 2001, *Astronomy and Astrophysics*, **375**, 739

Drury et al. 1994, *Astronomy and Astrophysics*, **287**, 959

Dwek et al. 1998, *Astrophysical Journal*, **508**, 106

GEANT C.P.L 1994, *GEANT Reference Manual, Version 3.21*

Gehrels et al. 2000, *Nature*, **404**, 363

Hara et al. 1993, *Nuclear Instruments and Methods in Physics Research Section A*, **332**, 300

Hartman et al. 1999, *The Astrophysical Journal Supplement Series*, **123**, 79

Heck et al. 1998, *CORSIKA: A Monte Carlo Code to Simulate Extensive Air Showers, tech report FZKA 6019*

Helene 1983, *Nuclear Instruments and Methods in Physics Research*, **212**, 319

Hillas 1996, *Space Science Reviews*, **75**, 17

Hillas et al. 1998, *Astrophysical Journal*, **503**, 744

Hinton et al. 2001, *Proceedings of the* 27^{th} *International Cosmic Ray Conference, Hamburg*, OG 2.03

Hoffman et al. 1999, *Reviews of Modern Physics*, **71(4)**, 897

Hofmann 2001, *Proceedings of the* 27^{th} *International Cosmic Ray Conference, Hamburg*, OG 2.05

Horan et al. 2002, *Astrophysical Journal*, **571**, 753

Kifune et al. 1995, *Astrophysical Journal*, **438**, L91

Knapp and Heck 1997, *Extensive Air Shower Simulation with CORSIKA: A User's Guide*

Koyama et al. 1995, *Nature*, **378**, 255

Krennrich et al. 2001, *Astrophysical Journal*, **560**, L45

Levinson and Blandford 1991, *Jets in Extragalactic Radio Sources*, ed. H. Röser, et al., New York: Springer-Verlag

Li and Ma 1983, *Astrophysical Journal*, **272**, 317

Mannheim 1993, *Astronomy and Astrophysics*, **269**, 67

Maraschi et al. 1992, *Astrophysical Journal*, **397**, L5

McCullough 1999, *Proceedings of the* 26^{th} *International Cosmic Ray Conference, Salt Lake City*, HE 6.01

McCullough 2001, *UC Santa Cruz Ph.D. Thesis*

Mukherjee et al. 1997, *Astrophysical Journal*, **490**, 116

Neshpor et al. 1998, *Astronomy Letters*, **24**, 134

Ong 1998, *Physics Reports*, **305**, 93

Oser et al. 2001, *Astrophysical Journal*, **547**, 949

Perlman 1999, *Proceedings of the GeV–TeV Gamma-Ray Astrophysics Workshop: Towards a Major Atmospheric Cherenkov Telescope VI, Snowbird, Utah*, p. 53

Primack et al. 1999, *Astroparticle Physics*, **11**, 93

Primack et al. 2000, *High Energy Gamma-Ray Astronomy*, Vol. 558, ed. F. Aharonian, et al., New York: American Institute of Physics Conference Proceedings

Protheroe et al. 1992, *Astroparticle Physics*, **1**, 113

Punch et al. 1992, *Nature*, **358**, 477

Quebert et al. 1995, *Towards a Major Atmospheric Cherenkov Detector IV, Padova*, p. 248

Quinn et al. 1996, *Astrophysical Journal*, **456**, L83

Quinn et al. 2001, *Proceedings of the* 27^{th} *International Cosmic Ray Conference, Hamburg*, OG 2.05

Sambruna et al. 1996, *Astrophysical Journal*, **463**, 444

Samuelson, F. 2002, *Private Communication*

Sikora et al. 1994, *Astrophysical Journal*, **421**, 153

Sinnis 2001, *Proceedings of the* 27^{th} *International Cosmic Ray Conference, Hamburg*, OG 2.02

Sullivan 2001, *Proceedings of the* 27^{th} *International Cosmic Ray Conference, Hamburg*, OG 2.05

Tanimori et al. 1998a, *Astrophysical Journal*, **497**, L25

Tanimori et al. 1998b, *Astrophysical Journal*, **492**, L33

Thompson 1997, *Neutron Stars and Pulsars*, ed. N. Shibazi, et al., Tokyo: University Academic Press

Tümer et al. 1999, *Astroparticle Physics*, **11**, 271

Ulrich et al. 1997, *Annual Review of Astronomy and Astrophysics*, **35**, 445

Urry 1999, *Astroparticle Physics*, **11**, 159

Urry and Padovani 1995, *Publications of the Astronomical Society of the Pacific*, **107**, 803

Vacanti et al. 1991, *Astrophysical Journal*, **377**, 467

Vermeulen and Cohen 1994, *Astrophysical Journal*, **430**, 467

Wascko 2001, *UC Riverside Ph.D. Thesis*

Weekes et al. 1989, *Astrophysical Journal*, **342**, 379

Yodh 2001, *Proceedings of the* 27^{th} *International Cosmic Ray Conference, Hamburg*, HE 1.01

Yoshikoshi et al. 1997, *Astrophysical Journal*, **487**, L65